UNIVERSITEIT VAN PRETORIA
UNIVERSITY OF PRETORIA
YUNIBESITHI YA PRETORIA

DEVELOPMENT OF A DESIGN TOOL FOR PCM BASED FREE COMFORT COOLING SYSTEM IN OFFICE BUILDINGS IN SOUTH AFRICA

TICHAONA KUMIRAI

Submitted in partial fulfilment of the requirements for the degree

MASTER OF APPLIED SCIENCE (MECHANICS)

in the

Department of Mechanical and Aeronautical Engineering
Faculty of Engineering, Built Environment and Information Technology

University of Pretoria

December 2017

ABSTRACT

Development of a Design Tool for PCM based Free Comfort Cooling System in Office Buildings in South Africa

Supervisor: Prof Jaco Dirker and Prof Josua P. Meyer

Department: Mechanical and Aeronautical Engineering

University: University of Pretoria

Degree: Master of Applied Science (Mechanics)

Keywords: PCM, Ventilation, cooling power, energy storage, phase transformation duration.

Abstract

Space cooling energy demand is projected to increase due to climate changes. For example, the South African climate change model projected warming to reach around 3 to 4°C along the coast, and 6 to 7°C in the interior. Such temperature increases will significantly increase the energy demand by building cooling applications. Thus, there is an urgent need to improve the energy efficiency in buildings and to reduce the peak cooling loads.

Various studies for building free cooling using phase change materials have shown to reduce or avoid the need for mechanical space cooling. Very few of these studies covered Southern African climatic conditions and no research was found reporting a comparison of free cooling thermal performance of different PCM types for an individual climate scenario. The purpose of this study was to experimentally evaluate and compare the cooling performance of three PCM materials in plate-air heat exchanger modules subjected to Southern African climatic conditions and to use the data to deduce empirical correlations that can be used by thermal designers to determine the number of modules required to maintain an objective cooling load within the range of operating conditions.

In this experimental investigation the cooling (discharging) performance of plate encapsulated Phase Change Materials (PCMs) for passive cooling applications were

evaluated as measured by its average effectiveness, cooling power, energy absorption and phase transformation duration. A test facility that mimics a PCM-air heat exchanger module installed in a ventilation duct was used to consider the impact of varying air flow rate and inlet air temperature. PCM plate encapsulations with a thickness of 10 mm orientated vertically and spaced at a pitch of 15 mm were investigated. The thermal storage characteristics of three commercial PCMs were considered. Two paraffin type PCMs with melting temperature ranges of 25 °C to 28 °C and 22 °C to 26 °C and one type salt hydrate with a phase change temperature range 24 °C to 25 °C were used in air flows ranging in temperature from 30 °C to 35 °C and duct air velocities ranging from 0.4 m/s to 0.9 m/s.

The results indicated that average effectiveness of the PCM modules decreased with increasing convective air mass flow rate. Increasing air mass flow rate (at constant inlet air temperature) or increasing the inlet air temperature (at constant air mass flow rate) increased the average cooling power. The phase transformation durations of the PCMs decreased as both the air flow rate and inlet air temperature increased. The salt hydrate (SP24E) module had the highest energy absorption capacity for all experimental conditions. The rate of energy absorption increased with inlet air temperature. From a design standpoint the desirable thermal performance of PCM is to have a high instantaneous heat absorption capacity and also extended over a longer period. Paraffinic PCMs met the first condition of high instantaneous heat absorption but did not meet the second condition of extended heat absorption duration. SP24E met the condition for extended heat absorption duration but had a lower instantaneous heat absorption capacity than the paraffin.

Empirically-based correlations for determining the number of modules to maintain an objective cooling load were developed using a multiple regression analysis technique. From this, air conditioning system designers can determine the number of modules (installed in parallel) required to maintain an objective cooling load within the range of operating conditions tested.
Keywords: PCM, Ventilation, cooling power, energy storage, phase transformation duration.

DECLARATION

I, the undersigned hereby declare that:

I understand what plagiarism is and I am aware of the University's policy in this regard;

The work contained in this thesis is my own original work;

I did not refer to work of current or previous students, lecture notes, handbooks or any other study material without proper referencing;

Where other people's work has been used this has been properly acknowledged and referenced;

I have not allowed anyone to copy any part of my thesis;

I have not previously in its entirety or in part submitted this thesis at any university for a degree.

Signature of student:

Name of student: Tichaona Kumirai

Student number: 14255988

Date: December 2017

DECLARATION ON PUBLICATIONS

The following manuscript was prepared and submitted for review in an international peer reviewed ISI rated journal of Building Engineering:

T. Kumirai, J. Dirker and J. Meyer, “Experimental analysis for thermal storage performance of three types of plate encapsulated phase change materials in air heat exchangers for ventilation applications”.

ACKNOWLEDGEMENT

I would like to acknowledge the following individuals and organizations for their assistance in my Master's research project:

a) Prof. Jaco Dirker, my supervisor for his technical guidance in designing the experimental test facility and designing the experiments, for the numerous technical discussions and for assistance in writing up.
b) Mr. Jan-Hendrik Grobler, Council for Scientific and Industrial Research (CSIR) Defence Peace Safety and Security for many discussions and his encouragement during the study.
c) Mr. Donald Kietse and Mr. Chris Govender, University of Pretoria Wind Tunnel Laboratory for their assistance with the construction of the experimental test facility.
d) The Council for Scientific and Industrial Research (CSIR) Built Environment for funding this research project.
e) Mak Langry, Marketing Development manager for BASF - The Chemical Company, Pretoria South Africa for providing with Neopor™ insulating material used in the experimental test facility.
f) Dr Pablo Dolado Thermal Engineering & Energy Systems Group University of Zaragoza, Spain for useful discussions during the study and also providing sample PCM plates.
g) My colleagues (Dr Joe Mapiravana, Dr Peter Klein, Sheldon Bole, Tobias Van Reenen and Dr Dirk Conradie) at the CSIR, Building Science and Technology (BST) competency area for their support and useful discussions during the study.
h) Mr. Theuns Knoetze, manager for BST competency area for believing in me and for his support.
i) My wife Adelaide and my two lovely daughters Ruvarashe (Tessa) and Ruvimbo (Tal) for the love and support.
j) The Almighty God (Covenant keeping God) for being my guide and helper throughout this project.

TABLE OF CONTENTS

LIST OF FIGURES

LIST OF TABLES

LIST OF ABBREVIATIONS

CFD	Computational Fluid Dynamics
CSIR	Council for Scientific and Industrial Research of South Africa
PCM	Phase Change Material
HX	Heat Exchanger
HVAC	Heating Ventilation and Air Conditioning
LHS	Latent Heat Storage
HTF	Heat Transfer Fluid
TES	Thermal Energy Storage
SANS	South Africa National Standard

LIST OF ALPHA-NUMERIC SYMBOLS

A	Cationic species	-
a_r	Fraction reacted	-
B	Anionic species	-
C_p	Specific heat capacity of sensible heat storage material at constant pressure	J/kg.K
$C_{p,s}$	Average specific heat capacity between T_{int} and T_m	J/kg.K
$C_{p,l}$	Average specific heat capacity between T_m and T_f	J/kg.K
$C_{p,air}$	Specific heat capacity of air	J/kg.K
$C_{p,dry\ air}$	specific heat capacity of dry air	J/kg.K
$C_{p,w}$	specific heat capacity of water vapour	J/kg.K
$C_{p,PCM}$	Specific heat capacity of PCM	J/kg.K
$C_0, C_1, C_2, C_3, C_4 C_5$	Correlation coefficients	-
e_{PCM}	Thickness of PCM	m
e_{Al}	Thickness of aluminium encapsulate	m
f_l	Fraction of heat storage material melted	-
h_m	Heat of fusion per unit mass	J/kg
h_r	Endothermic heat of reaction	J/kg
h_c	Convective heat transfer coefficient	$W/m^{2.}K$
H	Volumetric enthalpy	J/m^3
$L_{AD,}\ L_{BD,}\ L_{CD,} L_{EG,}\ L_{AH}$	Axial positions for components of the test section	m
m	Mass of heat storage medium	kg
m'	Absolute humidity	kg/m^3
$\dot{m}_{air}$	Air mass flow rate	kg/s
m_{PCM}	Mass of PCM	kg
n_{mod}	Number of modules	-
P_i	Instantaneous power delivered to the heating element	W
P	Barometric pressure	Pa
P_w	Partial pressure of water vapour	Pa
Q	Heat stored	J
q	Heat flux	W/m^2
$\dot{Q}_{Loss,Air}$	Rate of energy lost (cooling rate) from air	W
$\dot{Q}_{gain,ambient}$	Rate of energy lost to the surroundings	W
$\dot{Q}_{gain,PCM}$	Rate of heat absorbed by the PCM module	W
$\dot{Q}_{heater}$	Instantaneous rate of heat transfer from the heating element to the air	W
Q_{tot}	Energy stored by PCM during the experiments	Wh
$Q_{tot,spec}$	Theoretical energy stored by PCM as specified by PCM manufacturer	Wh
$\dot{Q}_{obj}$	Desired maintained cooling power	W
$\dot{Q}_i$	Cooling power delivered by PCM	W
$R_{duct(\dot{m})}$	Duct thermal resistance	K/W
$\bar{R}$	Average electrical resistance of heating element.	Ω

R_{Al}	Thermal resistance of the aluminium encapsulate	m^2K/W
$S(t)$	Position of phase change boundary at time t	m
T_m	PCM melting temperature	°C
T_{int}	Heat storage material initial temperature	°C
ΔT	Temperature change of heat storage medium	°C
T_f	Final temperature	°C
T_{PCM}	PCM temperature	°C
$\bar{T}_i$	Average inlet air temperature	°C
$\bar{T}_o$	Average outlet air temperature	°C
Δt	Phase transformation duration	seconds
$\bar{T}_{air}$	Mean bulk temperature	°C
T_a	Average room ambient air temperature	°C
ΔT_{pcm}	Temperature difference between air inlet temperature and PCM melting temperature.	°C
$\bar{T}_{od}$	Calculated average outdoor air temperature in the summer months	°C
$\bar{T}_{o,cor}$	Outlet air temperature corrected for heat losses	°C
T_{cal}	Calibrated temperature	°C
T_{PT100}	Temperature measured by PT100 probe	°C
V	Voltage	V
W	Air humidity ratio	kg/kg
z	Residual number of moles of water of crystallisation in the salt	-

GREEK SYMBOLS

δ	Uncertainty indicator	-
$\delta T_{cal,point}$	Thermocouple uncertainty for a calibration point	°C
δT_{PT100}	Uncertainty of PT100 temperature probe	°C
$\bar{\varepsilon}_m$	Effectiveness	-
ρ_{PCM}	PCM density	kg/m^3
$\rho_{i,air}$	Instantaneous air density	kg/m^3
λ_{Al}	Thermal conductivity of aluminium encapsulate	W/m.K
λ_{PCM}	PCM thermal conductivity	W/m.K
Δ	Difference	-

CHAPTER 1 **INTRODUCTION**

1.1 BACKGROUND

Due to South Africa's energy crisis and global climate change challenges, there is currently a major drive towards the use of renewable energy sources, and energy efficient and conservation interventions to ensure energy security for the country. Of all the energy users, the built environment has been identified as one of the largest untapped potential in energy efficiency opportunities and in reducing green-house gas emissions [1]. It has been estimated that as much as 30 to 40% of the world's primary energy is consumed by the building sector ("silent giant"). The biggest use in this sector is in heating and cooling applications, which contributes to at least a third of greenhouse gas emissions [2]. In South Africa, the largest single end-use contribution to energy consumption especially in commercial buildings (including office buildings, shopping centres, restaurants, and others) is from Heating, Ventilation and Air conditioning (HVAC) accounting as much as 26% of the total energy use (this excludes lighting, geysers, motors, pumps, and other specialised uses) [3]. South Africa is still dependent on conventional HVAC systems such as split unit air-conditioning systems, resistance heaters and centralised chiller plants which have high energy demands contributing an estimated 5400 MW (megawatts) nationally to electricity demand in peak periods. This figure is expected to increase due to climate changes [4]. The South African climate change model [5] predicts that by mid-century (2050) the South African coast will warm by around 1 to 2°C and the interior by around 2 to 3°C. By 2100, warming is projected to reach around 3 to 4°C along the coast, and 6 to 7°C in the interior [5]. There is an urgent need to improve the energy efficiency in buildings and reduce the peak heating and cooling loads. In order to reduce the energy demand of buildings, the South African government has implemented building regulations such as SANS 10400-XA [6] and SANS 204 [7] which attempts to save energy by means of the maximum allowable energy consumption per square meter of floor area per building classification for each of the climatic zones of South Africa.

The peak cooling energy demand and associated carbon emissions with regards to HVAC systems can be reduced by implementing thermal storage devices that are based on Phase Change Material (PCM) technology that operates using the “free cooling technique”.

This technique refers to a thermal energy storage device that is capable of storing cooling potential available in the night time ambient air. During the day time the cooling potential is retrieved from the thermal energy storage device in order to cool the building [8], [4], [9],[10].

The operation principle for a PCM-based free cooling technique is illustrated in Figure 1-1. During day time, dampers 1 and 4 are closed and dampers 2 and 3 are opened such that hot room air circulates through the PCM module. This causes the PCM to gradually melt which cools the air which is sent back to the room. During night time dampers 1 and 4 are opened and dampers 3 and 2 are closed. Hereby cool ambient air flows through the storage unit and receives heat from the liquid PCM which, as a result, solidifies if the temperature is below its phase change temperature. In this way melting and solidification of PCM occurs during the day and night respectively. Normally a separate thermal storage unit is used for storing of the cooling potential at night and generally a mechanical device (such as a fan) is used to move air (heat transfer fluid) [2], [8].

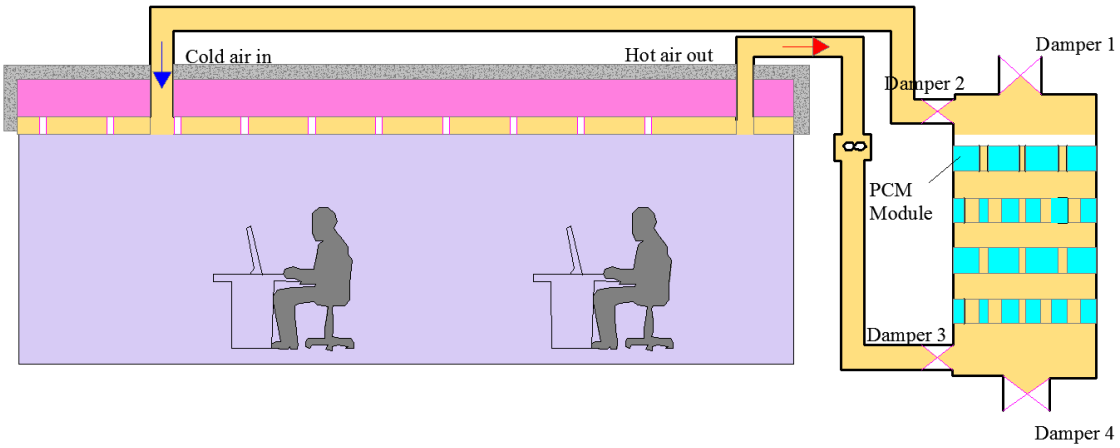

Figure 1.1. Working operation of a free cooling system adapted from [11].

Free cooling is unlike nocturnal ventilative (night) cooling which uses the building structure (e.g. walls) to act as the thermal storage medium. Free cooling is favoured over the nocturnal ventilative cooling because the cooling potential accumulated in free cooling can be extracted whenever it is needed by circulating outside ambient air or room air through the storage unit. The major problem with nocturnal ventilative cooling is that it is difficult to achieve a sufficiently high heat transfer coefficient to transfer heat between the room air and the building structure [12]. The heat transfer coefficients encountered in natural convection are usually much lower than those in forced convection [13]. In addition, night ventilation cooling is not effective due to relatively insufficient thermal capacity available in the building envelope [14].

Thermal energy storage in free cooling can be obtained via sensible heat transfer, latent heat transfer, or in some instances via a reversible chemical reaction. In sensible heat storage, thermal energy charging and discharging is accompanied with a temperature change of the storage media. Examples of sensible heat storage materials are rocks, masonry structures and water [15]. In latent heat storage, thermal energy is stored or released as a result of melting or solidification of the storage material [16]. This process occurs at a constant temperature for a pure material and within a small temperature range for impure materials [17]. Examples of latent heat storage materials (PCMs) suitable for building free cooling applications are inter alia paraffin wax, ice, fatty acids and salt hydrates.

Latent heat energy storage PCMs (and reversible chemical reaction materials) are favoured over sensible heat storage materials because of two major advantages:

- High energy density [18]: A PCM allows large amounts of energy to be stored in a relatively small volume, resulting in low storage media costs [4]. Morrison and Khalik [19] in their study aimed at assessing effects of phase change energy storage on the performance of air-based and liquid-based solar heating systems found that systems utilizing $Na_2SO_4 \cdot 10H_2O$ or paraffin wax required one quarter or one half the storage volume of a rock bed unit. PCM based heat storage store 5 to 14 times more heat per unit volume than sensible storage materials such as water, masonry and rock [15].

- Isothermal behaviour during melting and solidification [18]: Because the phase change at a constant temperature takes some time to complete, it becomes possible to smooth temperature variations.

PCM-based free comfort cooling is seen as a promising technology that can reduce building air-conditioning peak electrical energy demand significantly and which can also cut down on energy consumed for space cooling [20]. Many researchers [9], [21], [22] have demonstrated great potential electrical energy savings from the application of PCM-based free comfort cooling. However, based on research publications, limited studies [23–25] have been found which cover Southern African climatic conditions and there is no research reporting a comparison of free cooling thermal performance of different PCM types for an individual climate scenario.

An analysis of the climatic conditions in South Africa's Gauteng province (located at a Latitude of 26.27 ° S, a Longitude of 28.11 ° E , and an altitude of 1500 m) showed that the average summer maximum diurnal temperature is 33 °C whereas the average summer minimum diurnal temperature is 9 °C. See Appendix A. This province is important because it is home to a large proportion of South Africa's office building sector.

Even though PCM-based thermal storage systems utilising the free cooling principle has shown promise, its widespread practical application has been minimal due to lack of simple design tools. The design of latent thermal energy storage systems requires an in-depth analysis of the heat transfer behavior of the system for both charging (solidification) and discharging (melting) modes [26]. The latent energy storage capacity and effectiveness of thermal energy storage systems is governed by the energy conservation equations which can be expressed with partial differential equations [27],[28]. These equations are generally solved numerically. Although there are commercially available computer simulation tools such as Computational Fluid Dynamics (CFD) FLUENT and ANSYS CFX11, building energy analysis programs such as TRNSYS and EnergyPlus used in performance analysis of PCM-based thermal storage, they lack validation and the confidence in using them for designing is still too low [29]. Solving numerical equations and even using commercially available

computer simulation tools and building energy analysis programs for sizing PCM based storage systems can be a time consuming process. Therefore there is a need to develop an accurate alternative simplified method that a general designer for building HVAC would use for system sizing.

1.2 PROBLEM STATEMENTS

i. The cooling performance of commercially available PCM modules have not yet been specifically tested or characterised for the Southern African climate for different operating parameters.

ii. There is no clear design tool available that is useful to thermal HVAC engineers.

1.3 OBJECTIVES OF STUDY

- To evaluate and compare the cooling performance of three PCM materials in plate-air heat exchanger modules subjected to Southern African climatic conditions.
- To develop empirical correlations that can be used by thermal HVAC designers to determine the number of modules required to maintain an objective cooling load within the range of operating conditions tested.

1.4 ORIGINALITY AND CONTRIBUTION TO KNOWLEDGE

- New data for the detailed ventilation air cooling thermal performance (effectiveness, phase transformation duration, cooling power and energy absorption) comparison between two types of paraffinic PCMs and a salt hydrate PCM that can be used in climatic conditions with summer ambient temperatures of 30 to 35°C.
- A new empirical model with different coefficients for different PCMs was successfully developed. The model can be used for determining the number of modules installed in parallel with a plate pitch of 15 mm with a mass flux i.e air mass flow rate per module divided by the cross sectional area of each module in the range of 0.42 kg/m^{2}s to 0.85 kg/m^{2}s and inlet air temperatures ranging from 30°C to 35°C to maintain an objective cooling load for a desired time period.

1.5 SCOPE OF STUDY

Only the discharging (melting) mode of the plate PCM modules was investigated. Design parameters such as plate length, air channel gap, and number of plates per module were fixed for the PCM-air heat exchanger.

1.6 OVERVIEW OF THE DISSERTATION

This dissertation consists of seven chapters. Chapter 2 contains background information with regards to different kinds of PCMs and a detailed literature review of experimental and numerical investigations on PCM-air heat exchangers. Chapter 3 details the experimental facility. Chapter 4 presents data reduction equations used to analyse experimental data. Chapter 5 contains the results for the cooling performance for the three different kinds of modules. Chapter 6 presents the development of empirical correlations which can be used for plate PCM-air heat exchanger sizing. Chapter 7 presents the conclusions of the study and recommendations for future work.

CHAPTER 2 LITERATURE REVIEW

2.1 INTRODUCTION

This chapter contains background information on different methods of thermal energy storage, types of PCMs and heat exchanger designs. Review of experimental and modelling studies regarding PCM-air heat exchangers. Lastly a literature review of empirical mathematical characterisations of PCM thermal storage systems which are readily applicable to design of PCM based heat exchangers.

2.2 THERMAL ENERGY STORAGE

Thermal energy storage involves the storage of heat or cold to be used later. There are three basic methods for thermal energy storage. These include sensible heat storage, latent heat storage and reversible chemical heat storage.

2.2.1 Sensible heat storage

Sensible heat storage leads to a temperature change in the storage medium. The most common sensible heat storage media are solids like stone or brick, or liquids like water. Gases have a very low volumetric heat capacity due to their low densities and are therefore not used for sensible heat or cold storage. Sensible heat stored by a material is given by Equation 2-1 [30]:

$$Q = mC_p\Delta T \tag{2.1}$$

Where:

Q Heat stored

m Mass of heat storage medium

C_p Specific heat capacity of the storage material at constant pressure

ΔT Temperature change of heat storage medium

2.2.2 Latent heat storage

Latent heat is the energy released or absorbed by a body or a thermodynamic system during a relatively constant-temperature process. A typical example of latent heat is the

heat energy released or absorbed during a phase transition of matter. In both the solid and liquid phases of matter, intermolecular binding forces keep the atoms in close proximity. Thus, before a solid can melt, a certain amount of energy is required to overcome the binding forces that maintain its solid structure. This energy is referred to as latent heat of fusion of the material and represents the difference in thermal energy (enthalpy) levels between liquid and solid states [31]. The greater the energy required to cause the separation, the higher the latent heat of fusion. Phase change involves heat transfer, mass transfer, absorption or release of latent heat and changes in thermophysical properties.

The quantity of heat stored in a latent heat storage system undergoing phase change is given by Equations 2-2 and 2-3 [32]:

$$Q = \int_{T_{int}}^{T_m} m_{pcm} C_{p,s} dT + m_{pcm} f_l \Delta h_m + \int_{T_m}^{T_f} m_{pcm} C_{p,l} dT \quad (2.2)$$

The integrated form of equation 2-2 is as follows:

$$Q = m_{pcm}\left[C_{p,s}(T_m - T_{int}) + f_l h_m + C_{p,l}\left(T_f - T_m\right)\right] \quad (2.3)$$

Where:

T_m PCM melting temperature

T_{int} Heat storage material initial temperature

m_{pcm} Mass of PCM material

$C_{p,s}$ Average specific heat capacity between T_{int} and T_m

f_l Fraction of heat storage material melted

h_m Heat of fusion per unit mass

T_f Final temperature

$C_{p,l}$ Average specific heat capacity between T_m and T_f

2.2.3 Thermochemical energy storage

Thermochemical energy storage systems rely on the energy absorbed and released in breaking and reforming molecular bonds in a completely reversible chemical reaction [32]. The quantity of heat absorbed or released during such a chemical reaction is given by Equation 2-4 [32]:

$$Q = a_r m h_r \tag{2.4}$$

Where:

a_r Fraction reacted

h_r Endothermic heat of reaction

2.3 PHASE CHANGE MATERIALS (PCMS)

Since more than one PCM type are considered in this dissertation, it is important to review the similarities and differences between them. PCMs are substances capable of storing or releasing thermal energy as latent heat. The three main types of PCMs as shown in Figure 2-1 are organic, inorganic and eutectic of organic and inorganic compounds [2].

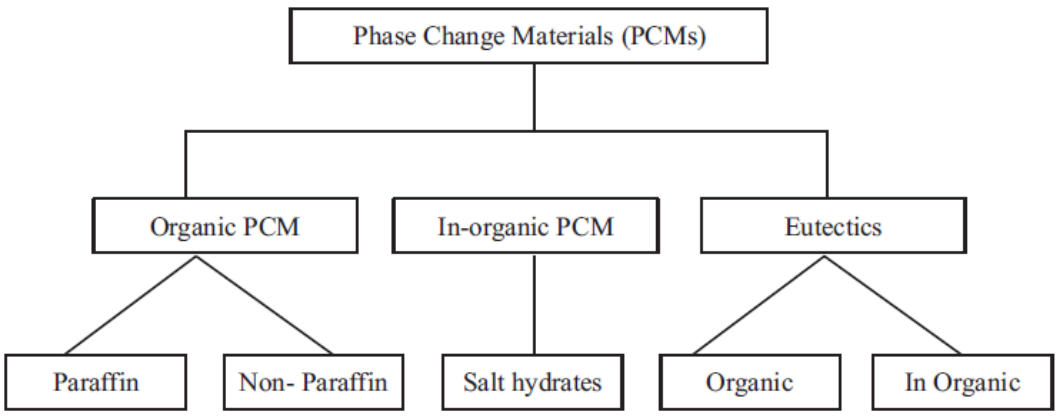

Figure 2.1. Types of PCMs [2].

2.3.1 Organic- paraffin

Paraffin is an alkane. It consists of only hydrogen and carbon atoms. All the bonds are single bonds. The carbon atoms are not joined in cyclic structures but instead form an open chain. Because paraffin contains single bonds and its structure is not cyclic, it is also referred to as a saturated hydrocarbon. In saturated hydrocarbons, every carbon atom is attached to two hydrogen atoms ($CH_3 - (CH_2) - CH_3$), except those at the ends of the chain, which bear three hydrogen atoms [32]. The general chemical formula for paraffin is C_nH_{2n+2} [33]. At room temperature paraffin is a liquid for the range of $5 \leq n \leq 15$ and in the other cases, it is a waxy solid [33]. Paraffin wax is mainly used in commercial organic heat storage PCM. Sharma, et al., [32] states that the melting point and latent heat of fusion for paraffin increases with an increased number of carbon atoms. Paraffin containing 14-40 carbon atoms has melting temperatures between 6 and 80 ºC [34]. Some examples of paraffins are listed in Table 2.1.

Commercial grade paraffin wax is obtained from petroleum distillation and is not a pure substance, but a combination of different hydrocarbons [15]. The advantages and disadvantages of paraffin are listed in the Table 2.2 as per [15]:

Table 2.1. Some examples of paraffins PCMs [15]

Name	**No. of carbon atoms**	**Melting temperature (°C)**	**Latent heat (kJ/kg)**
n-Tetradecane	14	4.5 to 5.6	231
n-Pentadecane	15	10	207
n-Hexadecane	16	18.2	238
n-Heptadecane	17	22	215
n-Octadecane	18	28.2	245

Table 2.2. Advantages and disadvantages of paraffin PCMs

Advantages	**Disadvantages**
• Paraffin waxes show no tendency to segregate. • They are chemically stable. • They have high heats of fusion • They have no tendency of super cooling. Therefore nucleating agents are not necessary. • Paraffin waxes are safe and non-reactive. • They are compatible with all metal containers.	• Paraffin has low thermal conductivity. This presents a problem when high heat transfer rates are required during the freezing cycle. • Paraffin has a high volume change between the solid and liquid stages. This causes many problems in container design. • Paraffins are flammable. • Paraffin can contract enough to pull away from the walls of the storage container greatly decreasing heat storage capacity. • Commercial paraffin generally do not have sharp well-defined melting points. This decreases the efficiency of the heat storage system, as is no longer isothermal.

2.3.2 Organic- non-paraffin

The non-paraffin organic PCMs group contains the largest number of types of the phase change materials. Each of these materials has its own properties unlike the paraffins, which all have very similar properties [32]. The non-paraffin organic PCMs consists of esters, fatty acids, alcohols and glycols [15]. Examples of organic non paraffin PCMs are listed in Table 2-3 and their advantages and disadvantages are given in Table 2-4. The most widely used non-paraffin organic PCM, as heat storage materials, are fatty acids like lauric, myristic, palmitic and stearic acid [35]. The general formula describing all the fatty acid is $CH_3(CH_2)_{2n} \cdot COOH$.

Table 2.3. Examples of organic non-paraffins PCMs [15]

Material	**Melting temperature (°C)**	**Latent heat (kJ/kg)**
Formic acid	7.8	247
Acetic acid	16.7	187
Glycerin	17.9	198.7
Butyl stearate	19	140
Polyethylene glycol-600	20-25	146
D-Lattic acid	26	184

Table 2.4. Advantages and disadvantages of organic non-paraffins PCMs

Advantages	**Disadvantages**
• Organic non-paraffins have high heat of fusion. This decrease the size of the thermal storage unit. • Organic non-paraffins have a well-defined melting point. This maximises the efficiency of the heat storage system [15].	• These materials are flammable and should not be exposed to excessively high temperature, flames or oxidizing agents [15]. • Low thermal conductivity. • Low flash points. • Instability at high temperatures. • 3-4 times more expensive than paraffins [15].

2.3.3 Salt hydrates

Salt hydrates are alloys of inorganic salts and water [32]. The salt and the water combines to form a crystalline matrix when the material is in a solid state [15]. The general formula for salt hydrates is $AB \cdot n\mathrm{H_2O}$ [32]. The solid–liquid transformations of salt hydrates are regarded to be dehydration during melting and hydration during solidification of the salt hydrate. At the melting point the salt hydrate crystals breakup into anhydrous salt and water as shown in Equation 2-5, or into a lower hydrate and water Equation 2-6.

$$AB \cdot n H_2O \rightarrow AB + n H_2O \quad (2.5)$$

$$AB \cdot n H_2O \rightarrow AB \cdot z H_2O + (n - z) H_2O \quad (2.6)$$

Where:

A Cationic species

B Anionic species

n number of moles of water of crystallisation

z Residual number of moles of water of crystallisation in the salt

Sharma, *et al.,* [15] states the three types of behaviour of salt hydrates undergoing a phase transformation namely congruent, incongruent and semi congruent. Congruent melting is whereby all the water in the crystalline matrix is separated from the salt as shown in Equation 2-6. Incongruent melting is whereby some of the water remains in the salt after melting as shown in Equation 2-5. Equation 2-5 shows the salt hydrate. The salt hydrate should melt completely (congruent melting) so that the liquid and solid phases are identical in composition, otherwise the difference in densities between the solid and liquid causes segregation resulting in changes in the chemical composition of the PCM [34]. This leads to a reduction in the heat storage capacity of the PCM. Examples of salt hydrate PCMs are shown in Table 2.5 and their advantages and disadvantages are given in Table 2.6.

Table 2.5. Examples of salt hydrates PCMs [15]

Material	**Melting point (°C)**	**Latent heat (kJ/kg)**
$K_2HO_4 \cdot 6H_2O$	14	108
$KF \cdot 4H_2O$	18	330
$K_2HO_4 \cdot 4H_2O$	18.5	231
$LiBO_2 \cdot 8H_2O$	25.7	289
$FeBr_3 \cdot 6H_2O$	27	105
$CaCl_2 \cdot 6H_2O$	29-30	170-192
$Na_2SO_4 \cdot 10H_2O$ (Glaubeur's salt)	32	251-254

Table 2.6. Advantages and disadvantages of Salt hydrates PCMs

Advantages	**Disadvantages**
• Low cost and easy availability. Many salt hydrates are sufficiently inexpensive for use in thermal storage [15]. • Single salt hydrates such as all the salt hydrates in Table 2.5 have well-defined melting points. This maximises the efficiency of the heat storage system [15]. • Salt hydrates have a high thermal conductivity when compared with other heat storage PCMs [15]. This can increase heat transfer in and out of the storage unit. • They have high heat of fusion [15]. This decrease the size of the thermal storage unit.	• Salt hydrates have problems of segregation [15]. Segregation of salt hydrates reduces the amount of salt hydrate that is actively available for heat storage. Abhat, [34] reports a decrease in latent heat of $Na_2SO_4 \cdot 10H_2O$ after 1000 cycles (melt and freeze). • Salt hydrates shows signs of supercooling [15]. • Salt hydrates causes corrosion in metal containers that are commonly used in thermal storage systems [15].

2.3.4 Selection criteria for candidate PCM for free cooling

The desirable thermodynamic, kinetic, chemical and economic properties for a candidate PCM for free cooling application are as follows:

PCM melting point

Butala and Stritih [36] states that if an unsuitable PCM is selected for a particular application, the PCM will neither totally solidify nor melt, and this leads to an insufficient cooling potential storage. For free cooling applications PCMs should be selected in such a way that the cooled air temperature out of the storage unit during the discharging process be within the range of defined comfort levels [2]. Researchers have provided different criteria to choose the melting point of a PCM that will be applicable in a given free cooling application:

- Stritih and Butala [37] state that in order to achieve sufficient heat transfer, the temperature difference between the ambient summer air temperature and the PCM melting temperature should be within the range of 3 to 5°C.
- Waqas and Din [2] states that the melting point of PCM must be close to the designed room temperature for thermal comfort.
- Arkar and Medved [38] experimentally determined a formula for estimating the optimum PCM melting temperature as:

$$T_m = \bar{T}_{od} + 2 \qquad (2.7)$$

Where:

T_m PCM melting temperature (°C)

$\bar{T}_{od}$ Calculated average outdoor air temperature in the summer months

- Geetha and Velraj [39] state that the melting temperature of the phase change material has to be equal to the average diurnal extreme temperatures $\left(T_m = \frac{T_{max}+T_{min}}{2}\right)$, then an equal temperature difference is available for charging and discharging.
- Turnpenny, *et al.*, [12] state that for a latent heat storage system with working fluid passing at different temperatures during the melting and freezing cycles, the optimum phase change temperature is the geometric mean of the two working fluid temperatures.

Heat of fusion

A high heat of fusion per unit mass is a merit point for the selection of a PCM so that a smaller amount of material is required to store a given amount of energy [34]. See Table 2.5.

Density

A higher density results in a smaller container to hold the material or more PCM material can be packed in a given volume [34].

Specific heat

High solid and liquid specific heats provide additional sensible heat capacities for the heat storage system [34].

Thermal conductivity

High solid and liquid thermal conductivities are desirable so that the temperature gradients required for charging and discharging the PCM are small [34]. Higher thermal conductivity ensures high heat transfer coefficients during storing and utilisation of thermal energy. The higher the heat transfer rates, the smaller is the required heat transfer area.

Congruent melting

The PCM should melt completely so that the liquid and solid phases are identical in composition. Otherwise the difference in densities between the solid and liquid causes segregation resulting in changes in the chemical composition of the PCM [34]. This leads to a reduction in the heat storage capacity of the PCM.

Super cooling

The PCM should exhibit little or no super cooling during solidification. The molten PCM must solidify at its thermodynamic solidification temperature. This is achieved through a high rate of nucleation and growth rate of the crystals. The super cooling may be suppressed by introducing an effective nucleating agent [34].

Chemical stability

The PCM should show chemical stability with no chemical decomposition so that a high latent thermal energy storage capacity is ensured throughout the life of the system. The PCM should not corrode construction materials [34].

Safety

The PCM should be non-poisonous, non-flammable and non-explosive.

Economic

The PCM should be available in large quantities and be inexpensive.

Abhat [34] states that there exist no single PCM that can fully satisfy all the desired properties listed above. However, for free cooling applications the PCM melting temperature is the most important factor and must always be selected carefully [30][9].

2.4 PCM APPLICATIONS IN BUILDINGS

Zhu et al., [40] divided the possible building applications of PCMs into three categories: passive building systems, active building systems and free cooling applications. The free cooling application was addressed already in Chapter 1 last paragraphs under section 1.1.

2.4.1 Passive building systems

For passive systems charging and discharging of PCM is done without any mechanical equipment. For passive applications, PCMs are integrated into the building envelopes to increase the thermal mass [41]. PCM- enhanced building envelops offer higher per unit heat storage capacity than conventional building materials and provide light weight building structures with increased thermal mass [29].

The major problem with passive building systems is that the PCM may not solidify completely at night due to the indoor air temperature not being low enough during summer to solidify the PCM and also due to very low heat transfer coefficient to transfer heat between the room air and the building structure [42].

2.4.2 Active building systems

For active systems charging and discharging of the PCM is achieved with the help of mechanical equipment such as heaters and coolers [40]. For example Mays et al., [43] applied a phase change material encapsulated in 40 mm aluminium container together with a solar powered heating element for underfloor heating for indoor heating. During the day the sun's radiation activate the heating element which provides indoor heating and also melts the PCM. At night the sun is not available and the stored heat from the PCM is discharged into the house. The result was that at an average ambient air temperature of 14 °C, the electrical energy consumption was shifted by 6 hours due to the latent heat stored in PCM.

2.5 PCM-AIR HEAT EXCHANGER DESIGNS

Different types of PCM-air heat exchangers have been designed, developed and studied for free cooling applications. This section provides the advantages and disadvantages for the different types of PCM based heat exchangers. The comparison motivated the choice of the plate PCM-air heat exchanger that was studied in this work.

2.5.1 Packed beds

A packed bed consists of PCM material that is encapsulated in small spheres, pellets or other geometrical shapes and placed in a larger container. The heat transfer fluid passes through the bed. An example packed bed (see Figure 2.2) which contained paraffin RT20 encapsulated into polyethylene spheres and located in a ventilation duct was studied by Arkar *et al.* [9]. The major drawback of packed bed PCM-air heat exchanger is the high pressure drop across the heat exchanger [44]. This causes an increase of the fan energy consumption.

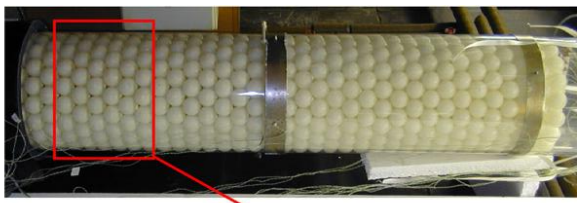

Figure 2.2. Packed bed PCM-air heat exchanger [9].

2.5.2 Shell and tube PCM-air heat exchangers

For a shell and tube heat exchanger, the PCM can be placed either in the shell with the heat transfer fluid (air) circulating inside the tubes or PCM inside the tubes with the air flow in the shell. Raj and Velraj [45] developed a shell and tube heat exchanger which had the PCM on the shell side and air flow on the tube side. The heat exchanger was modular in design. See the isometric view of a module in Figure 2-8. Air spacers 150 mm were provided between the modules. According to Raj and Velraj [45], these air spacers increase the retention time of the air. This increases heat transfer between the air and the PCM. This is only effective for air velocities below 2 m/s [45]. They also reported that the modular heat exchanger arrangement is suitable for free cooling application where the diurnal temperature variation is low.

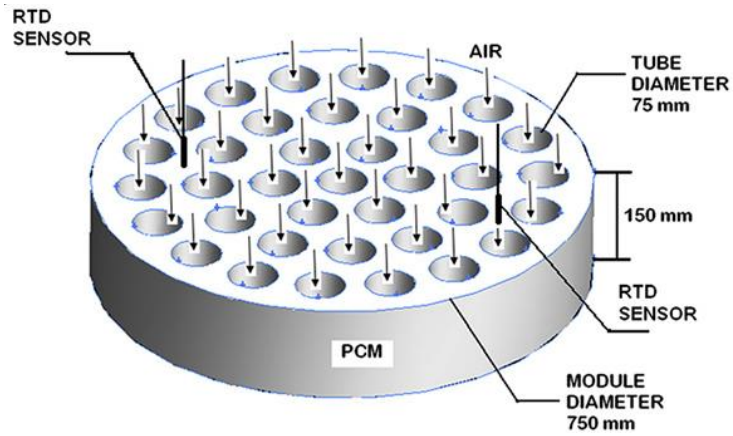

Figure 2.3. Isometric view of one module for the shell and tube PCM-air developed by Raj and Velraj [45].

2.5.3 Plate PCM-air heat exchangers

A plate PCM air heat exchanger consists of PCM material that is encapsulated inside a plate and placed in larger container. The plates can be oriented vertically or horizontally parallel to each other with air gaps between the plates. Studies have shown that the best plate orientation is vertical [46]. Charvat *et al.*, [46] used horizontally orientated Rubitherm™ compact storage modules (CSM) (See Figure 2.4) in their experiment. They found that the PCM in the fully melted state will collect at the lower part of the container (CSM panel) and there will be an air gap between the PCM and the upper surface of the container. That gap can significantly influence heat transfer between the PCM and the air passing through the heat storage unit. In support of this view Farid *et*

al, [44] states that in a horizontal plate orientation, volume contraction during solidification reduces the heat transfer surface area and also separates the PCM from the heat transfer surface, thus increasing the heat transfer resistance dramatically.

Figure 2.4. Illustration of a heat storage unit containing 100 Rubitherm™ compact storage modules used in the investigation by [46].

An example of a commercially available PCM encapsulated in a plate is the Rubitherm™ compact storage module (CSM) panels shown in Figure 2.5.

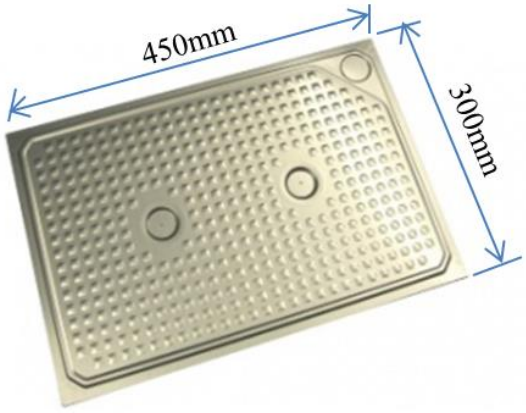

Figure 2.5. Rubitherm™ plate encapsulated PCM [47].

The panel is made of two identical cavities of aluminium plates filled with a PCM. The cavities are jointed at two centred points and stuck together at their frames [47]. The dimensions for these panels are 450 mm x 300 mm x 10 mm and 450 mm x 300 mm x 15 mm. Each panel has uniformly distributed bulges across its surface. The bulges enhance heat transfer by improving the convection coefficient value [17]. Higher number of bulges results in greater power peaks and shorter melting and solidification durations [17].

The 450 mm x 300 mm x 10 mm panel is loaded with 1 kg SP24E salt hydrate PCM with energy storage capacity of 50 Wh. The 450 mm x 300 mm x 10 mm panel is loaded with 0.5 kg RT25 paraffin PCM with energy storage capacity of 25 Wh.

Figure 2.6 shows a commercially available (FSL-B-PCM) fan coil air conditioning system which contains plate encapsulated PCM (labelled PCM-stack in Figure 2.6). The FSL-B-PCM unit is designed to be wall-mounted [48]. The unit obtains fresh summer outdoor air through an opening in the façade. The summer outdoor air is first cooled by the plate encapsulated PCM modules before it is discharged into the room. In case of very high outdoor air temperatures, the unit operates by mixing of secondary air and outdoor air or only recirculates secondary air [48]. This operation mode ensures a slower rate of melting of the PCM. This enables the PCM storage unit not to discharge rapidly. The product uses either paraffin or salt hydrates with melting points between 20°C and 25°C [48]. The manufacturer claims that a pleasant room temperature can be ensured for up to 10 hours [48].

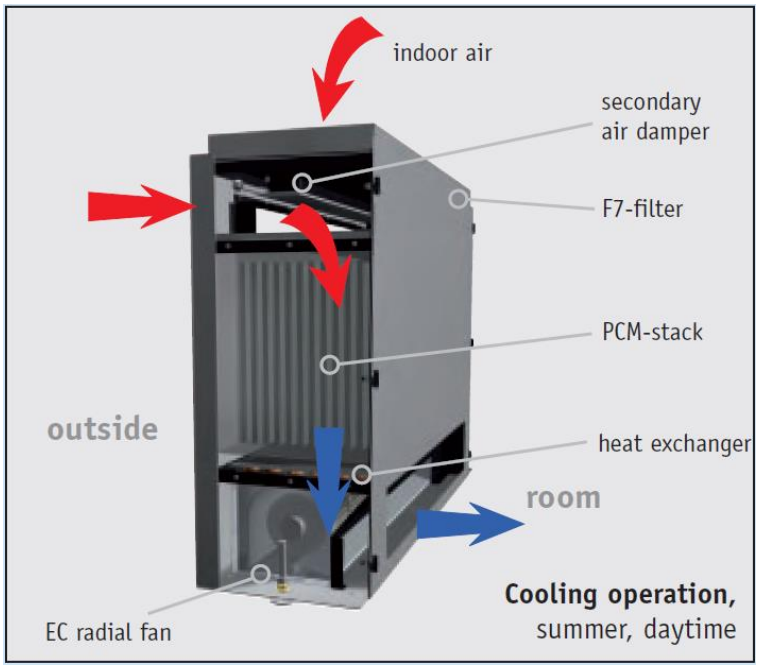

Figure 2.6. Illustration of FSL-B-PCM a commercially available air-conditioning system with plate encapsulated PCM [48].

Figure 2.7 shows a prefabricated plate PCM-air heat exchanger that was installed in a building air conditioning project in Germany. The PCM-air HX consist of 18 modules of Rubitherm PCM plates. Each module contains 15 plates which are separated by an air gap of 5 mm.

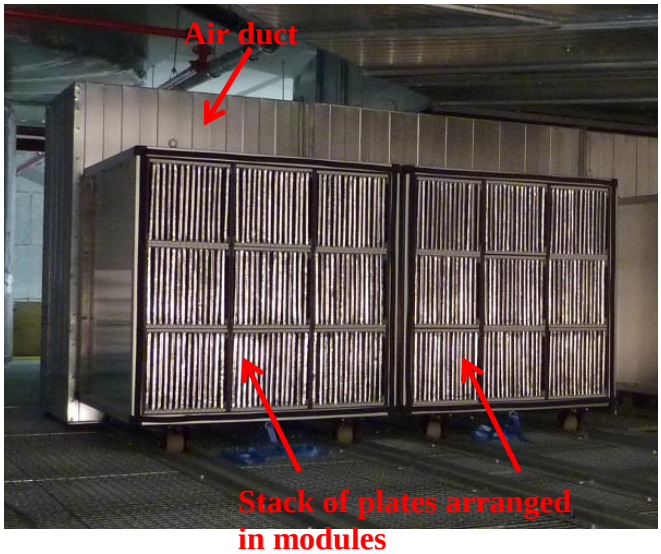

Figure 2.7. Illustration of PCM plates stacked in an air duct courtesy of Mr Tobias Lembeke Rubitherm.

Marin et al. [49] considered shell and tube and plate PCM-air heat exchangers in the design of their thermal storage unit; they opted for a plate heat exchanger because of the following advantages:

- The heat transfer rate in the PCM can be controlled with the choice of thickness of the encapsulation [49].
- Both processes of phase change are symmetric in relation to the two sides of the plates [49].
- Flat plates offer a larger heat transfer surface area per unit volume than other geometries of the thermal energy storage system; this enables smaller and effective system [49].
- Lower pressure drop of the air is experienced. This leads to a lower electrical power requirement of the fans [38].
- The use of flat plate encapsulation allows an easier design of the thermal energy storage system [49].
- Very effective heat transfer since a single plate is surrounded by two heat transfer fluid streams [13].
- Plate heat exchangers can be expanded with increased demand for heat transfer by simply mounting more plates [13].

2.6 MATHEMATICAL MODELLING OF PCM SYSTEMS

The thermal behaviour of the PCM systems can be modelled analytically and/or numerically. Models enable optimisation of thermal performance analytically or numerically. Design can be simplified with the use of models. Models can also be tested for validity by experimental work. Models can also be derived empirically from experimental work. This section reviews existing analytical and numerical models for evaluating thermal performance of PCM systems.

2.6.1 Analytical models

The simplest analytical model for heat transfer analysis of PCM systems is called the Stephan model [50]. Alexiades and Solomon [31] states that the classical Stephan model constitutes the foundation on which progressively more complex analytical models can be built by incorporating some of the effects initially omitted. The Stephan analytical

model applies to a 1-dimensional semi-infinite PCM layer [30]. During solid-liquid phase-change, an interface is formed which separate the solid phase and the liquid phase regions. The two regions have different thermophysical properties. The interface moves as the phase change is taking place. Energy is either absorbed or released at the moving interface. To mathematically solve the phase change problem, it is necessary to determine the rate at which the solid-liquid interface moves with time. Equations 2-8 and 2-9 describe the Stephan model. Interested readers are referred to the book by Mehling and Cabeza [30] for the derivation of these equations. Equation 2-8 calculates the location of the phase change boundary as a function of time. Equation 2-9 calculates the transient heat transfer rate at the solid-liquid interface.

$$S(t) = \sqrt{2 \cdot \frac{\lambda_{PCM} \cdot (T_m - T_{int})}{h_m} \cdot t} \tag{2.8}$$

Where:

$S(t)$ Position of phase change boundary at time t

T_{int} Heat storage material initial temperature

T_m PCM melting temperature

λ_{PCM} PCM thermal conductivity

h_m Heat of fusion per unit mass

t Time for the phase front to proceed a distance *S* away from the surface

$$\dot{Q}_i = \sqrt{\frac{(T_m - T_{int})}{2 \cdot t} \cdot h_m \cdot \lambda_{PCM}} \tag{2.9}$$

Where:

$\dot{Q}_i$ Cooling power delivered by PCM

Analytical solutions are valid for phase change materials that have constant thermophysical properties i.e. for pure phase change materials [51], however commercially available PCMs are impure materials consisting of two or more mixtures of phase change materials [17].

2.6.2 Numerical models

The numerical methods for studying heat transfer in PCM-air heat exchangers are divided in two broad categories, namely temperature model and enthalpy model [52].

2.6.2.1 Enthalpy formulation

The enthalpy formulation utilises the energy balance method. The PCM medium is subdivided into a sufficient number of volume elements and then an energy balance (energy conservation) is applied on each element [13]. The energy conservation equation written in terms of enthalpy for a single control volume can be written as follows:

$$\frac{\partial H}{\partial t} + \nabla q = 0 \qquad (2.10)$$

Where

$\frac{\partial H}{\partial t}$ Rate of change of enthalpy

q Heat flux

H Volumetric enthalpy

Neglecting the advective movements within the liquid phase change material, [17] [53],[52] and considering conduction heat transfer only;

$$q = -\lambda_{PCM} \nabla T_{PCM} \qquad (2.11)$$

Where

T_{PCM} PCM temperature

Combining equation 2-10 and 2-11:

$$\frac{\partial H}{\partial t} = \nabla\left(\lambda_{PCM}(\nabla T_{PCM})\right) \qquad (2.12)$$

Equation 2-12 consists of two unknowns: the enthalpy (H) per unit volume of PCM material and PCM temperature (T_{PCM}); therefore we require a second equation in order to solve equation 2-12. According to [52] the second equation is as follows:

$$H(T) = \begin{cases} \rho c_s(T_{PCM} - T_m), & T_{PCM} \leq T_m \\ \rho c_l(T_{PCM} - T_m) + \rho h_m, & T_{PCM} > T_m \end{cases} \quad (2.13)$$

An initial value of H i.e. H_0 is assumed in equation 2-12 and then a value of $T_{PCM(0)}$ is calculated from 2-12. The calculated value of $T_{PCM(0)}$ is substituted in equation 2-13 and then a new value of H is obtained. The process is repeated and PCM enthalpy and PCM temperature values are calculated for each control volume.

2.6.2.2 Temperature formulation

For the temperature formulation, the PCM domain is not separated in liquid and solid part as in the enthalpy formulation; the enthalpy is written as the sum of sensible and latent heat [52].

$$H(T) = \rho_{PCM} c_{l,s}(T_{PCM} - T_m) + \rho_{PCM} h_m f_l(T) \quad (2.14)$$

Where:

ρ_{PCM} PCM density

$C_{l,s}$ Average specific heat capacity of PCM between T_{int} and T_m

T_m PCM melting temperature

$f_l(T)$ Fraction liquid PCM at temperature T

h_m Heat of fusion per unit mass

Substituting for H in equation 2-12 with equation 2-14:

$$\frac{\partial \rho C_{l,s}(T_{PCM} - T_m)}{\partial t} + \frac{\partial \rho h_m f_l}{\partial t} = \nabla(\lambda_{PCM}(\nabla T_{PCM})) \quad (2.15)$$

The solution to Equation 2.15 is as follows:

$$\rho c_{l,s} \frac{\partial T}{\partial t} + \rho h_m \frac{\partial f_l}{\partial t} = \nabla(\lambda_{PCM}(\nabla T_{PCM})) \quad (2.16)$$

Equation 2-16 is a second order partial differential equation. For a second order differential equation, two boundary conditions must be specified. One of the boundary conditions that must be specified for the solution of this equation is the solid-liquid interface. Tracking the solid-liquid interface is very difficult to accomplish especially when dealing with commercially available PCMs which are not pure materials. They are mixtures and therefore their phase change takes place over a temperature range and therefore a two-phase zone (mushy region) appears between the solid and liquid phases [2]. When dealing with impure PCMs, it is appropriate to use the enthalpy formulation [2].

Zalba, et al., [53] states that the enthalpy formulation is favoured over temperature formulation for the following reasons:

- The equation is directly applicable to the three phases
- The temperature is determined at each point and the value of the thermophysical properties can be evaluated.

The design of PCM-based thermal storage systems requires an in-depth analysis of the heat transfer behaviour of the system for both melting and solidification of PCM. This in-depth analysis can only be achieved by the use of numerical models that describe the governing principles of the melting and solidification of the PCM. Using numerical models for the designing of the PCM-air heat exchangers may not be convenient for engineers. A general designer for building HVAC would not require detailed numerical analysis for system sizing but for system optimization numerical analysis can be applied.

2.7 PREVIOUS INVESTIGATIONS

Thermal storage performance of PCM based free cooling ventilation devices has been studied experimentally, analytically, numerically and using a combination of these.

Medved and Arkar [38] used an experimentally verified numerical model of a packed-bed PCM-air heat exchanger (RT20 packed in a cylinder) installed in a ventilation air duct to study it’s efficiency in six European cities with different climatic conditions. For

comparing the efficiency, cooling degree-hours were determined for three summer months for each city. The authors found that the PCM peak melting temperature should not differ by more than 2°C from the ambient air temperature in order to allow an effective use of the PCM. For the cases studied the authors concluded that the optimum size of the packed-bed unit should be between 1 and 1.5 kg of PCM per m3/hr of fresh ventilation air.

Lazaro *et al.,* [54] designed and tested two different real scale prototypes of PCM-air heat exchangers for a free cooling application. The aim of the study was to evaluate thermal performance of the two prototypes in terms of cooling power and duration of melting for a constant inlet air temperature. Prototype 1 had aluminium pouches filled with an inorganic PCM. Prototype 2 had aluminium panels filled with organic PCM. For the same time duration, prototype 2 showed high cooling power and short melting time when compared to Prototype 1. This finding is surprising since the thermal conductivity of PCM material for prototype 2 (organic PCM) is lower than that of PCM for prototype 1 (inorganic PCM). They concluded that for PCM thermal storage systems, emphasis should be placed on designing heat exchangers instead of enhancing PCM thermal conductivity.

Chaiyat and Kiatsiriroat [55], experimentally investigated the use of a packed bed PCM-air heat exchanger (paraffin wax RT20 encapsulated in spheres) for improving the cooling efficiency of an air-conditioner. They found that the electrical energy consumption of the modified air-conditioner was decreased by 3.09 kWh per day which was a cost saving of 9.1%.

Halawa and Saman [56] found that for airflow through plates, the temperature difference between inlet air and PCM melting temperature, the air gaps between plates, and plate thickness are critical parameters on the cooling rates for the plate type heat exchanger.

Kabbara and Abdallah [57] experimentally investigated the thermal storage capacity and the heat transfer rate of Calcium Chloride Hydrate ($CaCl_2 \cdot 6H_2O$) encapsulated in tubes with a melting temperature range of 27 to 28°C. Experiments were performed using 121.3 kg of PCM with maximum latent heat storage capacity of 20.6 MJ. It was found that the highest flow rate produced the highest heat flux and cumulative energy stored during the melting experiments. For solidification experiments they found that the power output is higher when using lower input air temperature.

Rajagopal and Velraj, [24] experimentally studied the room air cooling performance for a module of Rubitherm™ paraffin RT 27 encapsulated in 11 flat plates (775 mm × 400 mm × 24 mm). The room heat load was simulated by 200W electric bulbs installed at various locations in the room. Hot air from the room was recirculated through the module. They found that for a room heat load of 0.5kW, the temperature of the room air was maintained below 30°C for a continuous duration of 8 hours, which otherwise would reach 32°C. For a room heat load of 3 kW they found that the air temperature of the room was maintained below 34°C continuously for 5 hours, which otherwise would have reach 37.5°C. They suggested a possibility to design a modular heat exchanger with a proportional surface area when the room heat load increases beyond 0.5 kW, in order to maintain a minimum comfortable temperature of 30°C in the room.

Dolado et al., [17] developed a numerical model to simulate thermal performance of a real scale plate PCM-air heat exchanger. The model was validated by experimental data. Their study established the influence of operating conditions (air flow rate), PCM thermophysical properties (thermal conductivity, PCM average melting temperature, PCM enthalpy), and encapsulation material properties (thermal conductivity and roughness) on the thermal performance of a plate PCM-air heat exchanger.

Zalba et al. [10] designed, constructed and conducted experimental tests for plate encapsulated RT25 PCM. They found that the rate of melting and solidification is influenced by the thickness of the encapsulation, the inlet temperature of the air, the airflow, and the interaction thickness and temperature. Using the same experimental setup of Zalba et al., [10], Marin et al., [49] incorporated a porous matrix of graphite in

the RT25 PCM to improve heat transfer rates. They found that for the same thickness of plates, a response time much lower (50% in time) can be reached with very low reduction of the energy stored (12% and 20%).

Waqas and Kumar [25] studied the free cooling feasibility of a plate encapsulated PCM-air heat exchanger used for the pre-treatment of ambient air introduced in the building for a hot and dry climatic conditions. They found that, when the storage material phase change temperature is equal to the comfort temperature of hottest summer month; the performance of storage unit is maximized for all the summer months. They also found that air flow rates during night times should be higher than air flow rates during the day time because of very short summer nights and less temperature difference between phase change temperature of PCM and night temperatures.

Turnpenny, et al., [12] analysed a ceiling installed heat pipe-PCM heat exchanger for the maintenance of comfortable air temperature within a room. Air from the room was drawn over the exposed ends of the heat pipes using low powered fans. Their measurements showed that at least 15°C or more temperature difference between air and PCM was needed to melt and freeze PCM in practical time scales.

Takeda, et al., [21] developed an experimental ventilation system that directly exchanged heat between ventilation air and granules containing PCM. They varied inlet air temperature periodically to simulate changes of outdoor ambient air temperature. They found that outlet air temperature was stabilised and remained within the phase change temperature range.

Nagano et al., [58] studied a floor mounted packed bed PCM-air heat exchanger. The PCM was granulated and packed. Outdoor air was supplied into the room through grills located on the floor. The air was exhausted through high level outlet air terminals located in the ceiling. This form of ventilation is called displacement ventilation. The opinion was expressed that PCM-air heat exchanger for free cooling has a great potential to be applied in a displacement ventilation system when compared to a mixed

ventilation system. This is because of the lower temperature differential requirement between supply air and room air in a displacement ventilation system.

A review paper by Waqas and Din [2] states that the effectiveness to reduce ventilation cooling load of PCM-based free cooling mainly depend on the diurnal temperature range (the difference between the daily maximum and minimum temperature for a particular geographical location). According to Waqas and Din [2], the application of PCM performs efficiently in climatic conditions with a diurnal temperature range between 12 and 15ºC. Zalba, et al., [10] argued that for climates where the diurnal temperature range is less, PCM-based free cooling will require careful design consideration including selection of an appropriate PCM agent and encapsulation.

Alam et al., [42] compared the effectiveness of passive and free cooling application methods of Phase change materials when used as energy efficient retrofitting in a residential building for Melbourne, Australia summer climatic conditions. For passive application, PCM was installed in the ceilings of the house. In free cooling application, outdoor air was supplied to the indoor after passing it through a PCM storage unit. Validated simulation models were used to investigate the effectiveness of the two PCM application methods. Their results showed that the free cooling application was more effective than the passive application in terms of reducing the indoor air temperature. Free cooling application resulted in up to 1.8 °C reduction in indoor air temperature, compared to 0.5 °C for passive application.

Muthuvelan, et al., [23] experimentally investigated a flat plate PCM-air heat exchanger for the free cooling potential of a cabin under Pune city, India climatic conditions temperature variation between 22°C and 35°C. Their finding was that indoor air temperature was reduced by an average of 2.5 °C. They further state that the requirement for mechanical air conditioners can be eliminated totally if free cooling is integrated with other building passive cooling techniques.

2.8 EMPIRICAL MODELS

Very few studies have focused on developing empirical mathematical characterisations of PCM thermal storage systems that are readily applicable to design.

Castell, et al., [59] experimentally studied a PCM tank for cold storage applications. Two different tank configurations subjected to varying flow rates of the heat transfer fluid were studied. Castell, et al., [59] used the effectiveness (ε)-NTU method and developed an empirical model which correlated average effectiveness and mass flux (ratio of mass flow rate and heat transfer surface area) for a tube in tank PCM storage system. The average effectiveness gives an indication of how much energy can be extracted from the TES system [60]. Average effectiveness for charging and discharging a PCM based thermal storage system is given by [60]:

$$\overline{\varepsilon_{c,d}} = \frac{Q_{act}}{Q_{max}} = \frac{\bar{T}_i - \bar{T}_o}{\bar{T}_i - \bar{T}_{pcm}} \tag{2.17}$$

The results showed that the effectiveness of the system did not vary with time, decreased with increasing flow rate and increased with increasing heat transfer area. The effectiveness was experimentally determined to only be a function of the mass flux.

Tay, et al., [61] endeavoured to expand on the research of Castell, et al., [59] and validated the (ε)-NTU method for the design of tube in tank PCM storage systems. They carried out experiments for a one tube tank, two tubes tank and four tubes tank systems. They found that a single relationship exists for all the tested tube tank systems which correlated effectiveness and mass flux for a tube in tank PCM storage system.

Zalba et al., [10], developed empirical models with multiple regression analysis technique. The models predicted solidification and melting time as a function of inlet air temperature and encapsulation thickness.

Lazaro *et al.,* [62] developed an empirical model for a plate PCM-air heat exchanger which simulated its thermal behavior under different operating conditions. They tested the technical viability of the plate PCM-air heat exchanger in an application where it was used to offset a portion of the room cooling load by recirculating room air.

Even though it is clear that the presence of PCM-air based heat exchanger have advantageous energy usage implications, limited studies [23–25] have been found which cover Southern African climatic conditions and there is no research reporting a comparison of free cooling thermal performance of different PCM types for an individual climate scenario and also relatively few studies have focused on developing empirical mathematical characterisations of PCM thermal storage systems that are readily applicable to design.

The purpose of this study was to experimentally evaluate the cooling performance of three PCM materials in plate-air heat exchanger modules subjected to different operating conditions and to use the data to deduce empirical correlations that can be used by thermal designers to determine the number of modules required to maintain an objective cooling load within the range of operating conditions.

2.9 EXPERIMENTAL METHODS FOR TESTING THERMAL PERFORMANCE OF PCM-AIR HEAT EXCHANGERS

Experimental evaluation of thermal performance of PCM-air heat exchangers mainly focuses on measurements of the inlet air temperature before the PCM-air heat exchanger, air temperature at the outlet of the heat exchanger and the air flow rate across the heat exchanger [63],[54]. In some cases air humidity difference across the PCM-air heat exchanger [54] and pressure drop across the heat exchanger is also measured. In cases [17] where numerical models were validated using experimental measurements plate surface temperature and the encapsulated PCM temperature were measured.

Anemometers were used by [63],[46] , to measure the airflow rate across the heat exchanger. Flow obstruction methods e.g. venturis, nozzles and orifices are commonly

used in fluid flow rate measurements. A pressure-drop measurement is taken as an indication of the flow rate. The ANSI/ASHRAE standard 94.1-2010 [64] for the testing of thermal energy storage systems recommends the use of a nozzle for flow rate measurements. The nozzle is constructed as described in Section 6.3 of ASHRAE Standard 37 [65]. Only one study [54] measured the airflow rate across the PCM-air heat exchanger using the energy balance method across the electrical resistance heaters. The assumption that is used for flow obstruction methods is that the density of the fluid remains constant before and after the obstruction point; however in the melting experiments where air is heated to a desired temperature by using electrical resistance heaters; air density before and after the electrical heater have a significant difference.

2.10 SUMMARY

Even though it is clear that the presence of PCM-air based heat exchanger have advantageous energy usage implications, limited studies [23–25] have been found which cover Southern African climatic conditions and there is no research reporting a comparison of free cooling thermal performance of different PCM types for an individual climate scenario.

The literature review has highlighted that very few studies have focused on developing empirical mathematical characterisations of PCM thermal storage systems that are readily applicable to design. The design of PCM-based thermal storage systems requires an in-depth analysis of the heat transfer behavior of the system for both melting and solidification of PCM. This in-depth analysis can only be achieved by the use of numerical models that govern the melting and solidification of PCM. Using numerical models for the designing of the PCM-air heat exchangers may not be convenient for engineers. A general designer for building HVAC would not require detailed numerical analysis for system sizing but for system optimization numerical analysis can be applied.

CHAPTER 3 EXPERIMENTAL SET-UP

3.1 INTRODUCTION

This chapter details the experimental set-up that was used to evaluate the air cooling performance of a plate encapsulated PCM module subjected to different operating conditions covering air temperatures of 30 ºC to 35 ºC and air mass flow rates of 0.03 kg/s to 0.06 kg/s. Three types of plate encapsulated phase change materials were evaluated; paraffin-containing modules RT25 and RT27 and a salt-hydrate-containing module SP24E. Firstly the aim of the experiment is covered, secondly the layout of the experimental facility and a detailed description of each section of the facility are given, thirdly the environmental properties are described, fourthly the test facility calibration procedures are discussed, and lastly the experimental procedure and experimental matrix are covered.

3.2 AIM

The main aim of the experimental set-up was to determine the effective heat transfer rate in a PCM module by measuring the difference of the air temperature across the module from the inlet to outlet for varying inlet air temperatures and air mass flow rates.

3.3 TEST FACILITY LAYOUT

The test facility was located at the Council for Scientific and Industrial Research in Pretoria at an elevation of 1386 m above sea level resulting in an absolute barometric pressure of 87.8 kPa. The layout of the experimental test facility is schematically shown in Figure 3.1 and a dimensional drawing of the facility is shown in Figure 3.2. The set-up was an open-loop air circuit made mostly of rectangular air ducts. After the air passed through the test duct it was not directly recirculated. The experimental set-up consisted of several components and sections that were connected in series. These are: a conical inlet section, an electrical resistance heating element with a transformer, a section with passive free-rotating air mixing blades, an air temperature measuring station, the PCM test section, another section with passive free-rotating air mixing

blades, another air temperature measuring station, an inline tube fan with a fan motor controller, a manual damper and flexible ducting.

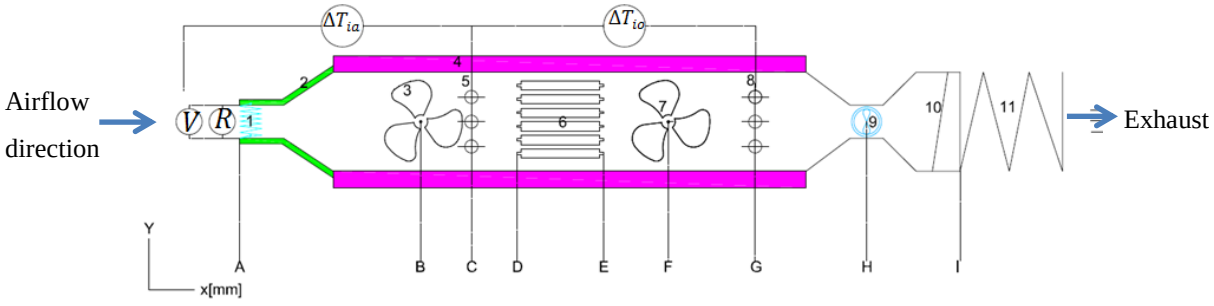

1	Electrical heating section
2	Mineral wool insulation
3	Air mixing station
4	Neopor insulation
5	Air temperature measuring station
6	Test section
7	Air mixing station
8	Air temperature measuring station
9	Inline tube fan
10	Manual damper
11	Spiral ducting

Figure 3.1. Schematic diagram of the experimental setup.

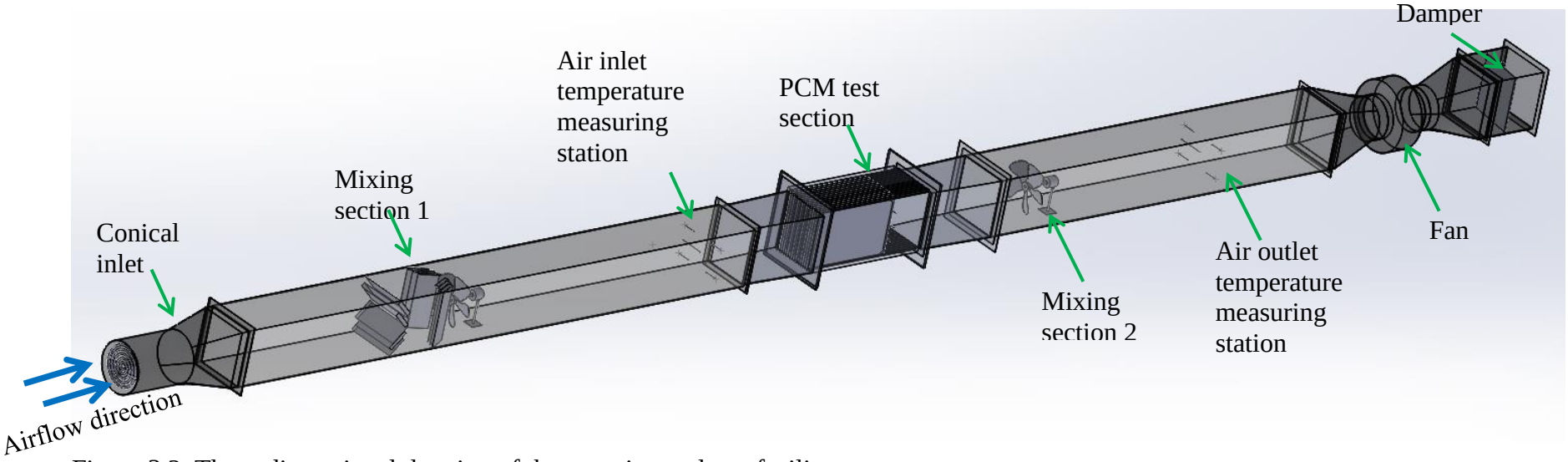

Figure 3.2. Three-dimensional drawing of the experimental test facility.

Figure 3.3. Illustration showing test room and the experimental set up

3.4 CONICAL INLET

The conical inlet transitioned the flow passage from a round duct to a rectangular duct. The outer diameter of the conical inlet was 250 mm and the inner diameter was 244 mm. The conical inlet section housed the electrical heating element coil. A front elevation and an end elevation of the conical inlet section are shown in Figure 3.3.

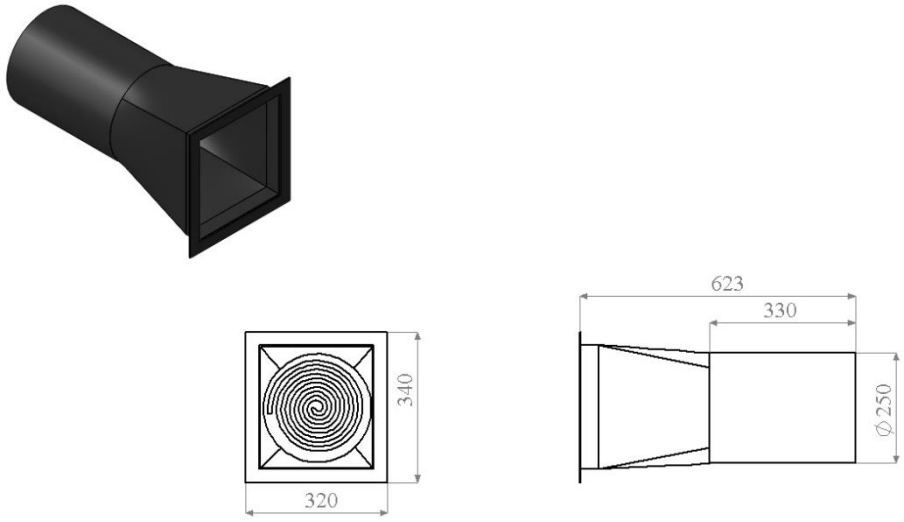

Figure 3.4. Conical inlet section (all dimensions are in mm).

3.5 ELECTRICAL HEATING SECTION

An electrical heating section was used to condition the incoming air temperature. The schematic diagram of the coil is shown in Figure 3.4.The heating section was made of a Nickel Chromium alloy coil with an outside diameter of 215 mm and coil pitch of 20 mm. The coil had a round cross section with a diameter of 10 mm thickness. The coil was located inside the conical inlet section (see the end elevation for the conical inlet section in Figure 3.3).

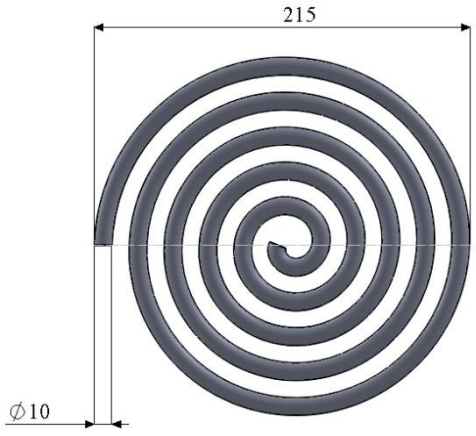

Figure 3.5. Schematic diagram for heating element coil (all dimensions are in mm).

The maximum supplier specified power rating of the heater was 750 W. The element was powered by a 230 V±5% alternating current which was assumed sinusoidal via a

transformer which regulated the voltage (between 0 V and 250 V) across the element. The heating section was placed at a distance of L_{AD} = 4 m (see Figure 3.2) from the inlet of the test section. This distance was selected so as to maintain at least a distance of ten hydraulic diameters from the inlet of the test section. This ensured that the air flow through the test section was fully developed. Even though this precaution was taken uneven melting of the PCM still occurred resulting in PCM in the center plates melting faster than peripheral plates.

Power input to the heating element was calculated from the measured voltage drop across heater and its resistance. The voltage and resistance were monitored and recorded by a data logger (see paragraph 3.13 for more information about the data logger).

3.6 MAIN DUCT

The main duct was rectangular and was made from 3 mm galvanised steel. It was also split into five sections with dimensions of each section measuring 255 mm along the Z-direction by 278 mm along the Y- direction by 1 m in length. To avoid air leakage from the main duct, silicon was applied in between the flanges of steel ducts.

3.7 AIR MIXING STATIONS BEFORE AND AFTER THE TEST SECTION

In-duct air temperature stratification due to buoyancy driven flow was observed at the inlet and outlet air temperature stations. Thermocouples located at the bottom quadrants of the duct were observed to read lower temperatures when compared to the top quadrant thermocouples.

Passive (driven by the air stream) free-rotating air mixing blades similar to fan blades with an outer diameter of 250 mm were placed at a distance LBD of 1.6 m. The location of the air mixing blades was calculated as per [64].

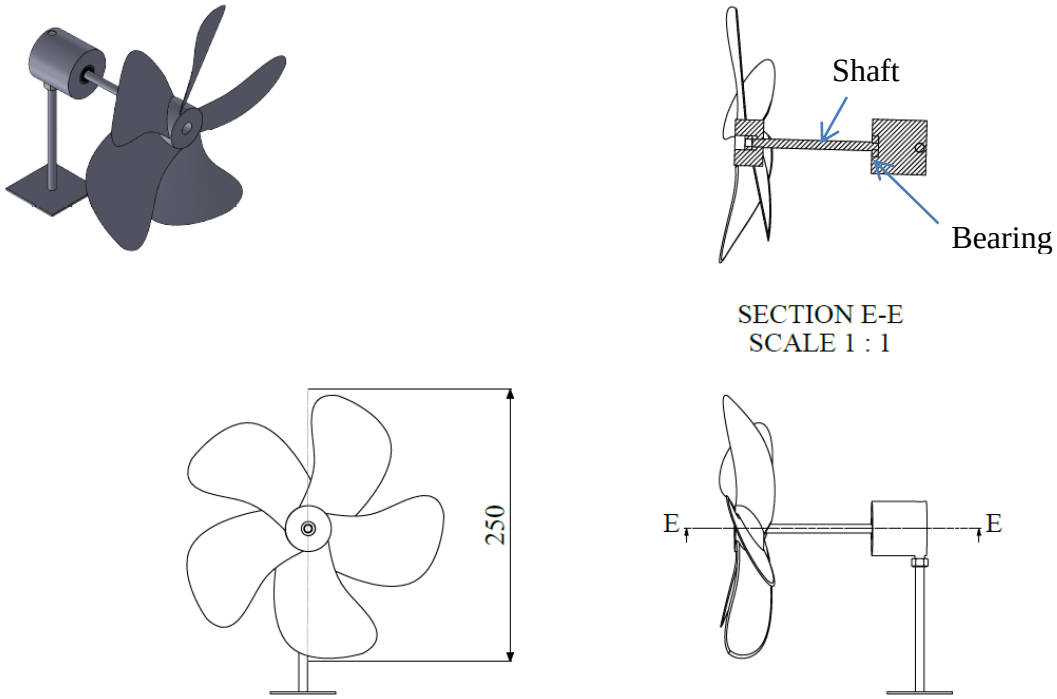

Figure 3.6. Assembly drawing of the passive free-rotating air mixing blades (all dimensions are in mm).

Air mixing blades were coupled to a shaft that was supported by a bearing as shown in section E-E of Figure 3.5.

The blades were used to disturb the thermal boundary layer to enhance uniform temperature distribution of the air as it entered the test section. In this experiment it was important to ensure that the temperature profiles of the airstreams as they enter the test section were completely even to avoid outlet air temperature gradients.

3.8 TEST SECTION INLET AND OUTLET AIR TEMPERATURE

The stations for measuring inlet and outlet air temperatures (before and after the PCM test section) were placed at distances L_{CD} of 0.7 m and L_{EG} of 1.7 m calculated as per [64]. The stations consisted of five thermocouples as shown in Figures 3.6 and 3.7. The duct was divided into four quadrants and one thermocouple was placed at the center of each quadrant. The fifth thermocouple was placed at the center of the duct. The use of five thermocouples reduced the uncertainty of the inlet and outlet air temperature

measurements. The instantaneous averaged inlet and outlet air temperatures of the test section were used in the calculation of the instantaneous air cooling power delivered by the PCM plates.

The thermocouples were T-type thermocouples with an outer diameter of 0.8 mm. The thermocouples were calibrated for a temperature range of 7 °C to 41 °C (see Appendix B). The measurement uncertainty of the thermocouples was ±0.1 °C (see Appendix C). The thermocouples were attached to the strings in the duct. The strings were set up to run across the duct at the centres of the top and bottom quadrants as well as center of duct.

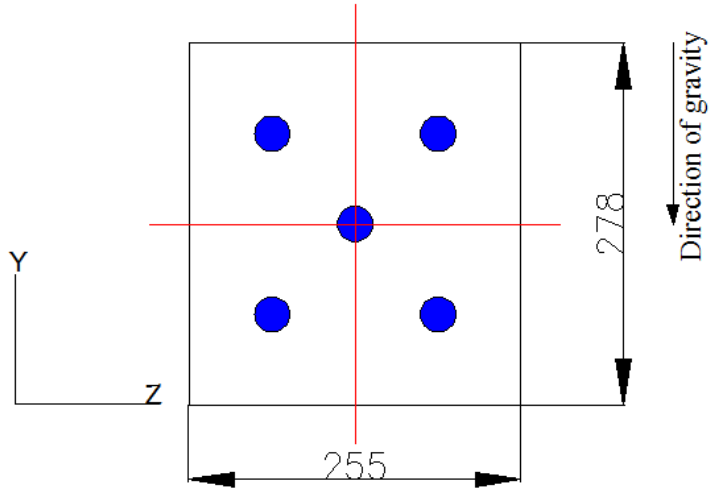

Figure 3.7. Arrangement of in-duct thermocouples (all dimensions are in mm).

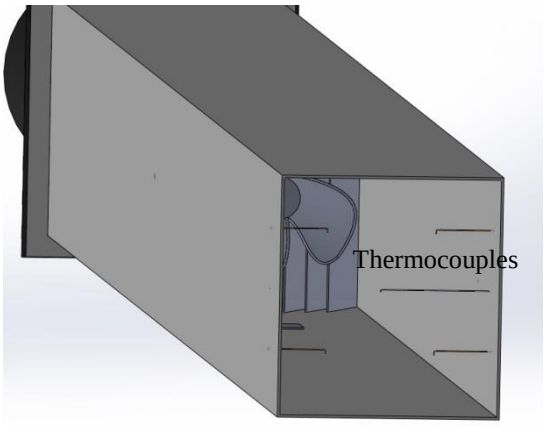

Figure 3.8. Three dimensional view illustrating position of thermocouples inside duct.

3.9 TEST SECTION

The cross section of the test section matched the cross section of the main duct (255 mm by 278 mm). The test section was fabricated from plexi-glass. Plexi-glass was used because it reduces heat loss from the test section to the surroundings and also it can be easily machined and the panels can be easily glued to each other. Fifteen slots (11 mm deep and 2 mm wide) with a pitch of 15 mm were machined running vertically in the Plexi-glass panels such that plate encapsulated PCM modules could be supported (See Figure 3.8).

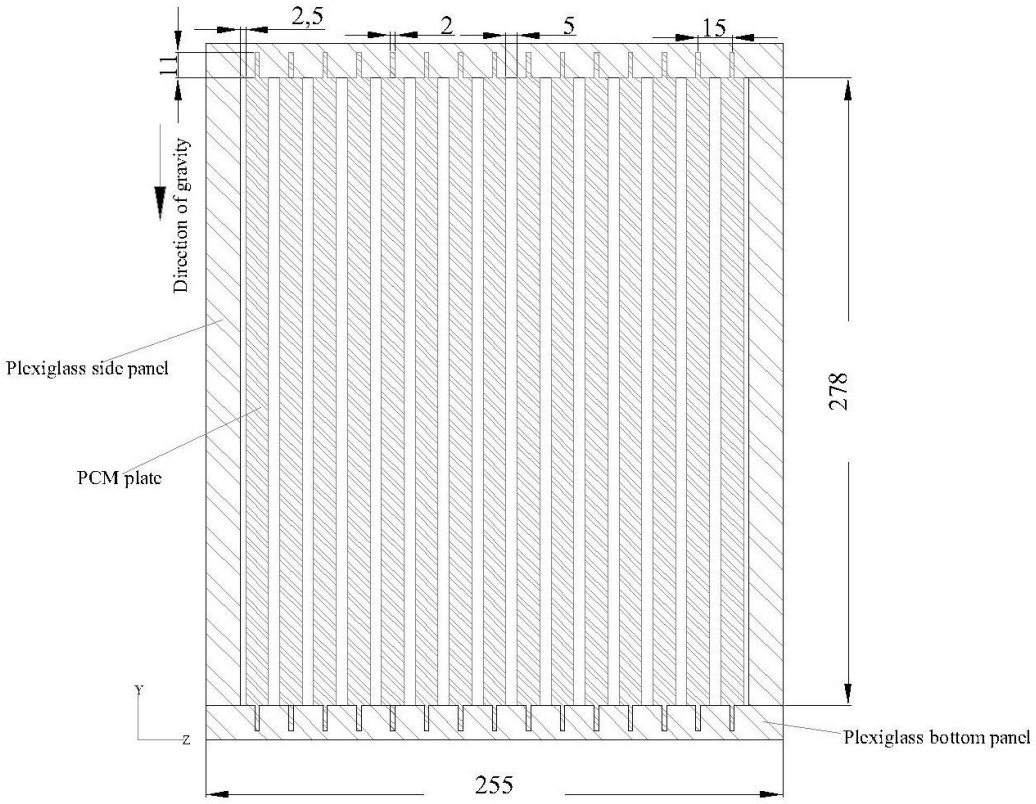

Figure 3.9. Cross-section for test section module (all dimensions are in mm).

The slots were spaced such that the air gap between successive plates was 5 mm except for the air gaps between side panels and end plates which were 2.5 mm. The basis for 5 mm air channel gap was the practical application as detailed in paragraph 2.5.3 and shown in Figure 2.7.

The test section was mounted to the steel rectangular air ducts by means of Plexi-glass flanges. In order to avoid air leakage between test section and air ducts, a rubber gasket was placed in between the flanges of steel duct and Plexi-glass flanges.

The test section was mounted to the air ducts in such a way that it could be disassembled to allow testing of three different types of plates (RT25, RT27 and SP24E). Fifteen PCM plates of each type were slid into the test section in a vertical orientation as shown in Figure 3.9. A vertical orientation was selected in order to reduce the effect of the volume contraction of PCM during solidification. Volume contraction during solidification separates the PCM from the heat transfer surface thereby increasing the heat transfer resistance [66] and reducing the efficiency of the modules.

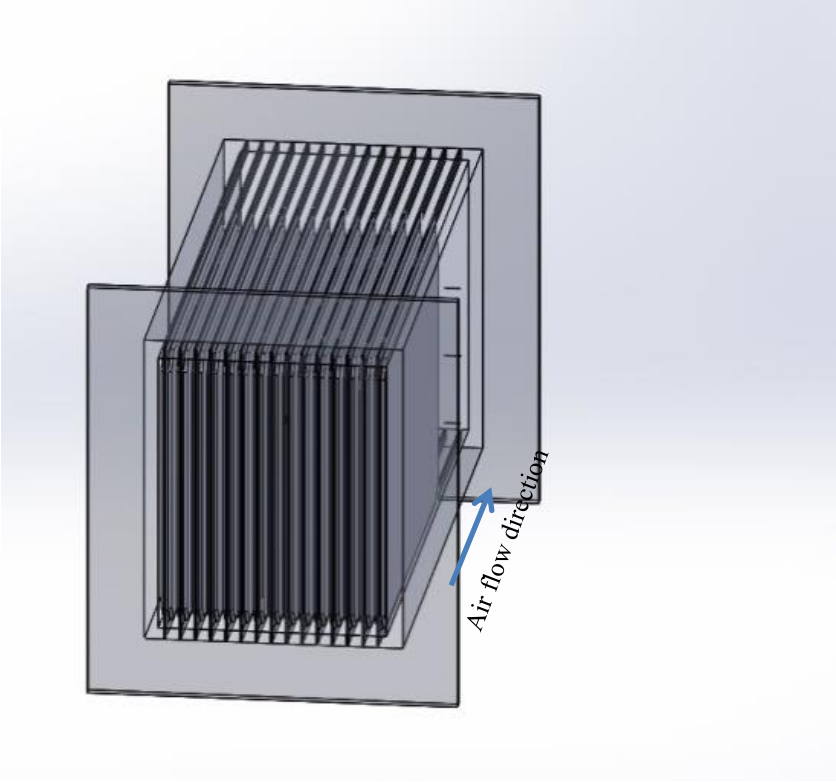

Figure 3.10. Three dimensional schematic drawing of test section module.

Note: The module consisted of 15 plates with a pitch of 15 mm and an air duct measuring 255 mm by 278 mm.

3.9.1 PCM temperature measurement

In order to measure PCM temperature, 15 thermocouples were inserted inside the plates (see Figure 3.10 and 3.11 for the location of the thermocouples). PCM temperature was measured for each plate to confirm uniform initial PCM temperature for all plates and that the PCM temperature was below PCM melting temperature before starting the melting experiments. In order to measure PCM temperature along the middle plates for the purpose of tracing the PCM melt front for plates 7 and 8, two additional thermocouples were placed as shown in Figure 3.11, one on the upstream section of the plate and another on the downstream section. In order to insert the thermocouples in position, 3 mm holes were drilled at the top edges of the plates and 3 mm outer diameter plastic tubes 13.5 cm in length were inserted and then glued to the edge of the plate. The thermocouples were inserted through these plastic tubes from the top of the plates. The holes were drilled at the top of the plates to avoid hydrostatic leakage of the PCM from the plates.

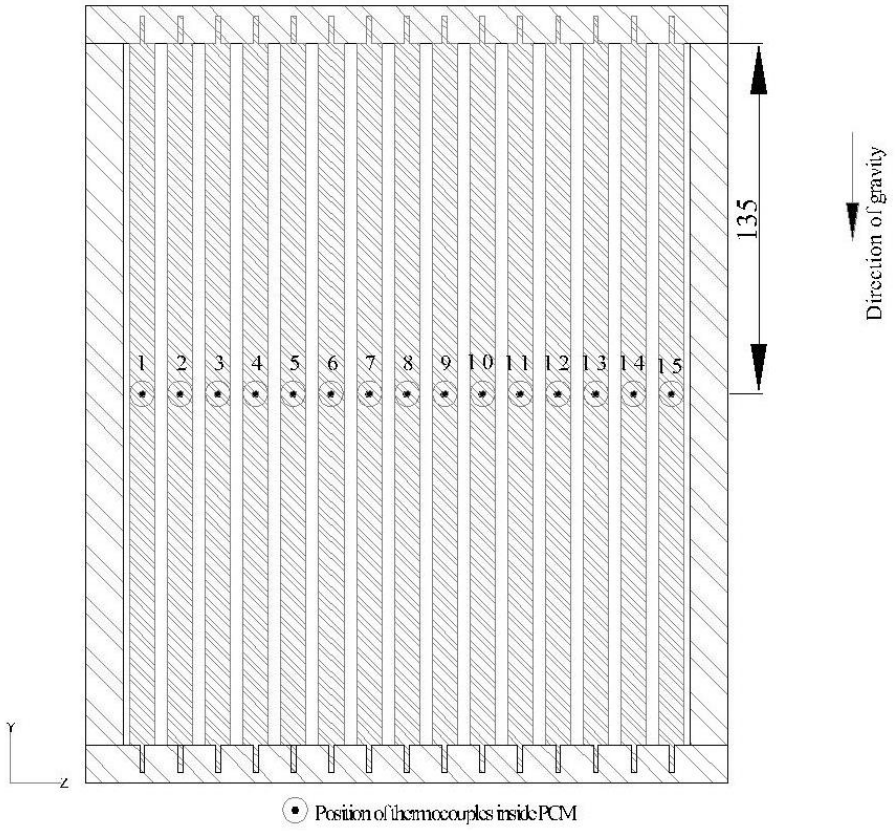

Figure 3.11. Middle vertical section of test section illustrating PCM thermocouples positions; 1-15 (all dimensions are in mm).

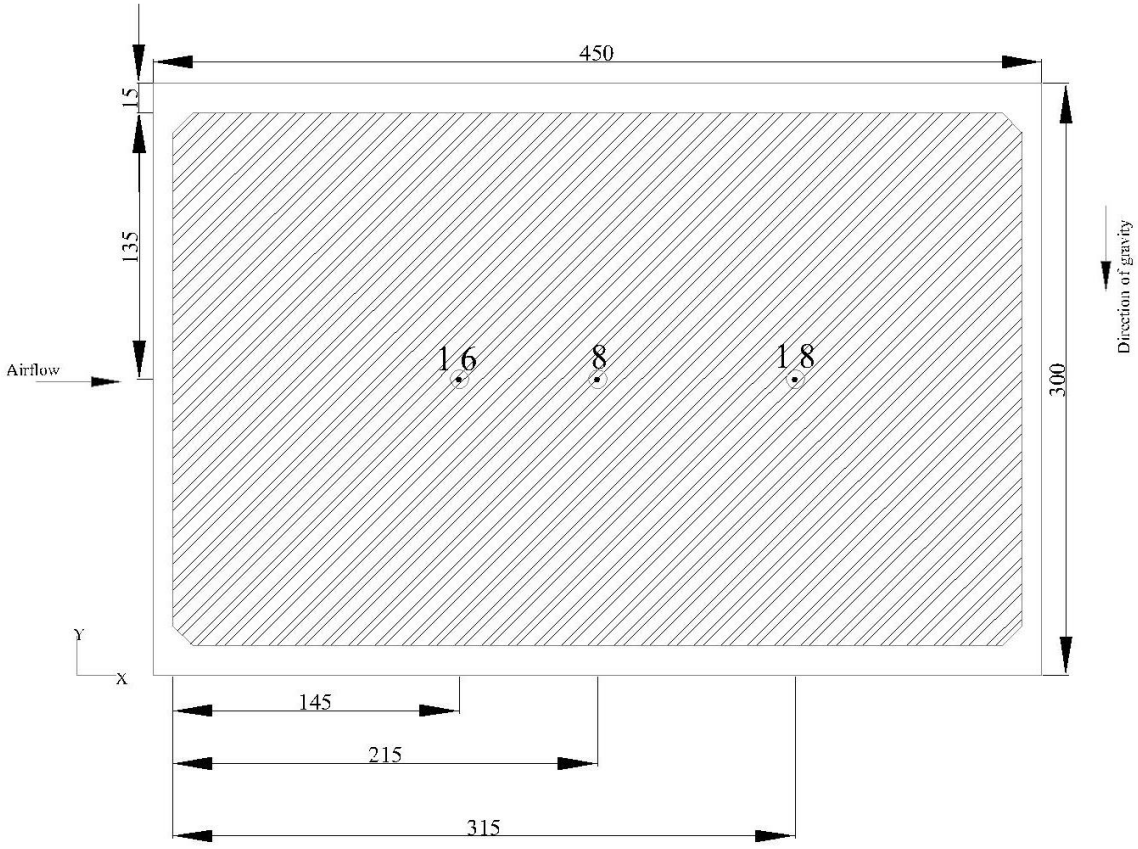

Figure 3.12. Section along middle plates (Plate 7 and 8) showing location of PCM thermocouples along plate length (all dimensions are in mm).

In total 32 channels on three data cards were used to measure inlet air temperature, PCM temperature, ambient air temperature, outlet air temperature, electrical voltage applied to heating element and electrical resistance for heating element using thermocouple junctions in various locations shown in Table 3.1.

Table 3.1. Matching of data card channel number and thermocouple position

Data card channel number	**Description of measurement**	**Location**
101	Inlet air temperature	Inlet air temperature measurement station labelled 6 in Figure 3.1.
102	Inlet air temperature	
103	Inlet air temperature	
104	Inlet air temperature	
105	Inlet air temperature	
201	PCM temperature (Plate 7)	Upstream of plate 7
202	PCM temperature (Plate 6)	Middle of plate 6
203	PCM temperature (Plate 5)	Middle of plate 5
204	PCM temperature (Plate 7)	Middle of plate 7
205	Ambient air temperature	room
206	Ambient air temperature	room
209	PCM temperature (Plate 3)	Middle of plate 3
210	PCM temperature (Plate 2)	Middle of plate 2
211	PCM temperature (Plate 1)	Middle of plate 1
213	PCM temperature (Plate 4)	Middle of plate 4
301	Outlet air temperature	Outlet air temperature measurement station labelled 9 in Figure 3.1.
302	Outlet air temperature	
303	Outlet air temperature	
304	Outlet air temperature	
305	Outlet air temperature	
307	PCM temperature (Plate 8)	Downstream of plate 8
308	PCM temperature (Plate 7)	Downstream of plate 7
309	PCM temperature (Plate 8)	Middle of plate 8
310	PCM temperature (Plate 14)	Middle of plate 14
311	PCM temperature (Plate 8)	Upstream of plate 8
312	PCM temperature (Plate 9)	Middle of plate 9
313	PCM temperature (Plate 10)	Middle of plate 10
314	PCM temperature (Plate 11)	Middle of plate 11
315	PCM temperature (Plate 13)	Middle of plate 13
316	PCM temperature (Plate 12)	Middle of plate 12
317	Electrical voltage applied to heating element	Electrical heating section
318	Electrical resistance for heating element	Electrical heating section

3.9.2 PCM thermophysical properties

As mentioned, three types of phase change materials modules were considered in this investigation. Two modules contained paraffin wax (RT25 and RT27) while the third contained salt hydrate (SP24E). “RT” refers to a paraffin type PCM while the number

after “RT” stands for the peak melting temperature of the PCM. “SP” refers to a salt hydrate type PCM. All the plates are the commercially available Rubitherm™ plates and had identical aluminium envelope structures measuring 450 by 300 by 10 mm. Uniformly distributed bulges are present on these enveloped on both panel surfaces to increase the convective heat transfer to the air (See Figure 2.5). The modules were selected because their melting temperatures correspond to the desired human thermal comfort temperatures for the Gauteng province in South Africa.

The thermophysical properties as stated by the manufacturer of the PCMs that were tested are given in Table 3.2. The volumetric density of the salt hydrate is almost twice that of paraffin. This means that the same dimensions of plate contains a mass of salt hydrate that is almost twice the amount of paraffin wax that can be placed in the same plate. The thermal conductivity of the salt hydrate is three times higher that of paraffin waxes. Higher thermal conductivity ensures high heat transfer rates during charging and discharging of the thermal energy. The higher the heat transfer rates, the smaller is the required heat transfer area. The three phase change materials have similar latent heat capacities. As mentioned, the density of the salt hydrate is almost twice that of paraffin waxes. This means that the salt hydrates overall heat capacity is twice that of paraffin waxes for the same volume of encapsulation.

Table 3.2. Thermophysical properties of RT25, RT27 and SP24E [47]

PCM	T_m (°C)	h_m (kJ/kg)	$C_{p,PCM}$ (kJ/kg.K)	λ_{PCM} (W/m.K)	ρ_{ss} (kg/m^3)	ρ_{Ls} (kg/m^3)	m_{pcm} (kg)	e_{PCM} (m)
RT25	22-26	170	2	0.2	880	760	0.5	0.01
RT27	25-28	180	2	0.2	880	760	0.5	0.01
SP24E*	24-25	180	2	0.6	1500	1400	1	0.01

*Note: The experimental results showed that the melting temperature for the SP24E as specified by the manufacturer was not well defined.

A DSC test for the salt hydrate SP24E was conducted at the CSIR’s National Center for Nano structured materials. The results for the DSC tests for heat absorption are shown in Figure 3.12. The results show that the SP24E has a wide phase transition temperature range of 11 °C to 30 °C with a peak transition temperature at 24.5 °C. The peak

transition temperature value of 24.5 °C is in good agreement with the manufacture's specified value of 24 °C -25 °C.

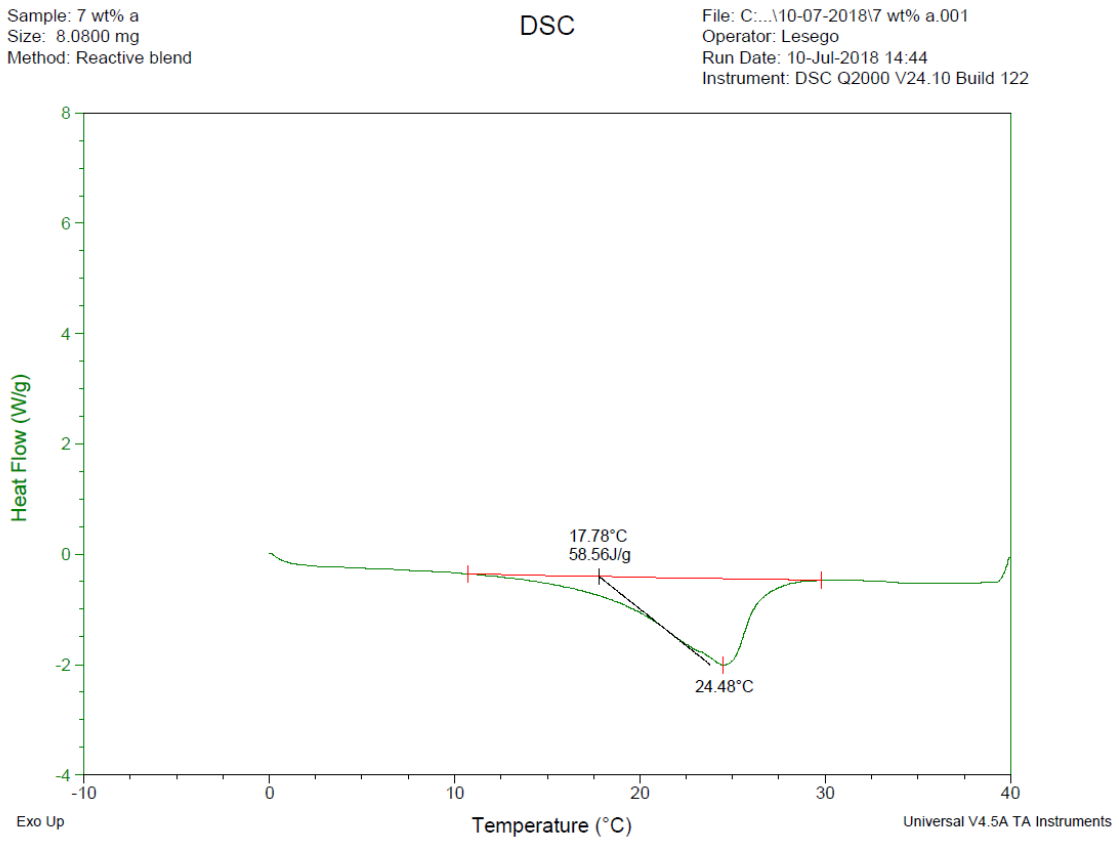

Figure 3.13. Results for the DSC tests for heat absorption for SP24E.

A total of 45 panels (15 panels of each type of paraffin RT25, RT27 and SP24E) manufactured were used. The technical data sheets of the PCM plates from the manufacturer (Rubitherm Technologies) specified the mass of PCM encapsulated in a plate and latent heat values for the PCMs (see Table 3.2). The theoretical total energy stored in Joules per module was calculated from Equation 3.1.

$$Q_{tot,spec} = x \times h_m \times m_{pcm} \quad (3.1)$$

h_m Heat of fusion (latent heat/enthalpy) per unit mass

x Number of PCM plates per module

m_{pcm} Mass of PCM in one plate

To convert the total energy stored into Watt-hour the following Equation 3.2 was used

$$Q_{tot,spec} = x\frac{h_m \times m_{pcm}}{3600\ (sec)} \times hr \quad (3.2)$$

$Q_{tot,spec}$ Theoretical energy stored by PCM as specified by PCM manufacturer

The calculated manufacturer specified total energy absorption for the PCMs in Table 3.3 were calculated from Equation 3.2 with $x = 15$ for all modules, h_m =170 000 J/kg, 180 000 J/kg and 180 000 J/kg for the RT25, RT27 and SP24E respectively. m_{pcm} = 0.5 kg, 0.5 kg and 1 kg for the RT25, RT27 and SP24E respectively.

The specified total energy absorption for the RT25, RT27 and SP24E PCM plates were calculated using Equation 3.2 and results are shown in Table 3.3.

Table 3.3. Theoretical calculation for total energy stored per module.

PCM type	Mass of PCM per plate (kg)	Total number of plates per module	$Q_{tot,15\ plates}$ (Wh)
RT25	0.5	15	354
RT27	0.5	15	375
SP24E	1	15	750

3.9.3 PCM encapsulation: Aluminium envelope

The thickness of the aluminium plate used for the PCMs encapsulation is 1 mm [17] and it thermal conductivity is expected to be between 200 W/m.K and 300 W/m.K [17].

3.9.4 PCM Selection criteria

The Waqas and Din [2] criterion which states that the melting point of PCM must be close to the designed room temperature for thermal comfort was employed for this study. SANS 204 [7] energy efficiency standard for South Africa gives the thermal comfort band for an air-conditioned building as 20°C to 24°C. Where 20°C is the winter set point temperature and 24°C is the summer set point temperature. Further to air conditioned thermal comfort band, the adaptive approach was also taken into

consideration. The adaptive approach method of ASHRAE standard 55 [67] for calculating the thermal comfort for naturally ventilated spaces was applied. Mean monthly outdoor summer air temperatures for one of the climatic zones for Gauteng region (Pretoria Central) was mapped to the 80% acceptability limit criteria (see Figure 3.13) and gives a summer thermal comfort temperature of 28 °C. Thus, the selected PCMs had to conform to the human thermal comfort temperatures specified by SANS 204 [7] (24 °C for summer) and the maximum thermal comfort temperature for Pretoria central (28 °C for summer). The PCMs selected for this study had melting temperature ranges from 22°C to 28°C (see Table 3.2).

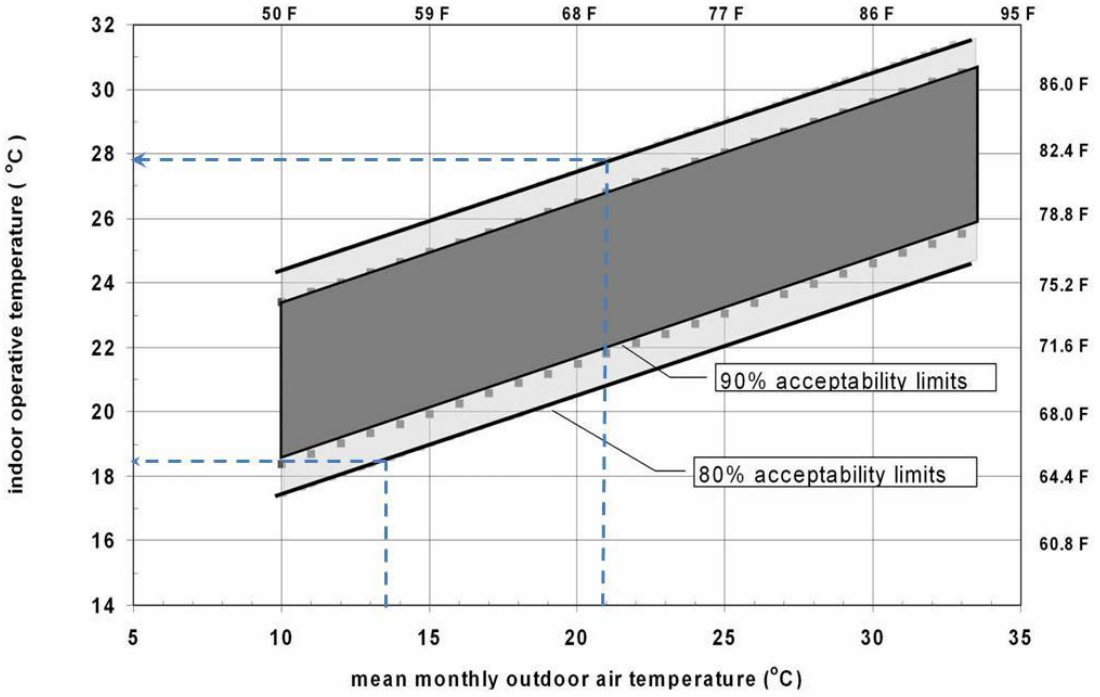

Figure 3.14. Acceptable operative temperature ranges for naturally conditioned spaces (Adapted from [67]).

3.10 FAN

The air was extracted through the system by a 200 mm diameter axial inline tube fan placed a distance L_{AH} of 7.5 m. The fan was designed to operate at three rotational speed levels (high, medium and low) as shown in the fan curve diagram in Figure 3.14. However, for this study a fan motor controller was acquired and installed that regulated the fan to operate at six different speeds. The fan had a capacity of 450 Pa static

pressure. The fan was powered by a 230 V±5% alternating current with 50 Hz frequency and its power rating was 155 W with a maximum of 2502 revolutions per minute [68].

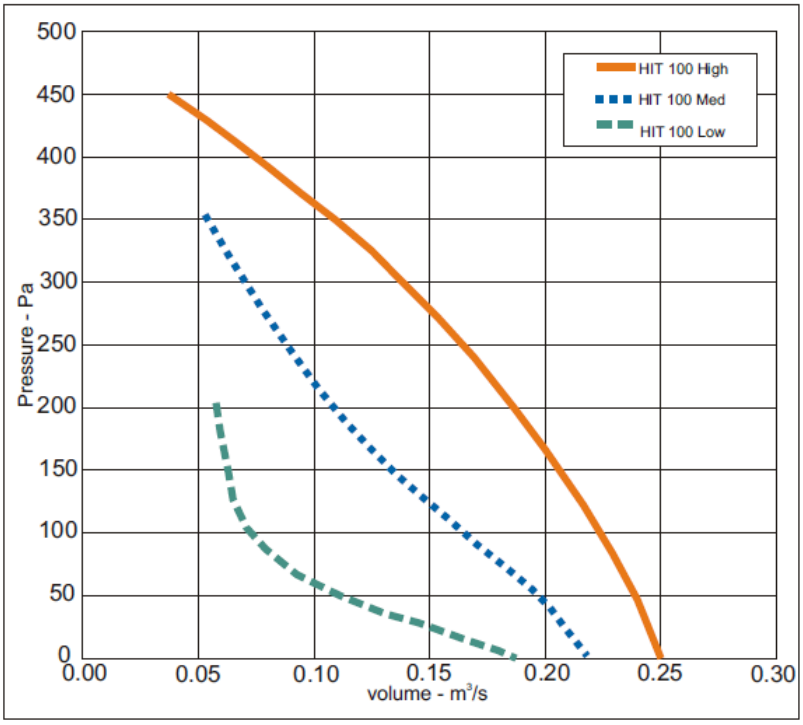

Figure 3.15. Fan curve for 200 mm diameter inline tube fan [68].

The air extraction mode was chosen as opposed to air supply mode. The air supply mode is known to cause air turbulence inside the air ducts whereas air extraction mode promotes uniform flow across the test section as is the requirement of the test as stipulated in [64].

3.11 MANUAL DAMPER

Besides the fan motor controller, airflow through the system was regulated by a manual damper. The damper positions were preselected calibration markings which were drawn at predetermined angles corresponding to the required airflow. The dimensions of the damper were 278 mm by 255 mm (see Figure 3.15). Calibration markings for the damper were drawn at predetermined angles corresponding to the required mass flow rates.

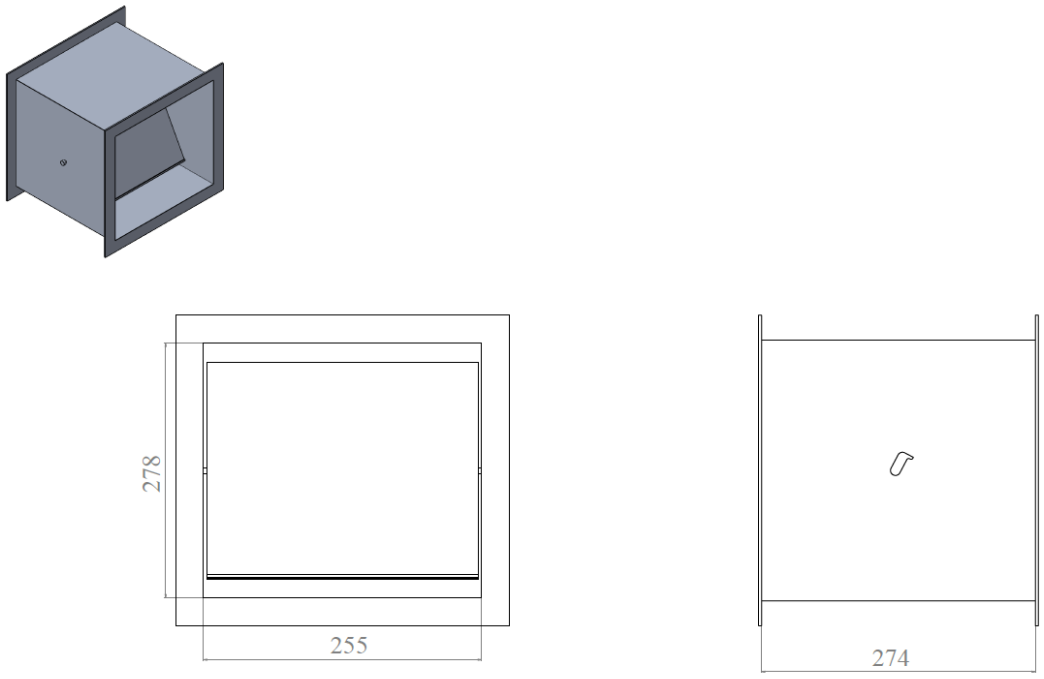

Figure 3.16. Manual damper (all dimensions are in mm).

3.12 NEOPOR INSULATION

100 mm Neopor™ insulation was attached with adhesive to the external walls of the ducts and strapped tight with cable ties. Insulation with an approximate thickness of 25 mm was grooved to accommodate the duct flanges and the grooves were filled with poly urethane insulation foam. The insulation had a density of 15 kg/m^3 and thermal conductivity of 0.032 W/mK.

3.13 FLEXIBLE DUCTING

Outlet air temperature ($\bar{T}_o$) from the test section was always higher than ambient temperature ($\bar{T}_a$) during experimental tests. Maintenance of a steady inlet air temperature ($\bar{T}_i$) was dependent on maintaining a steady room ambient air temperature. Therefore to avoid room ambient air temperature fluctuations, flexible ducting was used to exhaust outlet air from the test section to the outside of the test room.

3.14 DESCRIPTION OF CEILING CASSETTE SPLIT AIR-CONDITIONING UNIT

A Mitsubishi™ FDTC50VF ceiling cassette split unit air-conditioning unit with a heating and cooling capacity of 5.4 kW and 5 kW was used to cool laboratory room air which was drawn through the test section before the start of each melting experiment. This was done to ensure uniform initial PCM temperature for all plates that was lower than the PCM melting temperature.

3.15 DESCRIPTION OF AGILENT DATA ACQUISITION SYSTEM

An Agilent™ 34970A data logger switch unit was used for recording data. Thermocouples were connected into three multiplexer cards (34901A) giving a total of 60 channels of which 40 were T-type thermocouples connections. Values were measured in °C. One channel measured voltage across the heating element in Vac and another channel measured resistance across the heating element in ohms (Ω). The data logger has an output of 61/2 digits (22 bits) of resolution [69]. Experimental measurements were logged at 5 seconds intervals (scan rate of 0.2Hz) by the Agilent™ data logging equipment. The following data was logged:

- Date and time
- Ambient air temperature
- Test section inlet and outlet air temperature
- PCM temperature.
- Electrical voltage supplied across electrical heating element.
- Electrical resistance across electrical heating element.

3.16 ENVIRONMENTAL PROPERTIES

3.16.1 Room air temperature measurement

Two thermocouples were used to measure the room temperature. The thermocouples were located around the air inlet area. The thermocouples were located at a distance far enough to avoid radiation from the heating element. The average room ambient air temperature was the average of the room ambient air temperature measured by the two thermocouples. In order to maintain a steady room air temperature during the melting

experiments, outlet air from the test section was exhausted outside of the test room by the flexible ducting. As will be discussed in the next chapter, the average room air temperature was used in the energy balance over the electrical heating element A to C (Figure 3.1) for the calculation of the air mass flow rate through the test section.

3.16.2 Humidity ratio of air

A HOBO H8 logger was used to measure the air absolute humidity. Equations 4.13 and 4.14 were used to convert absolute humidity to the humidity ratio (W). The logger has an output of 8 bits of resolution. The accuracy of the logger for humidity measurements was ±5% over the range of 5°C to 50°C [70].

3.16.3 Barometric pressure

Barometric pressure (P) was measured by an Oregon Scientific WMR300 indoor barometer with an accuracy of ±100 Pa.

3.17 CALIBRATION PROCEDURES

3.17.1 Mixing devices

In this experiment it was important to ensure that the temperature profiles of the airstreams as they enter the PCM-air heat exchanger were completely even. In order to test the even temperature profiles of the air streams, the electrical resistance heater and the inline tube fan were switched on and air temperature readings from each of the five inlet air temperature thermocouples (101-105; see Table 3.1 and Figures 3.6 and 3.7) were recorded and plotted on Figure 3.16. Temperature stratification of the air was observed; thermocouples 103 and 105 which were located on the bottom quadrants of the duct were observed to read lower temperatures when compared to the top quadrant thermocouples.

The reason for temperature stratification can be explained as follows: The electrical resistance heating coil surface area (see Figure 3.3 and 3.4) is much smaller than the cross sectional area of the cylindrical part of the conical inlet; some air will pass directly over the coil surface and therefore will be heated up significantly. The other parts of the

inlet air flow will by-pass the coil surface and will not be heated up significantly. Buoyancy force caused the warmer air to rise to the top of the duct and hence higher air temperature recorded in the top quadrants of the duct and cooler air to settle at the bottom of the duct.

In order to ensure uniform air inlet temperature before the PCM-air heat exchanger, mixers were installed. The ASHRAE standard 41.1 [71] recommends two types of air mixers; shearing action mixers and propeller fan mixers (see Figure 3.5). Initially shearing action mixers as shown in Figure 3.2 were installed and tested. In order to test the even temperature profiles of the air streams after the installation of the shearing action mixers, the electrical resistance heater and the inline tube fan were switched on and air temperature readings from each of the five thermocouples were recorded and plotted on Figure 3.17. The line graphs of Figure 3.17 do not lie on top of each other; this is an indication of poor mixing although much better when compared to the line graphs of Figure 3.16 where there were no mixers installed. It was decided to add a propeller mixing fan to ensure effective mixing. In order to test the even temperature profiles of the air streams after the installation of the shearing action mixers and propeller mixing fan, the electrical resistance heater and the inline tube fan were switched on and air temperature readings from each of the five thermocouples were recorded and plotted on Figure 3.18. The line graphs of Figure 3.18 lie on top of each other; this is an indication of good mixing.

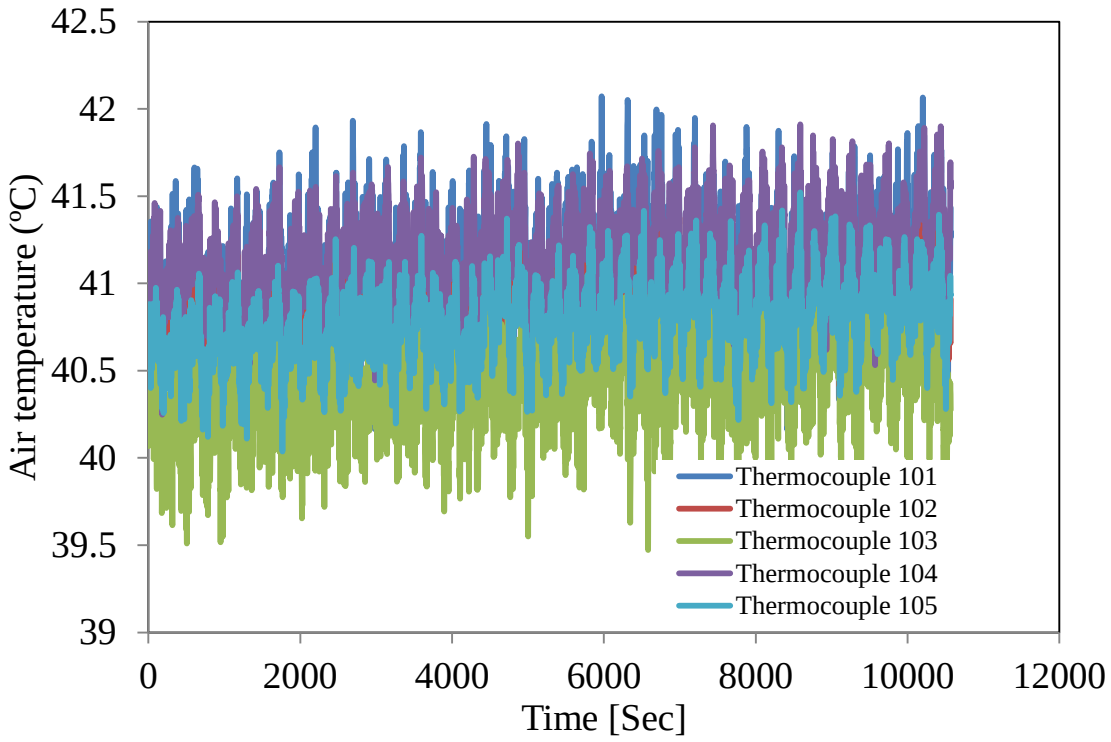

Figure 3.17. Inlet air temperature measurements from the five inlet thermocouples with heating element on.

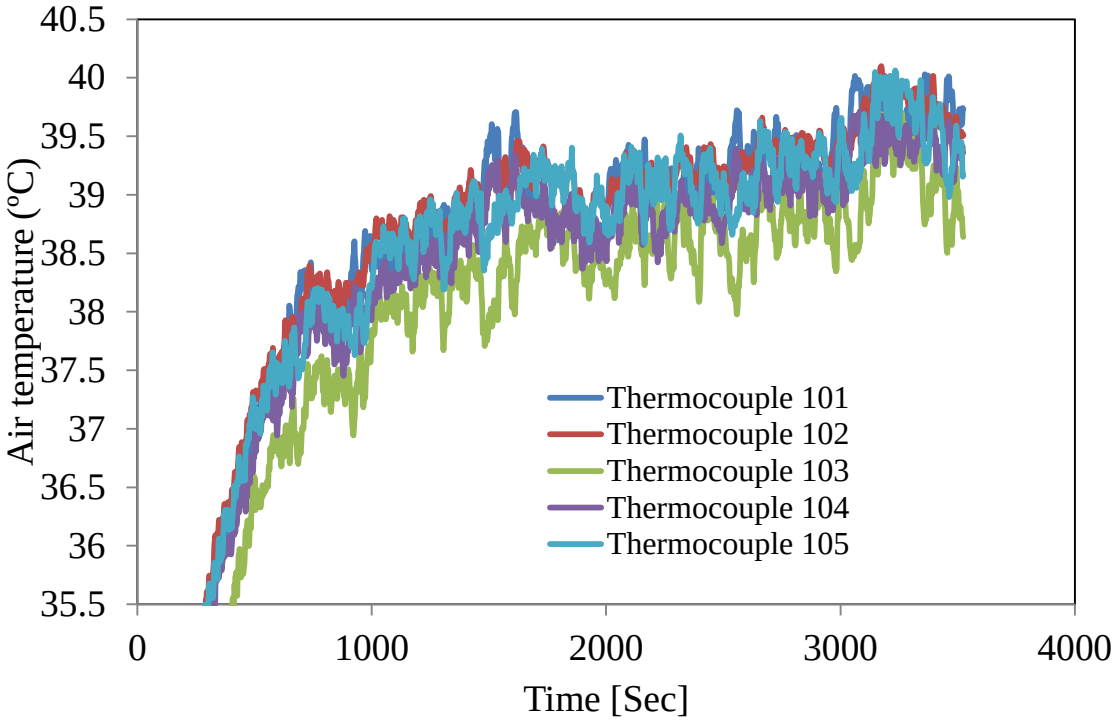

Figure 3.18. Inlet air temperature measurements from the five inlet thermocouples with heating element on and shearing action mixers installed.

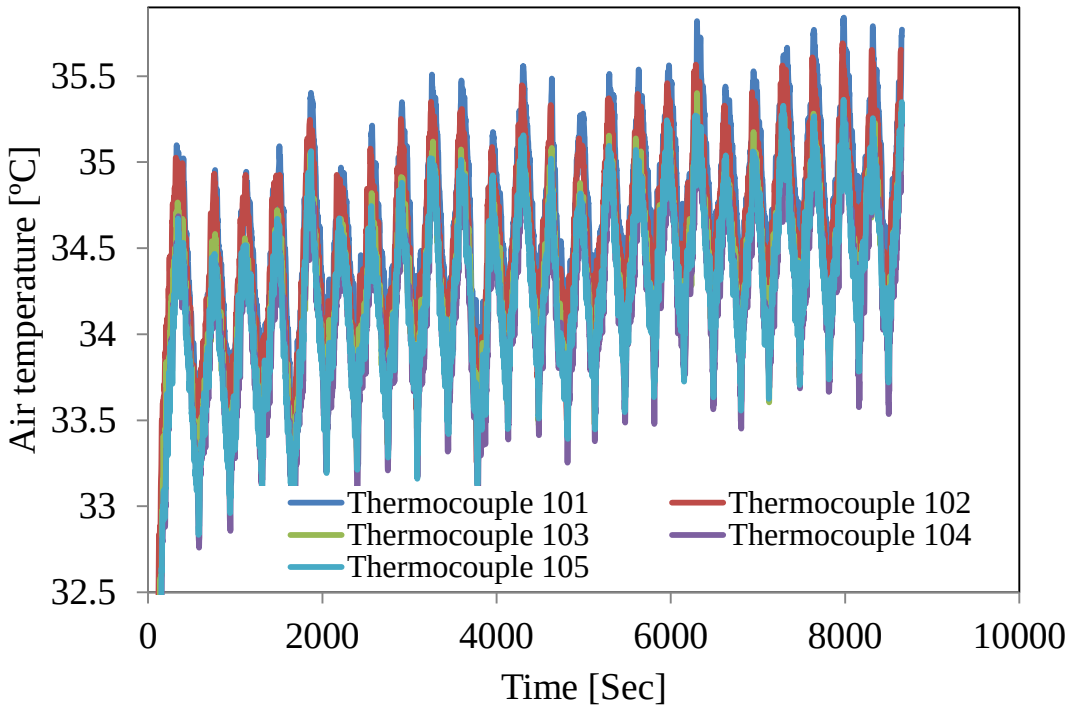

Figure 3.19. Inlet air temperature measurements from the five inlet thermocouples with heating element on, shearing action mixers and propeller fan mixer installed.

Note: The temperature measurements shown in Figures 3.16 to 3.18 were not stable because of the initial use of the Siemens temperature controller for controlling the inlet air temperature. The controller was programmed such that during a fixed time interval (say 180 seconds) power was switched on for a fraction of the time where this time fraction was related to the difference between the set temperature on the controller and the room temperature. When the room temperature was lower than the set temperature by 1.5°C or more, the heater was switched on and when the difference was less than 0.5°C the heater was switched off. In order to resolve the problem of air inlet temperature fluctuations, the Siemens temperature controller was disconnected from the electrical resistance heater. A variable voltage transformer with voltage range of 0 to 250 V was acquired and connected to the electrical resistance heater. Typical inlet air temperature obtained using this arrangement is as shown in Figures 5.1 to 5.3. The major objective for these measurements was to test if the 5 thermocouples for measuring inlet air temperature were giving the same temperature readings when the heating element was switched on and when the mixers were installed.

3.18 EXPERIMENTAL PROCEDURE

The ceiling mounted split unit air conditioning was set to its minimum set point temperature of 19°C. The fan in the experimental set-up was switched on and cold air was drawn through the test section. PCM temperature in each of the plates was monitored on the Agilent Data Acquisition system at five seconds intervals. The fan and the air-conditioning unit were switched off when PCM temperature was below PCM melting temperature and uniform for all the plates. Given that the set point temperature of ceiling cassette unit could only be adjusted down to 19 °C, PCM initial temperature was usually around 20.5 °C. The room air temperature was allowed to warm up to a steady state air temperature before starting the melting experiment. If room temperature was varying it would be difficult to control a steady inlet air temperature to the test section. The forced convective heat transfer to the PCM was significantly reduced by turning off the fan; lowering the PCM temperature using the air conditioning system and these measures prevented early melting of the PCM before starting the experiment. In order to condition the incoming air to a required temperature, the electrical resistance heater was switched on and a desired voltage was set through the transformer. The damper was then adjusted to the desired position and the desired fan speed was set on the fan motor controller. The damper positions were preselected (calibration markings for the damper were drawn at predetermined angles corresponding to the required mass flow rates. The fan motor controller had built in markings for fan speed selection. The experiment was left to run until inlet air temperature was almost equal to outlet air temperature. It was established that the transformer and the electrical resistance heating element were connected in parallel. This was established after observing very small measured resistance values (1Ω). Therefore to obtain the actual resistance of the heating element; the transformer was disconnected from the circuit once the experiment was considered finished and then the resistance of the heating element was logged.

The experimental procedure was followed to conduct a total of 27 melting experiments; 9 experiments for each module of RT25, RT27 and SP24E. The melting experiments matrix is shown in Table 3.3. The inlet air temperatures that were investigated were 30, 32 and 35°C. The air flow rates selected for the study were approximately 30 L/s, 50 L/s and 60 L/s.

Table 3.4. Melting experiments matrix for each PCM type

Experiment	Approximate inlet air temperature (°C)	Approximate air flow rate (L/s)
1	30	30
2	32	30
3	35	30
4	30	50
5	32	50
6	35	50
7	30	60
8	32	60
9	35	60

3.18.1 Steady state

The metallic duct was at an initial temperature that was lower than the desired steady state inlet air temperature. When the electric heating element and fan are switched on, the heat transferred to the air from the electrical heating element was then transferred from the air to the metallic duct until the duct reaches the steady state inlet air temperature. This process took 45 minutes to attain steady inlet air temperature. PCM temperature was already higher than its melting temperature before attaining steady state; waiting for the 45 minute to reach steady state would have meant the exclusion of valuable heat energy stored by the PCM during the phase transformation process which was the main objective of this study.

The steady state time was shortened to approximately 2 minutes by initially making the inlet air temperature very high which resulted in in a higher temperature difference

between the air and the walls of the metallic duct; thereby a higher heat transfer rate to the duct. The process involved trial and error to get it right.

It was found out through measurements that it was not feasible to wait for near perfect steady state conditions; otherwise we would have had very few data for analysis. A decision was made with regards start point for the measurements. The choice of the start point condition was an arbitrary decision. The steady state condition was declared a tolerance of ±0.8°C from the desired test inlet air temperature before the test section.

During the 2 minutes that was required to achieve steady state conditions, the PCM absorbed sensible heat and increased its temperature but did not start melting.

3.19 SUMMARY

A suitable experimental set-up that simulated a real application of a plate PCM-air heat exchanger module installed in a ventilation air duct for passively precooling outdoor summer ambient air was designed and constructed. Desired steady state air inlet temperatures to the test section were achieved within minutes. Induct air temperature stratification was minimised by installation of mixing stations before and after the test section. The rig enabled air temperature measurements within an accuracy of 0.1°C. The downside of the test rig design was the uneven airflow across the duct especially in the region that housed the test section. This resulted in PCM in the center plates melting faster than that in the peripheral plates. PCM temperatures were determined right across the test section.

CHAPTER 4 DATA REDUCTION AND UNCERTAINTY ANALYSIS

4.1 INTRODUCTION

This chapter illustrates how the measured data was reduced into the quantities of interest to this study. First the method is presented that was used to determine the phase transformation periods of the paraffinic PCMs. Then the formulae are described that were used to calculate the heat transfer performance as measured by cooling power, effectiveness, energy stored and phase transformation. The chapter also illustrates how the uncertainties in the values of the measured parameters were determined.

4.2 DETERMINATION OF PHASE TRANSFORMATION DURATION

The phase transformation period was the time interval during which the PCM changed from solid to liquid phase. During the same period both latent and sensible heat storage mechanisms were active. However, the latent heat storage component was the dominant mode of heat storage.

Values of the melting temperature ranges of the PCMs were supplied by the PCM supplier Rubitherm company (see Table 3.2). The thermocouples that were installed at specific points within the PCM indicated the PCM temperatures during the heat absorption period. As mentioned earlier, total of 18 thermocouples were placed at various points in the PCM plates to establish the PCM average temperature (see Figures 3.9 and 3.10 for the locations of thermocouples). The phase transformation period was defined as the time lapse between the moments when the average PCM temperature reached the manufacturer supplied solidus and liquidous temperatures. An example of a graph showing the PCM temperatures versus time is given in Figure 4.1. For convenience a number of PCM temperature profiles at axial distances of $X = 215$ mm from the leading edge for the middle plate (PCM_8) and the two plates directly next to the side walls of the air duct (PCM_2 and PCM_{13}) are given along with the solidus and liquidus temperature values. In this example the average PCM temperature breached the solidus and liquidus temperature at a time instance of approximately 18 minutes and

150 minutes respectively. Thus, for this test case, the phase transition period is approximately 132 minutes.

It was possible to determine the phase transition periods from the supplied temperature properties for the paraffin type PCMs (RT25 and RT27), but not for the salt-hydrate PCM (SP24E) because it was not clear from the manufacturer data if definite liquidus and solidus temperatures existed for this material type. Therefore, phase transformation periods are reported in this dissertation for the RT25 and RT27 only.

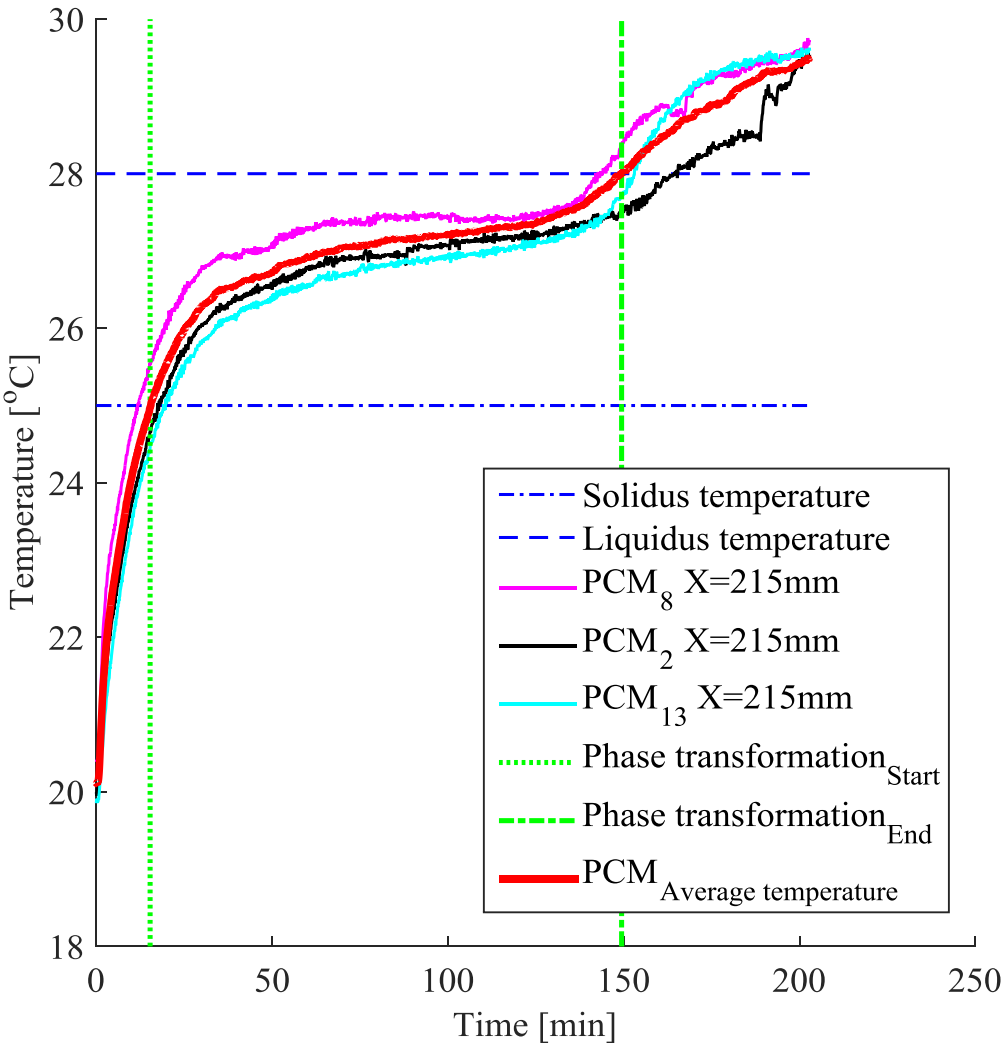

Figure 4.1. Illustration for the determination of phase transformation duration

4.3 INSTANTANEOUS COOLING POWER

The instantaneous cooling power ($\dot{Q}_i$ or $\dot{Q}_{gain,PCM}$) delivered by the test section (PCM plates) was evaluated by applying energy balance around the air in section C to G (See the schematic diagram Figure 3.1):

$$\dot{Q}_{Loss,Air} = \dot{Q}_{gain,PCM} + \dot{Q}_{gain,ambient} \quad (4.1)$$

Where:

$\dot{Q}_{Loss,Air}$ Rate of heat energy lost (cooling rate) from air in section C to G

$\dot{Q}_{gain,PCM}$ Rate of heat absorbed by the PCM module

$\dot{Q}_{gain,ambient}$ Rate of energy lost to the ambient in section C to G

In this equation the total heat loss from the air stream in the test section is attributed to the combined heat transfer to the PCM as well as the heat transfer to the ambient air around the test duct.

The total heat transfer rate from the air can be expressed in terms of the change of air enthalpy across the PCM test section by making use of the specific heat capacity of the air:

I. $\dot{Q}_{Loss,Air} = \dot{m}_{air} C_{p,air} (\bar{T}_i - \bar{T}_o)$

Where

$\dot{m}_{air}$ Air mass flow rate

$C_{p,air}$ Specific heat capacity of air

$\bar{T}_i$ Average inlet air temperature

$\bar{T}_o$ Average outlet air temperature

The heat rate gain rate into the PCM can also be expressed in terms of the change of the enthalpy of the PCM , however, because phase change occurs, the use of specific heat is not suitable. For demonstration purposes the process is assumed for a brief moment to occur fully within the phase transition period (Δt) which allows the enthalpy change to be expressed in terms of the latent heat of fusion:

II. $\dot{Q}_{gain,PCM} = m_{PCM} \frac{\Delta h_m}{\Delta t}$

Where

m_{PCM} Mass of PCM

Δh_m Latent heat of fusion

Δt Phase transformation duration

The heat transfer rate to the ambient air around the test duct can be expressed in terms of the relative temperature difference between the air flow in the test duct and the air outside the test duct, and the thermal resistance of the test duct wall:

III. $\dot{Q}_{gain,ambient} = \frac{\bar{T}_{air} - T_a}{R_{duct(\dot{m})}}$

Where

$\bar{T}_{air}$ Mean bulk temperature Note: $\bar{T}_{air} = \frac{1}{2}(\bar{T}_i + \bar{T}_o)$

T_a Average inlet air temperature before the heater as obtained from the room ambient air temperature

$R_{duct(\dot{m})}$ Duct wall thermal resistance

It should be noted that the thermal resistance of the duct wall is dependent on the inner convective heat transfer coefficient on the inside of the test duct, the effective conductive resistance of the duct wall layers (including the thermal insulation around the duct), and the outer convective heat transfer coefficient on the outside of the insulation layer. Of these, the inner convective heat transfer coefficient is dependent on the mass flow rate of the air inside the test duct, which explains the dependence of R_{duct} on $\dot{m}$.

By substituting I, II and III into equation 4.1, the instantaneous heat absorption into the PCM can be expressed as:

$$\dot{Q}_i = \dot{Q}_{gain,PCM} = m_{PCM} \frac{\Delta h_m}{\Delta t} = \dot{m}_{air} C_{p,air} (\bar{T}_i - \bar{T}_o) - \frac{\bar{T}_{air} - T_a}{R_{duct(\dot{m})}} \quad (4.2)$$

To determine $R_{duct(\dot{m})}$, the experiment was run without the PCM plates placed in the test section. Heated air was passed through the test duct and the temperatures before and after the test section was measured. Any steady state temperature decrease over the test section was thus due to only the heat loss from the internal air through the duct wall. Thus, with the absence of PCM mass in Equation 4.2, the thermal resistance can be expressed in terms of the specific heat of the air, the inlet air temperature, the outlet air temperature, the ambient air temperature and the air mass flow rate:

$$\rightarrow \qquad m_{PCM} = 0$$

$$\therefore \qquad \dot{m}_{air} C_{p,air} (\bar{T}_i - \bar{T}_o) = \frac{\frac{1}{2}(\bar{T}_i + \bar{T}_o) - T_a}{R_{duct(\dot{m})}}$$

$$\therefore \qquad R_{duct(\dot{m})} = \frac{\frac{1}{2}(\bar{T}_i + \bar{T}_o) - T_a}{\dot{m}_{air} C_{p,air} (\bar{T}_i - \bar{T}_o)} \qquad (4.3)$$

Note, as mentioned earlier $R_{duct(\dot{m})}$ is a function of the air mass flow rate (i.e. the higher the air mass flow rate, the lower the $R_{duct(\dot{m})}$ value) Therefore, to determine whether or not $\dot{Q}_{gain,ambient}$ contributed significantly in the energy balance (Equation 4.1), $R_{duct(\dot{m})}$ value for the highest tested air mass flow rate was evaluated. The calculated average $R_{duct(\dot{m})}$ (2.78 K/W) was then used to evaluate $\dot{Q}_{gain,ambient}$ for the experimental tests which had air mass flow rate of 0.06 kg/s. A range ($\% \frac{\dot{Q}_{gain,ambient}}{\dot{Q}_{gain,PCM}}$) of 0.2 % to 9.4 % was calculated for the entire experimental duration. For the phase transformation period the range ($\% \frac{\dot{Q}_{gain,ambient}}{\dot{Q}_{gain,PCM}}$) was 0.51 % to 0.98 %. These contributions were considered significant and therefore were taken into account in calculating of $\dot{Q}_{gain,PCM}$.

$$\therefore \qquad \dot{Q}_{gain,PCM} = \dot{Q}_{Loss,Air} - \dot{Q}_{gain,ambient} \qquad (4.4)$$

For the calculation of instantaneous cooling power delivered by a PCM module ($\dot{Q}_{\iota} = Q_{gain,PCM}$) for different operating conditions of air temperature and air mass flow rate, the following equation was applied on the experimental data.

$$\dot{Q}_i = \dot{m}_{air} C_{p,air} (\bar{T}_i - \bar{T}_o) - \frac{\bar{T}_{air} - T_a}{R_{duct(\dot{m})}} \quad (4.5)$$

Where

$R_{duct(\dot{m})}$ Was regarded to be a constant value of 2.78 K/W calculated as explained above.

The main parameters in Equation 4.5 are the air mass flow rate ($\dot{m}_{air}$), the specific heat capacity of air ($C_{p,air}$), the inlet air temperature to the test section ($\bar{T}_i$), the outlet temperature of the test section ($\bar{T}_o$), and the ambient air temperature (T_a). The following section presents the methods applied to the experimental data for the determination of the said parameters.

4.3.1 Air inlet, outlet and ambient temperatures

The test section average air inlet ($\bar{T}_i$) and outlet ($\bar{T}_o$) temperatures were calculated as the arithmetic average temperature of the 5 thermocouples installed between the upstream mixing section and the test-section and between the downstream mixing section and the inline tube fan.

$$(\bar{T}_i) = \left(\frac{\sum_{TC=101}^{TC=105} T_{TC}}{5} \right) \quad (4.6)$$

Where

TC Temperature measurement from a data card channel (See Table 3.1)

T Temperature value from the data card channel

$$(\bar{T}_o) = \left(\frac{\sum_{TC=301}^{TC=305} T_{TC}}{5} \right) \quad (4.7)$$

The average room ambient air temperature ($\bar{T}_a$) was the average of the room ambient air temperature measured by two thermocouples.

$$(\bar{T}_a) = \left(\frac{\sum_{TC=205}^{TC=206} T_{TC}}{2} \right) \quad (4.8)$$

4.3.2 Air mass flow rate

The air flow rate at time t through the test section was determined by applying an energy balance for the air across the electrical heating element. It was assumed that there is negligible heat loss through the insulation around the heating section due to its relatively shorter length, so that the instantaneous power input to the heating element (Equation 4.9) was equated to the instantaneous rate of heat transfer to the air (Equation 4.10).

Instantaneous power input to the heating element was calculated from the following formulae:

$$P_i = \frac{V^2}{\bar{R}} \tag{4.9}$$

Where:

P_i Instantaneous power delivered to the heating element

V Voltage logged at 5 seconds intervals
$\bar{R}$ Average of resistance logged at 5 seconds intervals

Instantaneous rate of heat transfer from the heating element to the air was given by:

$$\dot{Q}_{heater} = \dot{m}_{air} C_{p,air} (\bar{T}_i - \bar{T}_a) \tag{4.10}$$

Where:

$\dot{Q}_{heater}$ Instantaneous rate of heat transfer from the heating element to the air

Equating equation 4.9 to equation 4.10, the energy balance of air across the electrical heating element was given by:

$$\dot{m}_{air} = \frac{V^2}{\bar{R} C_{p,air} (\bar{T}_i - \bar{T}_a)} \tag{4.11}$$

The voltage and the electrical resistance was obtained from the data logger while the specific heat of the air was obtained according to the method described in the next section.

4.3.3 Air specific heat capacity

The instantaneous air specific heat capacity was calculated as follows:

$$C_{p,air} = C_{p,dry\ air} + W \cdot C_{p,w} \quad (4.12)$$

With:

$C_{p,dry\ air}$	Dry air specific heat
$C_{p,w}$	Specific heat capacity of water vapour
W	Air humidity ratio

The specific heat capacity of dry air was assumed to be 1.005 kJ/kg.K [13]. The room ambient air temperatures, inlet air temperatures and outlet air temperatures ranged between 20 °C to 40 °C for the experimental conditions. The specific heat capacity of dry air is constant at 1.005 kJ/kg.K for this temperature range [72]. The specific heat capacity of water vapour was assumed to be 1.82 kJ/kg.K and remained virtually constant within 20 °C to 40 °C as shown by [73].

The HOBO H8 logger recorded absolute humidity. The air humidity ratio was calculated from the Hobo H8 logger measurements using Equations 4.13 [74] and 4.14 [75].

$$W = 0.62198 \frac{P_w}{P - P_w} \quad (4.13)$$

Where

P_w	Partial pressure of water vapour
P	Measured barometric pressure

Partial pressure of water vapour was calculated using Equation 4.14.

$$P_w = \frac{461.9 \bar{T}_a \times m'}{1000} \quad (4.14)$$

Where

m' Absolute humidity

4.4 EFFECTIVENESS

The effectiveness of PCM-module ($\bar{\varepsilon}_m$) is defined as the ratio of actual energy absorbed during phase transformation to the maximum possible energy that can be absorbed or released by the air. The effectiveness calculation is valid for the phase transformation period only. Equation 4.15 [59, 76] was used to calculate the average effectiveness for the duration of phase transformation for the RT25 and RT27 modules. The average effectiveness of the SP24E module was not determined because SP24E did not melt but rather went through continuous dehydration reactions over a temperature range that was wider than that specified by the PCM supplier as explained later in paragraph 5.2.

$$\bar{\varepsilon}_m = \frac{\bar{T}_i - \bar{T}_o}{\bar{T}_i - \bar{T}_m} \tag{4.15}$$

Because there was an energy loss to the ambient through the air duct wall, the experimentally measured outlet temperature did not reflect the true cooling potential of the PCM plates. In order to determine the cooling potential of the PCM plates if they were operational in an adiabatic air duct, the heat loss as calculated earlier (0.2 % to 9.4 % of the $\dot{Q}_{gain,PCM}$ over the entire experimental duration and from 0.51 % to 0.98 % during the PCM phase transformation period), was taken into consideration to determine the hypothetical adiabatic air duct exit air temperature as follows:

Then $\bar{T}_o = \bar{T}_{o,cor}$

$$\dot{m}_{air} C_{p,air} \left(\bar{T}_i - \bar{T}_{o,cor}\right) = \dot{Q}_{gain,PCM} - \dot{Q}_{gain,ambient}$$

$$\frac{\dot{m}_{air} C_{p,air} \left(\bar{T}_i - \bar{T}_{o,cor}\right)}{\dot{m}_{air} C_{p,air} \left(\bar{T}_i - \bar{T}_o\right)} = \frac{\dot{Q}_{gain,PCM} - \dot{Q}_{gain,ambient}}{\dot{Q}_{gain,PCM}}$$

$$\bar{T}_{o,cor} = \bar{T}_i - \left(1 - \% \frac{\dot{Q}_{gain,ambient}}{\dot{Q}_{gain,PCM}}\right) \left(\bar{T}_i - \bar{T}_o\right) \tag{4.16}$$

Where

$\bar{T}_{o,cor}$ Outlet air temperature corrected for heat losses

4.5 ENERGY ABSORBED

The amount of total energy absorbed by the PCM modules during phase transformation was calculated by integrating the instantaneous heat rate with time during the phase transition period:

$$Q_{tot} = \int_{t=PTS}^{t=PTE} \dot{Q}_i dt \tag{4.17}$$

Where

$t = PTS$ Phase transformation start time (see Figure 4.1).

$t = PTE$ Phase transformation end time (see Figure 4.1).

Q_{tot} Energy absorbed by the PCM during the experiments

Similarly, the total energy absorbed for the whole duration of the experiment was calculated by:

$$Q_{tot} = \int_{t=0}^{t=Final} \dot{Q}_i dt \tag{4.18}$$

Where

$t = 0$ Starting time of the experiment

$t = Final$ Ending time of the experiment

4.6 UNCERTAINTY ANALYSIS

Experimental results must be accompanied with the relevant uncertainties (δ)[77]. The uncertainties of the mass flow rate, the air specific heat capacity, the inlet and outlet air temperatures, as well as the air temperature difference and instantaneous heat transfer rate were calculated using the uncertainty propagation method of Kline and McClintock's [78] (See Appendix C).

Tables 4.1 to 4.3 show the calculated uncertainties for humidity ratio, air specific heat capacity, atmospheric air pressure, ambient room temperature, air density, inlet air temperature, outlet air temperature, temperature difference between ambient and inlet air temperature, temperature difference between inlet and outlet air temperatures, voltage across heating element, electrical resistance across heating element, air mass flow rate, absolute value of the uncertainty of cooling power delivered by the PCM module and uncertainty of cooling power delivered by the PCM module expressed as a percentage of the theoretical value.

Tables 4.1 and 4.2 considered the phase transformation duration for RT27 and RT25. Table 4.3 considered the experimental range for SP24E. It was not possible to determine the phase transition period for the salt-hydrate PCM (SP24E) because it was not clear from the manufacturer data if definite liquidus and solidus temperatures existed for this material type.

The temperature difference between air inlet temperature $(\bar{T}_i)$ and air outlet temperature $(\bar{T}_o)$ was tending to zero towards the end of the experiment therefore the higher uncertainties in the thermocouple measurements lead to higher uncertainty in the calculation of cooling power. The cooling power tended to zero towards the end of the experiment as the temperature of PCM approached the inlet air temperature. Therefore the uncertainties considered for the paraffinic PCMS were for the phase transformation period.

Table 4.1. Uncertainity analysis considering phase transformation duration for RT27 module.

$\dot{m}_{air}$ (kg/s)	$\bar{T}_i$ (°C)	δW	$\delta C_{p,air}$ (kJ/kg.K)	δP (kPa)	$\delta \bar{T}_a$ (°C)	$\delta \bar{T}_i$ (°C)	$\delta \bar{T}_o$ (°C)	$\delta \Delta T_{i,a}$ (°C)	$\pm \Delta T_{i,o}$ (°C)	δV (V)	$\delta \bar{R}$ (Ω)	$\delta \dot{m}_{air}$ (kg/s)	$\delta \bar{Q}_i$ (kW)	$\delta \bar{Q}_i$ (%)
0.03	30	4.805E-05	6.483E-05	0.1	0.071	0.045	0.045	0.084	0.063	0.11	0.012	0.0013	0.011	14.5
0.03	32	4.815E-05	6.496E-05	0.1	0.071	0.045	0.045	0.084	0.063	0.11	0.012	0.0014	0.012	10.6
0.03	35	4.877E-05	6.58E-05	0.1	0.071	0.045	0.045	0.084	0.063	0.10	0.012	0.15	0.011	7.31
0.05	30	4.834E-05	6.521E-05	0.1	0.071	0.045	0.045	0.084	0.063	0.12	0.012	0.0017	0.015	14.4
0.05	32	4.865E-05	6.563E-05	0.1	0.071	0.045	0.045	0.084	0.063	0.12	0.012	0.0017	0.015	9.82
0.05	35	4.881E-05	6.585E-05	0.1	0.071	0.045	0.045	0.084	0.063	0.13	0.012	0.0018	0.014	6.54
0.06	30	4.862E-05	6.559E-05	0.1	0.071	0.045	0.045	0.084	0.063	0.11	0.012	0.0017	0.015	12.74
0.06	32	4.872E-05	6.573E-05	0.1	0.071	0.045	0.045	0.084	0.063	0.12	0.012	0.0019	0.016	9.19
0.06	35	4.907E-05	6.62E-05	0.1	0.071	0.045	0.045	0.084	0.063	0.13	0.012	0.0020	0.016	6.37

Table 4.2. Uncertainity analysis considering phase transformation duration for RT25 module.

$\dot{m}_{air}$ (kg/s)	$\bar{T}_i$ (°C)	δW	$\delta C_{p,air}$ (kJ/kg.K)	δP (kPa)	$\delta \bar{T}_a$ (°C)	$\delta \bar{T}_i$ (°C)	$\delta \bar{T}_o$ (°C)	$\delta \Delta T_{i,a}$ (°C)	$\delta \Delta T_{i,o}$ (°C)	δV (V)	$\delta \bar{R}$ (Ω)	$\delta \dot{m}_{air}$ (kg/s)	$\delta \bar{Q}_i$ (kW)	$\delta \bar{Q}_i$ (%)
0.03	30	4.855E-05	6.55E-05	0.1	0.071	0.045	0.045	0.084	0.063	0.087	0.012	0.0010	0.012	10.15
0.03	32	4.84E-05	6.53E-05	0.1	0.071	0.045	0.045	0.084	0.063	0.12	0.012	0.0015	0.013	6.8
0.03	35	4.86E-05	6.557E-05	0.1	0.071	0.045	0.045	0.084	0.063	0.12	0.012	0.0014	0.013	5.31
0.05	30	4.9E-05	6.611E-05	0.1	0.071	0.045	0.045	0.084	0.063	0.088	0.012	0.0012	0.014	7.83
0.05	32	4.9E-05	6.62E-05	0.1	0.071	0.045	0.045	0.084	0.063	0.097	0.012	0.0015	0.015	6.88
0.05	35	4.892E-05	6.599E-05	0.1	0.071	0.045	0.045	0.084	0.063	0.13	0.012	0.0019	0.015	4.75
0.06	30	4.866E-05	6.565E-05	0.1	0.071	0.045	0.045	0.084	0.063	0.11	0.012	0.0017	0.016	9.05
0.06	32	4.862E-05	6.559E-05	0.1	0.071	0.045	0.045	0.084	0.063	0.13	0.012	0.0020	0.016	7.49
0.06	35	4.868E-05	6.567E-05	0.1	0.071	0.045	0.045	0.084	0.063	0.13	0.012	0.0020	0.016	5.73

Table 4.3. Uncertainity analysis the experimental range for SP24E module.

$\dot{m}_{air}$ (kg/s)	$\bar{T}_i$ (°C)	δW	$\delta C_{p,air}$ (kJ/kg.K)	δP (kPa)	$\delta \bar{T}_a$ (°C)	$\delta \bar{T}_i$ (°C)	$\delta \bar{T}_o$ (°C)	$\delta \Delta T_{i,a}$ (°C)	$\pm \Delta T_{i,o}$ (°C)	δV (V)	$\delta \bar{R}$ (Ω)	$\delta \dot{m}_{air}$ (kg/s)	$\delta \bar{Q}_i$ (kW)	$\delta \bar{Q}_i$ (%)
0.03	30	4.91E-05	6.63E-05	0.1	0.071	0.045	0.045	0.084	0.063	0.087	0.012	0.00084	0.012	24.17
0.03	32	4.93E-05	6.66E-05	0.1	0.071	0.045	0.045	0.084	0.063	0.096	0.012	0.00094	0.010	33.68
0.03	35	4.92E-05	6.64E-05	0.1	0.071	0.045	0.045	0.084	0.063	0.12	0.012	0.00098	0.010	16.51
0.05	30	4.89E-05	6.60E-05	0.1	0.071	0.045	0.045	0.084	0.063	0.089	0.012	0.0013	0.014	19.55
0.05	32	4.91E-05	6.63E-05	0.1	0.071	0.045	0.045	0.084	0.063	0.097	0.012	0.0012	0.014	18.78
0.05	35	4.92E-05	6.64E-05	0.1	0.071	0.045	0.045	0.084	0.063	0.13	0.012	0.0014	0.013	23.06
0.06	30	4.91E-05	6.63E-05	0.1	0.071	0.045	0.045	0.084	0.063	0.10	0.012	0.0011	0.015	22.15
0.06	32	4.90E-05	6.60E-05	0.1	0.071	0.045	0.045	0.084	0.063	0.1.3	0.012	0.0015	0.015	25.28
0.06	35	4.94E-05	6.67E-05	0.1	0.071	0.045	0.045	0.084	0.063	0.13	0.012	0.0015	0.015	19.06

4.7 SUMMARY

In this chapter an overview was given of the formulae that were invoked to illustrate how the measured data was reduced into the quantities of interest to this study. The formulae were also going to be used to rationalise some of the experimental observations in the next chapter.

CHAPTER 5 RESULTS AND DISCUSSION

5.1 INTRODUCTION

In this chapter the data for PCM temperature distribution and the air inlet and outlet temperature during melting are presented. PCM axial temperature distribution data along the same plate was also analysed to determine the direction of movement of the PCM melt front. The results of average cooling power, average effectiveness and phase transformation duration were analysed for the phase transformation period. For the same period, the effects of air mass flow rate and inlet air temperature on average cooling power, average effectiveness and phase transformation duration were analysed. Finally the same analyses plus energy absorption analyses were done over the whole experimental duration for the three different PCM types.

5.2 PCM TEMPERATURE DISTRIBUTION DURING MELTING

Figures 5.1 to 5.3 give time plots of the inlet air temperature (T_i), the outlet air temperature (T_o) as well as the PCM-temperatures at an axial distance of $X = 215$ mm from the leading edge for the middle plate (PCM_8) and the two plates directly next to the side walls of the air duct (PCM_2 and PCM_{13}). See Figures 3.10 and 3.11 for the location of these plates within the test section and the locations of thermocouples. The green dotted line represents the incidence for the start of phase transformation and the green dash dot line represents the incidence of the end of phase transformation. The blue dash dot line represents the solidus temperature for the PCM and the blue dashed line represents the PCM liquidus temperature as supplied by the manufacturer. All of the figures are for an intended inlet air temperature of 30°C and a mass flow rate of 0.03 kg/s. It should be noted that the average inlet air temperature could not be maintained constant due to the difficulties as mentioned earlier. Figure 5.1 is for RT27, Figure 5.2 is for RT25 and Figure 5.3 is for SP24E.

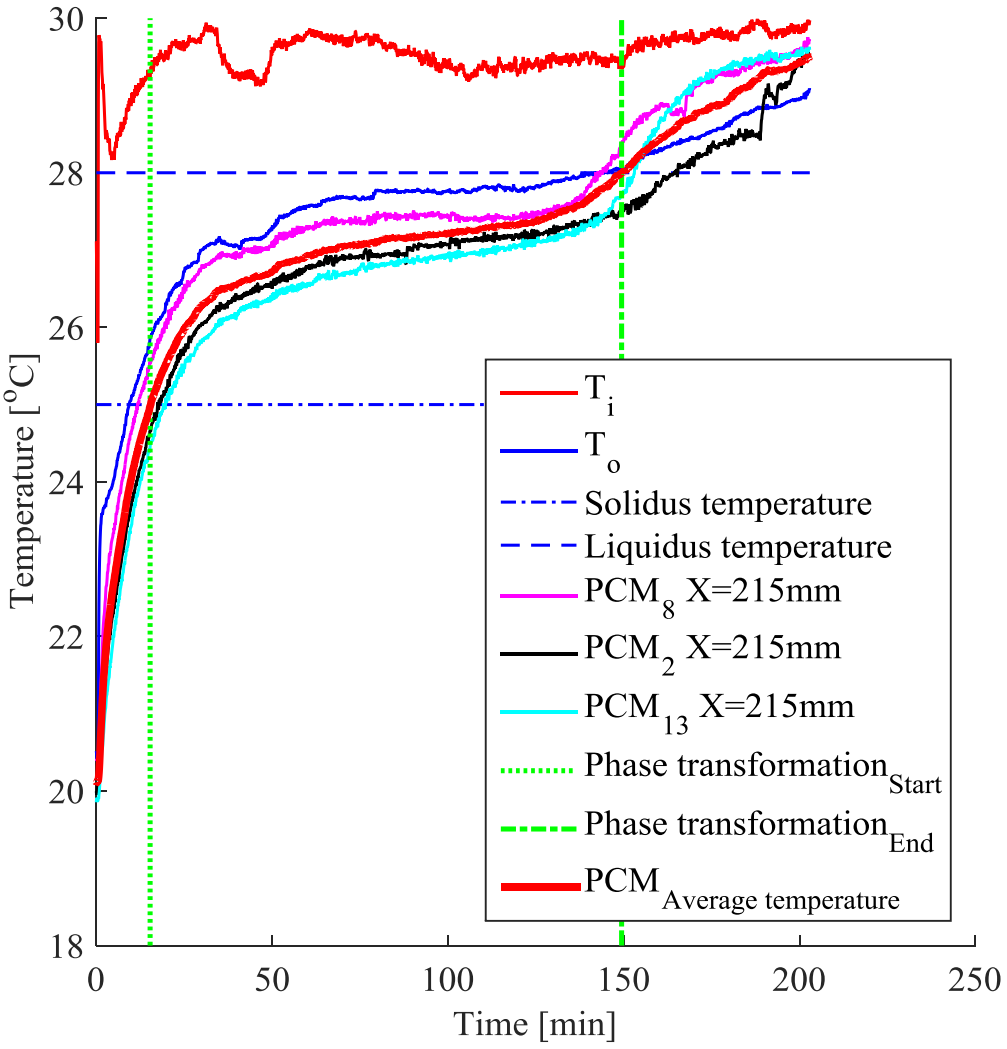

Figure 5.1. Logged temperatures for the RT27 module for an intended inlet air temperature of 30°C and an airflow rate of 0.03 kg/s.

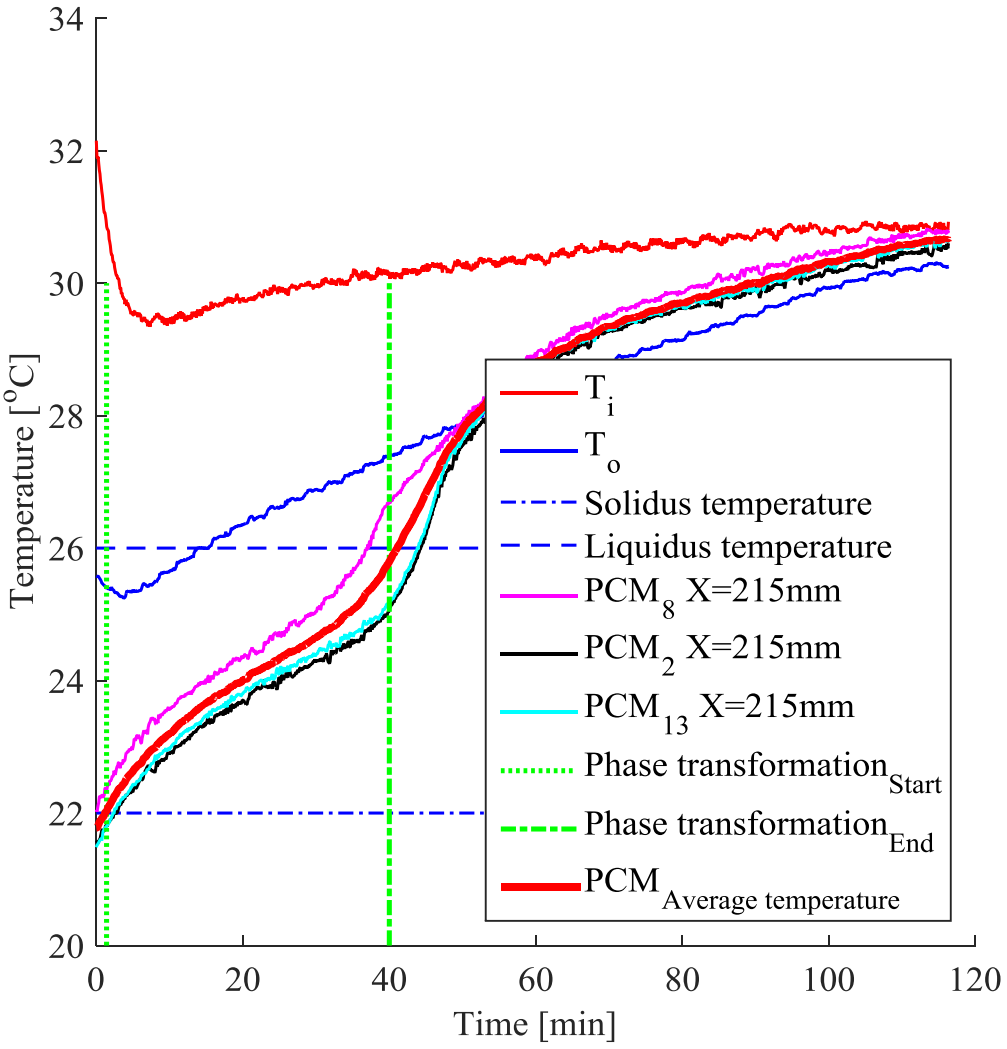

Figure 5.2. Logged temperatures for the RT25 module for an intended inlet air temperature of 30°C and an airflow rate of 0.03 kg/s.

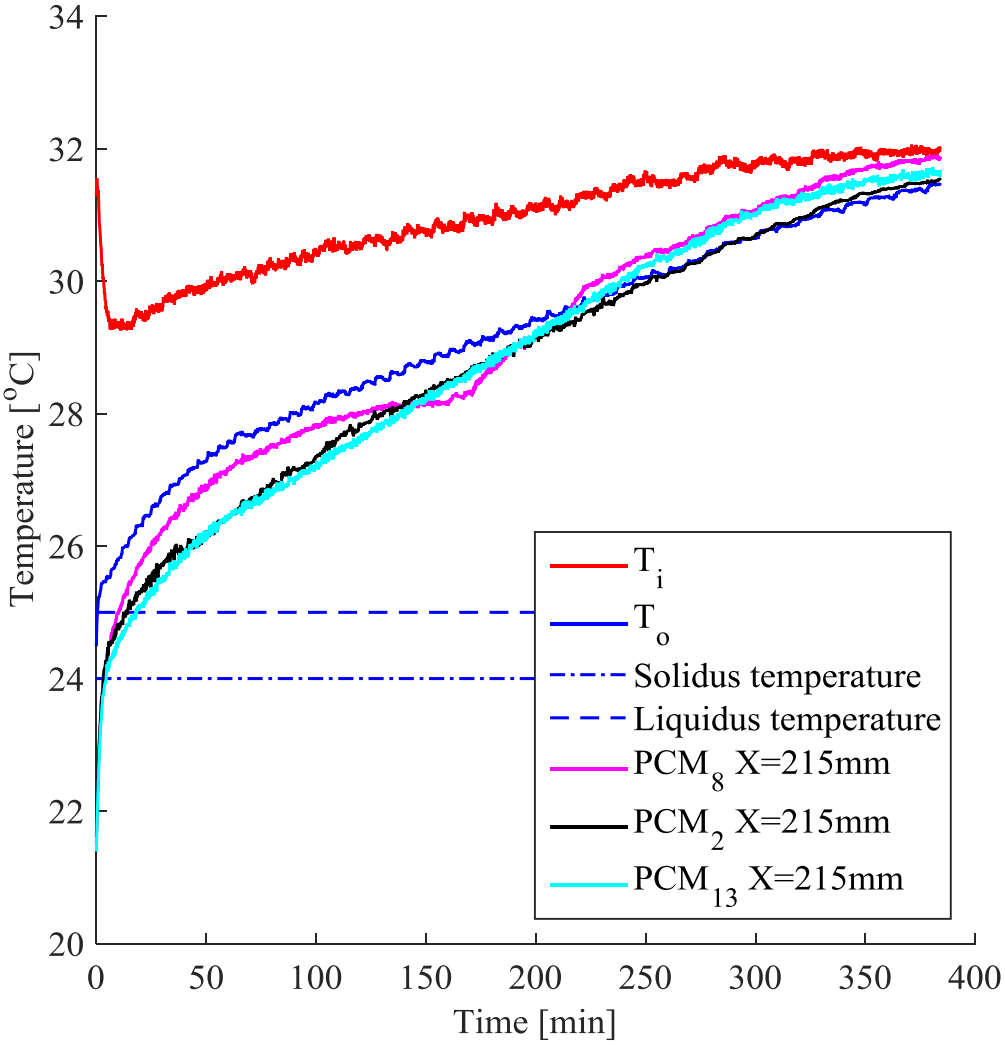

Figure 5.3. Logged temperatures for the SP24E module for an intended inlet air temperature of 30°C and an airflow rate of 0.03 kg/s.

Note: The term liquidus and solidus temperature in this figure for SP24E are not strictly suitable since dehydration reactions rather than melting occurred.

For all three cases the average outlet air temperature (T_o) was lower than average inlet air temperature (T_i). This trend was observed for all other air mass flow rates and inlet air temperatures for all the three PCM types; (See Appendix D). This indicates the air cooling behaviour of the PCM plates during heat absorption (predominately melting) into the PCM . For all the cases there was a higher temperature difference between T_i and T_o at the start of the experiments. This can be attributed to the higher temperature

difference between the inlet air temperature (approximately 30 ºC) and the initial PCM temperature (20 ºC) (see paragraph 3.18 for the procedure used to achieve PCM initial temperature). The higher initial temperature differences caused initially higher heat transfer rates between the air and the PCM (as will be discussed later).

The profiles of PCM temperature against time for SP24E are different when compared to that of RT27 and RT25. The profiles for SP24E are almost linear and that of RT27 are asymptotic for a lower temperature difference between inlet air temperature and PCM melting temperature (ΔT_{pcm}) until fully molten. For higher ΔT_{pcm} the profiles for both RT27 and RT25 are sigmoidal. The difference in the profiles is due to the different mechanisms by which heat is absorbed. For SP24E (salt hydrate) the heat is absorbed for dehydration reactions; the linear profile suggests that the dehydration reactions are continuous.

The PCMs did not have a single defined melting temperatures suggesting that they were not pure or single compounds but rather mixtures of compounds. Values of the melting temperature ranges of the PCMs were supplied by the PCM supplier (see Table 3.2). As mentioned, a total of 18 thermocouples were placed at various points in the PCM plates to establish the PCM average temperature. The PCM temperature profile at any single point was sigmoidal for the paraffins (see Figures 5.1 and 5.2 and additional figures in Appendix D). The calculated average PCM temperature profile was also sigmoidal (see Figures 5.1 and 5.2) and closely resembled the individual PCM temperature-time profiles. This established confidence in the use of the average PCM temperature-time profile (thick red line in Figures 5.1 to 5.3) to represent the phase transformation.

The salt hydrate SP24E did not melt but rather continuously lost structural water (dehydration) and cooled the ambient air during that process. The melting temperature range of SP24E specified by the manufacturer suggests a very short melting period for the salt hydrate (range of 25 to 285 seconds) but the experimental data suggested otherwise. The SP24E is not a single salt hydrate but rather a mixture of salt hydrates (40 to 60 % $CaCl_2$, 1 to 20 % KCl, 0 to 5 % NaCl, 1 to 20 % NH_4Cl and 0 to 5 % $MgCl_2$ [79]). This explains the absence of a single well defined melting temperature. The

SP24E PCM temperature- time profile in Figure 5.3 (see also same graphs in Appendix D) do not show the incidences of start and completion of the dehydration process hence making it difficult to estimate an accurate phase transformation duration. The determination of an accurate melting temperature range for SP24E lies outside of the scope of this work.

The PCM temperatures of the plates directly next to the side walls of the air duct (PCM_2 and PCM_{13}) were lower than middle plate PCM temperature (PCM_8). This can be attributed to the velocity boundary layer effect. The inlet air velocity towards the end plates is expected to be lower than the middle plates therefore lower heat transfer rates between air and PCM at the end plates when compared to middle plates.

5.2.1 PCM melt front

Figures 5.4 to 5.6 show the PCM temperature distribution in plate 8 (the centre-most plate). As mentioned earlier, three PCM temperatures were measured at the following axial distance from the leading edge: 145 mm (PCM_{16}- upstream side), 215 mm (PCM_{17}- middle of plate) and 315 mm (PCM_{18}- downstream side). For all of the figures the air mass flow rate was 0.03 kg/s with an inlet air temperature of 32 °C.

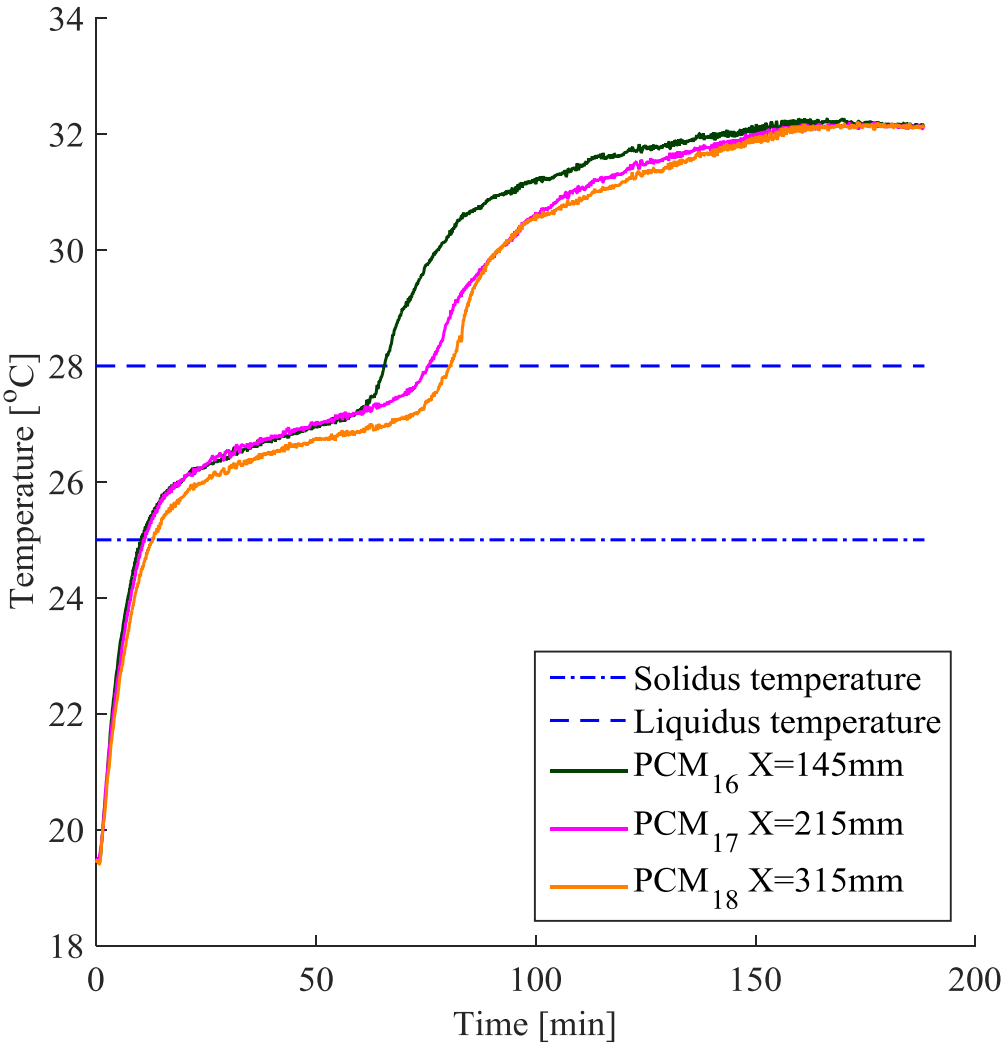

Figure 5.4. PCM temperature distributions for RT27 in the centre plate measured at three axial locations for an air mass flow rate of 0.03 kg/s and an inlet air temperature of 32 °C.

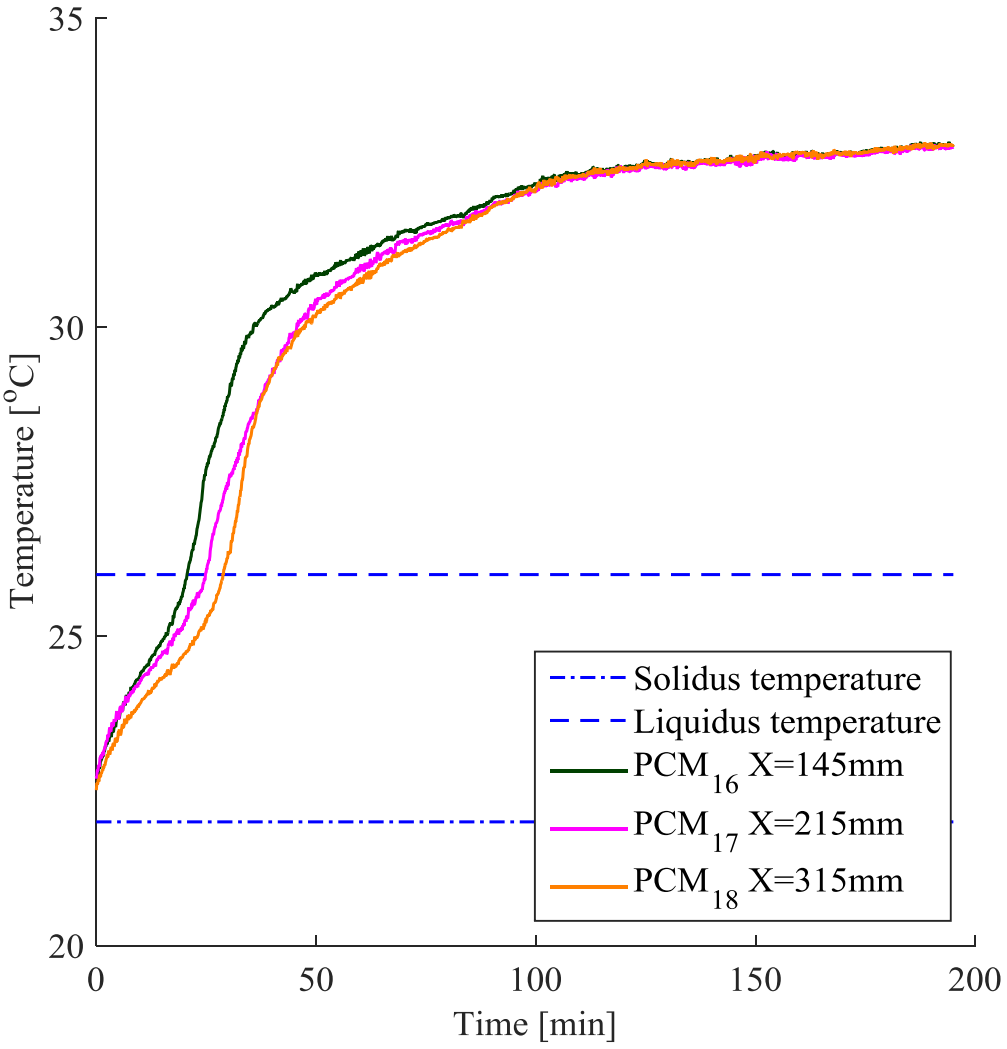

Figure 5.5. PCM temperature distributions for RT25 in the centre plate measured at three axial locations for an air mass flow rate of 0.03 kg/s and an inlet air temperature of 32 °C.

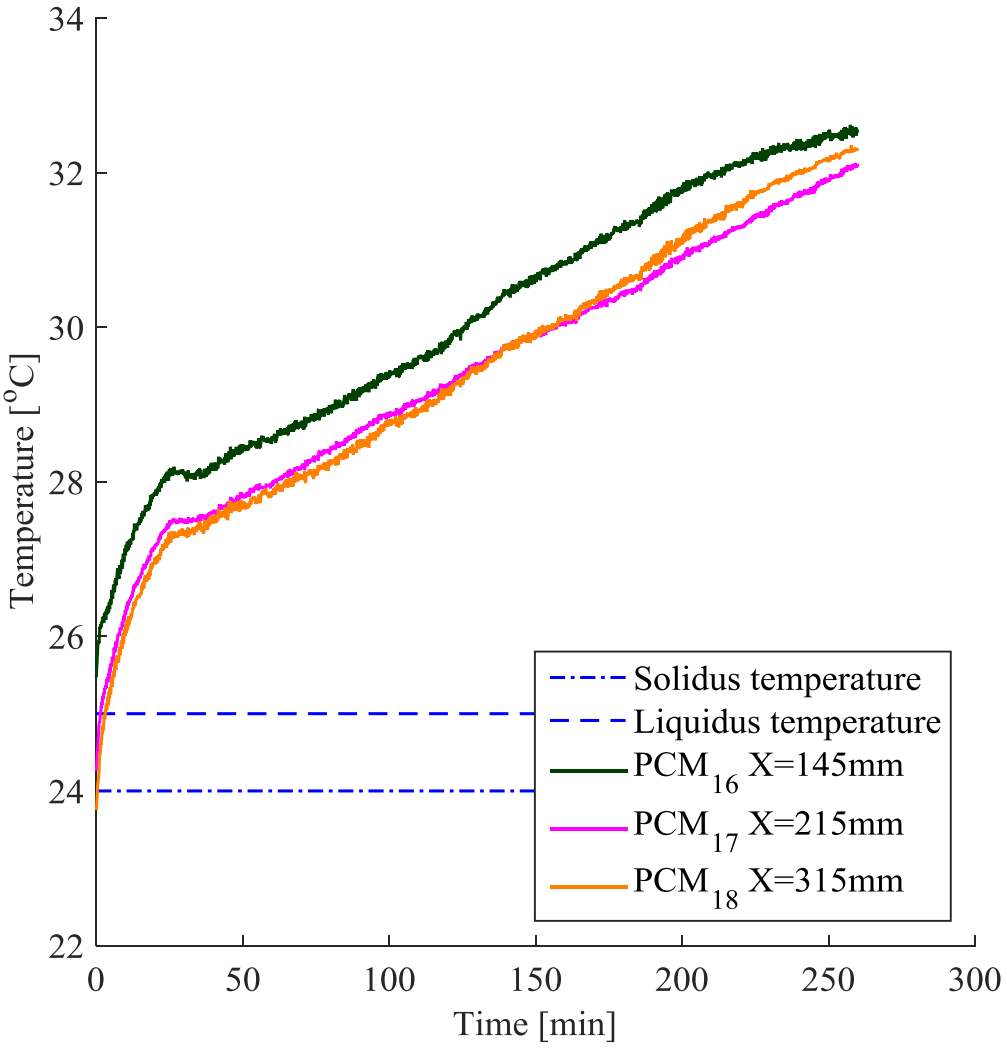

Figure 5.6. PCM temperature distributions for SP24E in the centre plate measured at three axial locations for an air mass flow rate of 0.03 kg/s and an inlet air temperature of 32 °C.

For all cases a general trend was observed that the upstream PCM temperature (PCM_{16}) was always greater than the middle (PCM_{17}) and downstream (PCM_{18}) PCM temperatures. The downstream PCM temperature was observed to be the lowest of the three PCM temperatures. This trend was repeated for other air mass flow rates and inlet air temperatures for all the three PCM types (see Appendix E). This shows that for thin PCM encapsulations for ventilation applications, the PCM melting front moves from the leading edge to the trailing edge.

5.3 RT27 AND RT25 PHASE TRANSFORMATION TIME, EFFECTIVENESS, AND AVERAGE COOLING POWER

Tables 5.1 and 5.2, show the air mass flow rates through the PCM modules, the average inlet air temperatures for the duration of the phase transformation, time average outlet air temperatures for the duration of the phase transformation, phase transformation times, calculated average effectiveness and calculated average air cooling power for the duration of the phase transformation.

Table 5.1. Experimental parameters and results for RT25 considering the phase transformation period only

Module type	$\dot{m}_{air}$ (kg/s)	$\overline{T_i}$ (°C)	$\overline{T_o}$ (°C)	Phase transformation time (min)	$\bar{\varepsilon}$	$\dot{Q}_{ave}$(W)
RT25	0.03	29.8	26.3	38.6	0.60	118
	0.03	31.7	27.1	25.3	0.59	202
	0.03	34.5	28	20.3	0.62	239
	0.05	30.9	27.1	25.3	0.56	186
	0.05	31.4	27.4	20.3	0.54	228
	0.05	34.6	28.5	14.1	0.57	285
	0.06	29.2	26.4	26.0	0.55	188
	0.06	31.4	27.3	17.2	0.55	258
	0.06	32.8	28	9.5	0.54	327

Table 5.2. Experimental parameters and results for RT27 considering the phase transformation period only

Module type	$\dot{m}_{air}$ (kg/s)	$\overline{T}_i$ (°C)	$\overline{T}_o$ (°C)	Phase transformation time (min)	$\bar{\varepsilon}$	$\dot{Q}_{ave}$(W)
RT27	0.03	29.5	27.5	134.2	0.66	60
	0.03	31.6	28.3	63.1	0.65	118
	0.03	34.6	29.4	32.8	0.65	154
	0.05	29.7	27.7	61.2	0.62	104
	0.05	31.8	28.8	37.0	0.56	154
	0.05	34.7	30.1	22.9	0.56	223
	0.06	30.4	28.2	48.8	0.56	126
	0.06	31.9	28.9	31.2	0.55	175
	0.06	34.7	30.4	19.3	0.52	254

5.3.1 Effectiveness analysis: effect of air mass flow rate and inlet air temperature on average effectiveness

Equation 4.15 was used to calculate average effectiveness. The equation applies only for the phase transformation duration. The calculation of phase transformation time for the paraffinic PCMs (RT27 and RT25) was determined by the use of the average PCM temperature-time profile as explained under paragraph 5.2 above. The averages of the melting temperature ranges for the paraffins (RT27 and RT25) were used to represent the peak melting temperature for the paraffins and were regarded as the PCM melting temperatures ($\overline{T}_m$) in Equation 4.15.

The determination of the phase transformation time for the salt hydrate was outside the scope of this work as explained under paragraph 5.2 above; therefore its effectiveness was not calculated.

Given the difficulties of maintaining a steady inlet air temperature as explained in paragraph 3.18.1, the average inlet air temperatures ($\overline{T}_i$) (in Tables 5.1 and 5.2) were rounded off to 30 °C, 32 °C and 35 °C.

The data from Tables 5.1 and 5.2 were used to plot the effect of air mass flow rate and air inlet temperature on average effectiveness for the RT25 and RT27 modules as are shown in Figures 5.7 and 5.8.

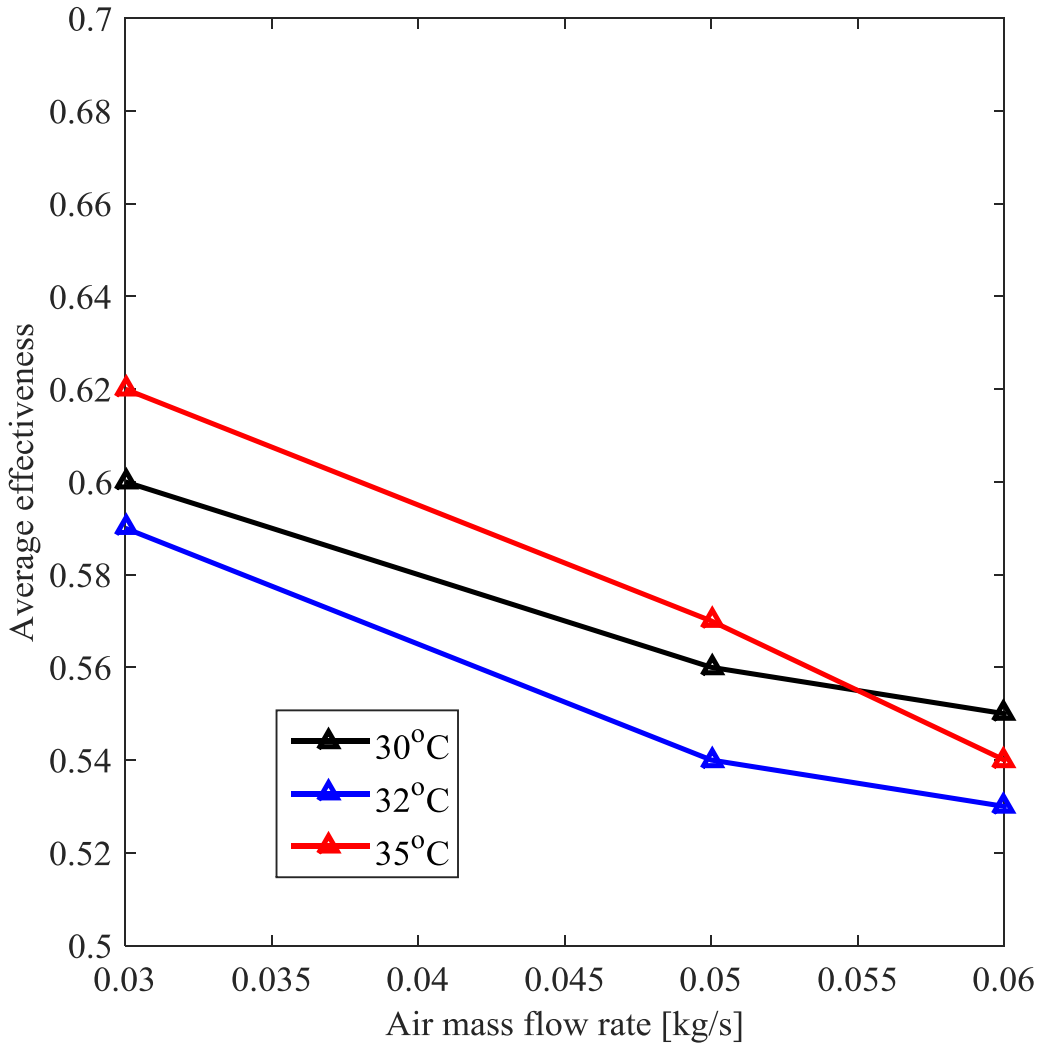

Figure 5.7. Effect of air mass flow rate and air inlet temperature on the average effectiveness of the RT25 module.

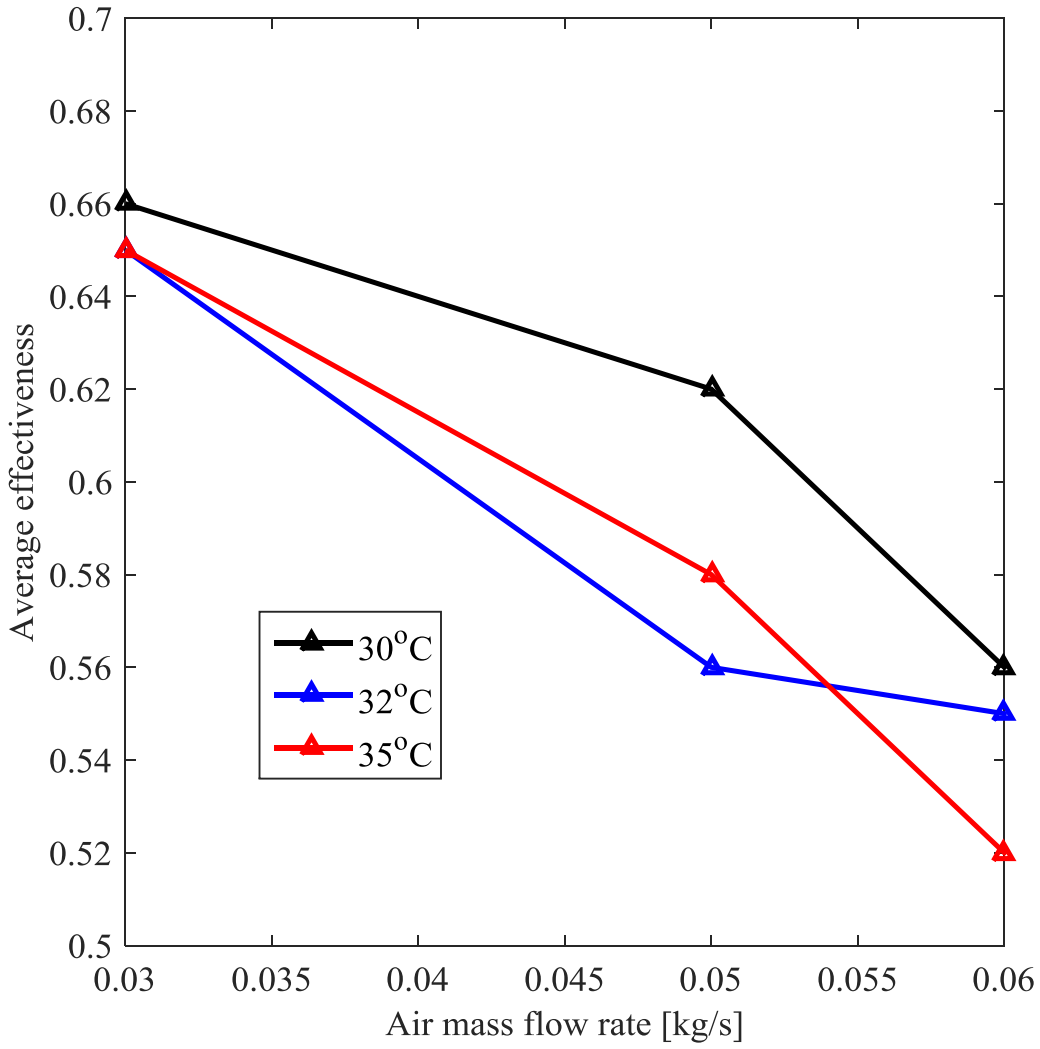

Figure 5.8. Effect of air mass flow rate and air inlet temperature on the average effectiveness of the RT27 module.

From Figures 5.7 and 5.8, the effect of air mass flow rate on the effectiveness can be interpreted considering a fixed average inlet air temperature ($\bar{T}_i$). Both Figures show that the average effectiveness of the PCM modules decreases with increasing convective air mass flow rate as expected [76]. Shorter residence time of the warm air at high air flow rate leads to a reduction of the convective heat transferred from the air to the PCM. This leads to a higher $\bar{T}_o$ and consequently a lower ($\bar{T}_i - \bar{T}_o$) thus reducing the effectiveness according to Equation 4.15. For the RT27 module, at 30 °C inlet air temperature, the

average effectiveness was 0.66 for an air mass flow rate of 0.03 kg/s and 0.56 for an air mass flow rate of 0.06 kg/s i.e. a 15 % reduction in effectiveness.

From Figure 5.7, it can be observed that by increasing the inlet air temperature at a fixed air mass flow rate does not severely influence the effectiveness. For an inlet air temperature of 30ºC and air mass flow rate of 0.03 kg/s the calculated average effectiveness was 0.60. For an inlet air temperature of 32 ºC and air mass flow rate of 0.03 kg/s the calculated average effectiveness was also 0.59 and for an inlet air temperature of 35 ºC and airflow rate of 0.03 kg/s the calculated effectiveness was also 0.62. The practical implication of these findings about effectiveness is that for a given plate configuration and PCM type, it is possible to determine the number of plates that are required to achieve a desired cooling load on the basis of effectiveness and air flow regardless of inlet air temperature.

The average effectiveness for the paraffins were similar due to their similar weight (0.5 kg per plate), thermal conductivity (0.2 W/m.K) and latent heat values (170 kJ/kg and 180 kJ/kg). The difference between PCM melting temperatures of the paraffins was 2.5 °C. The denominator ($\bar{T}_i - \bar{T}_m$) in the definition of the average effectiveness were 3.5 °C, 5.5°C and 8.5 °C for RT27 and 6 °C, 8 °C and 11 °C for RT25. Based on this, one would expect that the paraffin with a narrower difference ($\bar{T}_i - \bar{T}_m$) will give a higher average effectiveness for a given $\bar{T}_i - \bar{T}_o$ but this was not so. Therefore, the overriding term (the term with the greater influence on the average effectiveness) for average effectiveness was the numerator ($\bar{T}_i - \bar{T}_o$). To achieve the maximum effectiveness of 1, $\bar{T}_o$ must equal $\bar{T}_m$. This can be achieved by increasing plate length to ensure longer warm air residence time.

5.3.2 Average cooling power analysis: effects of the air mass flow rate and the inlet air temperature

Equation 4.5 was used to calculate instantaneous cooling power. The instantaneous cooling powers were averaged over the phase transformation duration. The data in Tables 5.1 and 5.2 were used to plot the effect of air mass flow rate and air inlet

temperature on the average cooling power for the RT25 and RT27 modules as is shown in Figures 5.9 and 5.10.

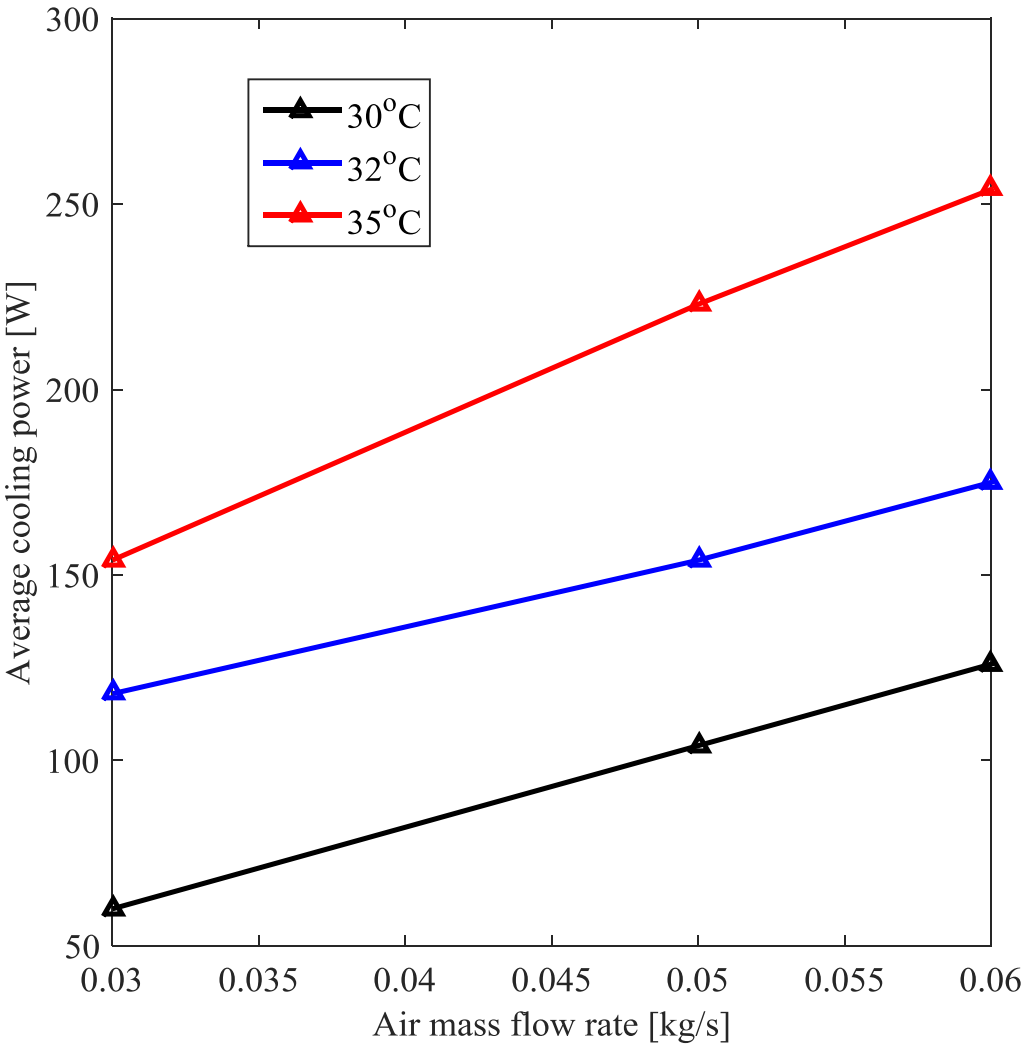

Figure 5.9. Effect of air mass flow rate and air inlet temperature on the average cooling power for the RT27 module.

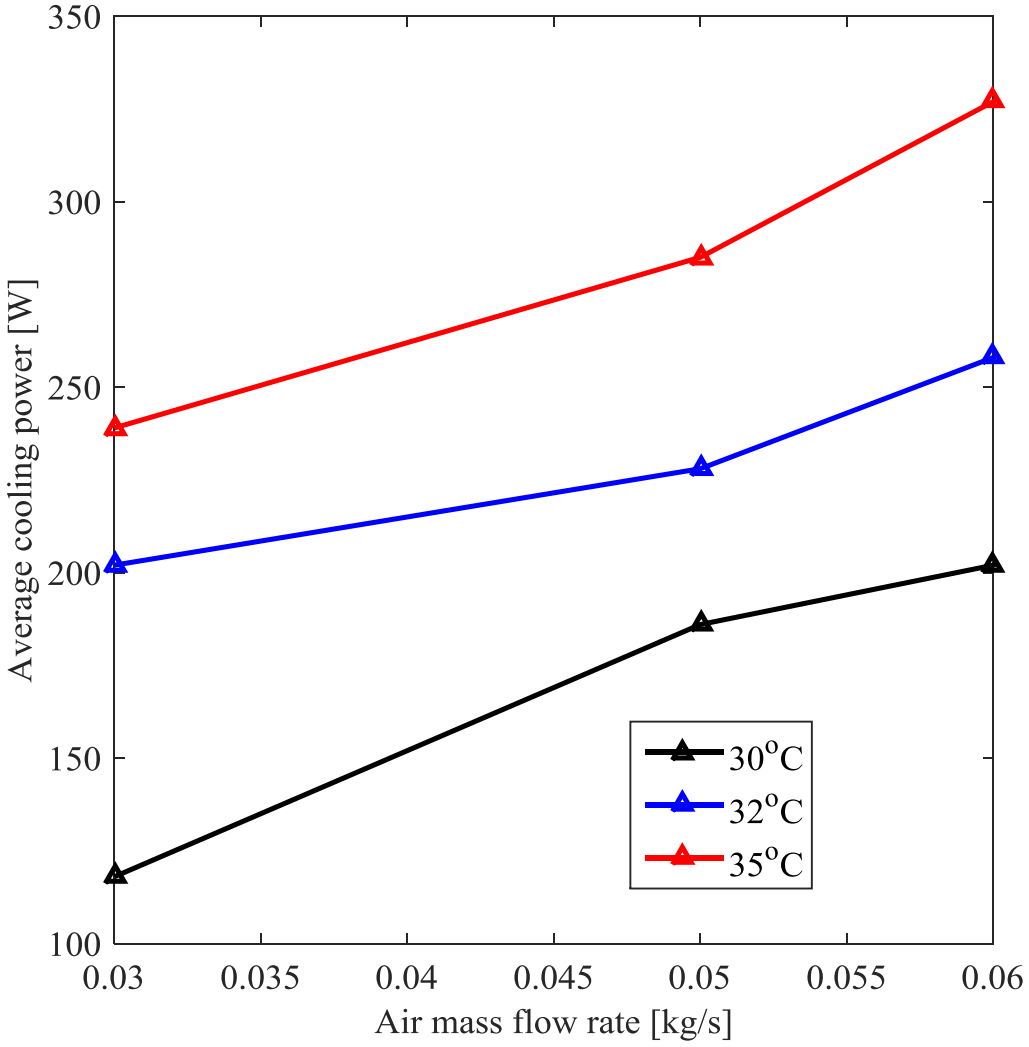

Figure 5.10. Effect of air mass flow rate and air inlet temperature on the average cooling power for the RT25 module.

From Figures 5.9 and 5.10, the effect of the air mass flow rate on cooling power can be observed by considering a fixed average inlet air temperature ($\overline{T}_i$). The effect of the inlet air temperature can be determined likewise by considering a fixed the air flow rate. It is clear from Figures 5.9 and 5.10 that either an increase in the air mass flow rate or an increase in the inlet air temperature increased the average cooling power. The Reynolds number for the air flow in the air channels between plates was calculated to be turbulent (Re = 9696.9 to 19393.9) over the range of the flow rates tested. For turbulent flow, the higher the air flow rate, the higher the convection heat transfer coefficient [80]. A

higher convection heat transfer coefficient increases the convective heat transfer rate from air to PCM according to Equation 6.1.

Equation 6.1 also shows that a higher temperature difference between inlet air temperature and PCM melting temperature ($\bar{T}_i - \bar{T}_m$) also increases convection heat transfer rate.

5.3.3 Phase transformation duration: effect of the air mass flow rate and the inlet air temperature

Figures 5.11 and 5.12 give the phase transformation durations of the PCMs. It can be seen that the durations decreased as either the air flow rates or the inlet air temperatures increased. For the RT27 module (Figure 5.12), for an inlet air temperature of 32ºC and airflow rate of 0.03 kg/s the melting duration was 3785 seconds. For an inlet air temperature of 32 ºC and airflow rate of 0.06 kg/s the melting duration was 1870 seconds. Doubling the air flow from 0.03kg/s to 0.06kg/s reduced the melting duration by 51%. This is attributed to higher heat transfer coefficient for higher air mass flow as will be discussed later. Given the effect of airflow rate and inlet air temperature on phase transformation duration, the experiments could not be run for similar durations at various flow rates and inlet air temperatures.

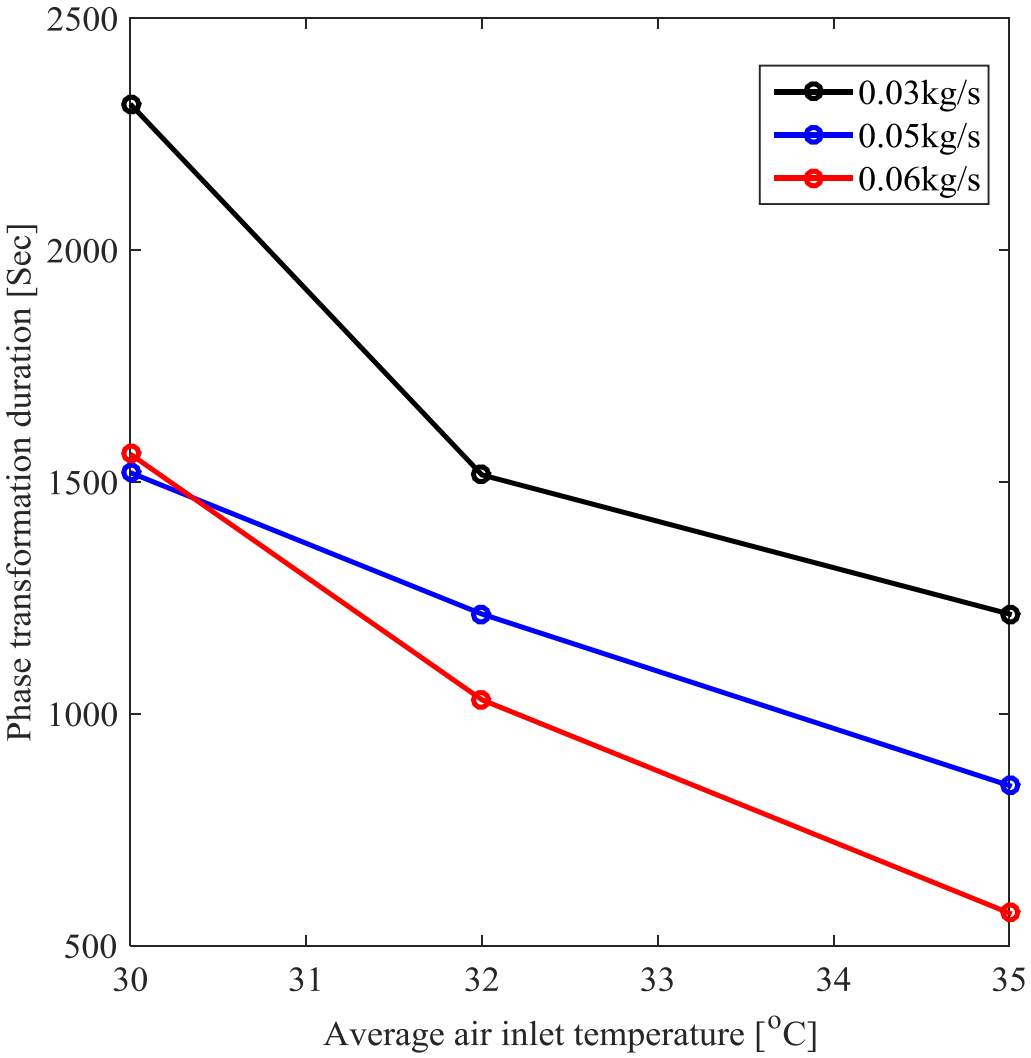

Figure 5.11. Effects of the air inlet temperature and the air mass flow rate on the phase transformation duration for the RT25 module.

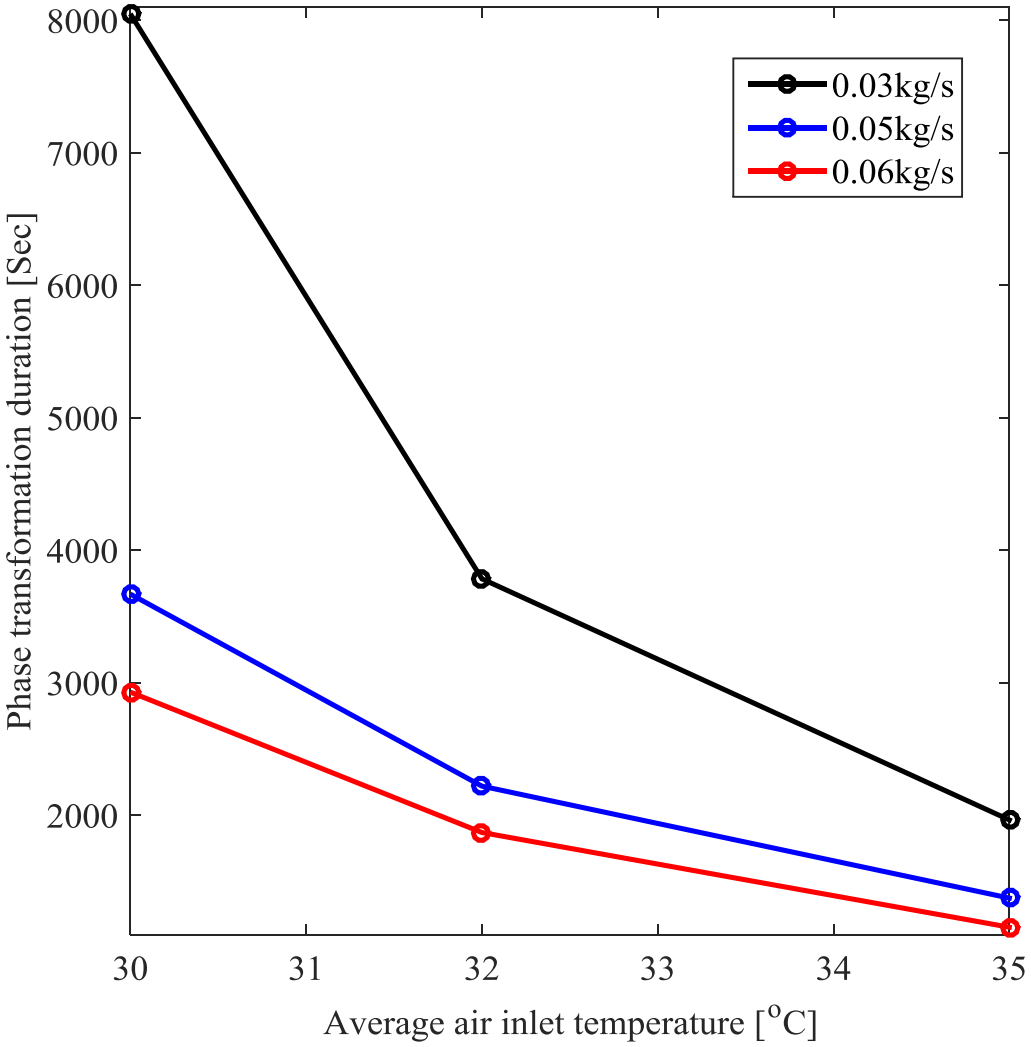

Figure 5.12. Effects of the air inlet temperature and the air mass flow rate on the phase transformation duration for the RT27 module.

For the RT27 module (Figure 5.12), for an inlet air temperature of 30ºC and airflow rate of 0.03 kg/s the melting duration was 8050 seconds. For an inlet air temperature of 35ºC and airflow rate of 0.03 kg/s the melting duration was 1965 seconds; i.e. a quarter of the melting duration at 30 ºC. This may be attributed to higher heat transfer rates for higher temperature differences between inlet air and PCM melting temperature as will be discussed later.

5.4 COOLING POWER AND CUMULATIVE ENERGY ABSORBED FOR THE ENTIRE TEST PERIOD.

This section focuses on the results of cooling power and energy absorbed for the entire duration of the experimental test for the three different PCM types (RT27, RT25 and SP24E) and the effects of the airflow rate and the temperature difference between inlet air and PCM melting temperature.

5.4.1 Comparison of cooling power for three modules

From Figure 5.13 it can be seen that the cooling power decayed with time. This was observed for all experimental conditions (See Appendix F). The rate of decay was more pronounced for the paraffinic PCMs when compared to the salt hydrate. SP24E which decayed from 150 W to about 50 W over a period of 250 minutes, giving an average cooling power decay rate of -0.4 W/min. The RT27 heat rate decayed from 450 W to 20 W over a period of 180 minutes, giving an average cooling power decay rate of -2.4 W/min while the RT25 heat rate decayed from 350 W to 20 W over a period of 150 minutes, giving an average cooling power decay rate of -2.2 W/min. From Figure 5.13 it can be observed that the initial cooling power for the SP24E (Salt hydrate) module was 150 W which was less than 50 % of that for the paraffinic PCMs (RT27 and RT25) which were initially 400 W and 350 W respectively. After about 50 minutes the cooling power of SP24E, RT25 and RT27 were almost the same (100W). After 75 minutes, the cooling power for the SP24E module remains higher than those for RT27 and RT25.

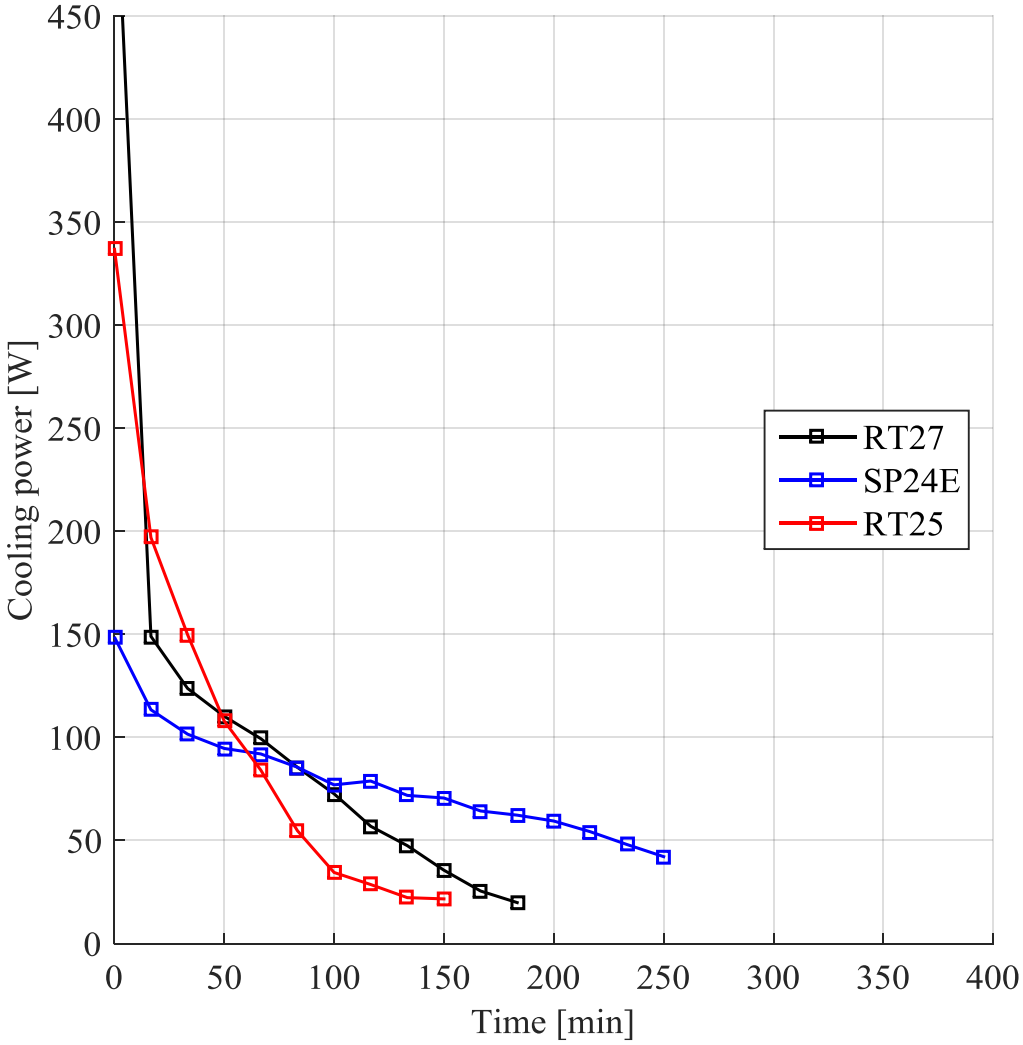

Figure 5.13. Comparison of the cooling power delivered by the RT25, RT27 and SP24E modules for an airflow rate of 0.03 kg/s at an air inlet temperature of 32°C.

5.4.2 Effect of the air mass flow rate on the cooling power

The effect of the air mass flow rate on the cooling power was evaluated by considering a fixed inlet air temperature of 35°C and varying air mass flow rate for the SP24E module.

Figure 5.14 indicates that higher cooling power values were achieved at higher air flow rates. Higher air flow rates did, however, also result in short heat absorption time spans. This shows that the melting of the PCM was completed earlier at higher air flow rates. Figure 5.14 also show that for lower airflow rates, the cooling power was lower.

However, longer periods of heat absorption could be maintained. The findings as stated above were confirmed for all PCM types and the other air mass flow rates and inlet air temperatures as shown in Appendix G.

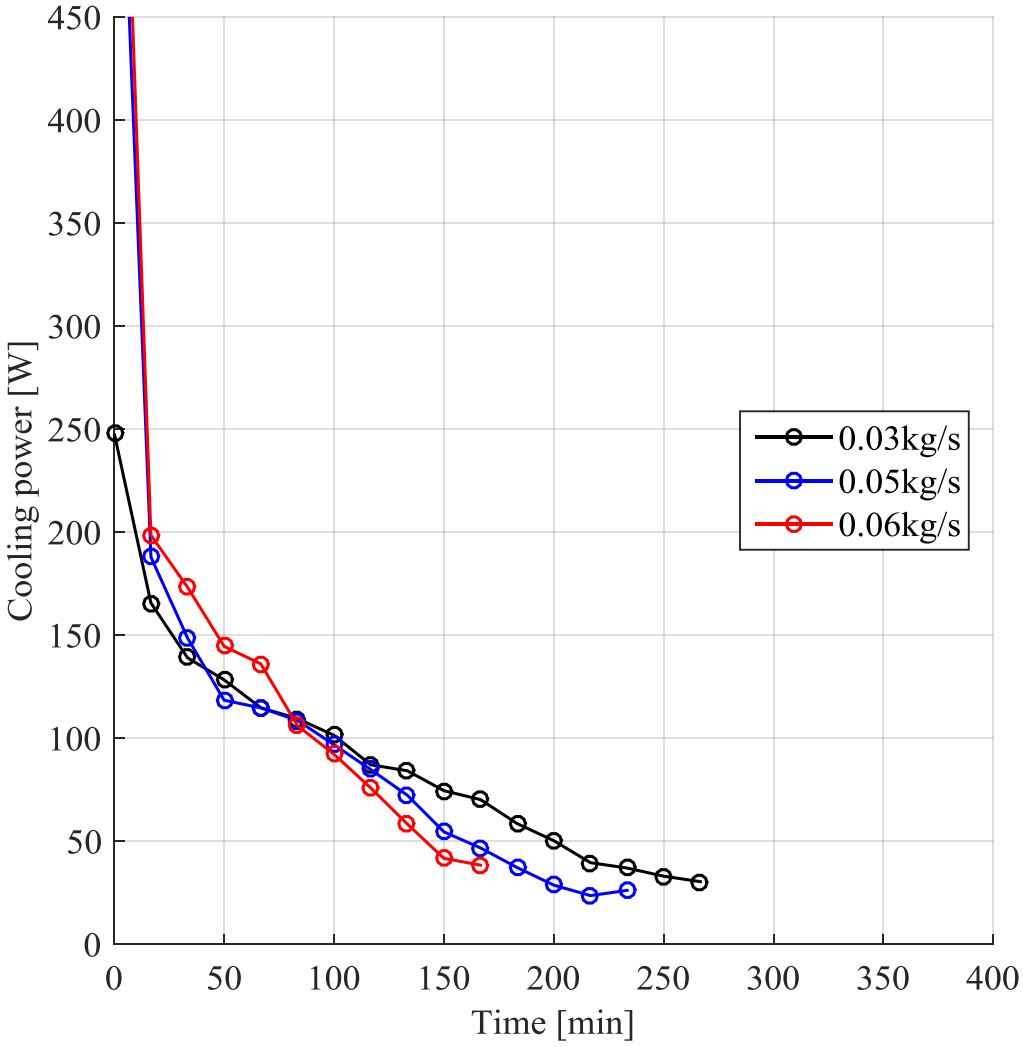

Figure 5.14. Effect of the air mass flow rate on the cooling power delivered by the SP24E module at an inlet air temperature of 35°C.

5.5 EFFECT OF THE AIR INLET TEMPERATURE ON COOLING POWER

The effect of the inlet air temperature on the cooling power was evaluated by considering a fixed air mass flow rate of 0.03 kg/s and varying inlet air temperature for the RT27 module.

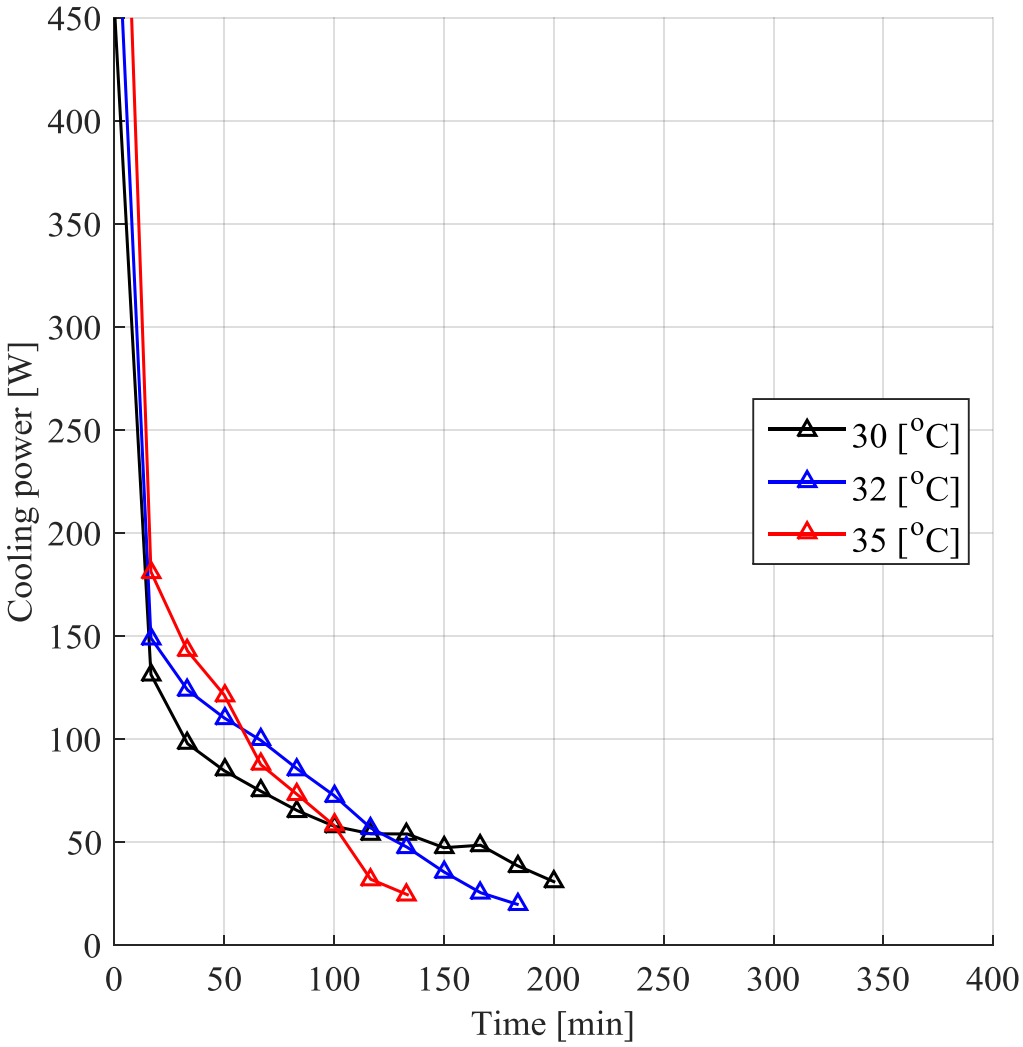

Figure 5.15. Effect of inlet air temperature on cooling power delivered by RT27 module at an air mass flow rate of 0.03 kg/s.

Figure 5.15 shows higher values of cooling power for higher inlet air temperature but reaches the minimum value within a short time. This shows that the phase transformation (melting) of the PCM completed earlier at higher inlet air temperature.

Figure 5.15 also shows that for lower inlet air temperature, the cooling power was relatively lower. However, the cooling power remained higher than the minimum value for a relatively longer period. The findings as stated above were confirmed for all PCM types and the other air mass flow rates and inlet air temperatures as shown in Appendix H.

5.6 CUMULATIVE ENERGY ABSORPTION

Equation 4.18 was used to calculate the total energy absorbed for the whole duration of the experiment.

5.6.1 Comparison of cumulative energy storage for RT25, RT27 and SP24E

A comparison of the energy absorption for RT25, RT27 and SP24E was done by subjecting the three PCMs modules under the same air mass flow rate and approximate inlet air temperature. The comparison is shown in Figure 5.16. Additional graphs for the comparisons are shown in Appendix I.

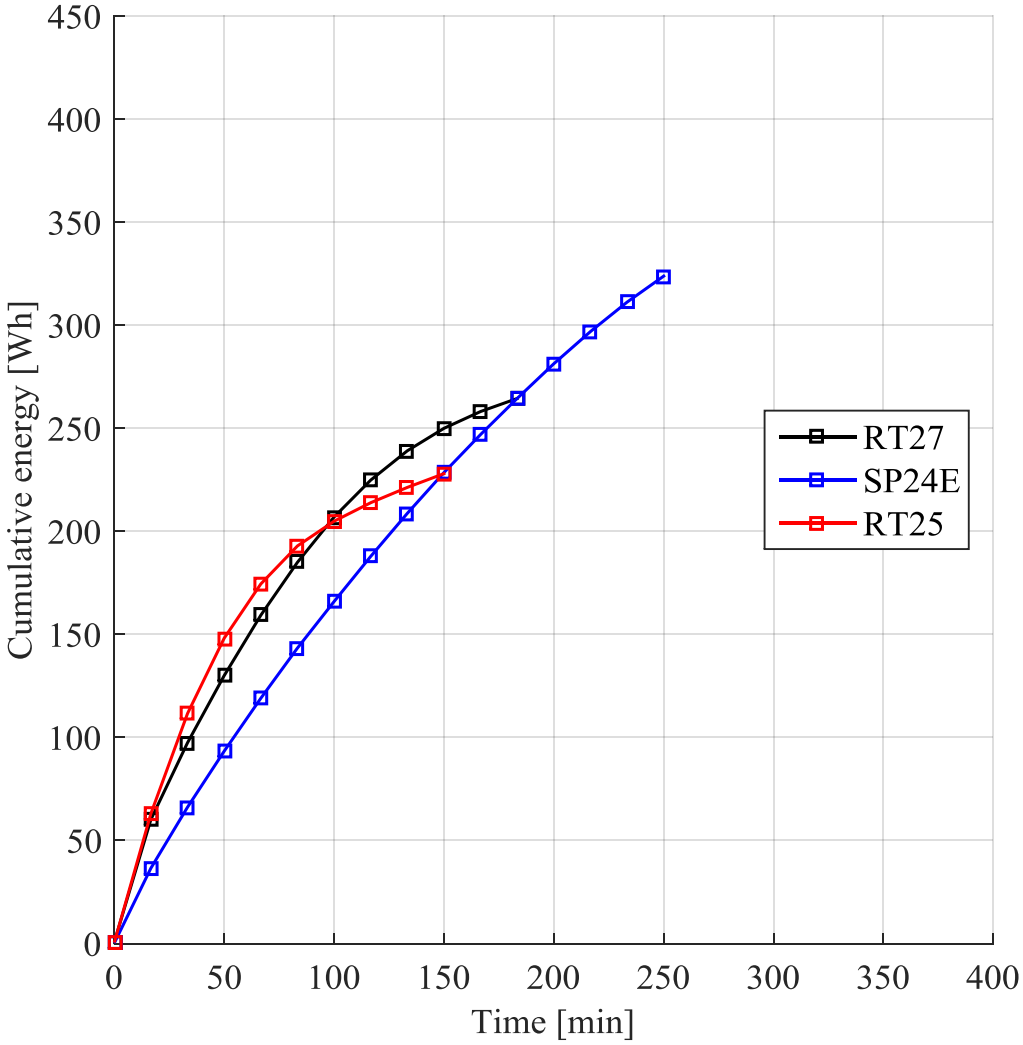

Figure 5.16. Comparison of cumulative energy absorption of the RT25, RT27 and SP2244E modules for an airflow of 0.03kg/s and an air inlet temperature of 32 °C.

From Figure 5.16 it can be seen that the SP24E (salt hydrate) module had the highest energy absorption capacity. This was confirmed for all the other air mass flow rates and inlet air temperatures as shown in Appendix I.

This is due to the high overall heat capacity of SP24E (salt hydrates) when compared to the paraffinic PCMs (RT25 and RT27).

The specific heat capacities and thicknesses of the RT5, RT27 and SP24E plates were the same, 2kJ/kg.K and 10 mm respectively. The difference between these PCMs is their densities; 880 kg/m^3 for RT25 and RT27 and 1500 kg/m^3 for SP24E. As mentioned, the density of the salt hydrate was almost twice that of paraffin waxes. This means that the salt hydrates overall heat capacity was almost twice that of paraffin waxes for the same volume of encapsulation.

The reasons why the measured energy stored came short of the specified energy storage maybe explained by the temperature difference between the air inlet temperature and air outlet temperature which did not get to zero. More time would have been required to equalise the inlet and outlet air temperatures but the experiment was terminated before this could be achieved.

From Figure 5.16, the rate of energy absorption was higher for paraffin waxes when compared to salt hydrates. This result was observed for all other air mass flow rates and inlet air temperatures as is shown in Appendix I. This result is surprising given that SP24E has the highest thermal conductivity (0.6 w/m.K; see Table 3.2) when compared to RT25 and RT27 (0.2 W/m.K; see Table 3.2). One would typically expect higher heat transfer rates for higher thermal conductivity PCMs. However there are other factors that can influence heat transfer rates such as thermal expansion coefficient of the liquid PCM and the viscosity of the liquid PCM.

From a design stand point the desirable thermal performance of PCM is to have a high instantaneous heat absorption capacity and also extended over a longer period. Paraffinic PCMs met the first condition of high instantaneous heat absorption but did not meet the second condition of extended heat absorption duration. SP24E met the condition for extended heat absorption duration but had a lower instantaneous heat absorption capacity than the paraffin.

5.7 EFFECT OF THE AIR MASS FLOW RATE ON THE CUMULATIVE ENERGY ABSORPTION

The effect of the air mass flow rate on the cumulative energy absorbed was evaluated by considering a fixed inlet air temperature of 30ºC and then varying the air flow rate from approximately 0.03 to 0.06 kg/s as is shown in Figure 5.17.

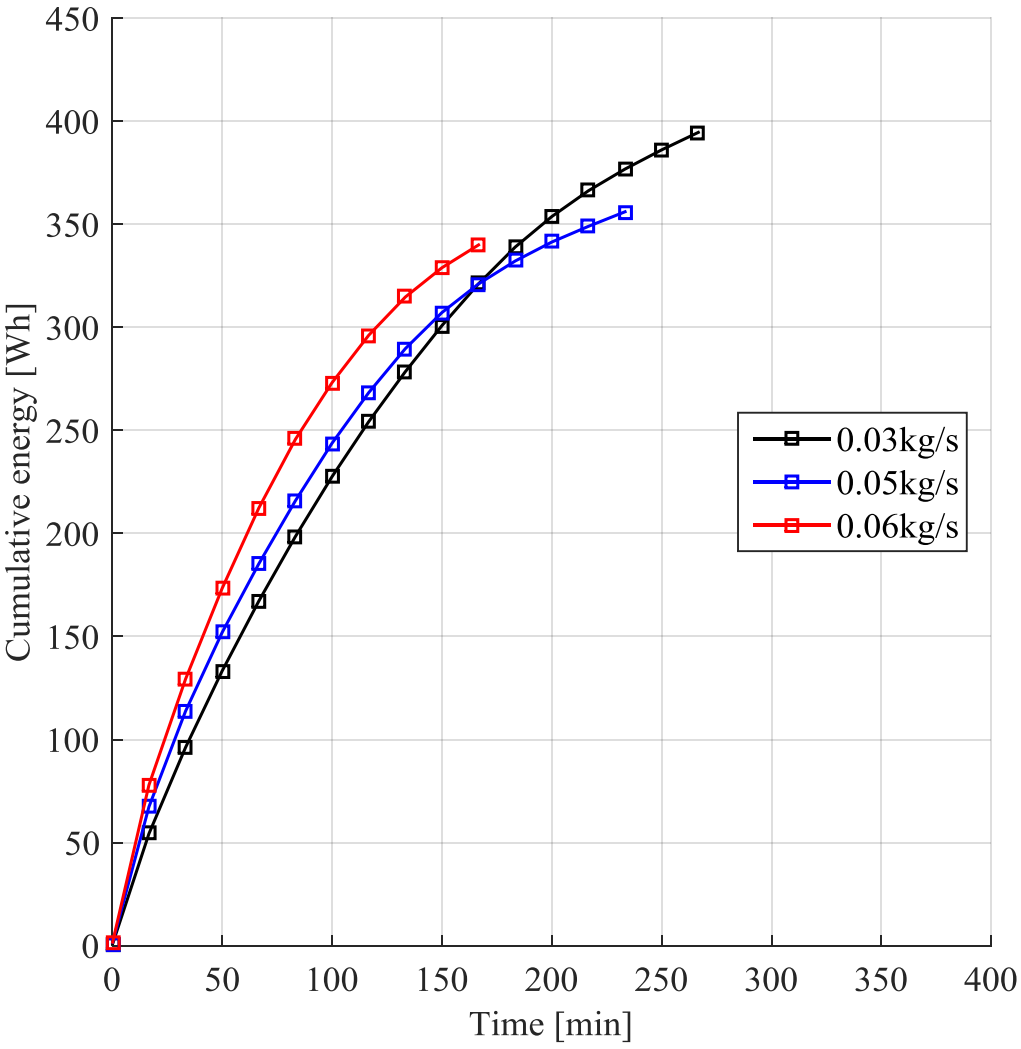

Figure 5.17. Effect of air mass flow rate on cumulative energy stored for SP24E module with air inlet temperature of 30°C.

From Figure 5.17, it was observed that the rate of energy absorption was higher at higher air flow rates. This can be attributed to high convection heat transfer coefficients as is typically expected at high air flow rates. Higher air flow rates result in lower

thermal convective resistance on the air side. If the thermal resistance is lower, then more heat is expected to flow from the high temperature region (air) to the lower temperature regions (PCM). Thus, more energy is expected to be absorbed in a given time span. Figure 5.17 also shows that more energy was absorbed at lower air mass flow rates when compared to higher air flow rates. This was confirmed for all of the PCM modules for all other inlet air temperature conditions as shown in Appendix J. The expected behaviour was that the total energy absorbed had to be the same regardless of the air mass flow rate for the same PCM initial and final temperatures and experimental duration. The unexpected behaviour may be explained by non-uniform inlet air temperatures for the different air mass flow rates as can be observed in Figure 5.18.

5.8 EFFECT OF THE AIR INLET TEMPERATURE ON THE CUMULATIVE ENERGY ABSORBED

The effect of inlet air temperature on the cumulative energy absorbed can be evaluated by considering a fixed air mass flow rate. In Figure 5.18 for instance, the impact of the air temperature for a mass flow rate of0.05 kg/s is shown for the SP24E module.

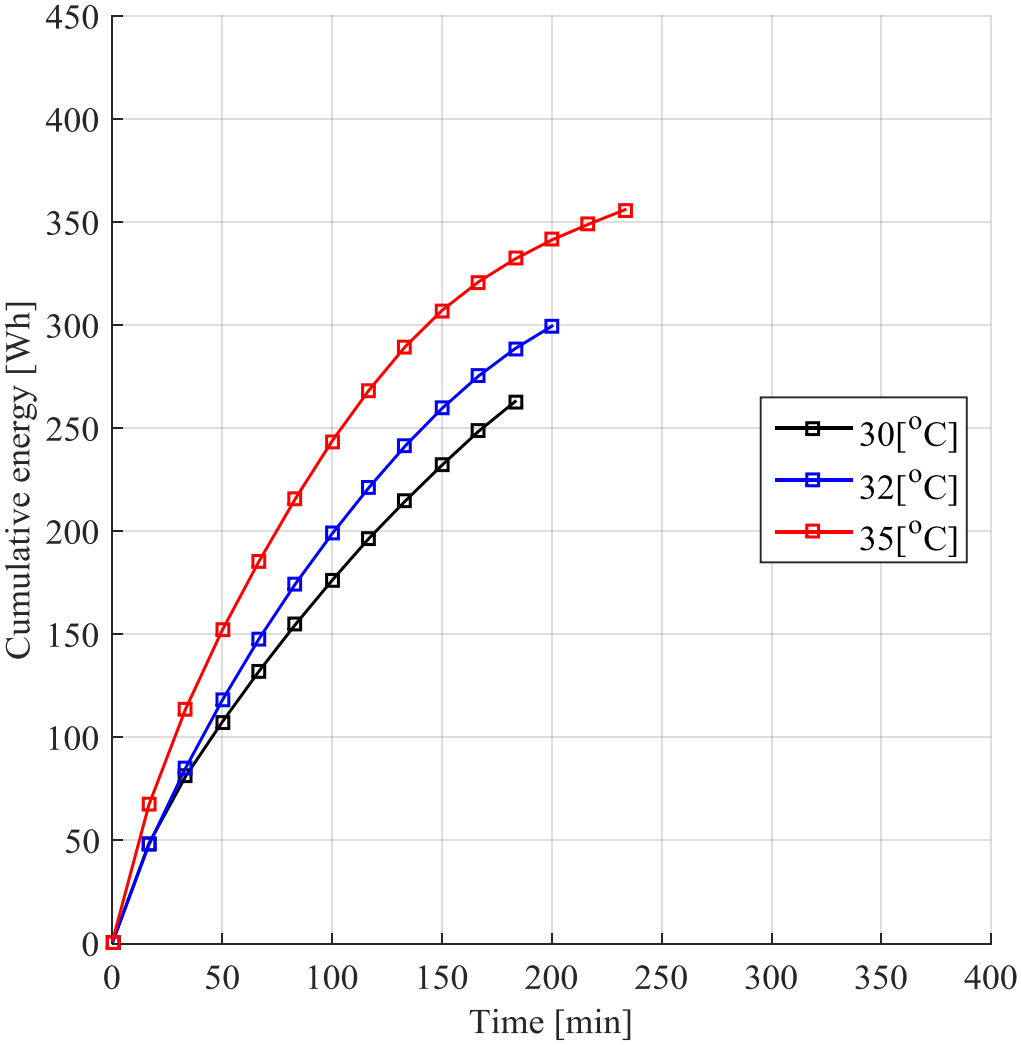

Figure 5.18. Effect of inlet air temperature on cumulative energy absorbed into the SP24E module for air mass flow rate of 0.05kg/s.

From Figure 5.18, the rate of energy absorption increased with inlet air temperature. This was confirmed for all of the PCM modules for all other inlet air temperature conditions as shown in Appendix K.

5.9 SUMMARY

All the three types of PCMs (RT27, RT25 (paraffin type) and SP24E (salt hydrate type)) investigated in this study exhibited air cooling behaviour. Paraffin and salt hydrate PCMs had different mechanisms of heat absorption- melting for paraffin as opposed to dehydration for salt hydrates. The average PCM temperature-time profile for paraffinic PCMs can be used to establish the phase transformation period. For thin PCM plates studied the melt front moved from the upstream section to the downstream section.

The average effectiveness of the PCM modules decreased with increasing convective air mass flow rate. Increasing the inlet air temperature at constant air mass flow rate did not affect average effectiveness significantly. In practice, it is possible to determine the number of plates that are required to achieve a desired cooling load on the basis of effectiveness and air flow regardless of inlet air temperature. The overriding term for the determination of average effectiveness was the numerator ($\bar{T}_i - \bar{T}_o$) - specifically $\bar{T}_o$ which was influenced by PCM weight, thermal conductivity and latent heat. Increasing air mass flow rate (at constant inlet air temperature) or inlet air temperature (at constant air mass flow rate) increased the average cooling power. The phase transformation durations of the PCMs decreased as both the air flow rates and inlet air temperatures increased. Over the duration of the tests, cooling power decayed with time. Factors that led to differences in heat absorption capacity of the PCMs were volumetric density, latent heat capacity, effectiveness. From a design stand point the desirable thermal performance of PCM is to have a high instantaneous heat absorption capacity and also extended over a longer period. Paraffins met the first condition of high instantaneous heat absorption but did not meet the second condition of extended thermal energy absorption duration. SP24E met the condition for extended thermal energy absorption duration but had a lower instantaneous heat absorption capacity than the paraffin. It is expected that that a mix of plates containing salt hydrates and paraffin PCMs should provide a desirable instantaneous heat absorption and extended thermal energy absorption duration.

CHAPTER 6 CORRELATION ANALYSIS

6.1 INTRODUCTION

In this chapter an attempt is made to develop a design chart that can be used to calculate the number of PCM module plates to cater for a particular objective cooling load and time for given operating conditions (air inlet temperature and airflow rate). A theoretical analysis of the heat transfer process between the air and the PCM is also carried out. The chapter also explains how the experimental transient cooling power of the plate PCM-air heat exchanger at different inlet air temperatures and different air flow rates are fitted into an empirical model.

6.2 DESIGN CHART

The design chart Figure 6.1 was generated using the instantaneous cooling power ($\dot{Q}_i$) results calculated for an RT25 module (15 plates containing RT25 PCM) operated at an air mass flow rate of 0.03 kg/s and an inlet air temperature of 30°C . Table 6.1 column 4 contains the $\dot{Q}_i$ values.

The design configuration that was considered in this study was that of the RT25, RT27 and SP24E PCM plates with dimensions of 450 mm x 300 mm x 10 mm (commercially available Rubitherm plates used in this investigation) arranged in parallel with a plate pitch of 15 mm (the pitch that was used in this investigation) in a ventilation air duct.

An approximation was made that the $\dot{Q}_i$ values for any number of modules (n) of the RT25 plates with each module receiving 0.03 kg/s air flow at 30°C configured as stated above would be $n \times \dot{Q}_i$ values for a single module. Columns 5-17 are for $\dot{Q}_i$ values for 2,3,4…14 modules. The above approximation is reasonable although no experimental tests were carried out using different number of modules to validate it. Differences from the approximation would arise as a result of the velocity boundary layer effect.

This chart can therefore be used to determine the number of modules that are required to achieve a desired cooling power for a desired time period for the listed air mass flow

rate, inlet air temperature for a design configuration as stated above. For other design configurations of different plate pitch, different plate PCMs and different plate geometries, their thermal performance characterisations will be required.

As an example of the application of the design chart, given that a designer chose to implement RT25 plates in a climate with peak summer ambient air temperature of 30°C and desires to maintain at least 1kW cooling power (objective cooling load, $\dot{Q}_{obj}$) for 2000 seconds with air flow rate of 0.03 kg/s per module, the number of modules, n, that would be required is 10 as illustrated by the red dotted lines in Figure 6.1.

Table 6.1. Sample data for transient cooling power for RT25 modules subjected to 0.03 kg/s airflow and 30°C inlet air temperature.

RT25			**Transient cooling power $\dot{Q}_i$(kW)**													
			Number of modules													
$\bar{T}_i$(℃)	$\dot{m}_{air}(\frac{kg}{s})$	**t (sec)**	1	2	3	4	5	6	7	8	9	10	11	12	13	14
30	0.03	0	0.1533	0.3065	0.4598	0.6131	0.7664	0.9196	1.0729	1.2262	1.3794	1.5327	1.6860	1.8392	1.9925	2.1458
30	0.03	5	0.1496	0.2993	0.4489	0.5985	0.7481	0.8978	1.0474	1.1970	1.3467	1.4963	1.6459	1.7955	1.9452	2.0948
30	0.03	10	0.1491	0.2981	0.4472	0.5963	0.7453	0.8944	1.0434	1.1925	1.3416	1.4906	1.6397	1.7888	1.9378	2.0869
30	0.03	15	0.1480	0.2959	0.4439	0.5918	0.7398	0.8878	1.0357	1.1837	1.3316	1.4796	1.6275	1.7755	1.9235	2.0714
30	0.03	20	0.1490	0.2980	0.4471	0.5961	0.7451	0.8941	1.0431	1.1922	1.3412	1.4902	1.6392	1.7882	1.9373	2.0863
30	0.03	25	0.1479	0.2959	0.4438	0.5917	0.7397	0.8876	1.0355	1.1835	1.3314	1.4793	1.6273	1.7752	1.9231	2.0711
30	0.03	30	0.1469	0.2938	0.4408	0.5877	0.7346	0.8815	1.0285	1.1754	1.3223	1.4692	1.6161	1.7631	1.9100	2.0569
30	0.03	35	0.1487	0.2973	0.4460	0.5946	0.7433	0.8919	1.0406	1.1892	1.3379	1.4865	1.6352	1.7838	1.9325	2.0811
30	0.03	40	0.1462	0.2924	0.4386	0.5848	0.7310	0.8772	1.0234	1.1696	1.3158	1.4621	1.6083	1.7545	1.9007	2.0469
30	0.03	45	0.1492	0.2983	0.4475	0.5967	0.7458	0.8950	1.0442	1.1933	1.3425	1.4917	1.6408	1.7900	1.9392	2.0884
30	0.03	50	0.1492	0.2985	0.4477	0.5970	0.7462	0.8955	1.0447	1.1940	1.3432	1.4924	1.6417	1.7909	1.9402	2.0894
30	0.03	55	0.1461	0.2921	0.4382	0.5843	0.7304	0.8764	1.0225	1.1686	1.3146	1.4607	1.6068	1.7529	1.8989	2.0450
30	0.03	60	0.1480	0.2960	0.4440	0.5920	0.7400	0.8880	1.0361	1.1841	1.3321	1.4801	1.6281	1.7761	1.9241	2.0721
30	0.03	65	0.1465	0.2930	0.4395	0.5860	0.7325	0.8790	1.0255	1.1720	1.3185	1.4650	1.6115	1.7580	1.9045	2.0510
30	0.03	70	0.1466	0.2932	0.4398	0.5864	0.7330	0.8796	1.0261	1.1727	1.3193	1.4659	1.6125	1.7591	1.9057	2.0523
30	0.03	75	0.1475	0.2951	0.4426	0.5902	0.7377	0.8853	1.0328	1.1803	1.3279	1.4754	1.6230	1.7705	1.9180	2.0656
30	0.03	80	0.1461	0.2923	0.4384	0.5846	0.7307	0.8768	1.0230	1.1691	1.3152	1.4614	1.6075	1.7537	1.8998	2.0459
30	0.03	85	0.1466	0.2932	0.4399	0.5865	0.7331	0.8797	1.0264	1.1730	1.3196	1.4662	1.6128	1.7595	1.9061	2.0527
30	0.03	90	0.1465	0.2931	0.4396	0.5862	0.7327	0.8793	1.0258	1.1724	1.3189	1.4655	1.6120	1.7586	1.9051	2.0517
30	0.03	95	0.1453	0.2906	0.4358	0.5811	0.7264	0.8717	1.0170	1.1622	1.3075	1.4528	1.5981	1.7433	1.8886	2.0339
30	0.03	100	0.1472	0.2944	0.4415	0.5887	0.7359	0.8831	1.0302	1.1774	1.3246	1.4718	1.6189	1.7661	1.9133	2.0605
30	0.03	105	0.1458	0.2916	0.4373	0.5831	0.7289	0.8747	1.0204	1.1662	1.3120	1.4578	1.6035	1.7493	1.8951	2.0409

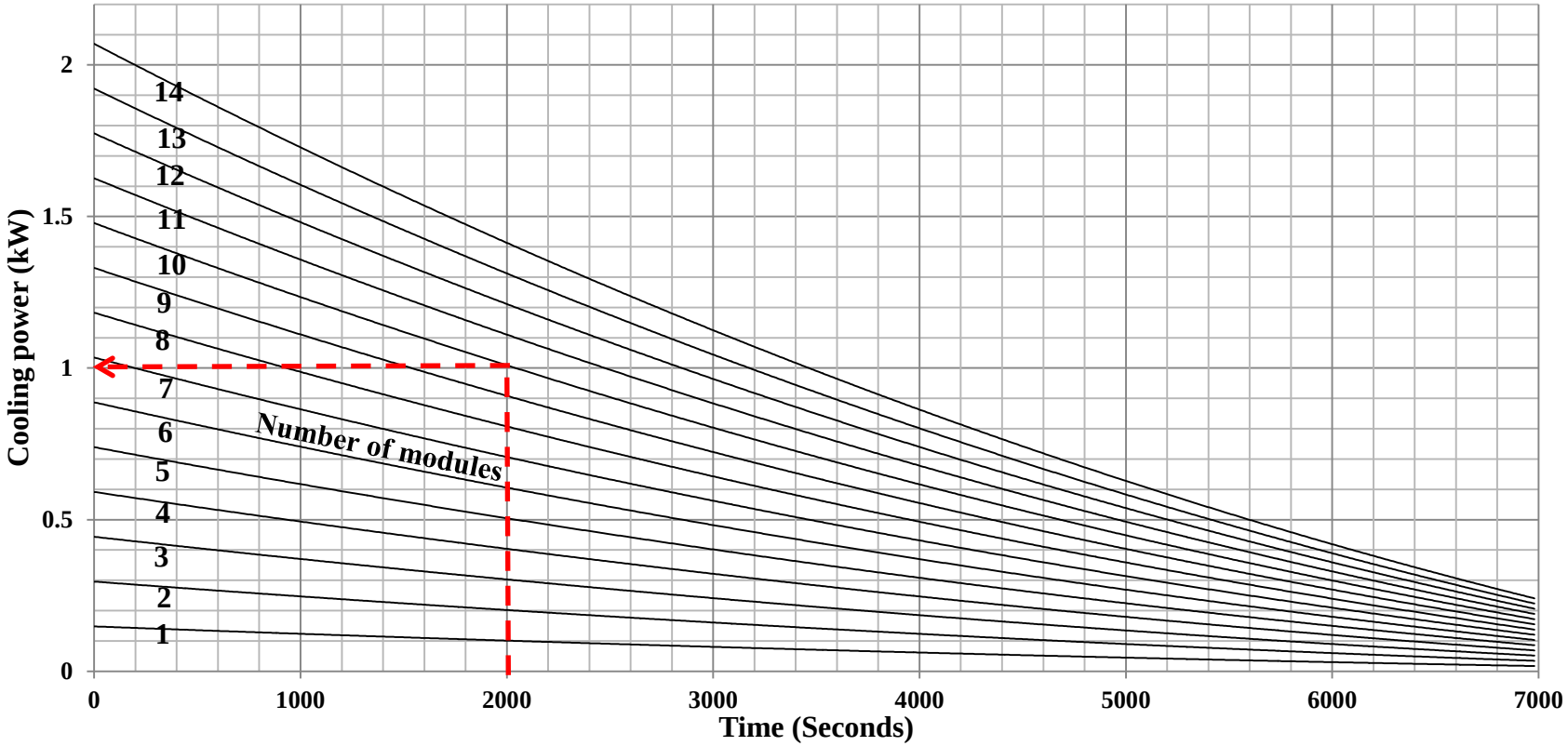

Figure 6.1. Design chart for calculating the number of RT25 plates for an air mass flow rate of 0.03 kg/s and inlet air temperature of 30 °C for the experimental test facility located at the Council for Scientific and Industrial Research in Pretoria at an elevation of 1386 m above sea level with barometric pressure of 87.8 kPa.

This design chart was generated as a demonstration of the type of tool that can be generated from the results of the investigation. In order to cater for the three types of plate PCMs tested and all the operating conditions of air temperature and flow rate investigated in this study, a total of 27 design charts has to be generated for use by designers in the HVAC industry. Thus use of design charts such as this can be a cumbersome task for the industry. The other limitation that can arise from using the design charts is that the design chart will not be applicable to operating conditions which lies between the ones that were specifically tested. Given these limitations in the application of design charts, it can be easily seen that there is need for a better model that will predict the number of modules that will cater for a particular objective cooling load.

6.3 THEORETICAL ANALYSIS OF THE HEAT TRANSFER PROCESS BETWEEN THE AIR AND THE PCM

In this section an empirical model is developed which could be used for different air mass flow rates and inlet air conditions. It should be noted that this is only a first order model to determine the type of function that is required to capture the dominant aspects at play.

6.3.1 Empirical model development

From Newton's law of cooling, the rate of heat transfer from a fluid in a passage can be expressed as [13]:

$$\dot{Q}_i = h_c A_s \Delta T_{ave} \tag{6.1}$$

Where

h_c Convective heat transfer coefficient
A_s Heat transfer surface area

$$\Delta T_{ave} = T_s - \frac{\bar{T}_i + \bar{T}_o}{2} \quad [13] \tag{6.2}$$

Where

T_s Surface temperature (in this case the plate surface temperature)

$\bar{T}_i$ Average air inlet temperature

$\bar{T}_o$ Average air outlet temperature

$\frac{\bar{T}_i+\bar{T}_o}{2}$ is defined as the bulk mean fluid temperature.

Thermal resistance of the aluminium encapsulate was calculated from the following equation:

$$R_{al} = \frac{e_{Al}}{\lambda_{Al}} \qquad [13] \qquad (6.3)$$

Where

R_{al} Thermal resistance of the aluminium encapsulate

e_{Al} Thickness of aluminium encapsulate

λ_{Al} Thermal conductivity of aluminium encapsulate

Substituting for e_{Al} [17] and λ_{Al} [17]

$$\rightarrow R_{al} = \frac{0.001}{300} to \frac{0.001}{200} = 3.33 \times 10^{-6} to 5 \times 10^{-6} \frac{m^2K}{W}$$

The above calculation was made to show that the thermal resistance of the encapsulation is very low and negligible and the PCM temperature can be assumed to be equal to the plate surface temperature.

The PCM- test section was well insulated and the heat losses to the surroundings were in the range of 0.4 W to 2.3 W. For the purpose of simplifying the derivation of the heat transfer rate to the PCM using Equation 6.1, these heat losses were ignored. The main mechanism by which the heat transfer from air to the plate occurred was convection.

Substituting for ΔT_{ave}, Equation 6.1 becomes

$$\dot{Q}_i = hA_s \left(T_s - \frac{\bar{T}_i+\bar{T}_o}{2}\right) \qquad (6.4)$$

Considering the energy balance of air between the inlet and outlet of the PCM-air heat exchanger,

$$\dot{Q}_i = hA_s\left(T_s - \frac{\bar{T}_i+\bar{T}_o}{2}\right) = \dot{m}C_p(\bar{T}_o - \bar{T}_i) \quad (6.5)$$

Where

$\dot{m}$ Fluid mass flow rate

C_p Fluid specific heat capacity

Rearranging Equation 6.5

$$\bar{T}_o = \bar{T}_i + \frac{\dot{Q}_i}{\dot{m}C_p} \quad (6.6)$$

Substituting for $\bar{T}_o$ in Equation 6.4.

$$\dot{Q}_i = hA_s\left[T_s - \frac{1}{2}\cdot\left(\bar{T}_i + \bar{T}_i + \frac{\dot{Q}_i}{\dot{m}C_p}\right)\right] \quad (6.7)$$

$$\dot{Q}_i = hA_s\left[T_s - \bar{T}_i - \frac{\dot{Q}_i}{2\dot{m}C_p}\right] \quad (6.8)$$

Now $T_s - \bar{T}_i = \Delta T_{pcm}$

$$\dot{Q}_i = \frac{hA_s\Delta T_{pcm}}{\left(1+\frac{hA_s}{2\dot{m}C_p}\right)} \quad (6.9)$$

Where

ΔT_{pcm} Temperature difference between inlet air temperature and PCM melting temperature.

From this derived Equation 6.9; cooling power is increased by:

- Higher temperature difference between PCM melting temperature and inlet air temperature (ΔT_{pcm}). This is demonstrated in Figure 5.15.
- Higher air flow rate ($\dot{m}$) which translates to a higher heat transfer coefficient (h). This is demonstrated in Figure 5.14.

- Larger heat transfer surface area (A_s). In the experimental set up for this study surface area of plates was constant.
- For a heat transfer fluid with high specific heat capacity the denominator in equation 6.9 becomes smaller and hence the cooling power increases.

Equation 6.9 was derived for steady state conditions and may not be strictly applicable for transient conditions where the cooling power decreases with time as shown in Figure 5.13.

6.4 CORRELATION ANALYSIS

From the derived steady state equation 6.9, it is clear that the cooling power of the heat exchanger is influenced by air flow rate ($\dot{m}$) and the difference between inlet and PCM melting temperatures ($\Delta Tpcm$), heat transfer surface area (A_s) and specific heat capacity of heat transfer fluid. Different empirical functions were analysed using Eureka curve fitting Software for each of the experimental data variables: PCM instantaneous cooling power ($\dot{Q}_i$), air mass flow rate ($\dot{m}$), difference between inlet and PCM melting temperatures ($\Delta Tpcm$) and phase transformation (melting) duration (t). Heat transfer surface area (A_s) and specific heat capacity of heat transfer fluid were kept constant. Eureka predictions showed that the general function representing the relationship is an exponential function of the form:

$$\dot{Q}_i = C_0 {\Delta T_{pcm}}^{C1} C_2 \dot{m}^{C3} e^{(-C4t\Delta T_{pcm}\dot{m})} \quad (6.10)$$

6.4.1 Comparison of measured and predicted cooling power for PCM modules for entire experimental test period.

The data ($\dot{Q}_i$, ΔT_{pcm}, $\dot{m}$ and t) that was plugged into equation 6.10 was obtained from the start to the end of the experimental period including the phase transformation period. Predicted functions for a module, correlation coefficients and the root mean square errors for the 3 PCM modules are shown in Table 6.2.

Table 6.2. R^2 and RMSE for the different functions of each material

Plate	Empirical model	R^2	RMSE
RT25	$\dot{Q}_i = 0.293\Delta T_{pcm}{}^{1.18}\dot{m}^{0.733}e^{(-0.00124t\Delta T_{pcm}\dot{m})}$	0.94	0.1%
RT27	$\dot{Q}_i = 0.506\Delta T_{pcm}{}^{0.835}\dot{m}^{0.689}e^{(-0.00108t\Delta T_{pcm}\dot{m})}$	0.94	0.05%
SP24E	$\dot{Q}_i = 0.115\Delta T_{pcm}{}^{0.859}\dot{m}^{0.477}e^{(-0.000279t\Delta T_{pcm}\dot{m})}$	0.94	0.02%

From Figures 6.2 –6.18 (comparison of measured cooling power and predicted cooling power for the RT27 module and SP24E module), the phase transformation period can be defined as from the initial inflection point until the final inflection point. Before the phase transformation period, the measured cooling power deviated from the modelled cooling power. The measured cooling power was higher than predicted by the model. During the phase transformation period the model was in good agreement with the measured cooling power.

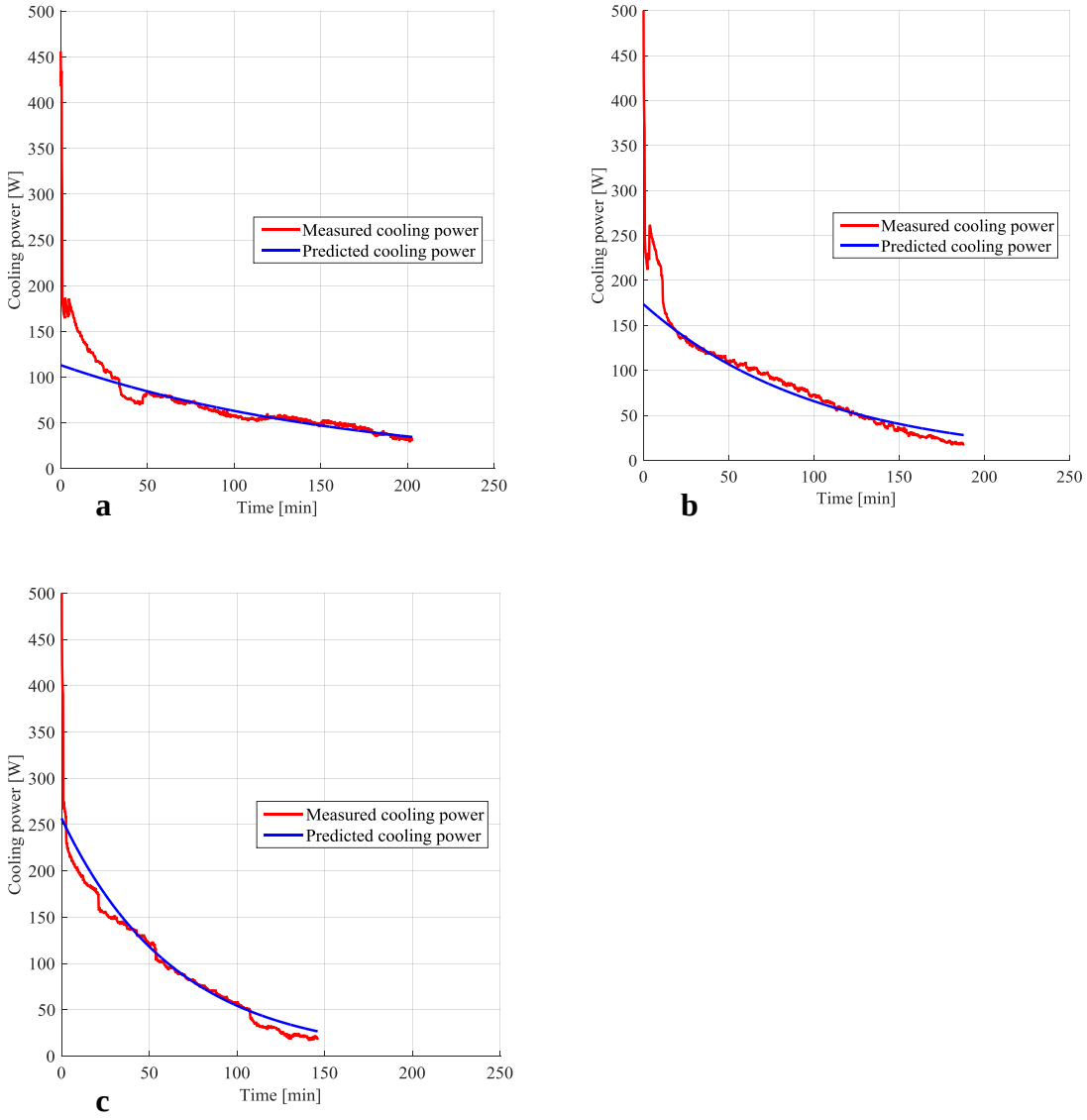

Figure 6.2. Comparison of measured cooling power and predicted cooling power for RT27 module for an air flow rate of 0.03 kg/s at air temperatures of **a**: 30°C, **b**: 32°C and **c**: 35°C.

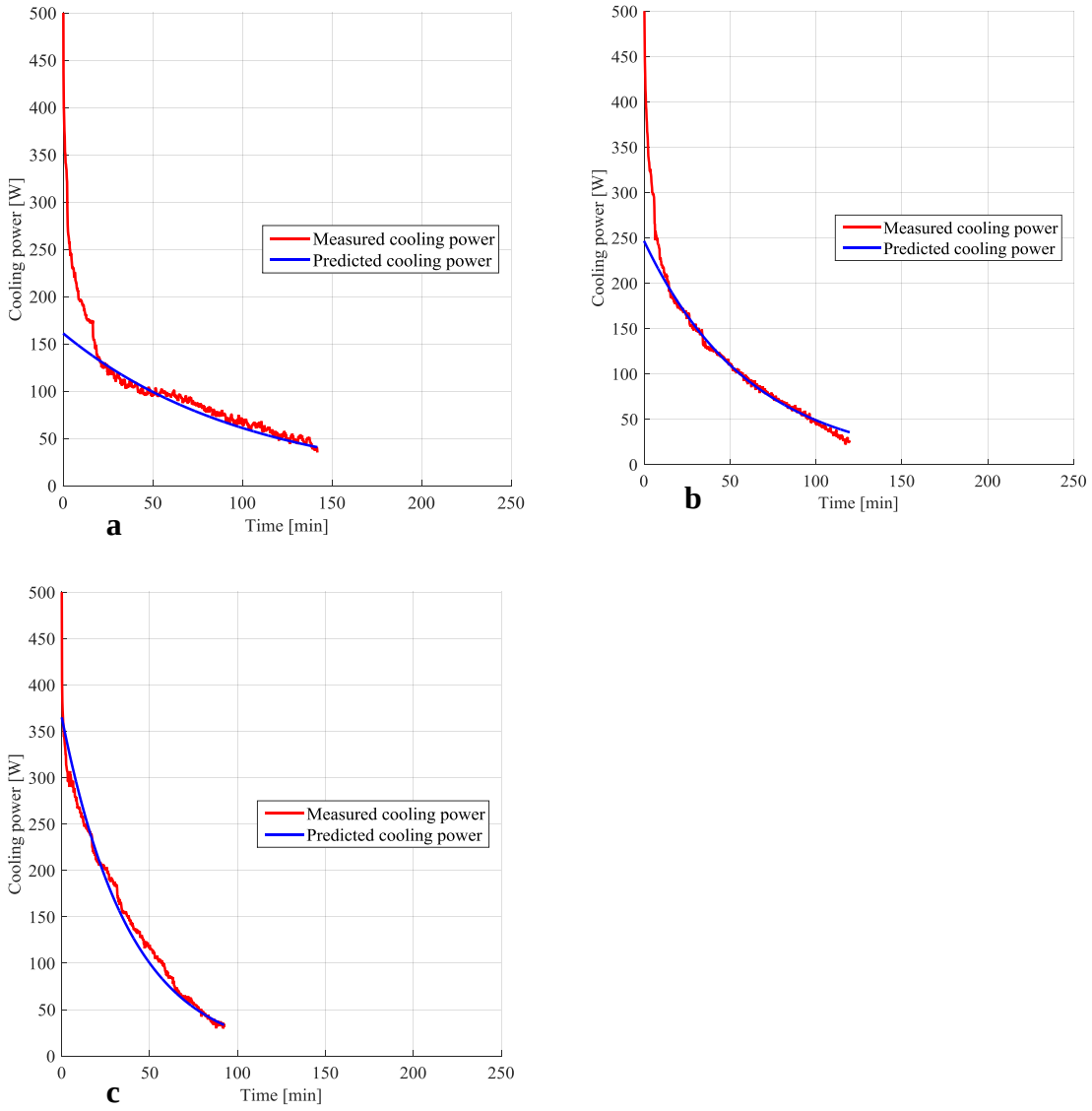

Figure 6.3. Comparison of measured cooling power and predicted cooling power for RT27 module for an air flow rate of 0.05 kg/s at air temperatures of **a**: 30°C, **b**: 32°C and **c**: 35°C.

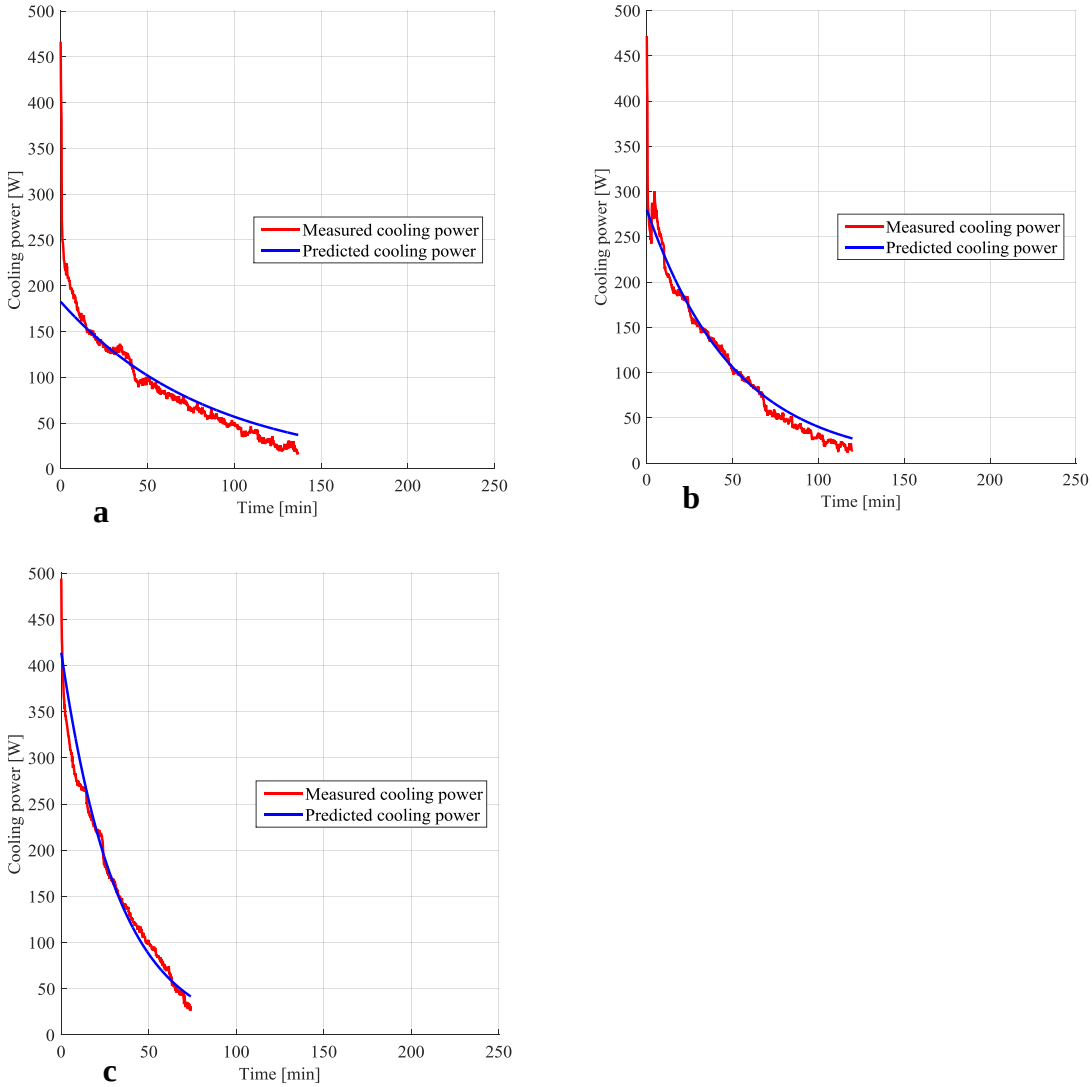

Figure 6.4. Comparison of measured cooling power and predicted cooling power for RT27 module for an air flow rate of 0.06 kg/s at air temperatures of **a**: 30°C, **b**: 32°C and **c**: 35°C.

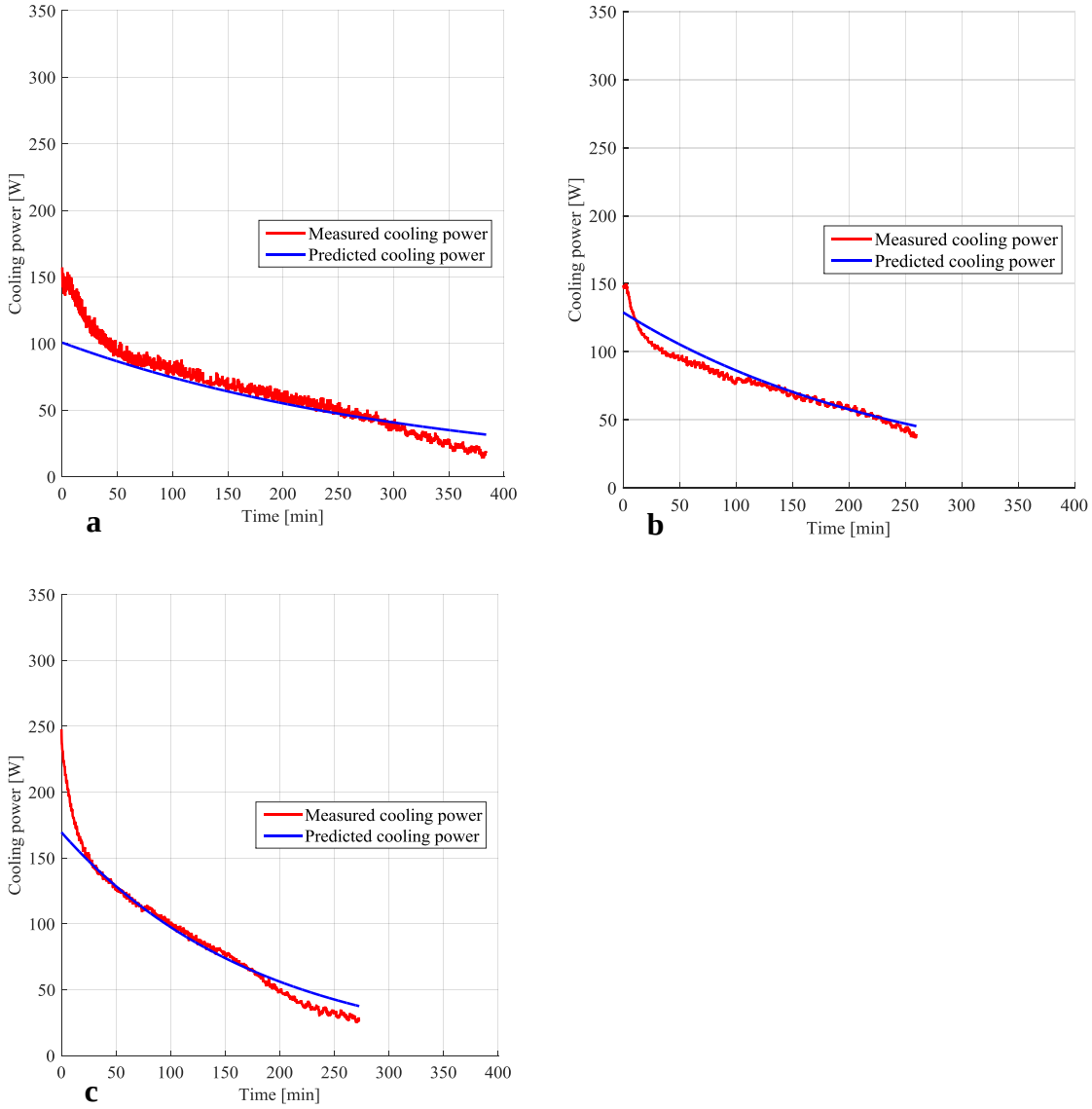

Figure 6.5. Comparison of measured cooling power and predicted cooling power for SP24E module for an air flow rate of 0.03 kg/s at air temperatures of **a**: 30°C, **b**: 32°C and **c**: 35°C.

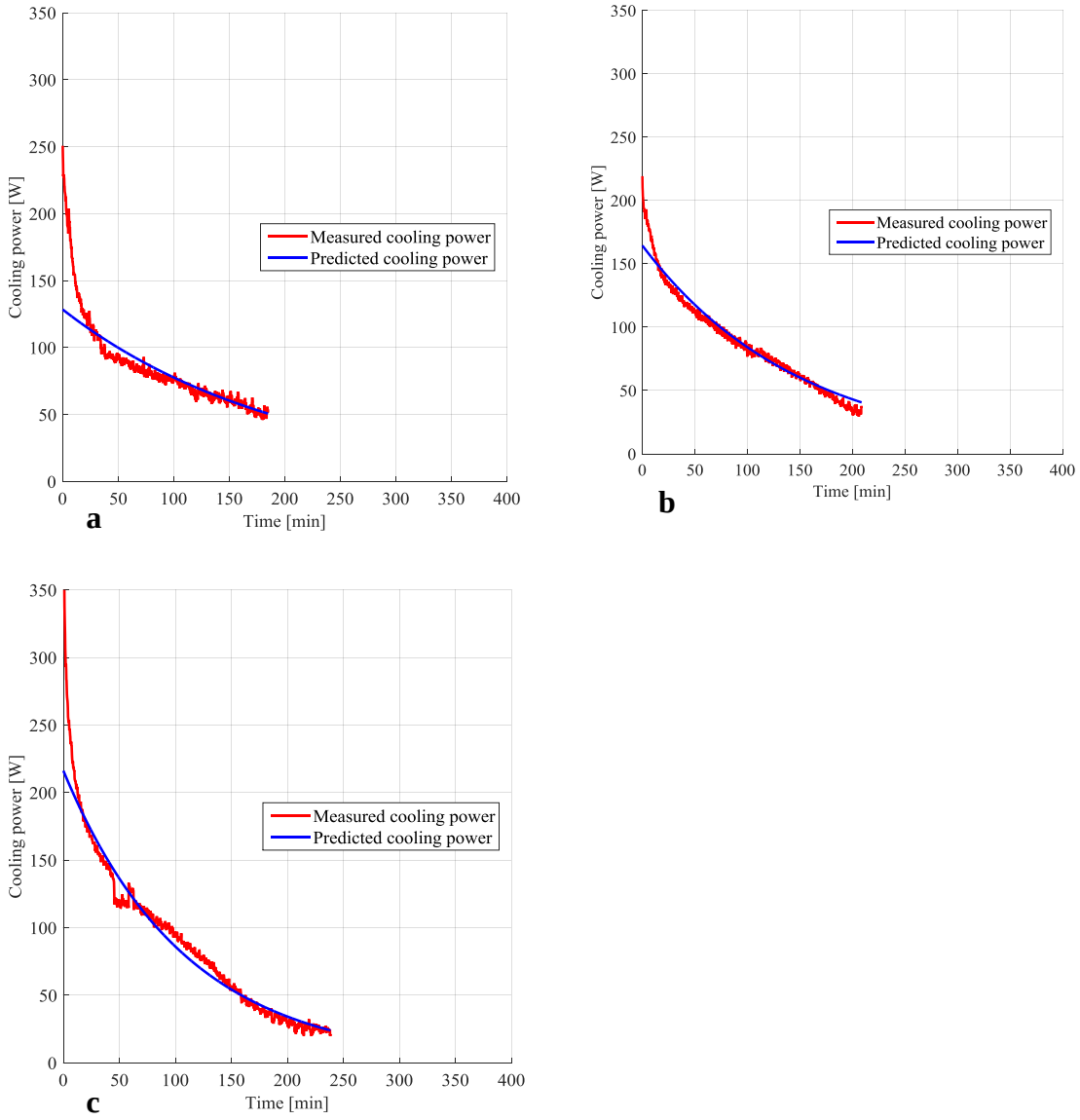

Figure 6.6. Comparison of measured cooling power and predicted cooling power for SP24E module for an air flow rate of 0.05 kg/s at air temperatures of **a**: 30°C, **b**: 32°C and **c**: 35°C.

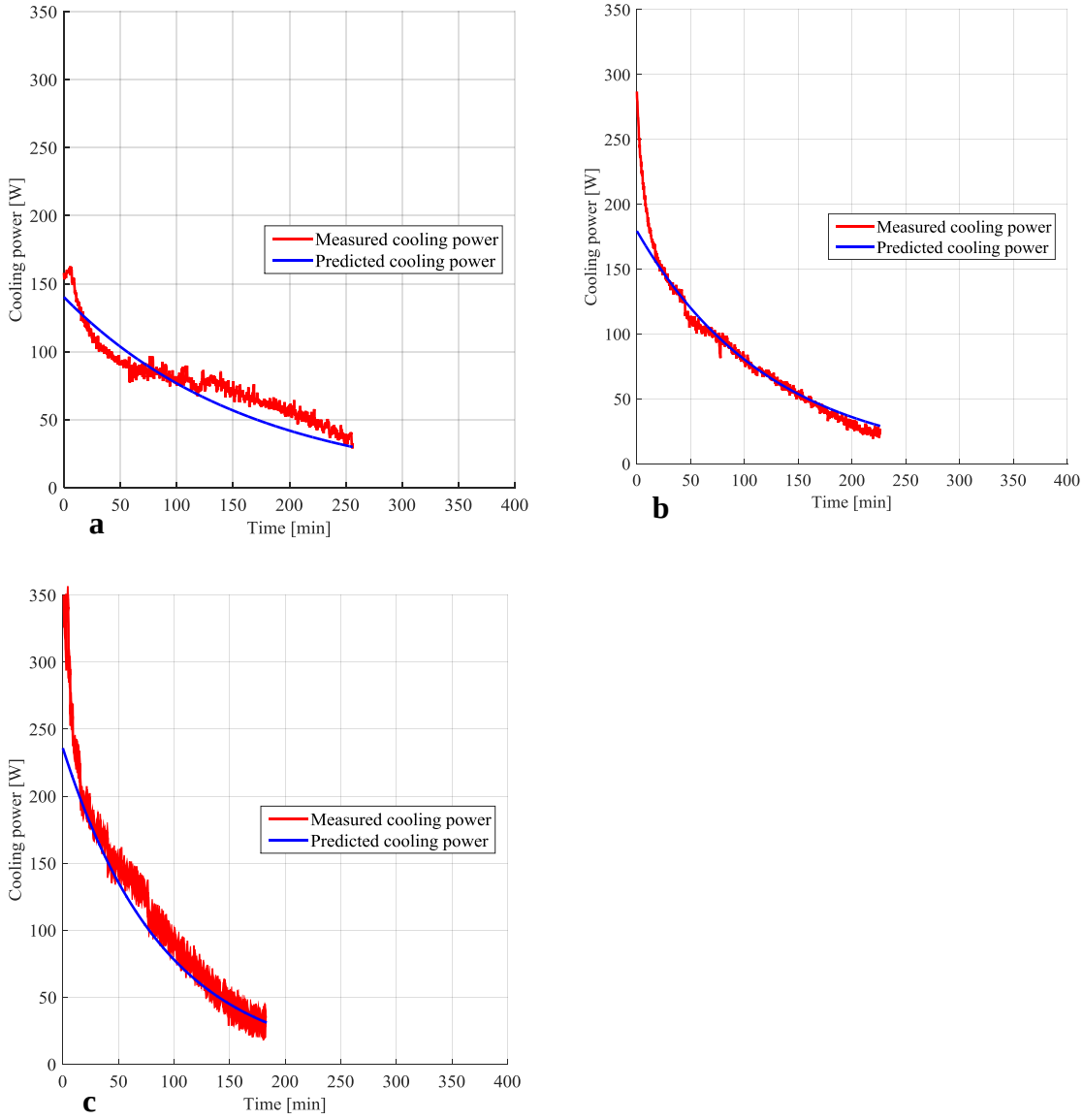

Figure 6.7. Comparison of measured cooling power and predicted cooling power for SP24E module for an air flow rate of 0.06 kg/s at air temperatures of **a**: 30°C, **b**: 32°C and **c**: 35°C.

6.4.2 Comparison of measured and predicted cooling power for PCM modules during phase transformation period.

As mentioned, the phase transformation period was the time interval during which the PCM changed from solid to liquid phase. During the same period both latent and sensible heat storage mechanisms were operative. However the latent heat storage component was the major mode of heat storage. The data ($\dot{Q}_i$, ΔT_{pcm}, $\dot{m}$ and t) that was substituted into equation 6.10 was obtained from the averaged PCM-temperature-time profile within the melting period (see Paragraph 5.2 for the determination of phase transformation duration for paraffinic PCMs) of the PCM as defined by the melting temperature ranges supplied by the Rubitherm company (22 °C to 26 °C for RT25 and 25 °C to 28 °C for RT27).

The salt hydrate SP24E did not melt but rather continuously lost structural water (dehydration) and cooled the ambient air during that process. The SP24E PCM temperature- time profiles Figure 5.3 do not show the incidence and completion of the dehydration process. The data ($\dot{Q}_i$, ΔT_{pcm}, $\dot{m}$ and t) that was plugged into equation 6.10 for SP24E was obtained from the whole period of experimental measurements.

Predicted functions, correlation coefficients and the root mean square errors for the 3 PCM modules are shown in Table 6.3. The goodness of fit was higher than that obtained when considering the entire experimental test range (See Table 6.2). The reason for the higher R2 values was that the model more accurately predicted the cooling power within the phase transformation period.

Table 6.3. R^2 and RMSE for the and different functions for each material per module.

Module	Empirical model	R^2	RMSE
RT25	$\dot{Q}_i = 0.223\Delta T_{pcm}{}^{0.981}\dot{m}^{0.6}e^{(-0.000898t\Delta T_{pcm}\dot{m})}$	0.98	0.02%
RT27	$\dot{Q}_i = 0.352\Delta T_{pcm}{}^{0.748}\dot{m}^{0.627}e^{(-0.000851t\Delta T_{pcm}\dot{m})}$	0.98	0.01%
SP24E	$\dot{Q}_i = 0.115\Delta T_{pcm}{}^{0.859}\dot{m}^{0.477}e^{(-0.000279t\Delta T_{pcm}\dot{m})}$	0.94	0.02%

The goodness of fit of the data to the empirical model equation 6.10 was better for the paraffin PCMs than the salt hydrate (SP24E). The lower correlation coefficient for the SP24E can be attributed to the different PCM heat storage mechanisms (dehydration as

opposed to melting). Therefore, the model equation 6.10 may not be strictly applicable to salt hydrates. The determination of a better fitting model for the salt hydrate lies outside of the scope for this work when considering the manufacturer's melting temperature range for SP24E. However, the model may still be applicable within the appropriate phase transformation temperature range. Figures 6.11 to 6.18 shows that the predicted and measured cooling power for SP24E were in good agreement between the initial and final inflection points.

Figures 6.19 and 6.20 show a comparison of real measured cooling power ($\dot{Q}_i$) values v values predicted by the empirical models for RT5 and RT27 modules for the phase transformation period only. The red line in Figures 6.19 to 6.20 represents the exact correlating line. The cooling power ($\dot{Q}_i$) data points below this line shows cases where a measured cooling power was higher than the predictions of the empirical model. Points above the line show cases where the empirical model predicts a higher cooling power than the real measured value. The points that are on the exact correlation line show cases where the empirical model predicts a cooling power value that is equal to the real measured value. The black lines represent a deviation of ±15 % from the experimental data. The 15% is the maximum percentage error between the predicted and measured cooling power. Hence for the purposes of system sizing, the minimum permissible safety factor must be 15% for the paraffinic PCMs.

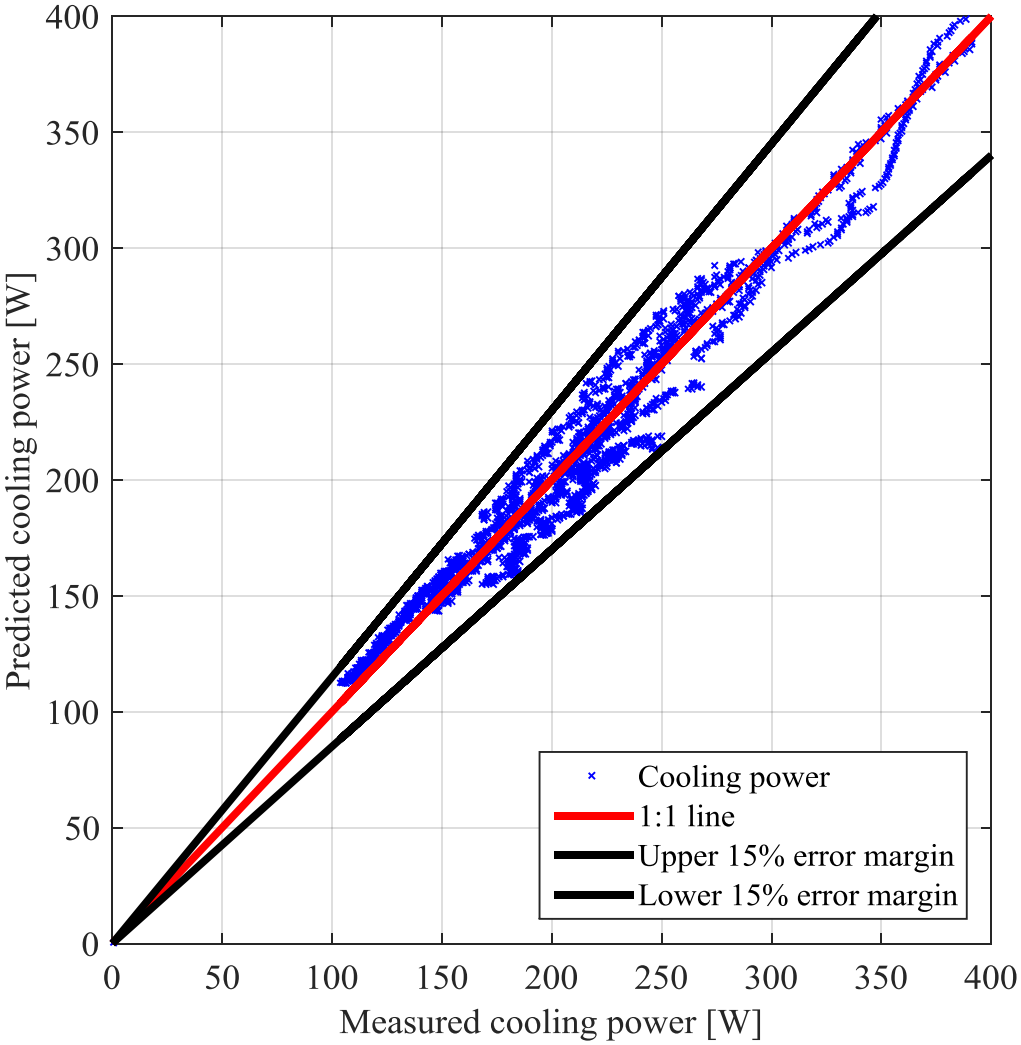

Figure 6.8. Predicted cooling power versus the measured cooling power for RT25

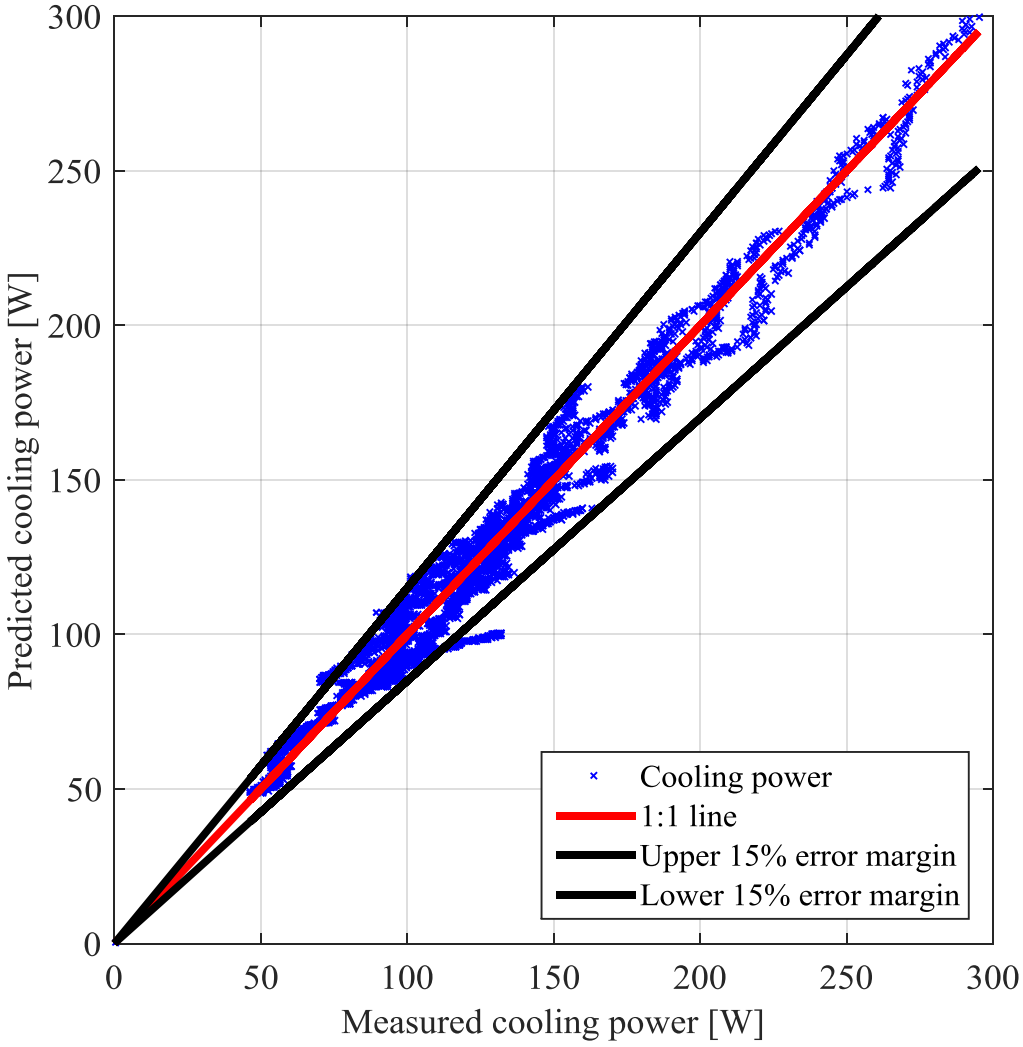

Figure 6.9. . Predicted cooling power versus the measured cooling power for RT27

6.5 APPLICATION OF EQUATIONS TO DESIGN.

The coefficients in the empirical models are valid for the design of the plate PCM-air heat exchanger that was studied.

$$\dot{Q}_i = C_0 \Delta T_{pcm}{}^{C1} C_2 \dot{m}^{C3} e^{(-C4t\Delta T_{pcm}\dot{m})} \tag{6.11}$$

Given a desired objective cooling load, inlet air temperature, air mass flow rate and time, the number of modules n installed in parallel is given by Equation 6.12.

$$n_{mod} = \frac{\dot{Q}_{obj}}{C_0 \Delta T_{pcm}{}^{C1} C_2 \dot{m}^{C3} e^{(-C4t\Delta T_{pcm}\dot{m})}} \quad (6.12)$$

In order to maintain the desired objective cooling load (Q_{obj}), a safety factor of 15% should be applied to the calculated number of modules as the maximum permissible error for RT25 and RT27 modules as shown in Figures 6.19 and 6.20. was 15 %. Note that the correlation is only valid for the test geometries considered in this investigation in terms of plate pitch and air velocity.

6.6 SUMMARY

Using design charts as illustrated in Figure 6.1 can be a cumbersome task since a different chart has to be generated for specific operating conditions. The design charts also did not cater for air flow rates in between. They catered only for specific operating conditions tested. Given these limitations in the application of design charts, it can be easily seen that there is need for a better model that will predict the number of modules that will cater for a particular objective cooling load.

The derived empirical model is valid for the tested duct and plate geometry for the paraffinic PCMs. It is valid within the defined PCM phase transformation temperature ranges as specified by the manufacturer. The model equation 6.10 may not be strictly applicable to salt hydrates. The model may also be applicable salt hydrates but there is a need to determine the applicable phase transformation temperature range. The determination of a better fitting model for the salt hydrate lies outside of the scope for this work when considering the manufacturer's melting temperature range for SP24E.

CHAPTER 7 CONCLUSIONS AND RECOMMENDATIONS

7.1 CONCLUSIONS

The passive air cooling performance of three types of PCMs 2 paraffin types RT25 and RT27 and a salt hydrate SP24E encapsulated in thin aluminium plates was experimentally investigated. An experimental test facility was designed, built and commissioned to characterise the cooling performance. The test facility consisted of several components and sections that were connected in series. These were: a conical inlet section, an electrical resistance heating element with a transformer, a section with passive free-rotating air mixing blades, an air temperature measuring station, the PCM test section, another section with passive free-rotating air mixing blades, another air temperature measuring station, an inline tube fan with a fan motor controller, a manual damper and flexible ducting.

Based on the experimental results, the following conclusions were derived:

- All the three types of PCMs (RT27, RT25 (paraffin type) and SP24E (salt hydrate type)) investigated in this study exhibited air cooling behaviour, therefore they can be applied for building free cooling applications under Southern African climatic conditions. However a huge number of the PCM plates are required to offset a mere portion of the cooling load.
- It was found that paraffinic PCMs exhibited high air cooling power with short heat absorption duration. Salt hydrate exhibited longer heat absorption duration but had a lower air cooling power than the paraffin.
- The salt hydrate (SP4E) module had the highest energy absorption capacity for all experimental conditions.

- A new empirical model with different coefficients for different PCMs was successfully developed. The model can be used for determining the number of modules installed in parallel with a plate pitch of 15 mm with a mass flux i.e air mass flow rate per module divided by the cross sectional area of each module in the range of 0.42 kg/m^{2}s to 0.85 kg/m^{2}s and inlet air temperatures ranging from 30°C to 35°C to maintain an objective cooling load for a desired time period.

7.2 RECOMMENDATIONS

- It is recommended to increase the number of modules calculated using the developed models by 15% in order to maintain the desired objective cooling load (Q_{obj}) with certainty.
- The desirable thermal performance characteristic of PCM is to maintain a high air cooling power over a longer period. Paraffins met the first condition of high cooling power but did not meet the second condition of extended thermal energy storage duration. SP24E met the condition for extended thermal energy storage duration but had a lower air cooling power than the paraffins. It is recommended to have a mix of plates containing salt hydrates and paraffin PCMs within one module.

7.3 SUGGESTIONS FOR FUTURE RESEARCH

- Future research can focus on development of blends of salt hydrate and paraffin and characterise their thermal performance for Southern African climatic conditions.
- To enhance the thermal performance of salt hydrates the incorporation of highly conductive admixtures is recommended for future research. This will enhance the instantaneous heat absorption capacity for salt hydrates in addition to their favourable extended heat absorption capabilities.
- Development and characterisation of PCMs applicable for passive heating of buildings during winter periods for Southern Africa.

REFERENCES

1. Eskom (2014) Energy Efficiency Opportunities in South Africa : Commercial Sector. South Africa
2. Waqas A, Din ZU (2013) Phase change material (PCM) storage for free cooling of buildings - A review. Renew Sustain Energy Rev 18:607–625.
3. Milford R Perspective on Energy Efficiency Building Regulations; A South African Perspective.
4. Osterman E, Tyagi V V, Butala V, et al (2012) Review of PCM based cooling technologies for buildings. Energy Build 49:37–49.
5. South Africa Department of Environmental Affairs. National climate change response: White paper. Pretoria, South Africa.
6. South African Bureau of Standards (SABS) (2011) SANS 10400-XA: The application of the National Building Regulations Part X : Environmental sustainability Part XA : Energy usage in buildings. Pretoria, South Africa.
7. South African Bureau of Standards (SABS) (2011) SANS 204 : 2011 Energy efficiency in buildings. Pretoria, South Africa.
8. Raj VA, Velraj R (2011) Heat transfer and pressure drop studies on a PCM-heat exchanger module for free cooling applications. Int J Therm Sci 50:1573–1582.
9. Arkar C, Vidrih B, Medved S (2007) Efficiency of free cooling using latent heat storage integrated into the ventilation system of a low energy building. Int J Refrig 30:134–143.
10. Zalba B, Marin JM, Cabeza LF, Mehling H (2004) Free-cooling of buildings with phase change materials. Int J Refrig 27:839–849.
11. Kalaiselvam S, Sureshkumar KR, Sriram V (2016) Study of heat transfer and pressure drop characteristics of air heat exchanger using PCM for free cooling applications. Therm Sci 20:1543–1554.
12. Turnpenny JR, Etheridge DW, Reay DA (2000) Novel ventilation cooling system for reducing air conditioning in buildings . Part I : testing and theoretical modelling. Appl Therm Eng 20:1019–1037.
13. Cengel YA (2008) Heat transfer: A practical approach., Second. McGraw-Hill, New York
14. Yanbing K, Yi J, Yinping Z (2003) Modeling and experimental study on an innovative passive cooling system — NVP system. Energy Build 35:417–425.
15. Sharma SD, Kitano H, Sagara K (2004) Phase Change Materials for Low Temperature Solar Thermal Applications. Res Rep Fac Eng Mie Univ 29:31–64.
16. Zhou D, Zhao CY, Tian Y (2012) Review on thermal energy storage with phase change materials (PCMs) in building applications. Appl Energy 92:593–605.
17. Dolado P, Lazaro A, Marin JM, Zalba B (2011) Characterization of melting and solidification in a real scale PCM-air heat exchanger : Numerical model and experimental validation. Energy Convers Manag 52:1890–1907.
18. Yinping Z, Yi J, Yi J (1999) A simple method , the T -history method , of determining the heat of fusion , specific heat and thermal conductivity of phase-change materials. Meas Sci Technol 10:201–205.
19. Morrison DJ, Abdel-Khalik S. I (1978) Effects of phase change energy storage on the perfomance of air based and liquid based solar heating systems. Sol Energy 20:57–67.

20. Yau YH, Rismanchi B (2012) A review on cool thermal storage technologies and operating strategies. Renew Sustain Energy Rev 16:787–797.
21. Takeda S, Nagano K, Mochida T, Shimakura K (2004) Development of a ventilation system utilizing thermal energy storage for granules containing phase change material. Energy Build 77:329–338.
22. Butala V, Stritih U (2009) Experimental investigation of PCM cold storage. Energy Build 41:354–359.
23. Muthuvelan T, Panchabikesan K, Munisamy R, et al (2016) Experimental investigation of free cooling using phase change material-filled air heat exchanger for energy efficiency in buildings. Adv. Build. ENERGY Res. 2549:
24. Rajagopal M, Velraj R (2016) Experimental investigation on the phase change material-based modular heat exchanger for thermal management of a building. Int J Green Energy 13:1109–1119.
25. Waqas A, Kumar S (2010) PCM thermal energy storage and cooler night temperatures for pretreatment of ambient air introduced in the building. In: PEA-AIT Int. Conf. Energy Sustain. Dev. Issues Strateg. (ESD 2010). Chiang Mai, Thailand., pp 1–8
26. Li P, Lew JV, Karaki W, et al (2011) Generalized charts of energy storage effectiveness for thermocline heat storage tank design and calibration. Sol Energy 85:2130–2143.
27. Al-abidi AA, Mat SB, Sopian K, et al (2013) CFD applications for latent heat thermal energy storage : a review. Renew Sustain Energy Rev 20:353–363.
28. Verma P, Varun, Singal SK (2008) Review of mathematical modeling on latent heat thermal energy storage systems using phase-change material. Renew Sustain Energy Rev 12:999–1031.
29. Kośny J PCM-Enhanced Building Components An application of Phase Change Materials in building envelopes and internal structures. Springer, Switzerland
30. Mehling H, Cabeza LF (2008) Heat and cold storage with PCM an up to date introduction into basics and applications. Springer-Verlag, Berlin: Germany
31. Alexiades V, Solomon AD (1993) Mathematical modelling of melting and freezing processes. Taylor & Francis, Washington
32. Sharma A, Tyagi V, Chen CR, Buddhi D (2009) Review on thermal energy storage with phase change materials and applications. Renew Sustain Energy Rev 13:318–345.
33. Sharma SD, Sagara K (2005) Latent heat storage materials and systems : A review. Int J Green Energy 2:1–56.
34. Abhat A (1983) Low temperature latent heat thermal energy storage: Heat storage materials. Sol Energy 30:313–332.
35. Trp A (2005) An experimental and numerical investigation of heat transfer during technical grade paraffin melting and solidification in a shell-and-tube latent thermal energy storage unit. Sol Energy 79:648–660.
36. Butala V, Stritih U (2009) Experimental investigation of PCM cold storage. Energy Build 41:354–359.
37. Stritih U, Butala V (2007) Energy saving in building with PCM cold storage. Int J ENERGY Res 31:1532–1544.
38. Medved S, Arkar C (2008) Correlation between the local climate and the free-cooling potential of latent heat storage. Energy Build 40 40:429–437.
39. Geetha NB, Velraj R (2012) Passive cooling methods for energy efficient

buildings with and without thermal energy storage – A review. Energy Educ Sci Technol Part A Energy Sci Res 29:913–946.
40. Zhu N, Ma Z, Wang S (2009) Dynamic characteristics and energy performance of buildings using phase change materials : A review. Energy Convers Manag 50:3169–3181.
41. Kalnæs SE, Jelle BP (2015) Phase change materials and products for building applications : A state-of-the-art review and future research opportunities. Energy Build 94:150–176.
42. Alam M, Sanjayan J, Zou PXW, et al (2017) A comparative study on the effectiveness of passive and free cooling application methods of phase change materials for energy efficient retrofitting in residential buildings. Procedia Eng. 0:
43. Mays E, Mays E (2017) Using phase change material in under floor heating. Energy Procedia 119:806–811.
44. Farid MM, Khudhair AM, Razack KS., Al-Hallaj S (2004) A review on phase change energy storage : materials and applications. Energy Convers Manag 45:1597–1615.
45. Aroul VA, Velraj R (2011) Heat transfer and pressure drop studies on a PCM-heat exchanger module for free cooling applications. Int J Therm Sci 50:1573–1582.
46. Charvat P, Klimes L, Ostry M (2014) Numerical and experimental investigation of a PCM-based thermal storage unit for solar air systems. Energy Build 68:488–497.
47. Rubitherm (2017) Rubitherm website.pdf. https://www.rubitherm.eu/index.php/produktkategorie/makroverkaspelung-csm. Accessed 27 Oct 2017
48. Trox Technik Air-water systems for air conditioning Design manual.
49. Marin J., Zalba B, Cabeza L., Mehling H (2005) Improvement of a thermal energy storage using plates with paraffin – graphite composite. Int J Heat Mass Transf 48:2561–2570.
50. Hu H, Argyropoulos SA (1996) Mathematical modelling of solidification and melting : a review. Model Simul Mater Sci Eng 4:371–396.
51. Dutil Y, Rousse DR, Salar NB, et al (2011) A review on phase-change materials : Mathematical modeling and simulations. Renew Sustain Energy Rev 15:112–130.
52. Brusche JH, Segal A, Vuik C, Urbach HP (2006) A comparison of an enthalpy and a temperature methods for melting problems on composite domains. Eur. Conf. Comput. Fluid Dyn.
53. Zalba B, Marin JM, Cabeza LF, Mehling H (2003) Review on thermal energy storage with phase change: materials , heat transfer analysis and applications. Appl Therm Eng 23:251–283.
54. Lazaro A, Dolado P, Marín JM, Zalba B (2009) PCM – air heat exchangers for free-cooling applications in buildings : Experimental results of two real-scale prototypes. Energy Convers Manag 50:439–443.
55. Chaiyat N, Kiatsiriroat T (2014) Energy reduction of building air-conditioner with phase change material in Thailand. Case Stud Therm Eng 4:175–186.
56. Halawa E, Saman W (2011) Thermal performance analysis of a phase change thermal storage unit for space heating. Renew Energy 36:259–264.

57. Kabbara MJ, Abdallah N Ben (2013) Experimental investigation on phase change material based thermal energy storage unit. Procedia - Procedia Comput Sci 19:694–701.
58. Nagano K, Takeda S, Mochida T, et al (2006) Study of a floor supply air conditioning system using granular phase change material to augment building mass thermal storage — Heat response in small scale experiments. Energy Build 38:436–446.
59. Castell A, Belusko M, Bruno F, Cabeza LF (2011) Maximisation of heat transfer in a coil in tank PCM cold storage system. Appl Energy 88:4120–4127.
60. Amin NAM, Bruno F, Belusko M (2012) Effectiveness – NTU correlation for low temperature PCM encapsulated in spheres. Appl Energy 93:549–555.
61. Tay NHS, Belusko M, Bruno F (2012) Experimental investigation of tubes in a phase change thermal energy storage system. Appl Energy 90:288–297.
62. Lazaro A, Dolado P, Marin JM, Zalba B (2009) PCM-air heat exchangers for free-cooling applications in buildings : Empirical model and application to design. Energy Convers Manag 50:444–449.
63. Iten M, Liu S (2015) Experimental Study on the Performance of RT 25 to be Used as ambient energy storage. In: Int. Conf. Sol. Heat. Cool. Build. Ind. SHC 2014. Elsevier, pp 229–240
64. ASHRAE (2010) ASHRAE Standard 94.1: Method of testing active latent-heat storage devices based on thermal performance. Georgia Atlanta
65. ASHRAE (2009) Methods of testing for rating electrically driven unitary air-conditioning and heat pump equipment.
66. Farid MM, Khudhair AM, Ali S, Razack K (2004) A review on phase change energy storage : materials and applications. Energy Convers Manag 45:1597–1615.
67. ASHRAE (2004) ASHRAE Standard 55: Thermal environmental conditions for human occupancy. Georgia Atlanta
68. Ebmpapst HIT Series In-line tube fan. http://www.ebmpapst.com/en/products/overview.html. Accessed 7 Dec 2017
69. Technologies A (2012) Agilent 34970A/ 34972A Data acquisition switch unit User guide. Malaysia
70. Onset Indoor HOBO H8 family. Onset, Bourne, Massachusetts
71. ASHRAE (1986) Standard method for temperature measurement. Georgia Atlanta
72. Box. TET Air properties. https://www.engineeringtoolbox.com/air-properties-d_156.html. Accessed 29 Jun 2016
73. Morvay ZK, Gvozdenac DD Toolbox 6 Thermodynamic and transport properties of moist air. Appl. Ind. energy Environ. Manag. part III Fundam. Anal. Calc. energy Environ. perfomance.
74. ASHRAE (2002) Psychrometrics. ASHRAE Fundam. Handb. SI
75. (NPTEL) NP on TEL LECTURE – 2: Different ways of expressing humidity. http://nptel.ac.in/courses/123106002/MODULE - III/Lecture 2.pdf. Accessed 29 Jun 2016
76. Tay NHS, Belusko M, Bruno F (2012) An effectiveness-NTU technique for characterising tube-in-tank phase change thermal energy storage systems. Appl Energy 91:309–319.
77. Moffat RJ (1988) Describing the Uncertainties in Experimental Results. Exp

Therm Fluid Sci 1:3–17.
78. Holman JP Experimental methods for engineers., Eighth. McGraw-Hill, New York, USA
79. Rubitherm Phase Change Material (2016) Safety data sheet SP24E. https://www.rubitherm.eu/index.php/produktkategorie/anorganische-pcm-sp. Accessed 7 Dec 2017
80. Mills AF (1999) Basic heat and mass transfer., 2nd Editio. Prentice Hall, Upper Saddle River, NJ, USA.
81. Conradie DCU (2012) South Africa's climatic zones: Today, tomorrow. Int. Green Build. Conf. Exhib. Futur. Trends Issues Impacting Built Environ.
82. Garach D (2014) Heat transfer and pressure drop in microchannels with different inlet geometries for laminar and transitional flow of water. University of Pretoria

APPENDIX A. GAUTENG CLIMATIC ANALYSIS

AppendixA.1. Introduction

The climatic analysis for the Gauteng province was done using the Köppen-Geiger climatic map for South Africa. According to Conradie [81] the map is based on a high resolution grid (1 km x 1 km) and uses 20 years monthly temperature and precipitation data from 1985 to 2005. The map groups places with similar ambient air temperatures and precipitation under the same climatic region. The map indicates that Gauteng has four climatic regions classified as Bsh, Cwa, Cwb and Bsk in Figure A.1.

An analysis of six months summer temperatures (October to March) was carried out for four different climate files for Johannesburg Jan Smut, Pretoria Forum, Pretoria Irene, and Pretoria Roodeplat which represented the said climatic regions. The analysis is shown in Figures A2 to A5. The analysis indicated peak ambient temperature range of 30 °C to 35 °C across the Gauteng region.

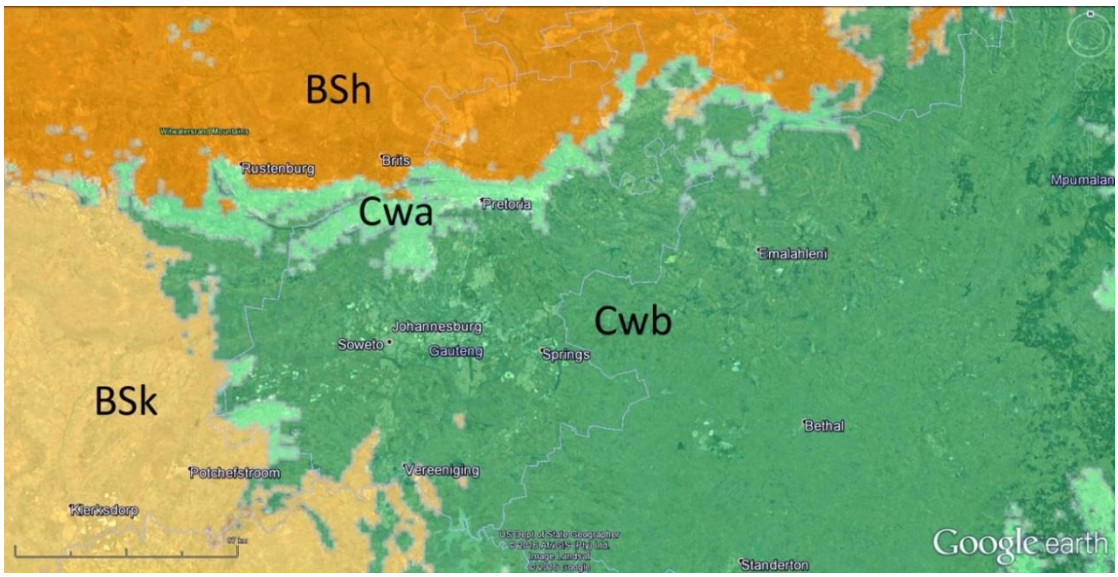

Figure A.1. Illustration of the Köppen-Geiger climate classification map for Gauteng region developed by the CSIR.

Gauteng region was targeted because it has the highest concentration of commercial buildings, thus there are greater electrical energy savings potential when the PCM-air cooling mechanism is implemented on many commercial buildings.

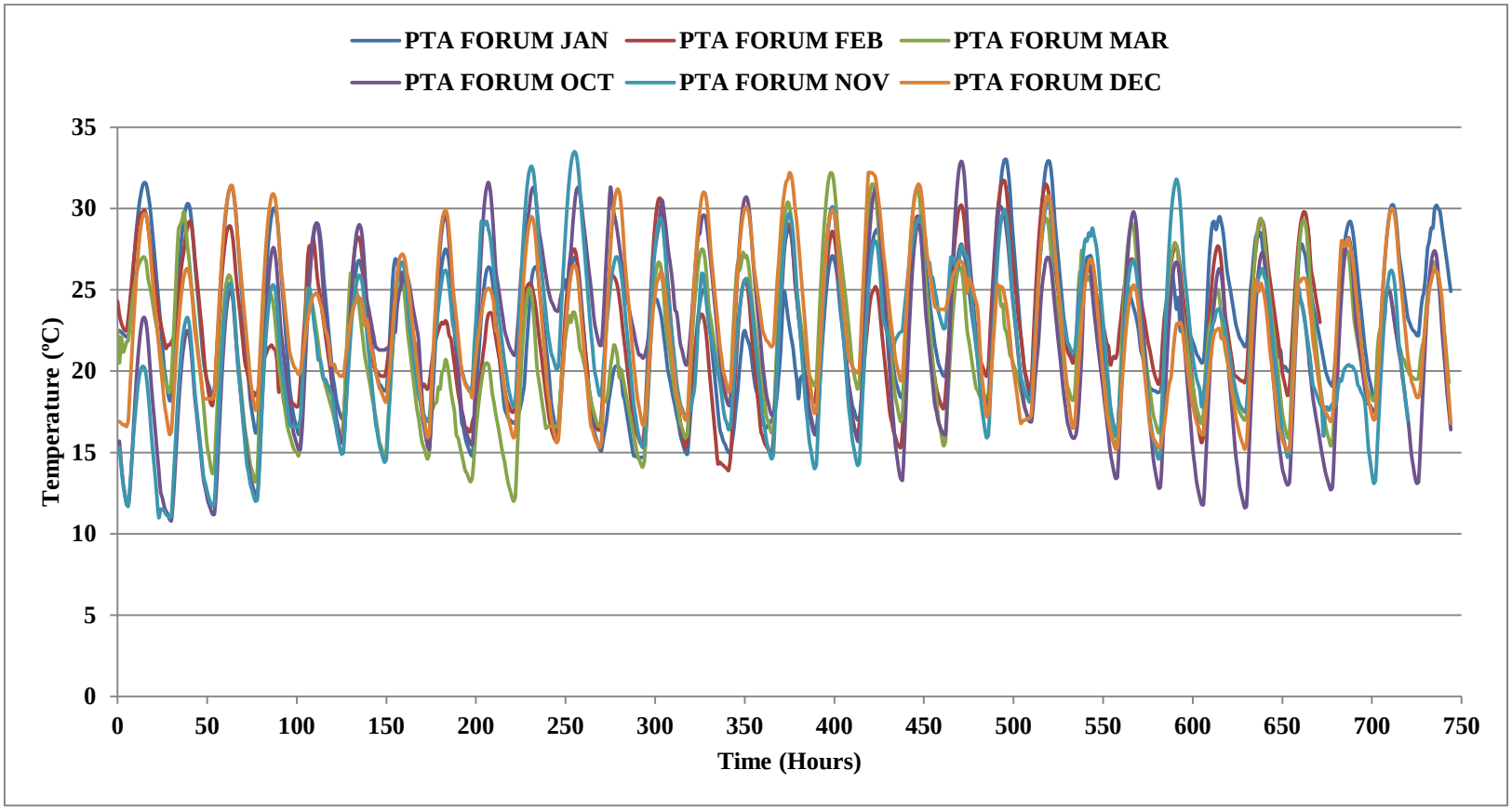

Figure A.2: Hourly temperature distribution for summer months: Pretoria Forum

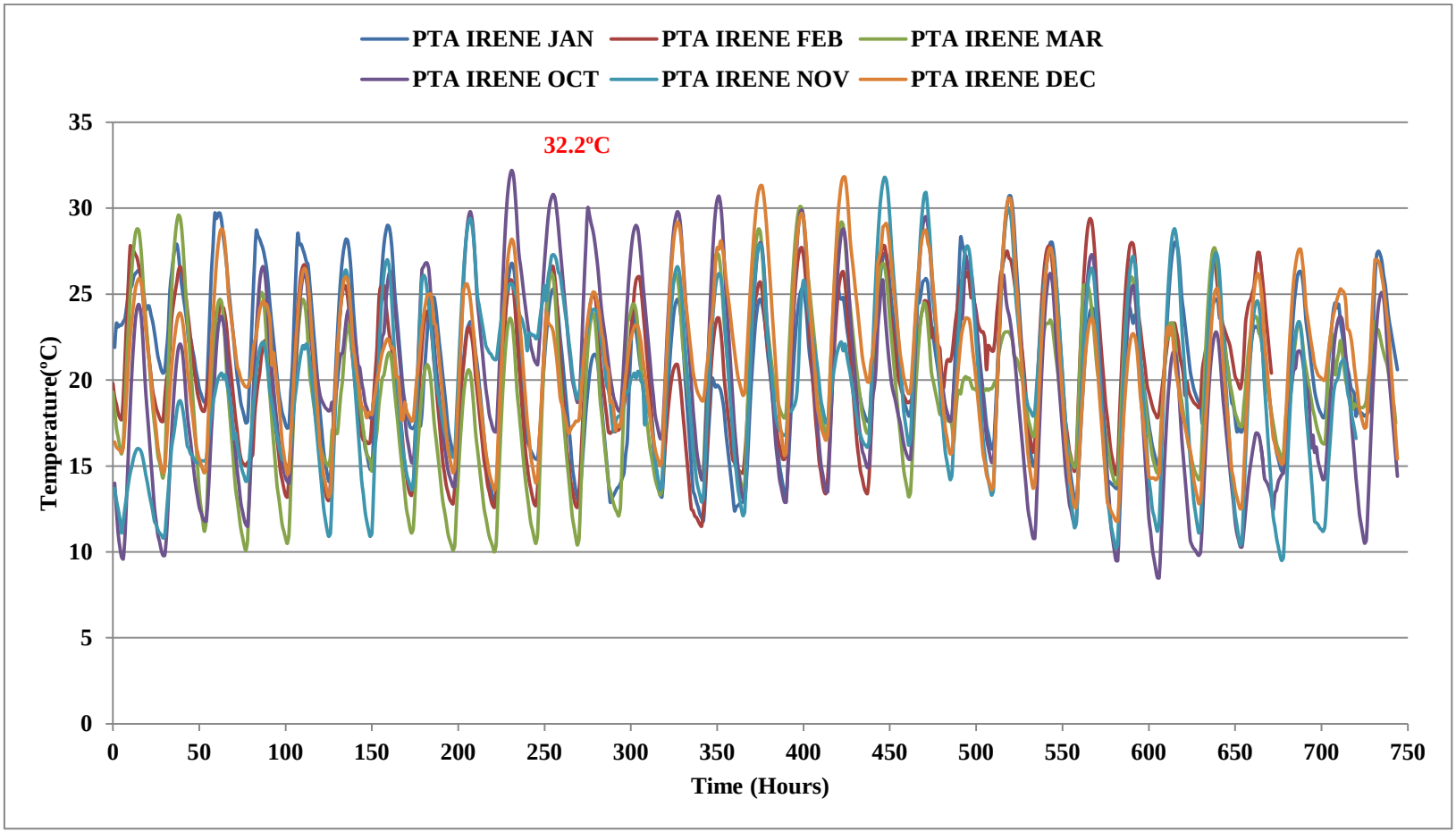

FigureA.3: Hourly temperature distribution for summer months: Pretoria Irene

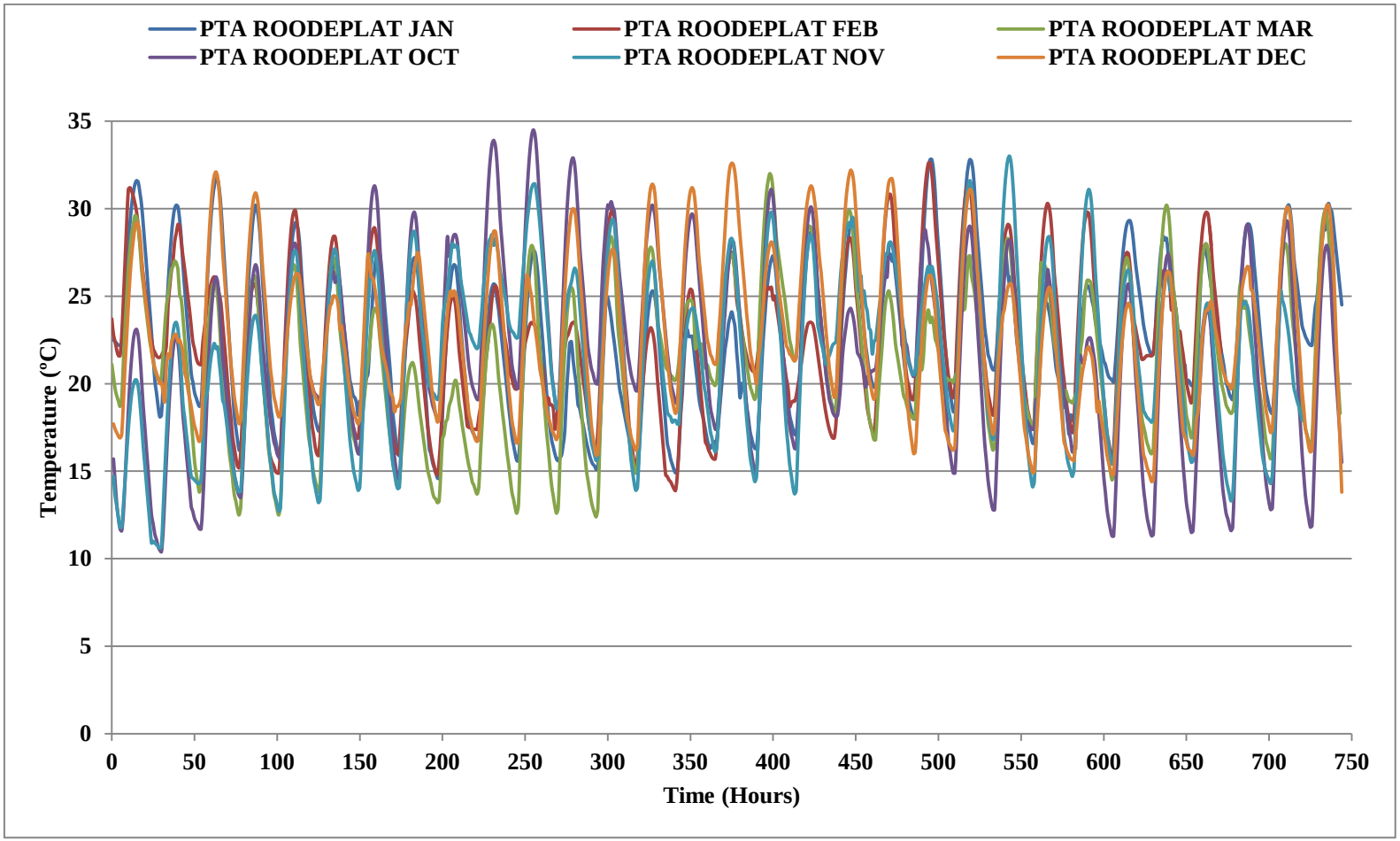

Figure A.4. Hourly temperature distribution for summer months: Pretoria Roodeplat

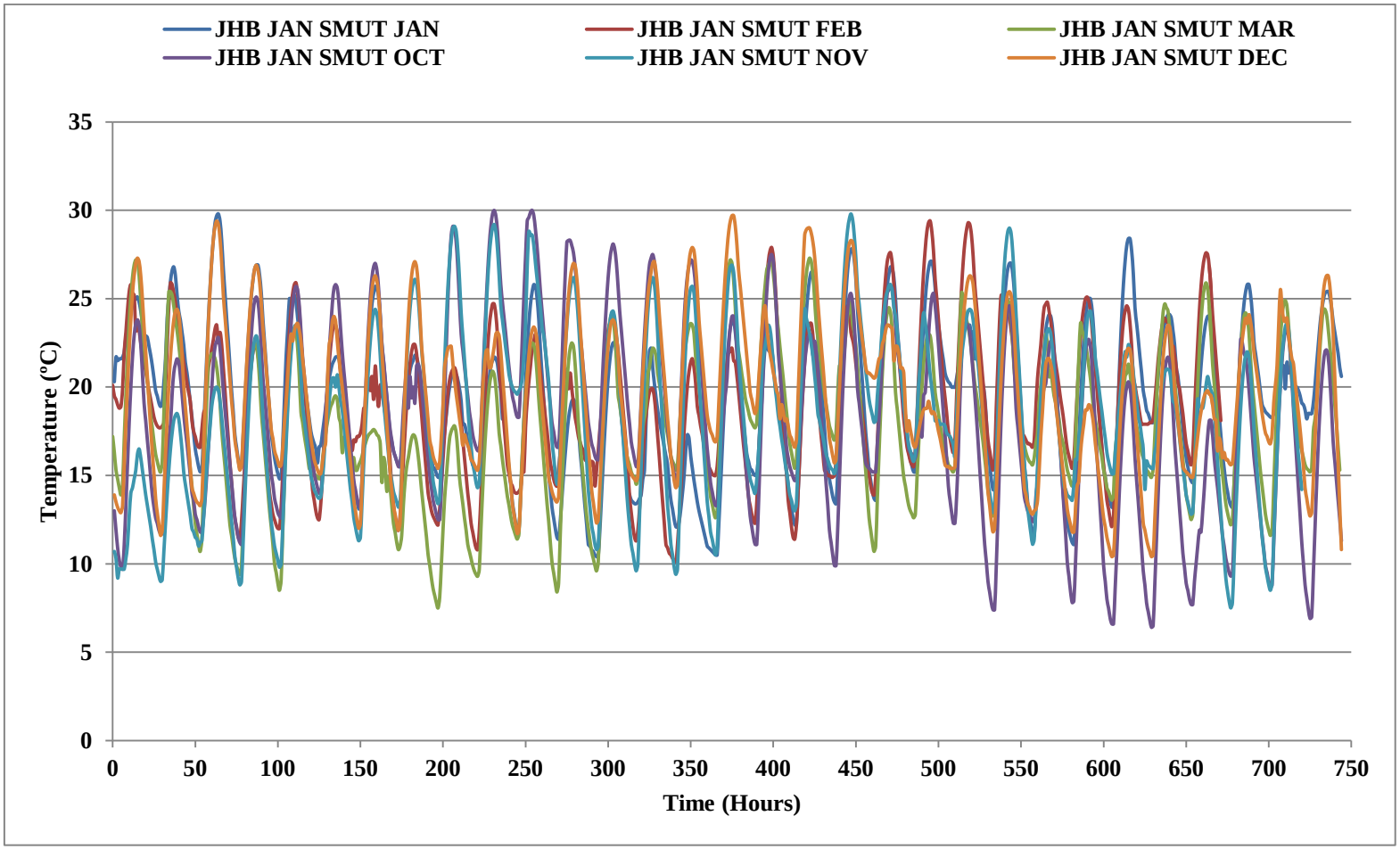

Figure A.5: Hourly temperature distribution for summer months: Johannesburg

APPENDIX B. THERMOCOUPLE CALIBRATION

AppendixB.1. Thermocouple calibration

56 thermocouples were constructed and calibrated. The calibration equipment set up is shown in Figure B.1. The PD20R-30-A12E, refrigerating/heating unit labelled (3) in Figure 4-3 is equipped with a performance digital temperature controller labelled (2) which is capable of maintaining a temperature stability of ±0.005°C in the water bath (1). The thermocouple tips were immersed into water at the same depth (See 1 in Figure B.1).The other ends of the thermocouples were connected to the data cards (See 4 in Figure B.1).The thermocouples were labelled in accordance with the channel number on the data cards. Each data card consisted of 20 channels. The thermocouples were calibrated to measure temperature from 7 °C to 41 °C in steps of 2 °C. The temperature range was selected to cover the diurnal temperature variations for Pretoria and Johannesburg Köppen climatic regions.

For the first calibration the water bath temperature was first set to be 7 °C, and after 15 minutes when the water bath temperature was stabilized, temperature readings from the thermocouples were logged at two seconds intervals by the Agilent data logger labelled number 5 in Figure B.1. The performance digital temperature controller labelled 2 in Figure B.1 was then set to 9 °C and after 15 minutes when the water bath temperature was stabilised, temperature readings from the thermocouples were logged at two seconds intervals by the Agilent data logger labelled number 5 in Figure B.1. The procedure was repeated in steps of 2 °C until 41 °C.

1 http://www.anmalliance.com/uploads/newproducts/Polyscience.pdf
15

FigureB.1. Thermocouples calibration equipment

The difference between set water bath temperature and the thermocouple measured water temperature (PT100-TC; row 3 of Table B.1) was plotted in the vertical axis against the thermocouple measured water temperature in the horizontal axis as shown in Figure B.2. A polynomial trend line of best fit was plotted and a polynomial regression equation was obtained for each of the 56 thermocouples. The regression equation determined for each thermocouple was used to calculate a correction factor for any temperature measurement between 7 °C and 41 °C done by the thermocouple.

Regression equations for each of the thermocouples that were used for this study are shown in Table B.2.

Table B.1. Example calibration results for thermocouple 120

°C																		
PT100	7	9	11	13	15	17	19	21	23	25	27	29	31	33	35	37	39	41
TC	7.32	9.33	11.34	13.33	15.33	17.32	19.31	21.30	23.33	25.30	27.26	29.29	31.28	33.29	35.32	37.22	39.23	41.23
PT100-TC	-0.32	-0.33	-0.34	-0.33	-0.33	-0.32	-0.31	-0.30	-0.33	-0.30	-0.26	-0.29	-0.28	-0.29	-0.32	-0.22	-0.23	-0.23
Calc. Corr	-0.32	-0.33	-0.34	-0.34	-0.33	-0.32	-0.31	-0.30	-0.30	-0.30	-0.29	-0.29	-0.29	-0.29	-0.27	-0.26	-0.24	-0.23
TC Corr	7.00	9.00	11.01	12.99	15.00	17.00	18.99	20.99	23.04	25.01	26.97	29.00	30.98	33.00	35.05	36.97	38.99	41.01
Error	0.00	0.00	-0.01	0.01	0.00	0.00	0.01	0.01	-0.04	-0.01	0.03	0.00	0.02	0.00	-0.05	0.03	0.01	-0.01

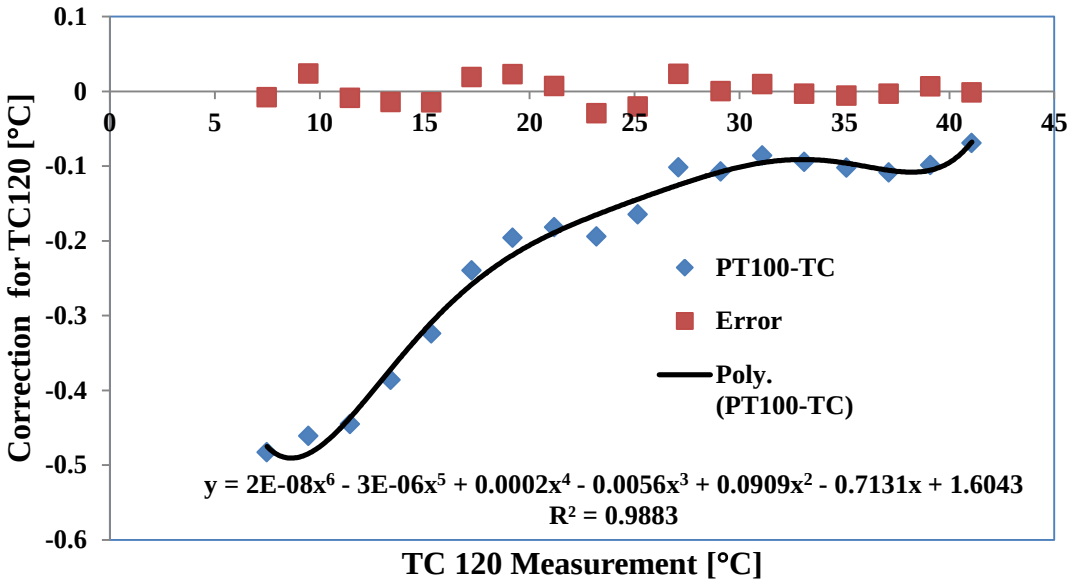

Figure B.2: Calibration curve for thermocouple number 120

Table B.2. Polynomial regression equations for thermocouples.

TC	Calibration equation	R^2 value	Calculated Thermocouple uncertainty (Refer to equations C3 to C6)
101	y = -6E-09x6 + 9E-07x5 - 5E-05x4 + 0.0012x3 - 0.016x2 + 0.0968x - 0.5353	0.74	0.069
102	y = -5E-09x^6 + 8E-07x^5 - 4E-05x^4 + 0.0011x^3 - 0.0137x^2 + 0.0772x - 0.5192	0.79	0.087
103	y = -3E-09x^6 + 4E-07x^5 - 2E-05x^4 + 0.0004x^3 - 0.003x^2 - 0.0038x - 0.315	0.89	0.076

104	$y = -6E\text{-}10x^6 + 3E\text{-}08x^5 + 2E\text{-}06x^4 - 0.0003x^3 + 0.0079x^2 - 0.0946x - 0.0751$	0.91	0.071
105	$y = 2E\text{-}09x^6 - 4E\text{-}07x^5 + 3E\text{-}05x^4 - 0.001x^3 + 0.0187x^2 - 0.1814x + 0.1664$	0.91	0.087
201	$y = 1E\text{-}08x^6 - 2E\text{-}06x^5 + 1E\text{-}04x^4 - 0.0032x^3 + 0.0563x^2 - 0.4771x + 0.855$	0.98	0.073
202	$y = 7E\text{-}09x^6 - 1E\text{-}06x^5 + 8E\text{-}05x^4 - 0.0027x^3 + 0.0489x^2 - 0.428x + 0.6984$	0.97	0.088
203	$y = 8E\text{-}09x^6 - 1E\text{-}06x^5 + 9E\text{-}05x^4 - 0.0031x^3 + 0.0561x^2 - 0.4896x + 0.903$	0.98	0.068
204	$y = 8E\text{-}09x^6 - 1E\text{-}06x^5 + 9E\text{-}05x^4 - 0.0031x^3 + 0.056x^2 - 0.489x + 0.9408$	0.98	0.068
205	$y = 9E\text{-}09x^6 - 1E\text{-}06x^5 + 1E\text{-}04x^4 - 0.0033x^3 + 0.0596x^2 - 0.5128x$	0.98	0.058

	+ 1.038		

206	$y = 6E\text{-}09x^6 - 9E\text{-}07x^5 + 7E\text{-}05x^4 - 0.0023x^3 + 0.0446x^2 - 0.4024x + 0.7148$	**0.98**	**0.084**
207	$y = 8E\text{-}09x^6 - 1E\text{-}06x^5 + 9E\text{-}05x^4 - 0.003x^3 + 0.0553x^2 - 0.4856x + 1.0156$	**0.98**	**0.064**
208	$y = 6E\text{-}09x^6 - 1E\text{-}06x^5 + 7E\text{-}05x^4 - 0.0026x^3 + 0.0497x^2 - 0.4442x + 0.9146$	**0.98**	**0.071**
209	$y = 6E\text{-}09x^6 - 1E\text{-}06x^5 + 7E\text{-}05x^4 - 0.0027x^3 + 0.0516x^2 - 0.4687x + 1.0169$	**0.98**	**0.071**
210	$y = 8E\text{-}09x^6 - 1E\text{-}06x^5 + 9E\text{-}05x^4 - 0.0033x^3 + 0.0611x^2 - 0.5404x + 1.2193$	**0.99**	**0.076**
211	$y = 8E\text{-}09x^6 - 1E\text{-}06x^5 + 9E\text{-}05x^4 - 0.0033x^3 + 0.062x^2 - 0.5499x + 1.2613$	**0.99**	**0.076**

213	$y = 7E\text{-}09x^6 - 1E\text{-}06x^5 + 9E\text{-}05x^4 - 0.0031x^3 + 0.0596x^2 - 0.5391x + 1.2472$	**0.98**	**0.088**
215	$y = 7E\text{-}09x^6 - 1E\text{-}06x^5 + 8E\text{-}05x^4 - 0.003x^3 + 0.0569x^2 - 0.5062x + 1.1923$	**0.98**	**0.074**
216	$y = 7E\text{-}09x^6 - 1E\text{-}06x^5 + 9E\text{-}05x^4 - 0.0031x^3 + 0.0593x^2 - 0.5213x + 1.2676$	**0.99**	**0.055**
217	$y = 7E\text{-}09x^6 - 1E\text{-}06x^5 + 9E\text{-}05x^4 - 0.0032x^3 + 0.0617x^2 - 0.5415x + 1.2837$	**0.99**	**0.078**
218	$y = 9E\text{-}09x^6 - 2E\text{-}06x^5 + 0.0001x^4 - 0.0039x^3 + 0.0734x^2 - 0.634x + 1.5068$	**0.99**	**0.078**
219	$y = 8E\text{-}09x^6 - 1E\text{-}06x^5 + 0.0001x^4 - 0.0038x^3 + 0.0721x^2 - 0.6284x + 1.439$	**0.99**	**0.098**

220	$y = 5E\text{-}09x^6 - 1E\text{-}06x^5 + 8E\text{-}05x^4 - 0.0031x^3 + 0.0609x^2 - 0.5397x + 1.1146$	**0.99**	**0.12**
301	$y = 2E\text{-}08x^6 - 3E\text{-}06x^5 + 0.0002x^4 - 0.0058x^3 + 0.0948x^2 - 0.7541x + 1.809$	**0.98**	**0.04**
302	$y = 2E\text{-}08x^6 - 3E\text{-}06x^5 + 0.0002x^4 - 0.0052x^3 + 0.0863x^2 - 0.692x + 1.5328$	**0.98**	**0.05**
303	$y = 2E\text{-}08x^6 - 3E\text{-}06x^5 + 0.0002x^4 - 0.0053x^3 + 0.0895x^2 - 0.7277x + 1.5731$	**0.99**	**0.059**
304	$y = 1E\text{-}08x^6 - 2E\text{-}06x^5 + 0.0001x^4 - 0.0045x^3 + 0.0772x^2 - 0.6355x + 1.2915$	**0.99**	**0.067**
305	$y = 1E\text{-}08x^6 - 2E\text{-}06x^5 + 0.0001x^4 - 0.0042x^3 + 0.074x^2 - 0.613x + 1.1551$	**0.99**	**0.078**

306	$y = 1E\text{-}08x^6 - 2E\text{-}06x^5 + 0.0001x^4 - 0.0038x^3 + 0.0663x^2 - 0.5545x + 0.9597$	**0.99**	**0.082**
307	$y = 1E\text{-}08x^6 - 2E\text{-}06x^5 + 0.0001x^4 - 0.0038x^3 + 0.0677x^2 - 0.5686x + 1.0036$	**0.99**	**0.092**
308	$y = 1E\text{-}08x^6 - 2E\text{-}06x^5 + 0.0001x^4 - 0.0037x^3 + 0.0668x^2 - 0.5604x + 1.0473$	**0.99**	**0.081**
309	$y = 8E\text{-}09x^6 - 1E\text{-}06x^5 + 9E\text{-}05x^4 - 0.0033x^3 + 0.0603x^2 - 0.5141x + 0.9243$	**0.99**	**0.09**
310	$y = 1E\text{-}08x^6 - 2E\text{-}06x^5 + 0.0001x^4 - 0.0038x^3 + 0.0698x^2 - 0.5924x + 1.1732$	**0.99**	**0.092**
311	$y = 1E\text{-}08x^6 - 2E\text{-}06x^5 + 0.0001x^4 - 0.004x^3 + 0.0733x^2 - 0.6219x + 1.3355$	**0.99**	**0.083**

312	$y = 6E\text{-}09x^6 - 1E\text{-}06x^5 + 8E\text{-}05x^4 - 0.0029x^3 + 0.0549x^2 - 0.4774x + 0.9732$	**0.99**	**0.066**
313	$y = 8E\text{-}09x^6 - 1E\text{-}06x^5 + 1E\text{-}04x^4 - 0.0034x^3 + 0.0639x^2 - 0.5531x + 1.2168$	**0.99**	**0.068**
314	$y = 2E\text{-}08x^6 - 3E\text{-}06x^5 + 0.0002x^4 - 0.0059x^3 + 0.0997x^2 - 0.8097x + 1.9364$	**0.99**	**0.065**
315	$y = 8E\text{-}09x^6 - 1E\text{-}06x^5 + 1E\text{-}04x^4 - 0.0036x^3 + 0.0664x^2 - 0.5719x + 1.2882$	**0.99**	**0.072**
316	$y = 1E\text{-}08x^6 - 2E\text{-}06x^5 + 0.0001x^4 - 0.0043x^3 + 0.0801x^2 - 0.6819x + 1.5702$	**0.99**	**0.077**

APPENDIX C. UNCERTAINTY ANALYSIS

Experimental results must be accompanied with the relevant uncertainties. This Appendix shows the methods employed for the determination of instrument uncertainties and uncertainties in the calculated results from experimental data.

AppendixC.1. Uncertainty of Barometer

Barometric pressure (P) was measured by an Oregon Scientific WMR300 indoor barometer with an accuracy of ±100 Pa.

AppendixC.2. Uncertainty of HOBO H8 logger

The logger has an output of 8 bits of resolution. The accuracy of the logger for humidity measurements was ±5 % over the range of 5 °C to 50 °C [70].

AppendixC.3. Uncertainty of electrical resistance: Agilent data logger

The electrical resistance measurement error for the Agilent 34970A data logger switch unit was calculated from ± (% of reading + % of range) [69]. The resistance across the heating element was found to be constant and value of 80 Ω.

The uncertainty was calculated as according to[69]:

$$\delta\bar{R} = \frac{0.01}{100}(80) + \frac{0.004}{100}(100) = 0.012\Omega \quad \text{(C.1)}$$

AppendixC.4. Uncertainty of electrical voltage: Agilent data logger

The electrical voltage measurement error for the Agilent 34970A data logger switch unit was calculated from ± (% of reading + % of range) [69].

$$\delta V = \frac{0.06}{100}(V) + \frac{0.004}{100}(300) \quad \text{(C.2)}$$

V Voltage

AppendixC.5. Uncertainty of Specific heat capacity of dry air and specific heat capacity of water vapour.

The specific heat capacity of dry air and water vapour were regarded as constant hence their uncertainties were not considered in the uncertainty analysis.

AppendixC.6. Uncertainty of the Ideal gas constant

The ideal gas constant was regarded as constant hence its uncertainty was not considered in the uncertainty analysis.

AppendixC.7. Uncertainty of thermocouple

The uncertainty of thermocouples was calculated using the method proposed by Garach [82]:

The method calculates the uncertainty of the PT100 temperature probe using equation C.3.

$$\delta T_{PT100} = \sqrt{\frac{\sum_{cal=1}^{n}(T_{cal} - T_{PT100})^2}{(n-2)}} \quad \text{(C.3)}$$

Where:

δT_{PT100} Uncertainty of PT100 temperature probe

T_{cal} Calibrated temperature (TC Corr in Table B.2)

T_{PT100} Temperature measured by PT100 probe (PT100 in Table B.2)

n number of calibration points 18 points in this case i.e. (7 °C-41 °C)

The calculated uncertainty of the PT100 was applied to calculate thermocouple uncertainty for each calibration point (7 °C-41 °C) of the thermocouple using equation C.4.

$$\delta T_{cal,point} = \delta T_{PT100}\sqrt{1+\frac{1}{n}+\frac{(T_{cal}-\bar{T}_{uncal})^2}{\sum_{uncal=1}^{n}(T_{uncal}-\bar{T}_{uncal})^2}} \quad \text{(C.4)}$$

$\delta T_{cal,point}$ Thermocouple uncertainty for a calibration point (ºC)

T_{uncal} Uncalibrated temperature

$$\bar{T}_{uncal} = \frac{\sum_{uncal=1}^{N} T_{uncal}}{n} \quad \text{(C.5)}$$

The maximum thermocouple uncertainty considered from the uncertainties calculated for each calibration point of each thermocouple was substituted in equation C.6 for the calculation of the uncertainty for a particular thermocouple.

$$\delta TC = \left(\left(\delta T_{PT100}{}^2\right) + 2\left(max\left(\delta T_{cal,point}\right)^2\right)\right)^{\frac{1}{2}} \quad \text{(C.6)}$$

δTC Uncertainty of thermocouple

The results of the uncertainty for each thermocouple are shown in Table B.2. A constant value of ±0.1 °C was adopted as the thermocouple uncertainty.

Uncertainty of air specific heat capacity, air density, temperature difference between ambient air and inlet air, airflow rate, temperature difference between inlet air and outlet air and instantaneous heat transfer rate was calculated using the method of Kline and McClintock. This method determines the uncertainty in the calculated result (experimental measurements used to calculate some desired result of the experiments) on the basis of the uncertainties in the primary measurements. The explanation of the method is as follows [78]:

If the calculated result (R) is a function of the independent variables $x_1, x_2, x_3, \ldots, x_n$.
Let w_R be the uncertainty in the result and $w_1, w_2, w_3 \cdots w_n$ be the uncertainties in the independent variables. The uncertainty in the calculated result is given by:

$$w_R = \left[\left(\frac{\partial R}{\partial x_1} w_1\right)^2 + \left(\frac{\partial R}{\partial x_2} w_2\right)^2 + \cdots + \left(\frac{\partial R}{\partial x_n} w_n\right)^2\right]^{\frac{1}{2}} \quad \text{(C.7)}$$

AppendixC.8. Uncertainty of air Specific heat capacity

The specific heat capacity of air was calculated from equation 1.

$$C_{p,air} = C_{p,dry\ air} + W \cdot C_{p,w} \quad \text{(C.8)}$$

$$\delta C_{p,air} = \left[\left(\frac{\partial C_{p,air}}{\partial C_{p,dry\ air}} w_{cp,dry\ air}\right)^2 + W\left(\frac{\partial C_{p,air}}{\partial C_{p,w}} w_{cp,w}\right)^2 + C_{p,w}\left(\frac{\partial C_{p,air}}{\partial W} w_W\right)^2\right]^{\frac{1}{2}}$$

(C.9)

$$\delta C_{p,air} = \left[\left(w_{cp,dry\ air}\right)^2 + W\left(w_{cp,w}\right)^2 + C_{p,w}(w_W)^2\right]^{\frac{1}{2}} \quad \text{(C.10)}$$

AppendixC.9. Uncertainty of air density

The density of any gas is a function of the temperature and pressure at which it exist. The formula relating these parameters is the ideal gas law:

$$\rho_{i,air} = \frac{P}{R\bar{T}_a} \quad \text{(C.11)}$$

$$\delta\rho_{i,air} = \left[R^{-1}\bar{T}_a{}^{-1}\left(\frac{\partial \rho_{i,air}}{\partial P} w_P\right)^2 + P\bar{T}_a{}^{-1}\left(\frac{\partial \rho_{i,air}}{\partial R} w_R\right)^2 + PR^{-1}\left(\frac{\partial \rho_{i,air}}{\partial \bar{T}_a} w_{\bar{T}_a}\right)^2\right]^{\frac{1}{2}} \text{(C.12)}$$

$$\delta\rho_{i,air} = \left[\left(R^{-1}\bar{T}_a{}^{-1}(w_P)^2\right) + \left(P\bar{T}_a{}^{-1}(-R^{-2})(w_R)^2\right) + \left(PR^{-1}\left(-\bar{T}_a{}^{-2}\right)\left(w_{\bar{T}_a}\right)^2\right)\right]^{\frac{1}{2}}$$

(C.13)

AppendixC.10. Uncertainty of averaged ambient air, inlet air and outlet air temperatures

Multiple thermocouples were used to measure a single value of ambient air temperature, inlet air temperature and outlet air temperature. The single value of temperature was calculated as the average of the measured temperature using equation C.14.

$$T_i = \bar{T}_i = \frac{T_{i,1}+T_{i,2}+\cdots+T_{i,n}}{n} \quad \text{(C.14)}$$

$$\delta\bar{T}_i = \left[\left(\frac{w_{T_{i,1}}}{n}\right)^2 + \left(\frac{w_{T_{i,2}}}{n}\right)^2 + \cdots + \left(\frac{w_{T_{i,n}}}{n}\right)^2\right]^{\frac{1}{2}} \quad \text{(C.15)}$$

Since the value of the thermocouple uncertainty was assumed constant as explained above; equation C.15 simplified to

$$\delta\bar{T}_{i,a,o} = \left[\frac{\delta T^2}{n}\right]^{\frac{1}{2}} \quad \text{(C.16)}$$

Equation C.16 was used to calculate the uncertainty of average ambient air temperature, average inlet air temperature and average outlet air temperature.

AppendixC.11. Uncertainty of the temperature difference between ambient and inlet

In the calculation of uncertainty of air mass flow rate, the uncertainty of the temperature difference between ambient air temperature and inlet air temperature needs to be calculated.

$$\Delta T_{i,a} = \bar{T}_i - \bar{T}_a \quad \text{(C.17)}$$

$$\delta\Delta T_{i,a} = \left[\left(\frac{\partial\Delta T_{i,a}}{\partial\bar{T}_i} w_{\bar{T}_i}\right)^2 + \left(-\frac{\partial\Delta T_{i,a}}{\partial\bar{T}_a} w_{\bar{T}_a}\right)^2\right]^{\frac{1}{2}} \quad \text{(C.18)}$$

$$\delta\Delta T_{i,a} = \left[\left(w_{\bar{T}_i}\right)^2 + \left(w_{\bar{T}_a}\right)^2\right]^{\frac{1}{2}} \quad \text{(C.19)}$$

AppendixC.12. Uncertainty of the temperature difference between inlet and outlet

In the calculation of uncertainty of the cooling power evolution of the PCM-air heat exchanger, the uncertainty of the temperature difference between inlet air temperature and outlet air temperature needs to be calculated.

$$\delta\Delta T_{i,o} = \left[\left(w_{\bar{T}_i}\right)^2 + \left(w_{\bar{T}_o}\right)^2\right]^{\frac{1}{2}} \quad \text{(C.20)}$$

AppendixC.13. Uncertainty of the air mass flow rate

$$\dot{m}_{air} = \frac{V^2}{rC_{p,air}(\bar{T}_i - \bar{T}_a)} \quad \text{(C.21)}$$

$$\delta\dot{m}_{air} = \left[\left(\frac{\partial\dot{m}_{air}}{\partial V}w_V\right)^2 + \left(\frac{\partial\dot{m}_{air}}{\partial r}w_r\right)^2 + \left(\frac{\partial\dot{m}_{air}}{\partial C_{p,air}}w_{C_{p,air}}\right)^2 + \left(\frac{\partial\dot{m}_{air}}{\partial(\bar{T}_i-\bar{T}_a)}w_{(\bar{T}_i-\bar{T}_a)}\right)^2\right]^{\frac{1}{2}} \quad \text{(C.22)}$$

$$\delta\dot{m}_{air} = \Big[r^{-1}{C_{p,air}}^{-1}(\bar{T}_i - \bar{T}_a)^{-1}(2Vw_V)^2 + V^2{C_{p,air}}^{-1}(\bar{T}_i - \bar{T}_a)^{-1}(-r^{-2}w_r)^2 + V^2r^{-1}(\bar{T}_i - \bar{T}_a)^{-1}\left(-{C_{p,air}}^{-2}w_{C_{p,air}}\right)^2 + V^2r^{-1}{C_{p,air}}^{-1}\left(-(\bar{T}_i - \bar{T}_a)^{-2}w_{(\bar{T}_i-\bar{T}_a)}\right)^2\Big]^{\frac{1}{2}} \quad \text{(C.23)}$$

Uncertainty for power evolution of heat exchanger

$$\dot{Q}_\iota = \dot{m}_{air} C_{p,air} (\bar{T}_i - \bar{T}_o) \quad \text{(C.24)}$$

$$\delta \dot{Q}_i = \left[\left(\frac{\partial \dot{Q}_i}{\partial \dot{m}_{air}} w_{\dot{m}_{air}} \right)^2 + \left(\frac{\partial \dot{Q}_i}{\partial C_{p,air}} w_{C_{p,air}} \right)^2 + \left(\frac{\partial \dot{Q}_i}{\partial (\bar{T}_i - \bar{T}_o)} w_{(\bar{T}_i - \bar{T}_o)} \right)^2 \right]^{\frac{1}{2}} \text{(C.25)}$$

$$\delta \dot{Q}_i = \left[C_{p,air} (\bar{T}_i - \bar{T}_o) \left(w_{\dot{m}_{air}} \right)^2 + \dot{m}_{air} (\bar{T}_i - \bar{T}_o) \left(w_{C_{p,air}} \right)^2 + \dot{m}_{air} C_{p,air} \left(w_{(\bar{T}_i - \bar{T}_o)} \right)^2 \right]^{\frac{1}{2}}$$
(C.26)

APPENDIX D. MELTING BEHAVIOUR

This Appendix gives all the experimental results for the melting behaviours of the PCMs studied.

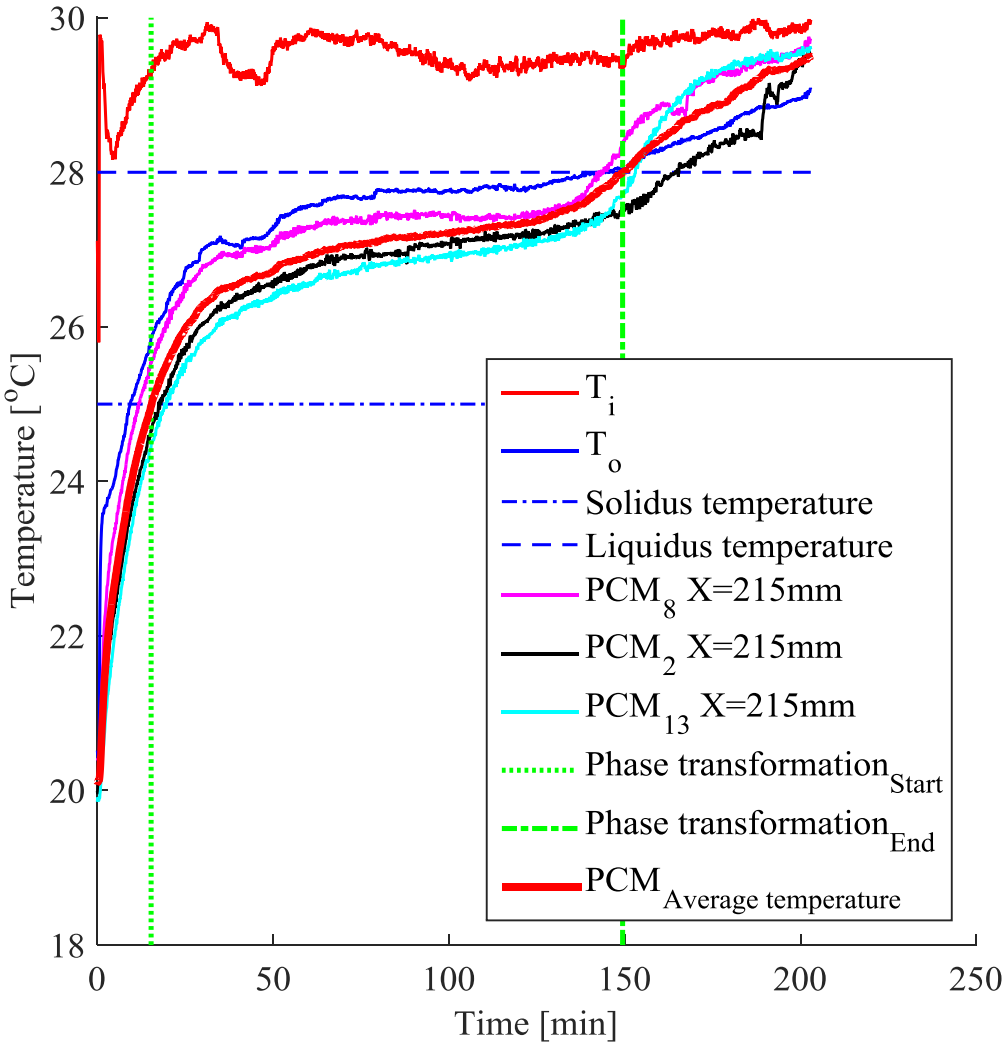

Figure D.1. PCM temperature distribution during melting for RT27 module for an inlet air temperature of 30 °C and air flow rate of 0.03 kg/s.

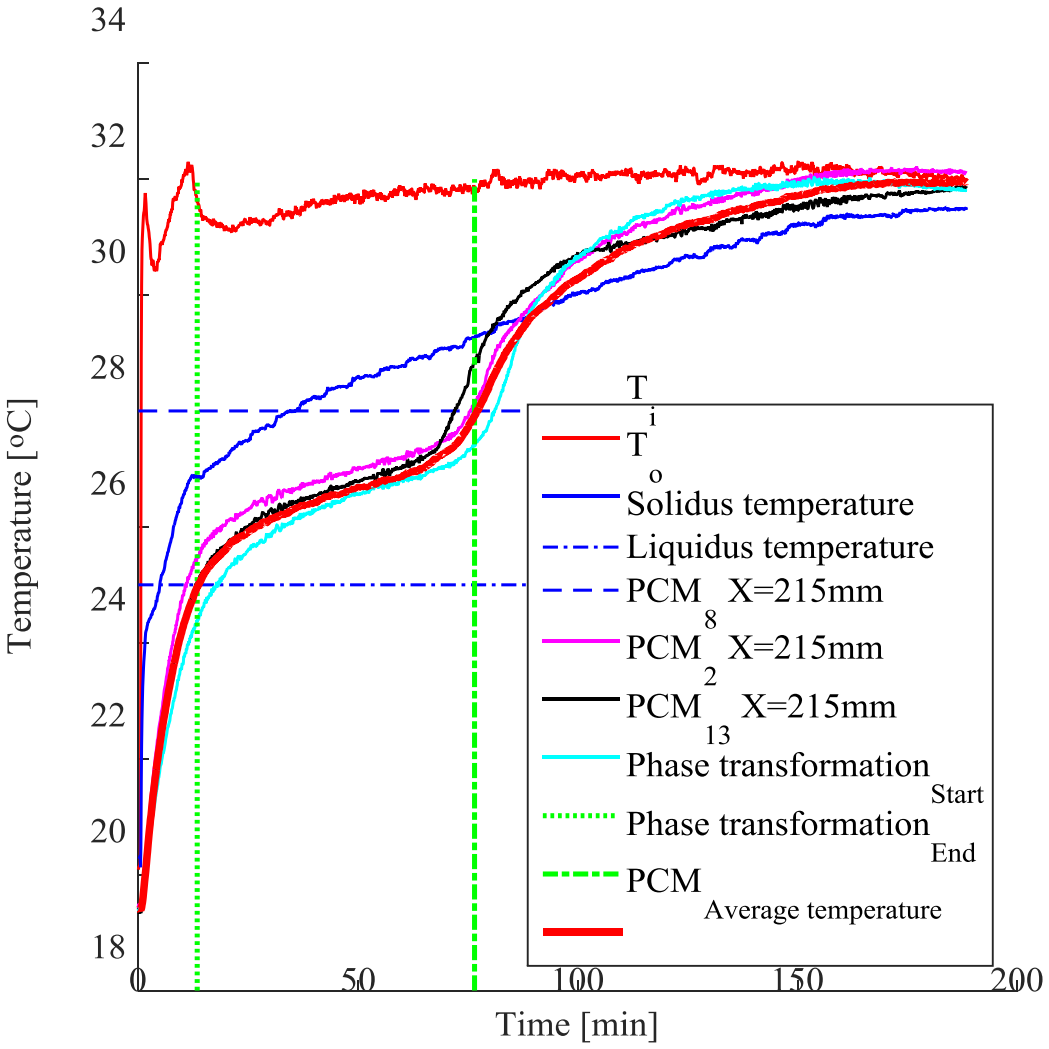

Figure D.2. PCM temperature distribution during melting for RT27 module for an inlet air temperature of 32 °C and air flow of 0.03 kg/s.

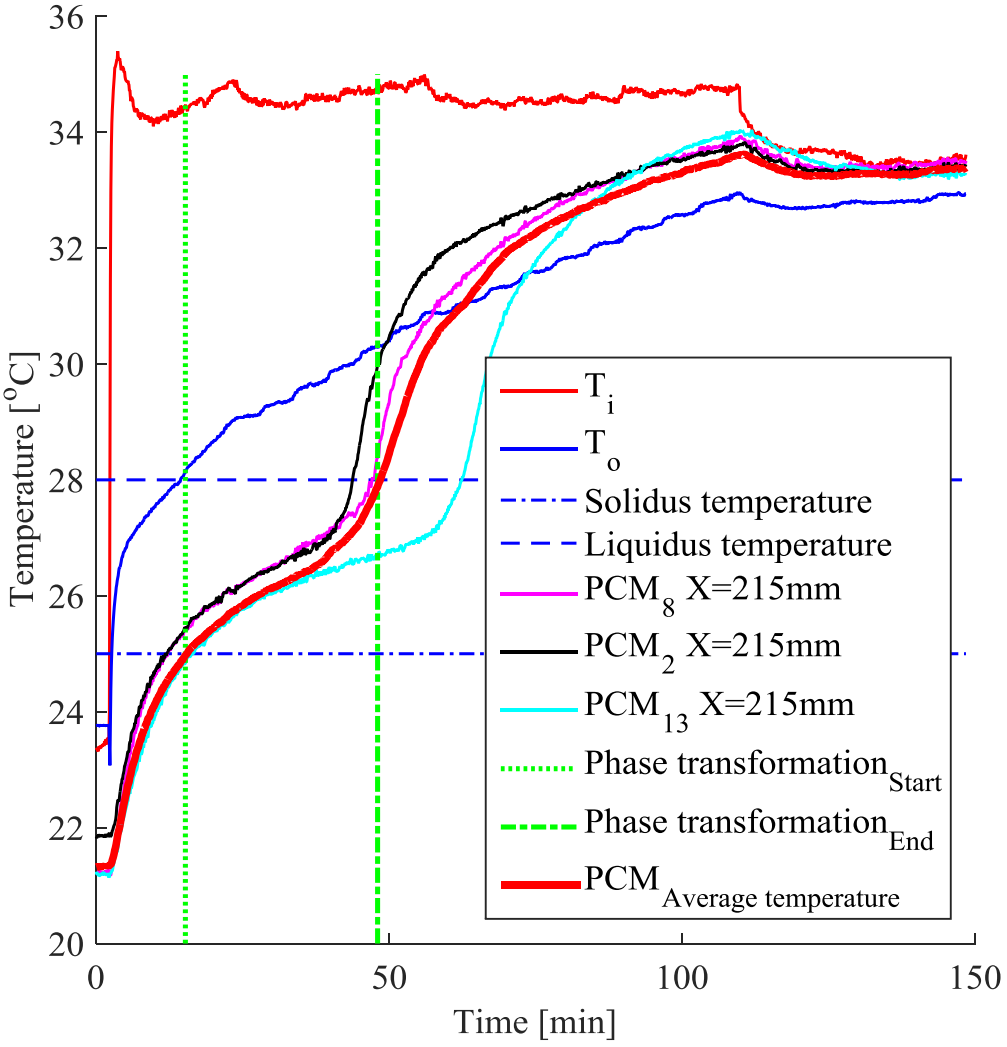

Figure D.3. PCM temperature distribution during melting for RT27 module for an inlet air temperature of 35 °C and air flow of 0.03 kg/s.

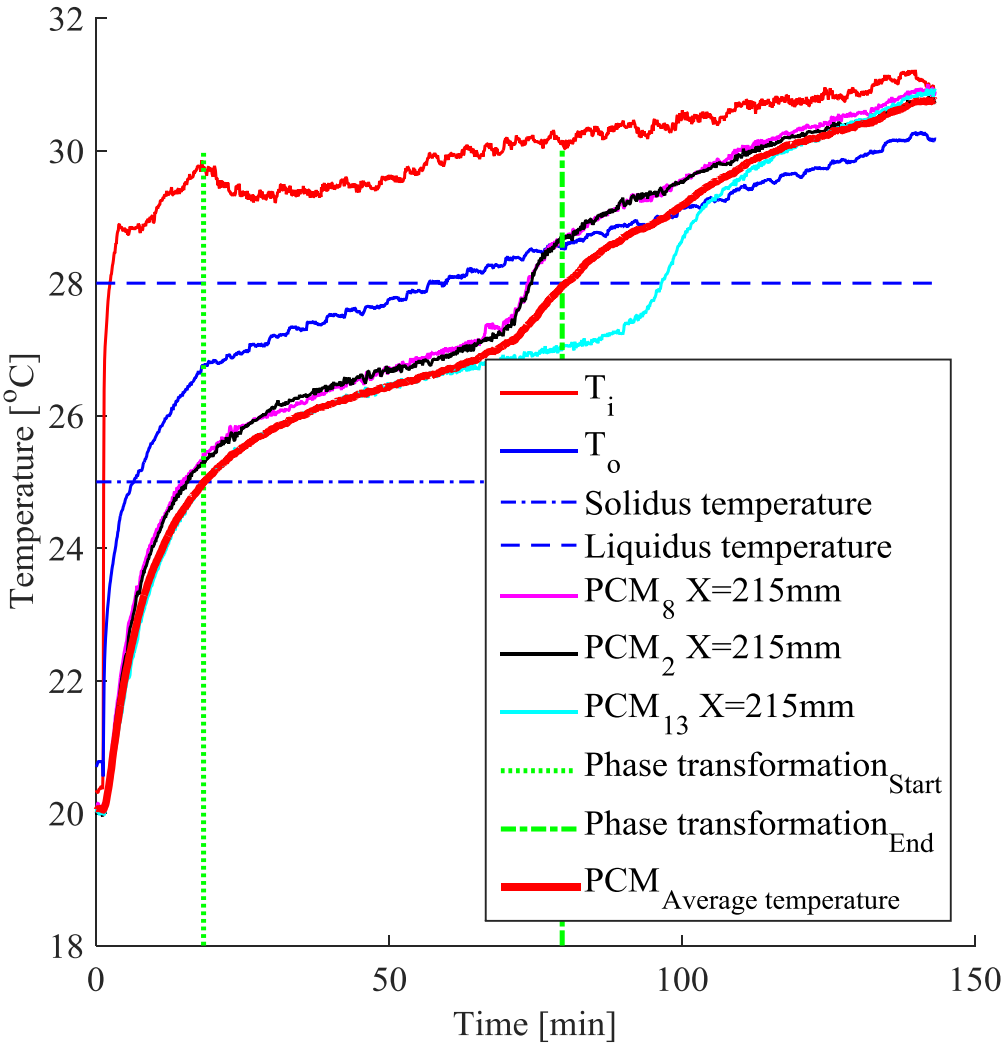

Figure D.4. PCM temperature distribution during melting for RT27 module for an inlet air temperature of 30 °C and air flow of 0.05 kg/s.

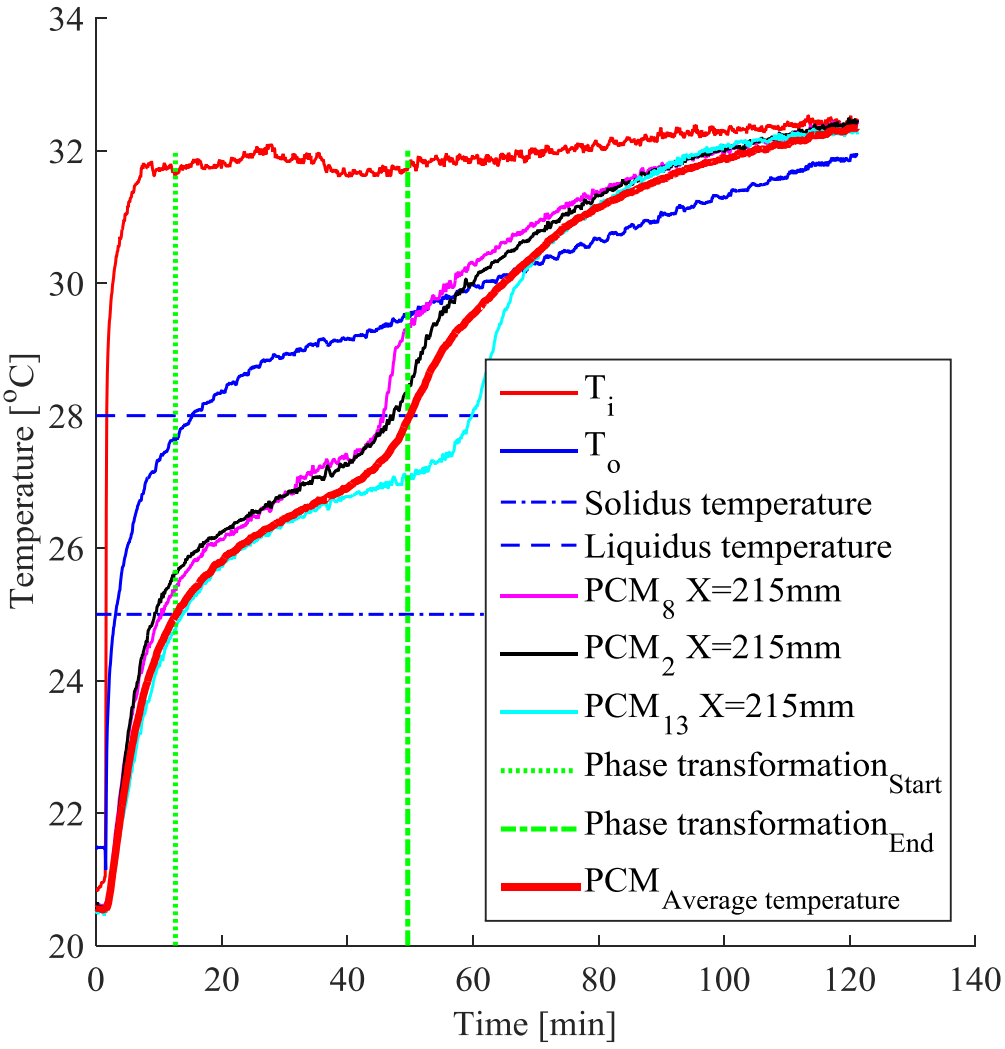

Figure D.5. PCM temperature distribution during melting for RT27 module for an inlet air temperature of 32 °C and air flow of 0.05 kg/s.

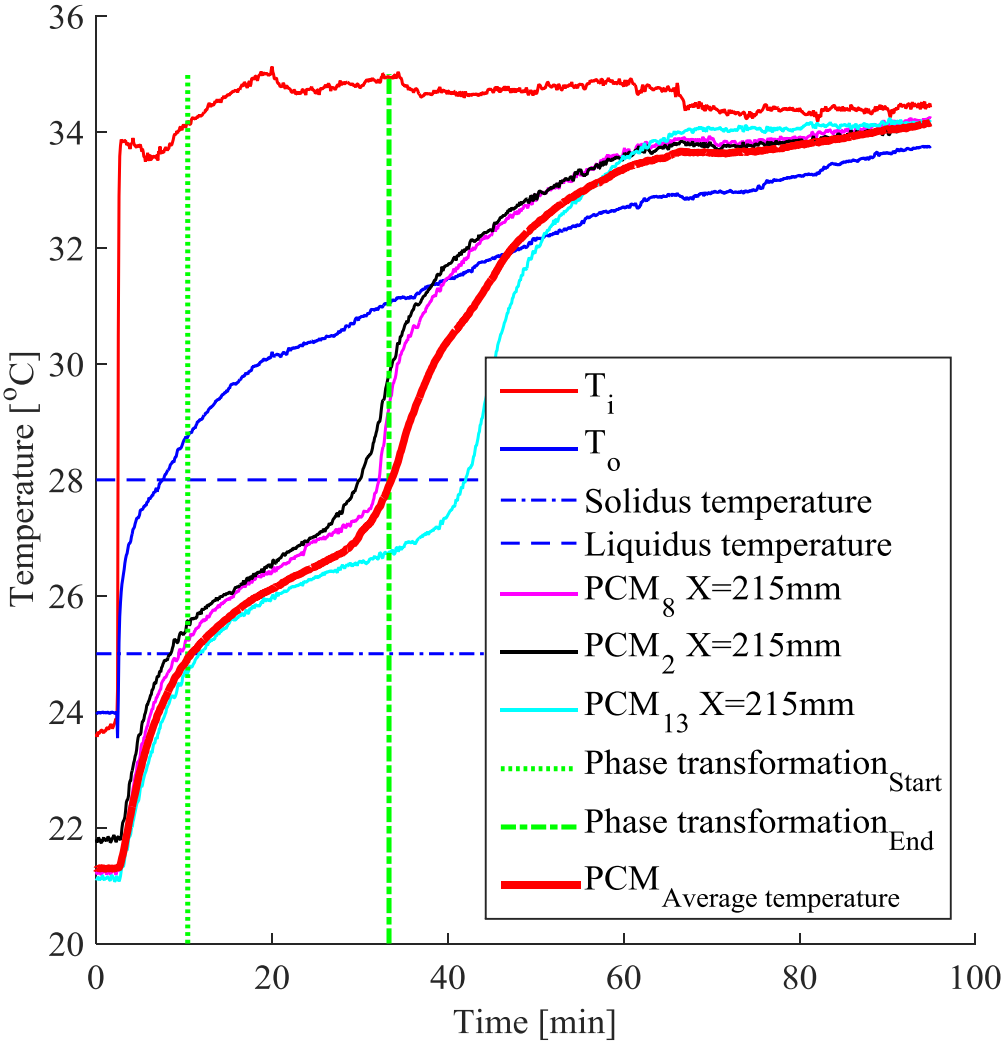

Figure D.6. PCM temperature distribution during melting for RT27 module for an inlet air temperature of 35 °C and air flow of 0.05 kg/s.

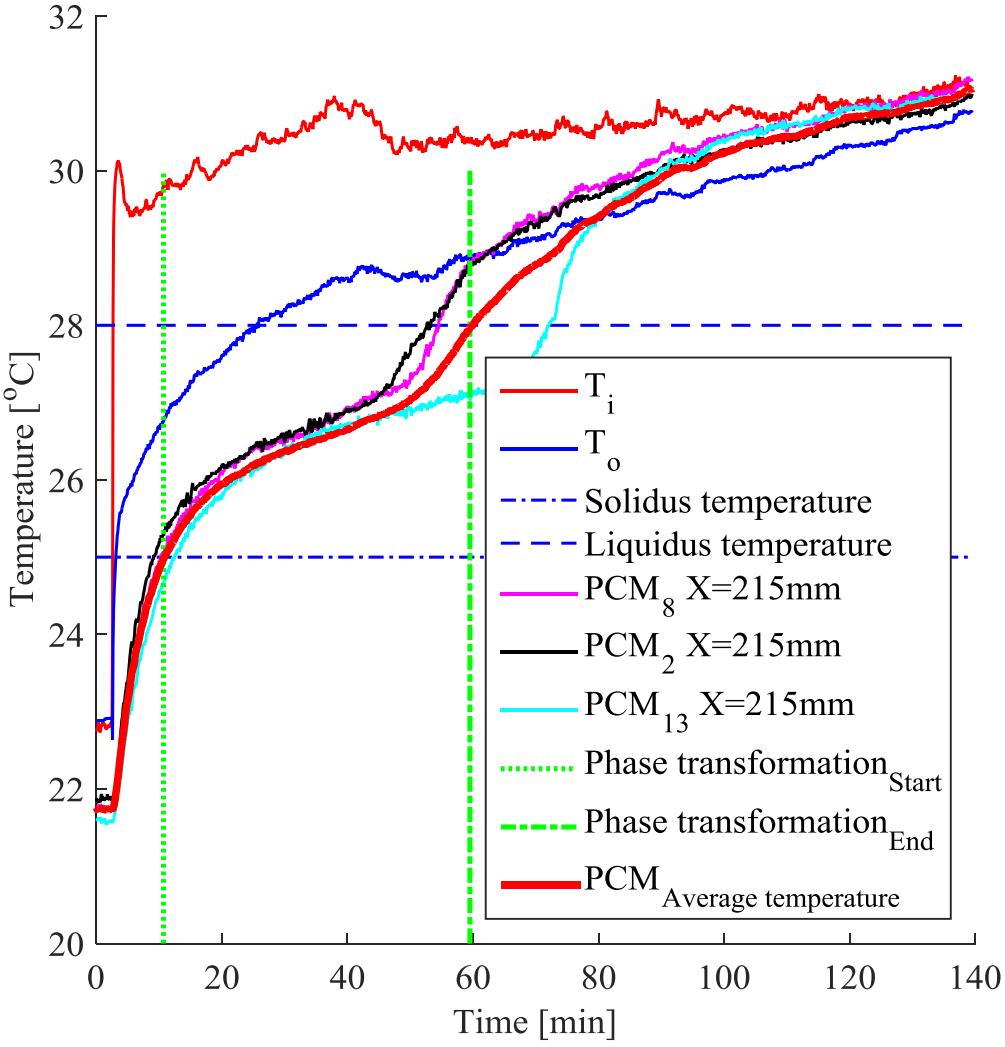

Figure D.7. PCM temperature distribution during melting for RT27 module for an inlet air temperature of 30 °C and air flow of 0.06 kg/s.

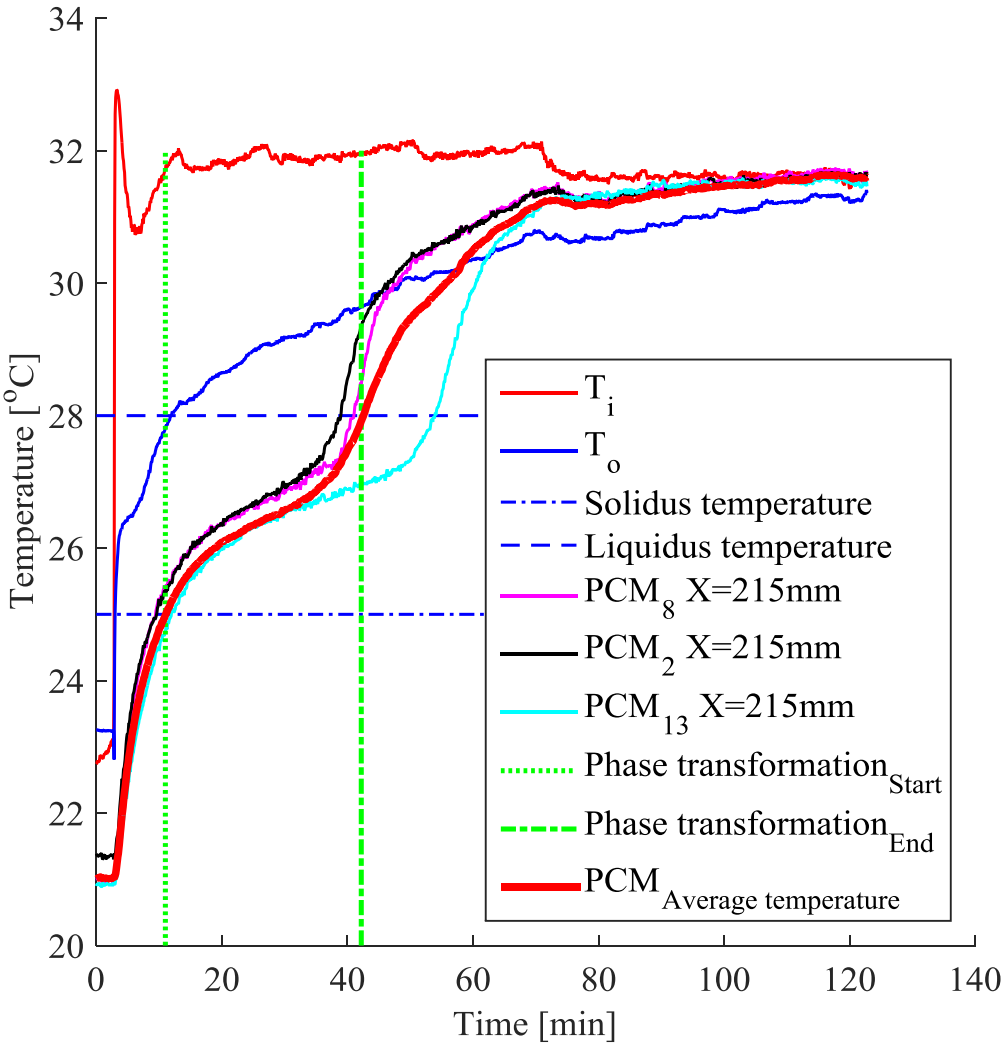

Figure D.8. PCM temperature distribution during melting for RT27 module for an inlet air temperature of 32 °C and air flow of 0.06 kg/s.

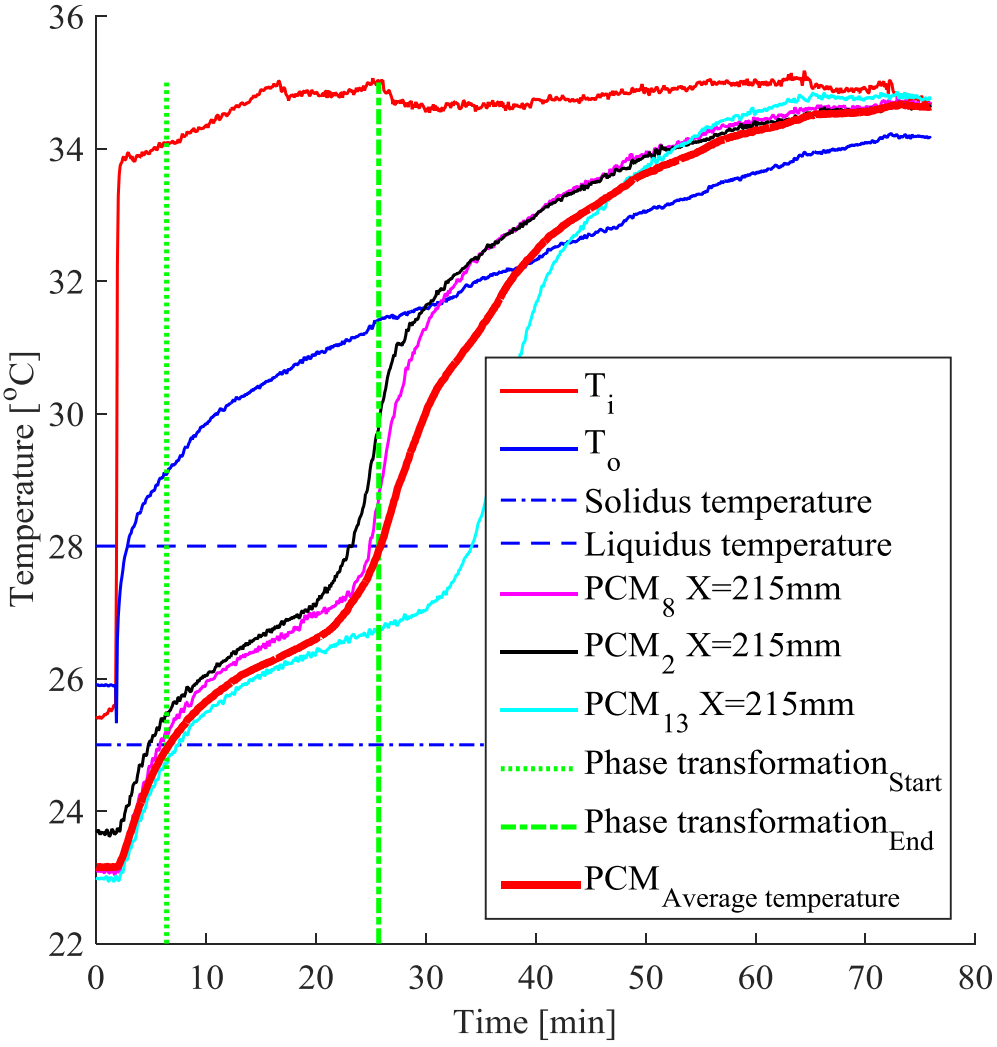

Figure D.9. PCM temperature distribution during melting for RT27 module for an inlet air temperature of 35 °C and air flow of 0.06 kg/s.

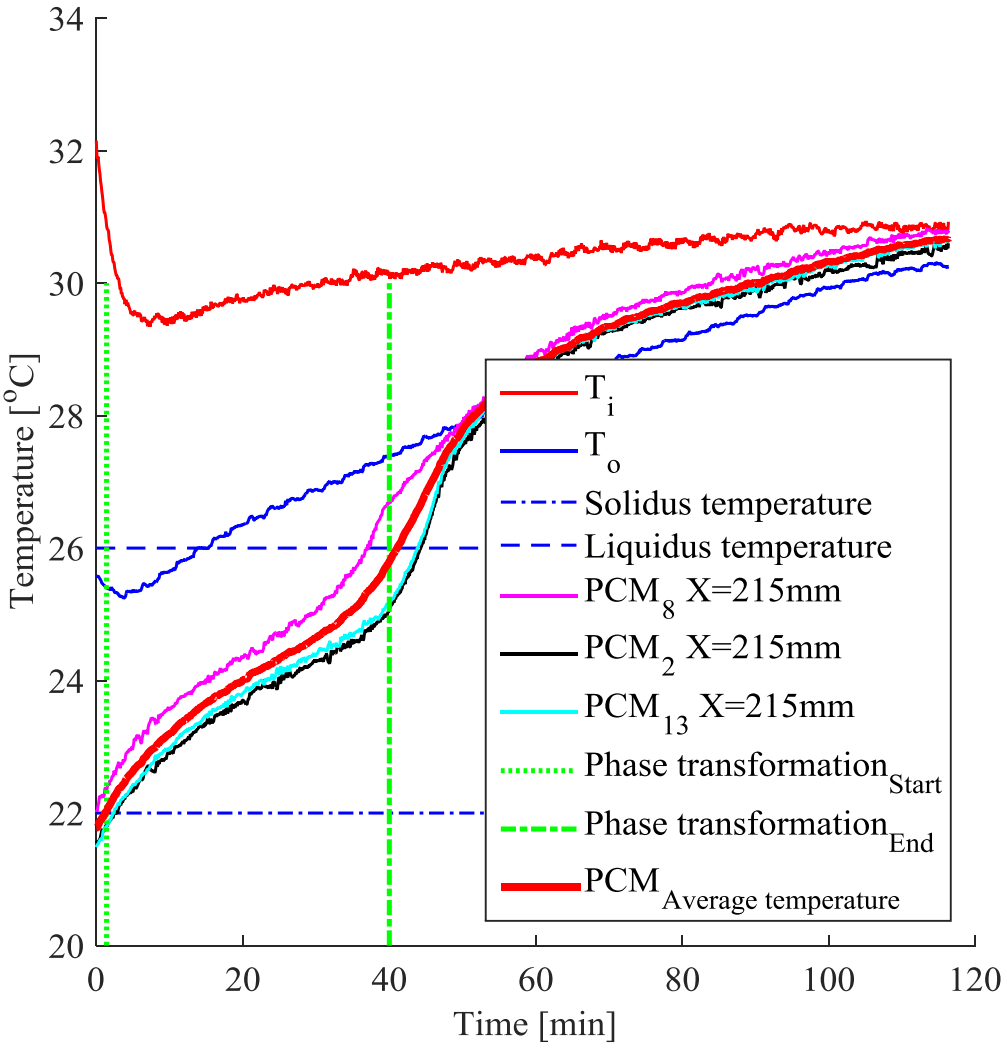

Figure D.10. PCM temperature distribution during melting for RT25 module for an inlet air temperature of 30 °C and air flow of 0.03 kg/s.

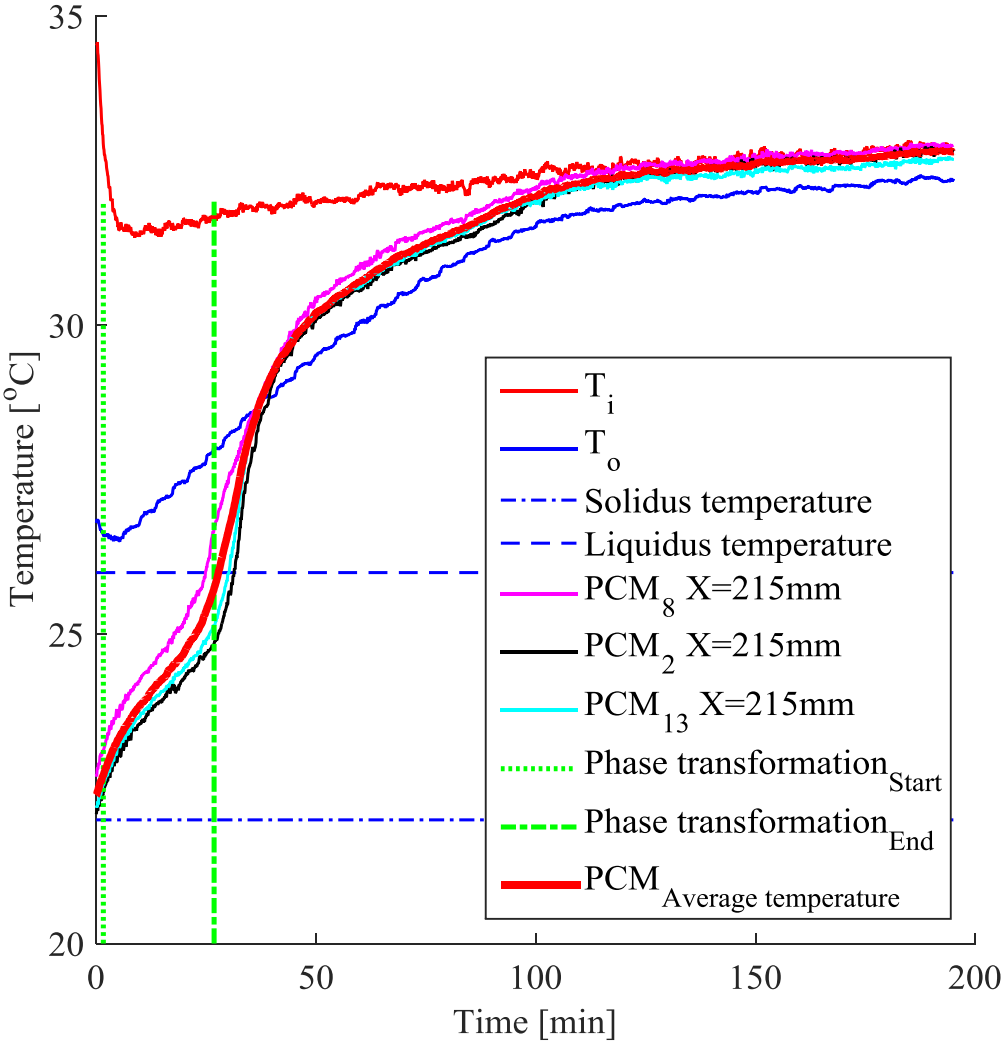

Figure D.11. PCM temperature distribution during melting for RT25 module for an inlet air temperature of 32 °C and air flow of 0.03 kg/s.

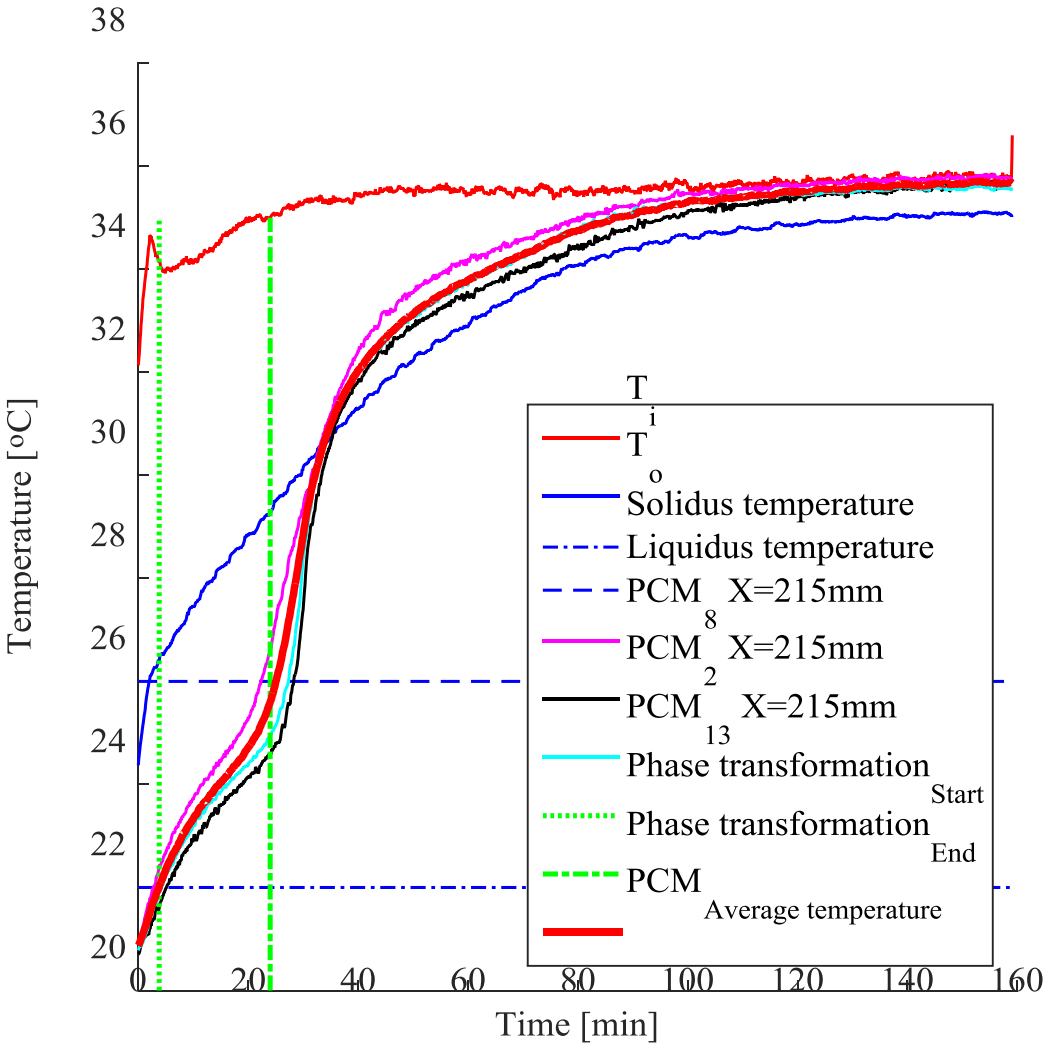

Figure D.12. PCM temperature distribution during melting for RT25 module for an inlet air temperature of 35 °C and air flow of 0.03 kg/s.

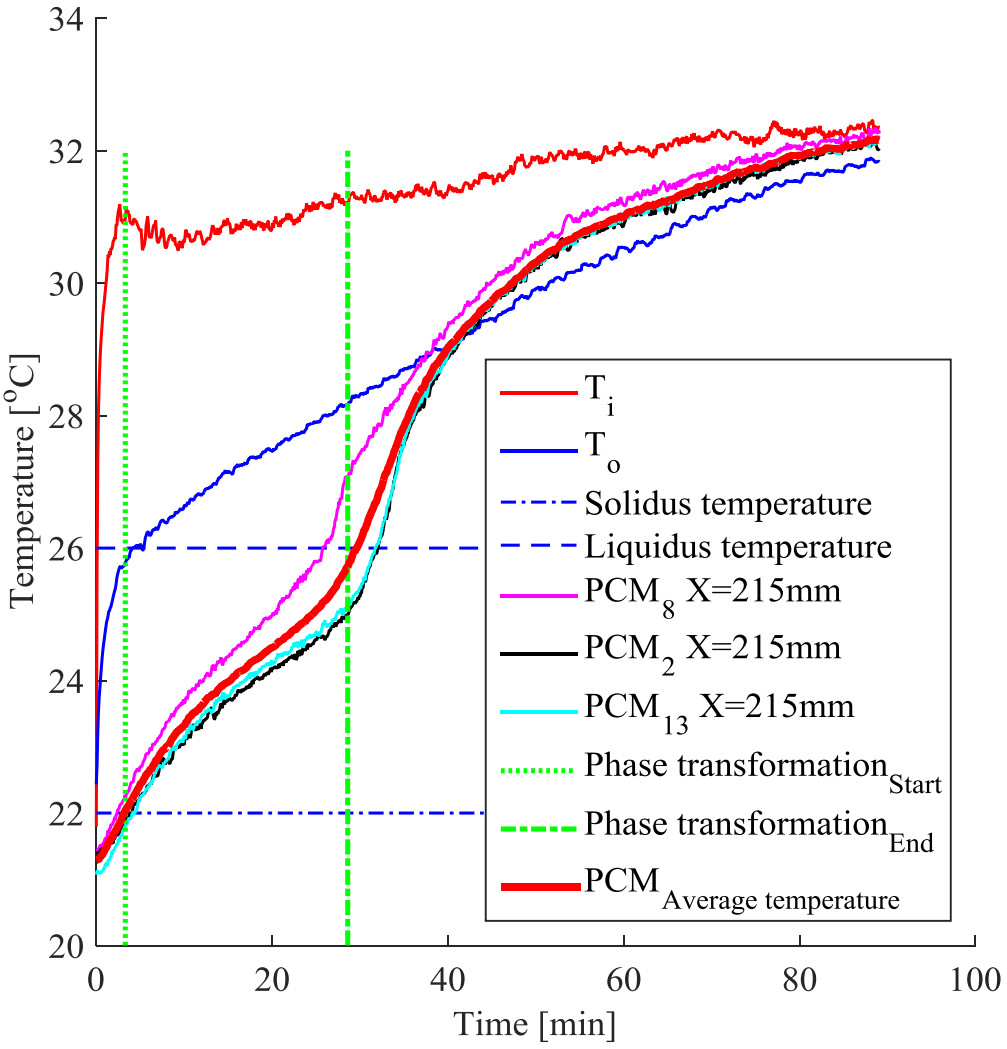

Figure D.13. PCM temperature distribution during melting for RT25 module for an inlet air temperature of 30 °C and air flow of 0.05 kg/s.

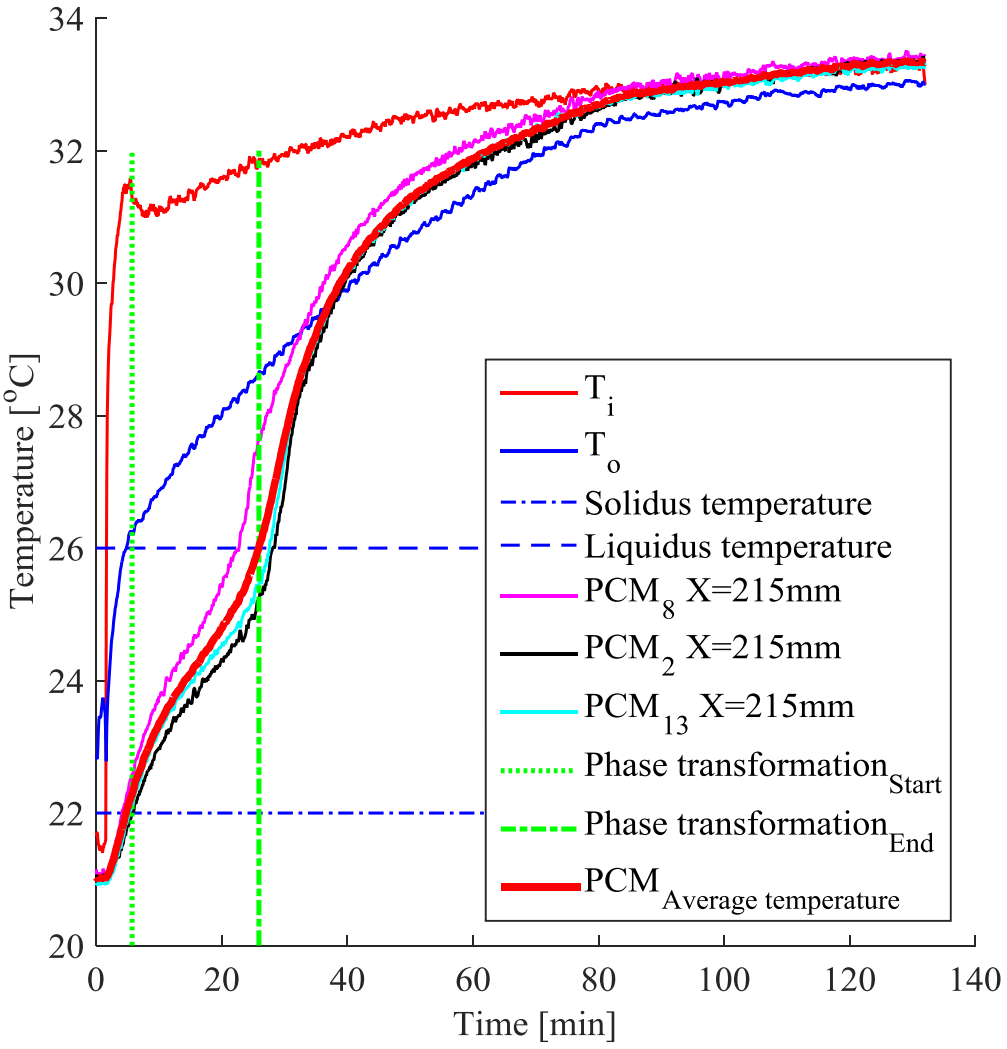

Figure D.14. PCM temperature distribution during melting for RT25 module for an inlet air temperature of 32 °C and air flow of 0.05 kg/s.

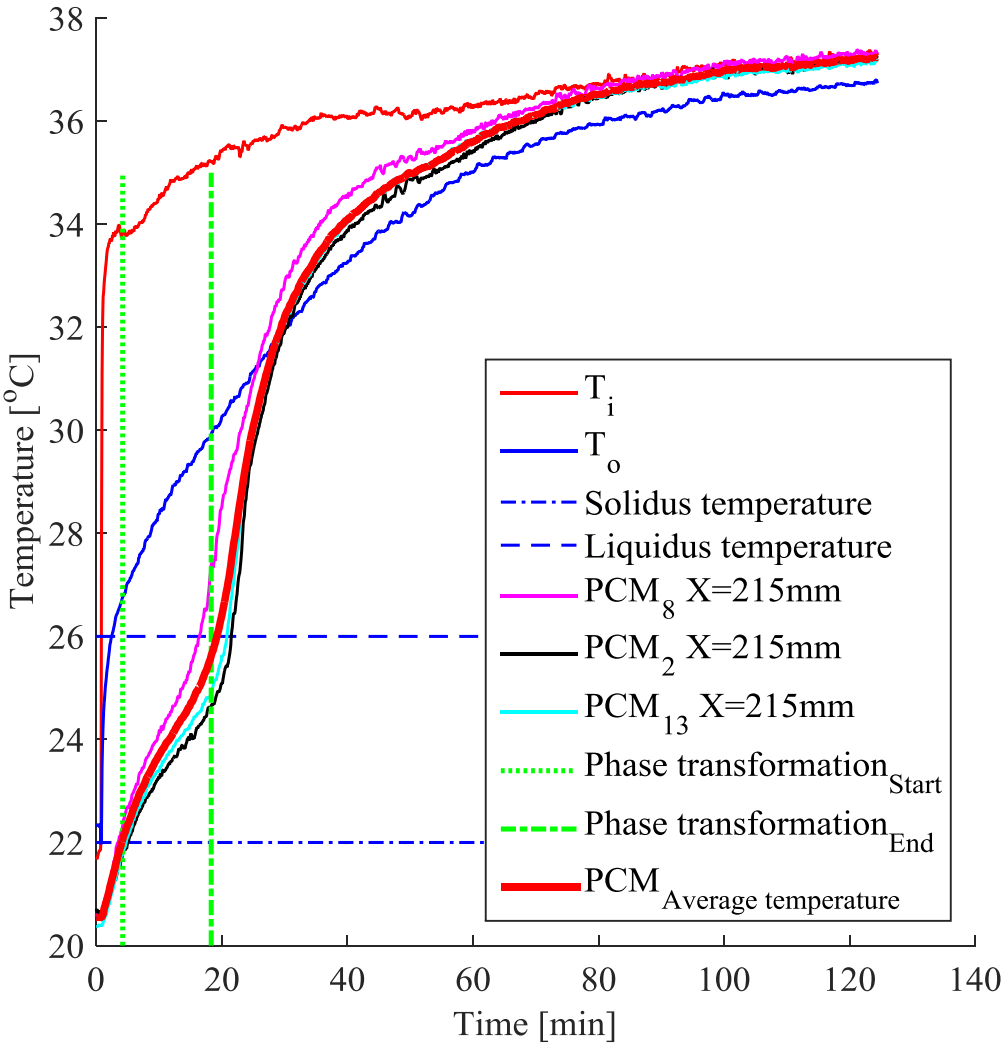

Figure D.15. PCM temperature distribution during melting for RT25 module for an inlet air temperature of 35 °C and air flow of 0.05 kg/s.

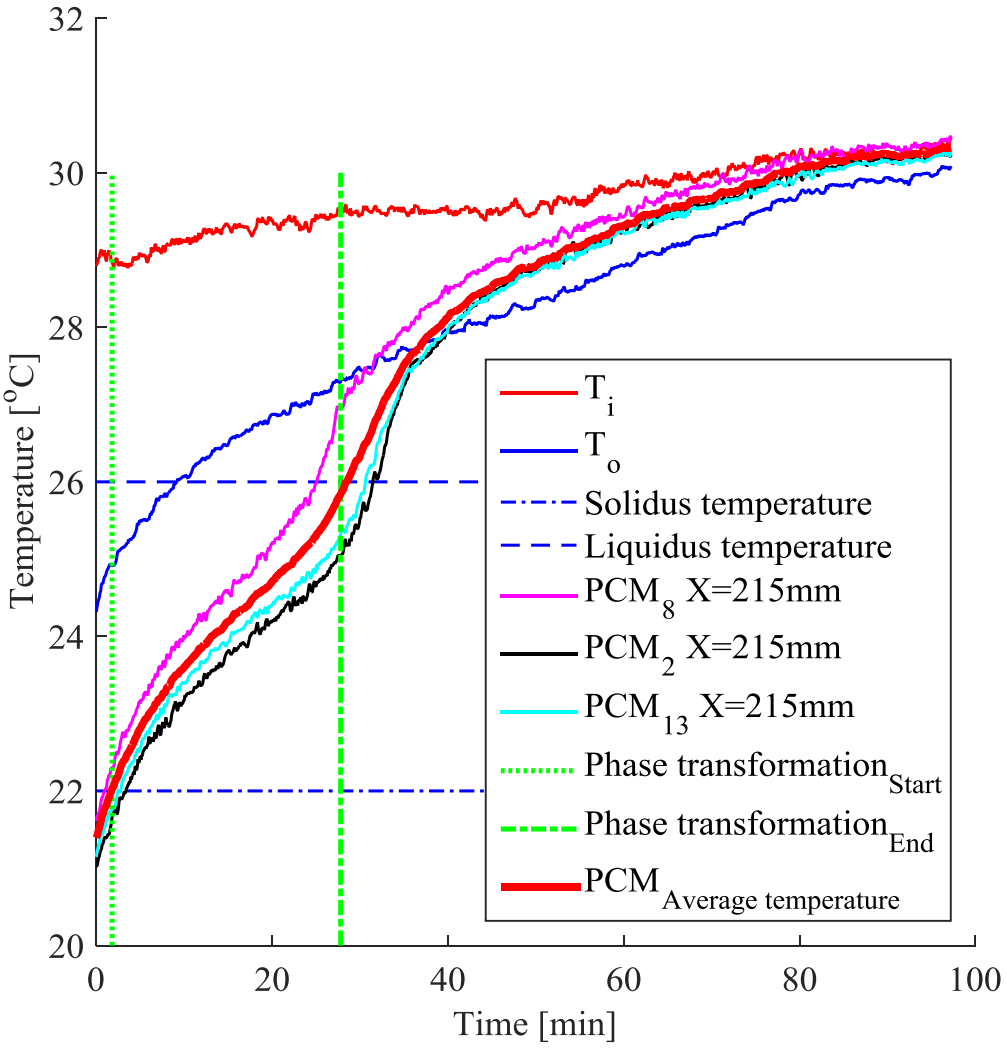

Figure D.16. PCM temperature distribution during melting for RT25 module for an inlet air temperature of 30 °C and air flow of 0.06 kg/s.

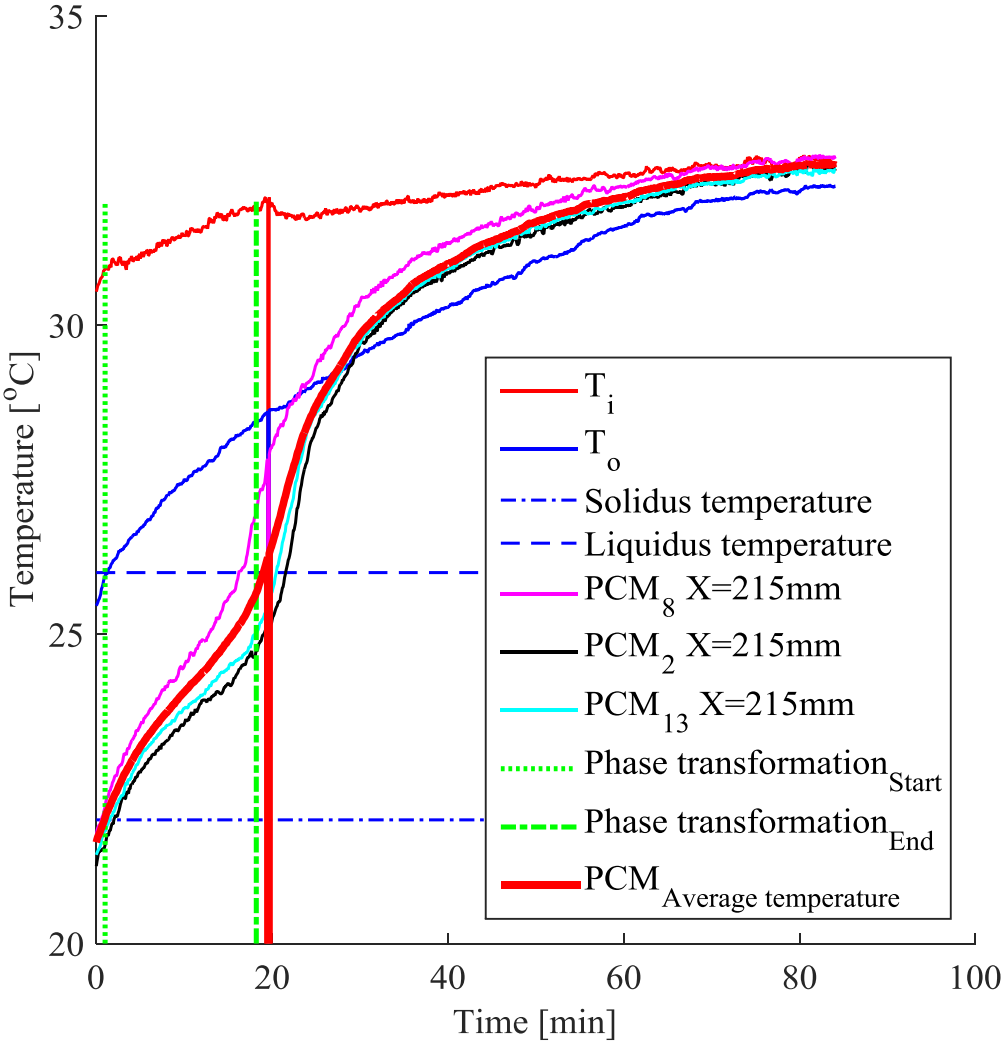

Figure D.17. PCM temperature distribution during melting for RT25 module for an inlet air temperature of 32 °C and air flow of 0.06 kg/s.

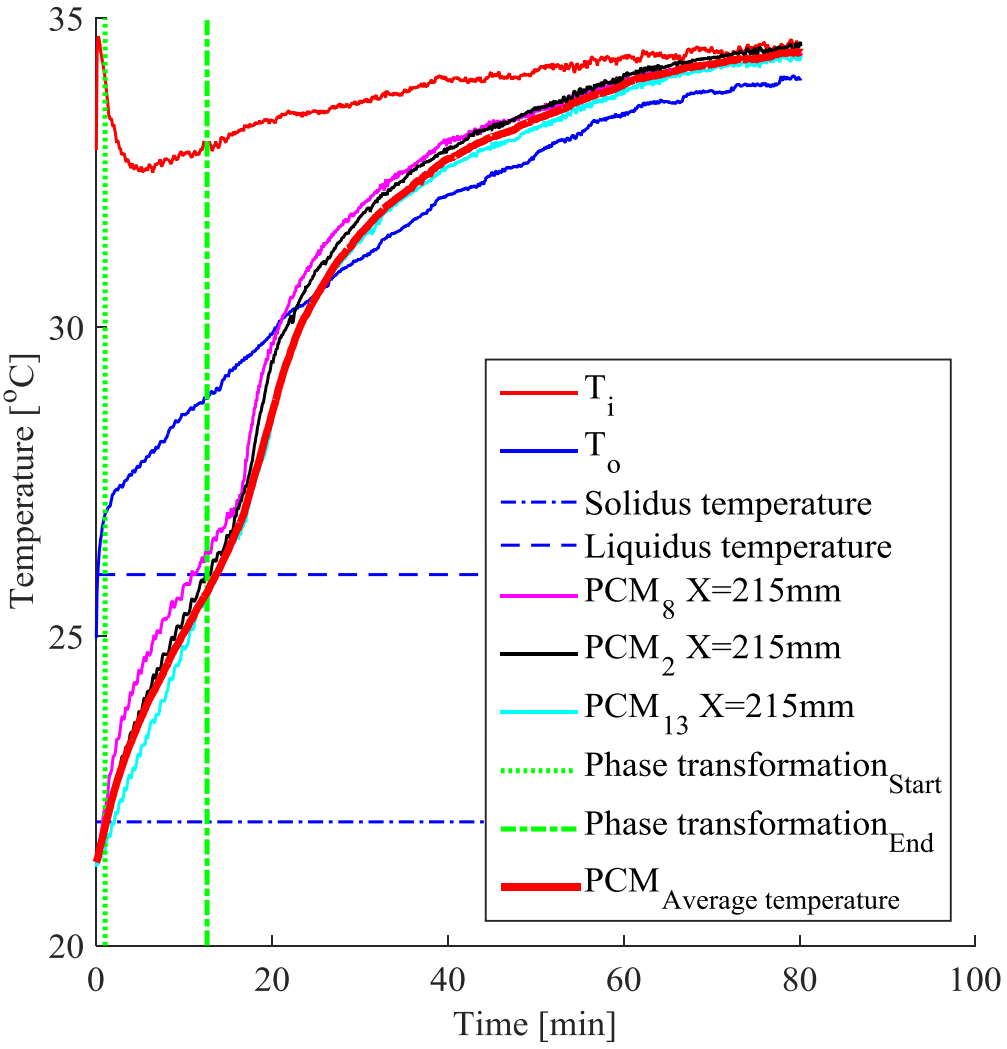

Figure D.18. PCM temperature distribution during melting for RT25 module for an inlet air temperature of 35 °C and air flow of 0.06 kg/s.

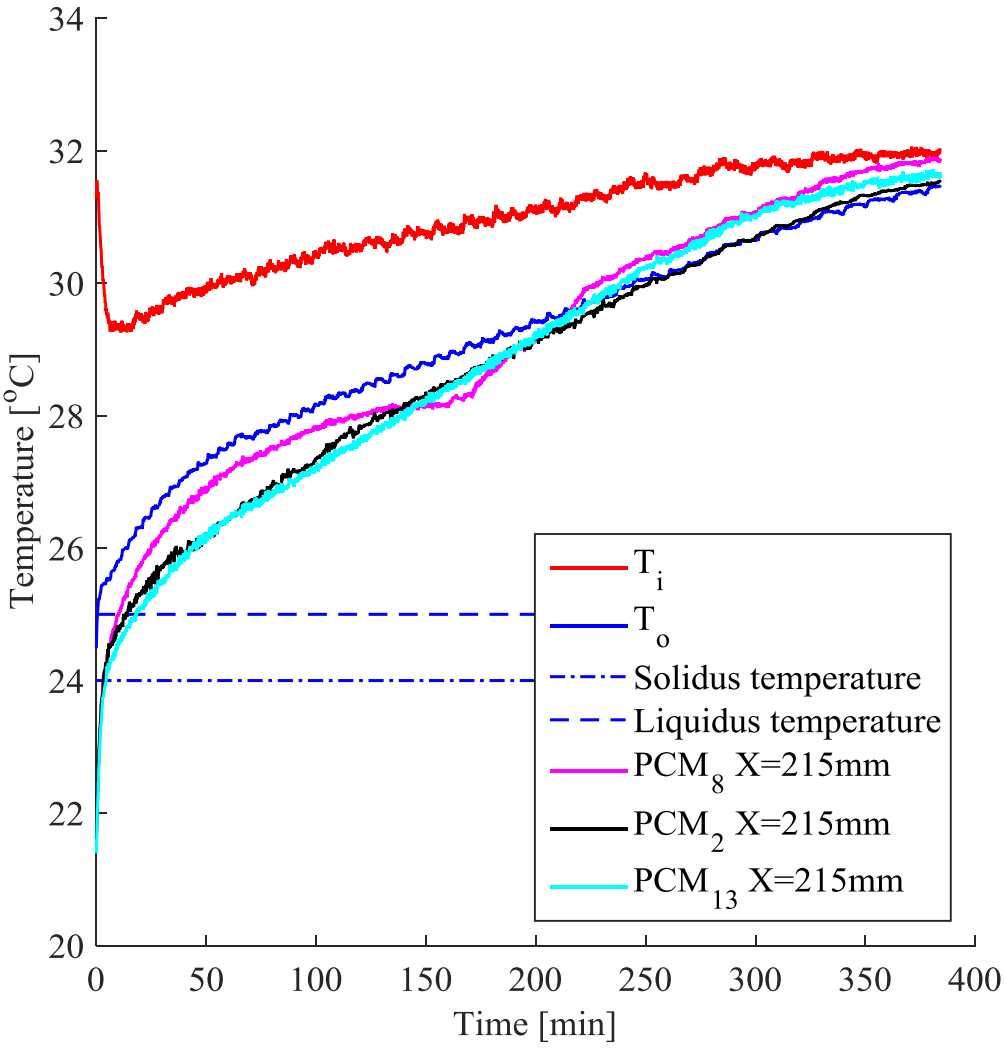

Figure D.19. PCM temperature distribution during melting for SP24E module for an inlet air temperature of 30 °C and air flow of 0.03 kg/s.

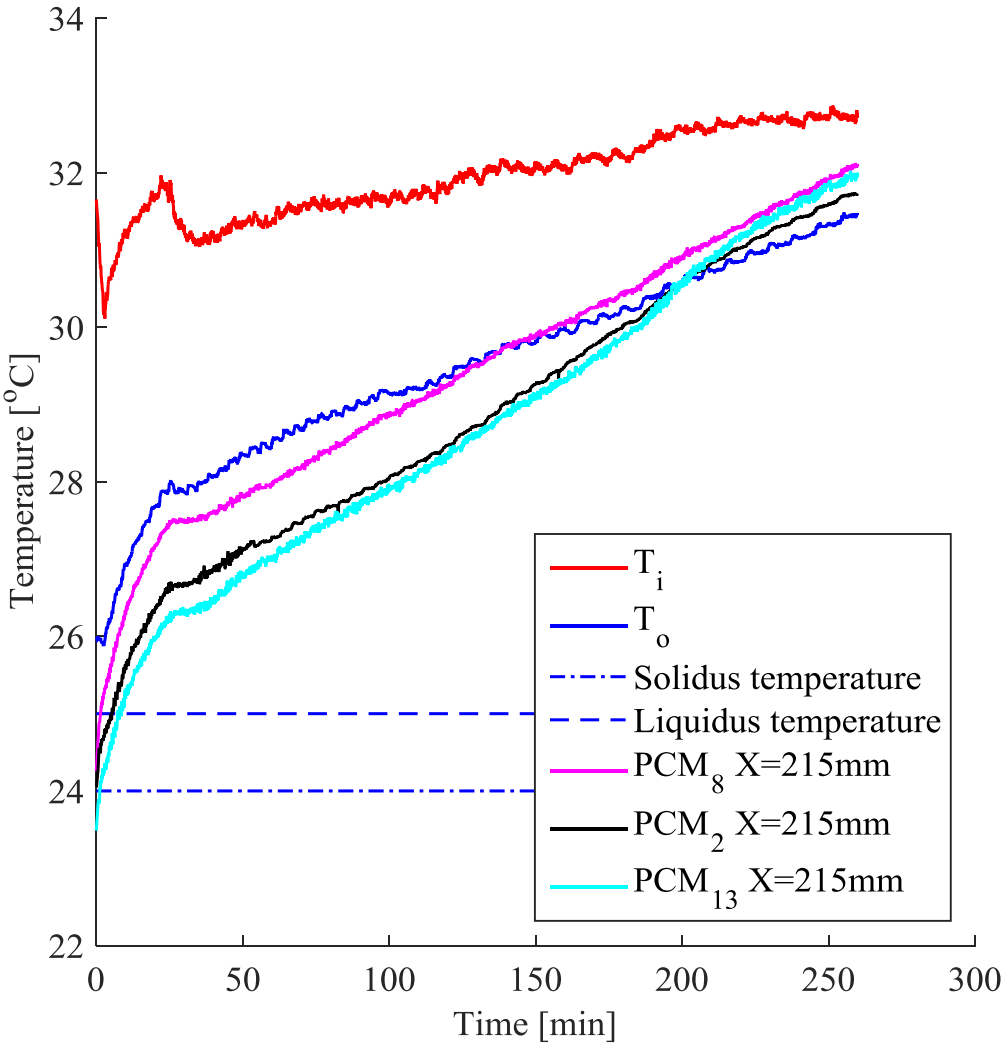

Figure D.20. PCM temperature distribution during melting for SP24E module for an inlet air temperature of 32 °C and air flow of 0.03 kg/s.

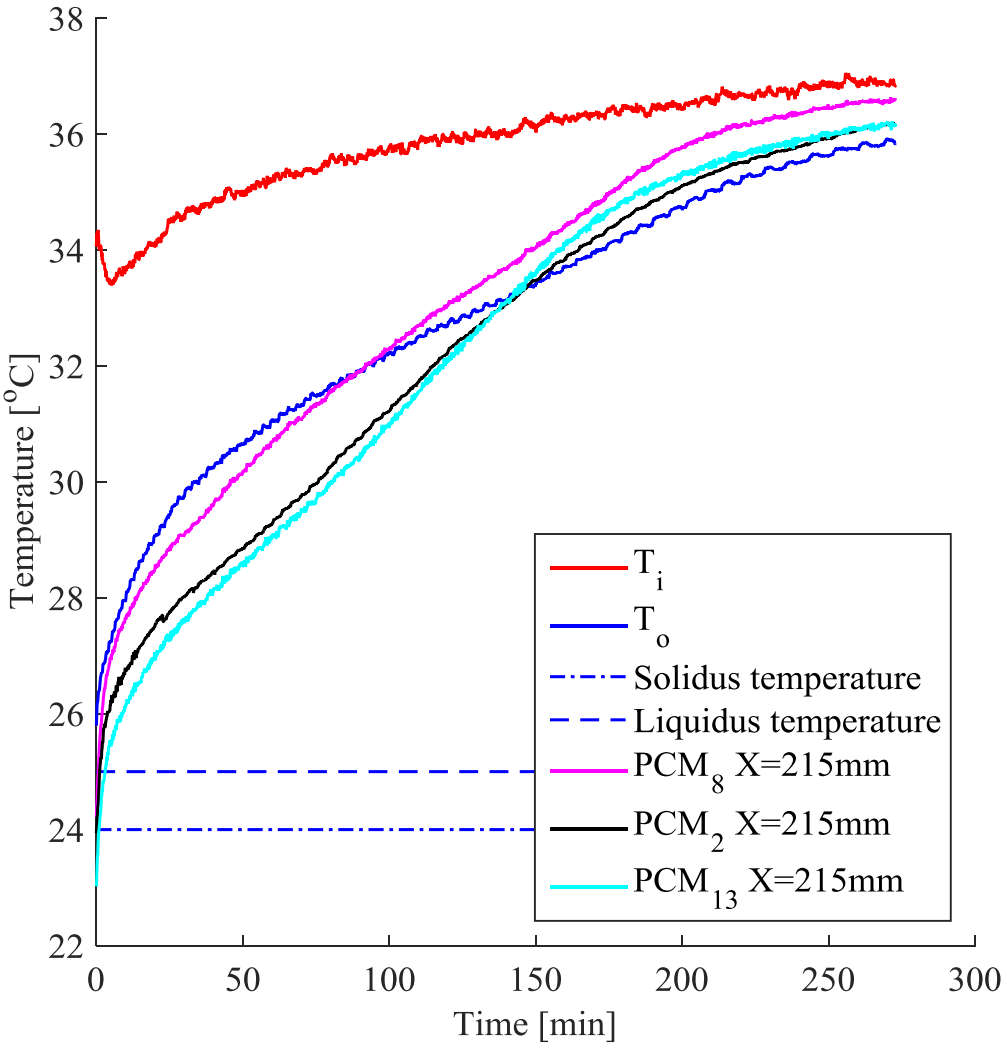

Figure D.21. PCM temperature distribution during melting for SP24E module for an inlet air temperature of 35 °C and air flow of 0.03 kg/s.

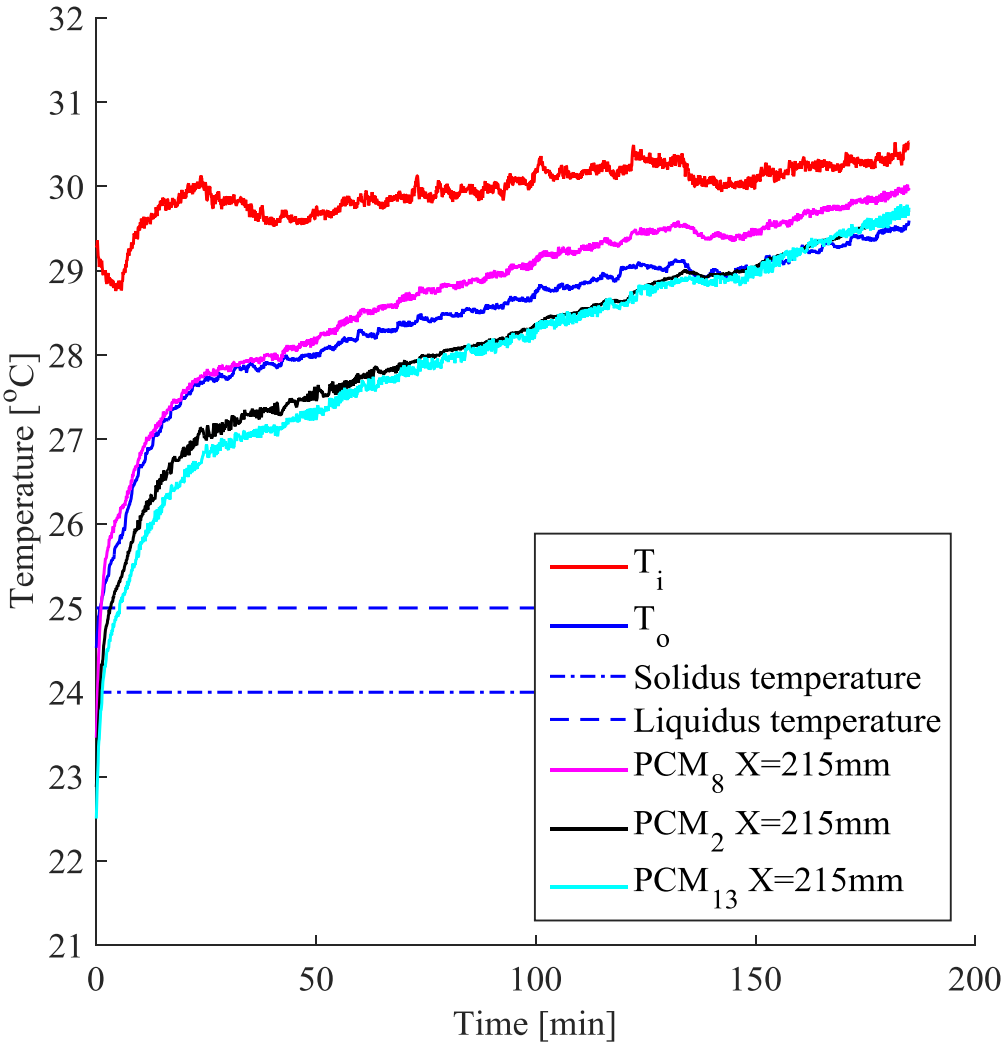

Figure D.22. PCM temperature distribution during melting for SP24E module for an inlet air temperature of 30 °C and air flow of 0.05 kg/s.

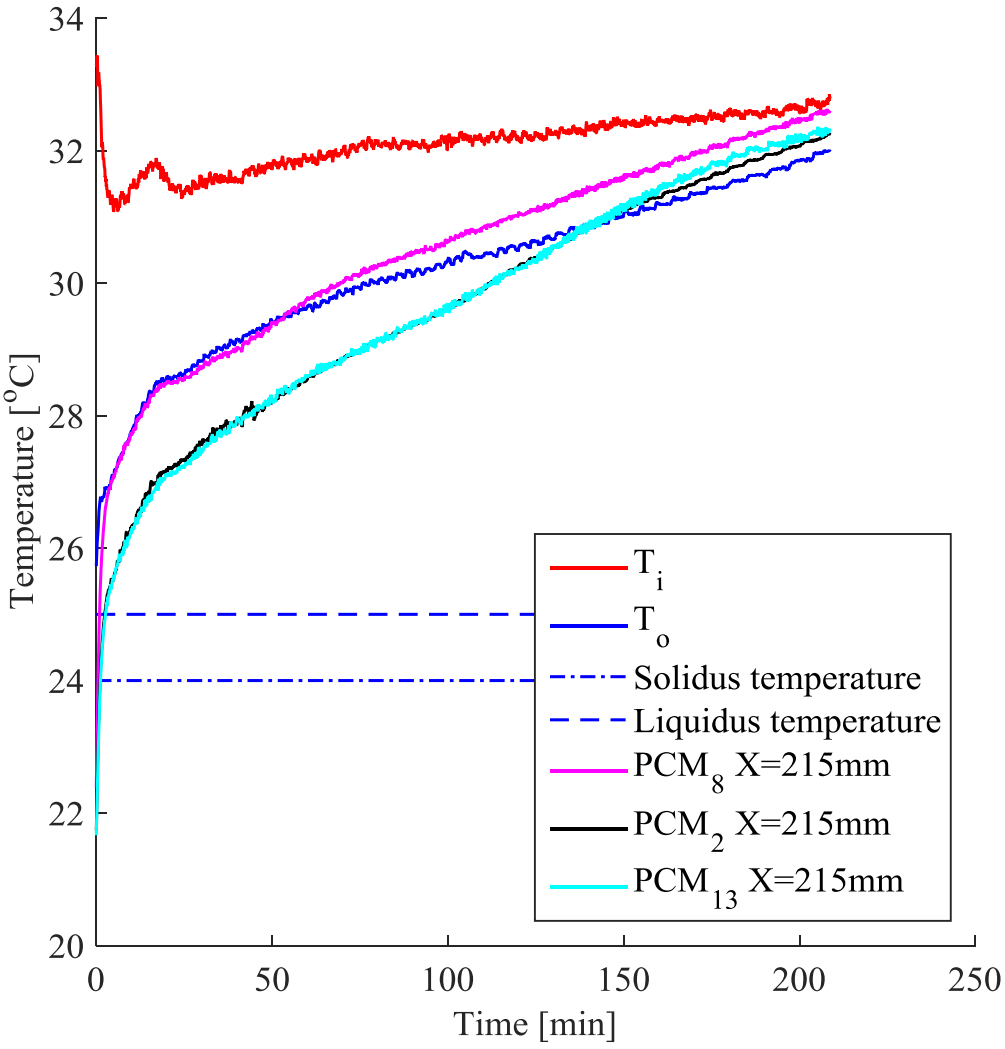

Figure D.23. PCM temperature distribution during melting for SP24E module for an inlet air temperature of 32 °C and air flow of 0.05 kg/s.

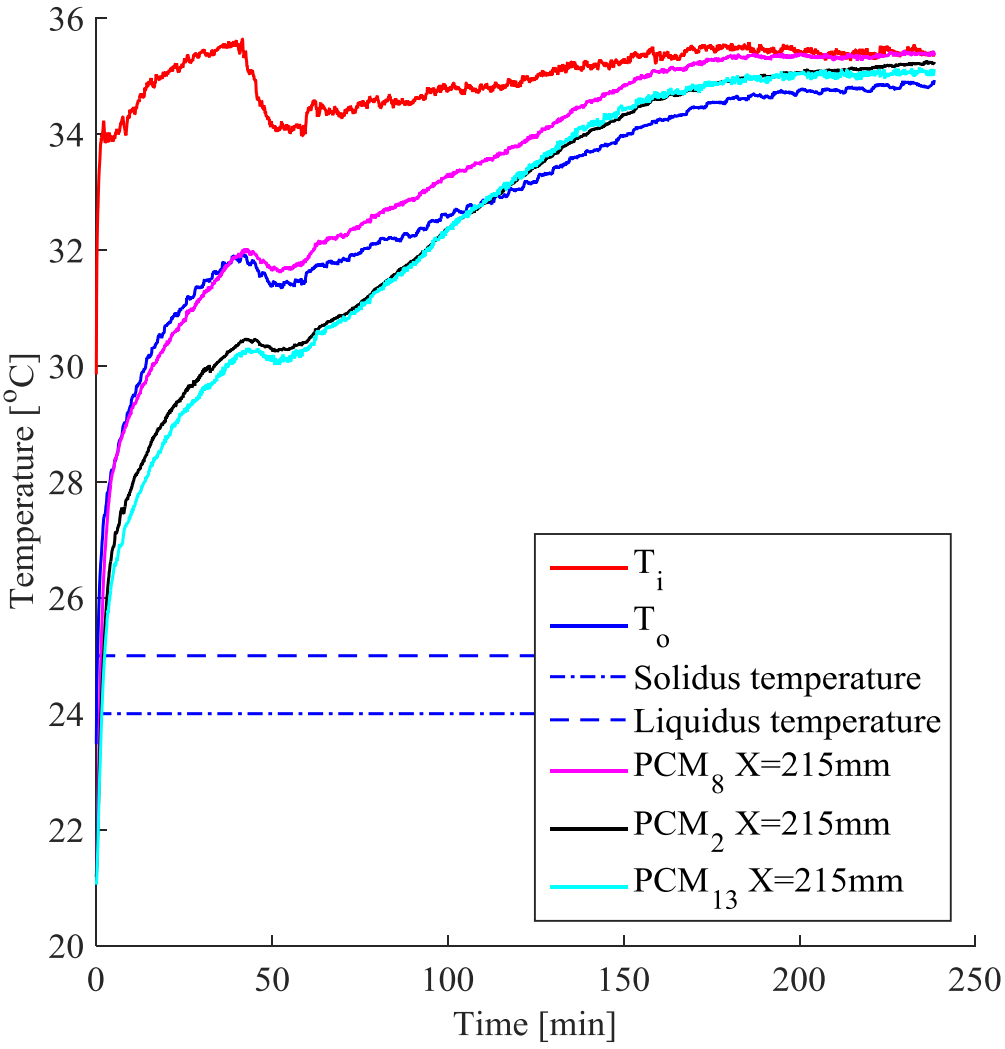

Figure D.24. PCM temperature distribution during melting for SP24E module for an inlet air temperature of 35 °C and air flow of 0.05 kg/s.

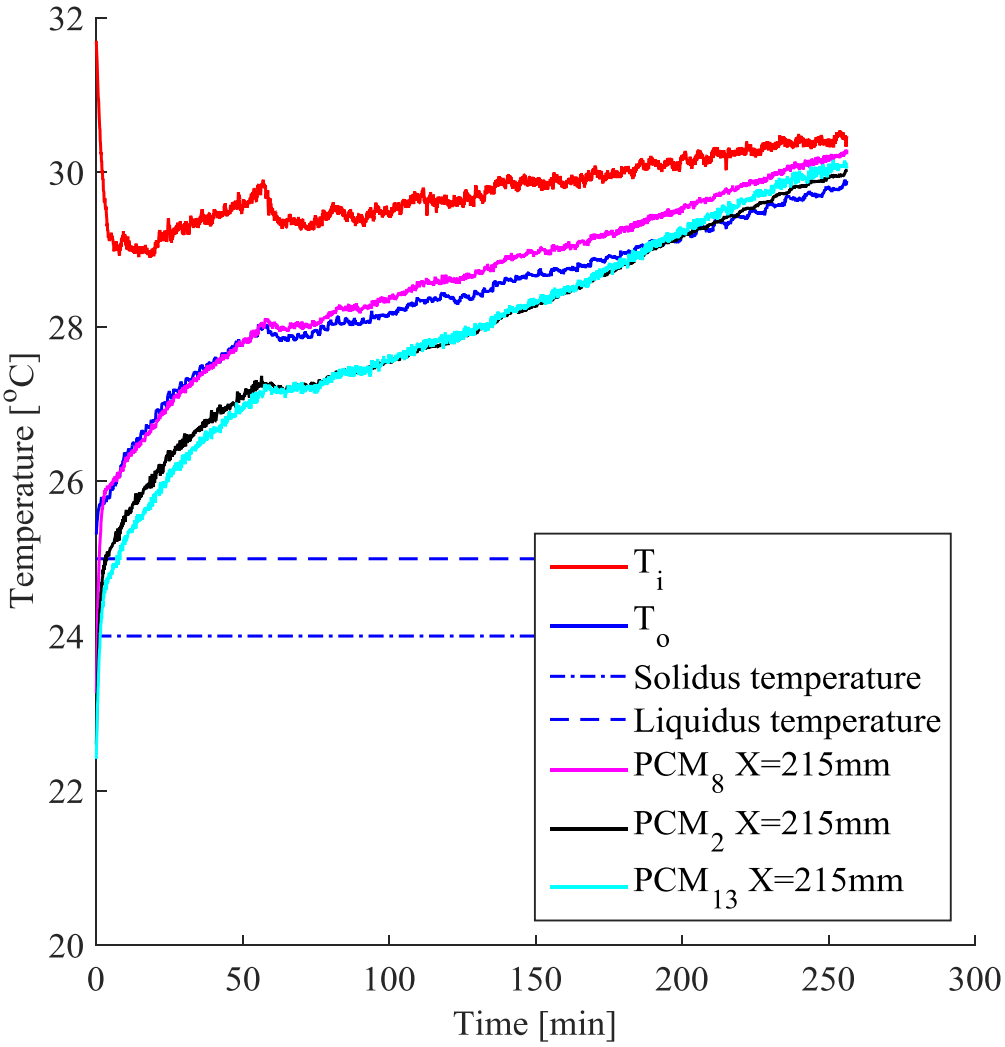

Figure D.25. PCM temperature distribution during melting for SP24E module for an inlet air temperature of 30 °C and air flow of 0.06 kg/s.

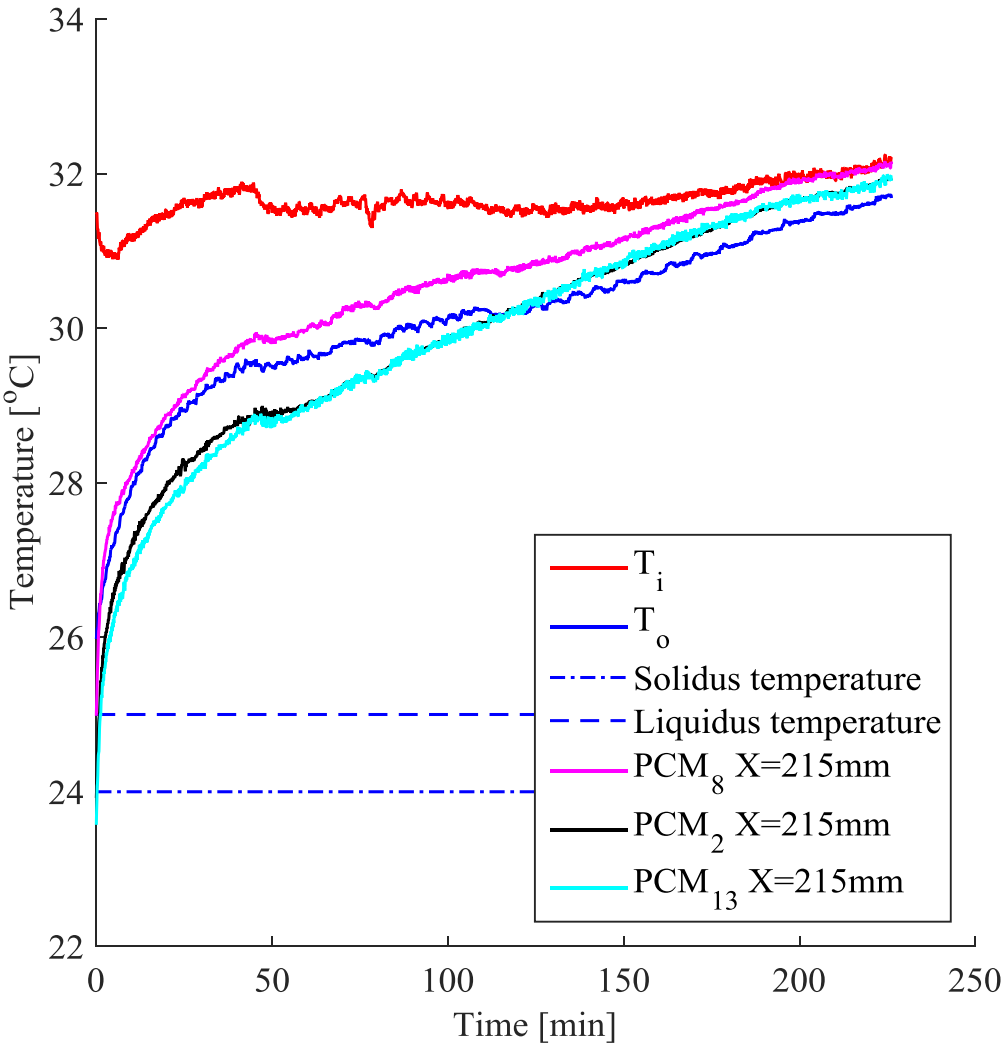

Figure D.26. PCM temperature distribution during melting for SP24E module for an inlet air temperature of 32 °C and air flow of 0.06 kg/s.

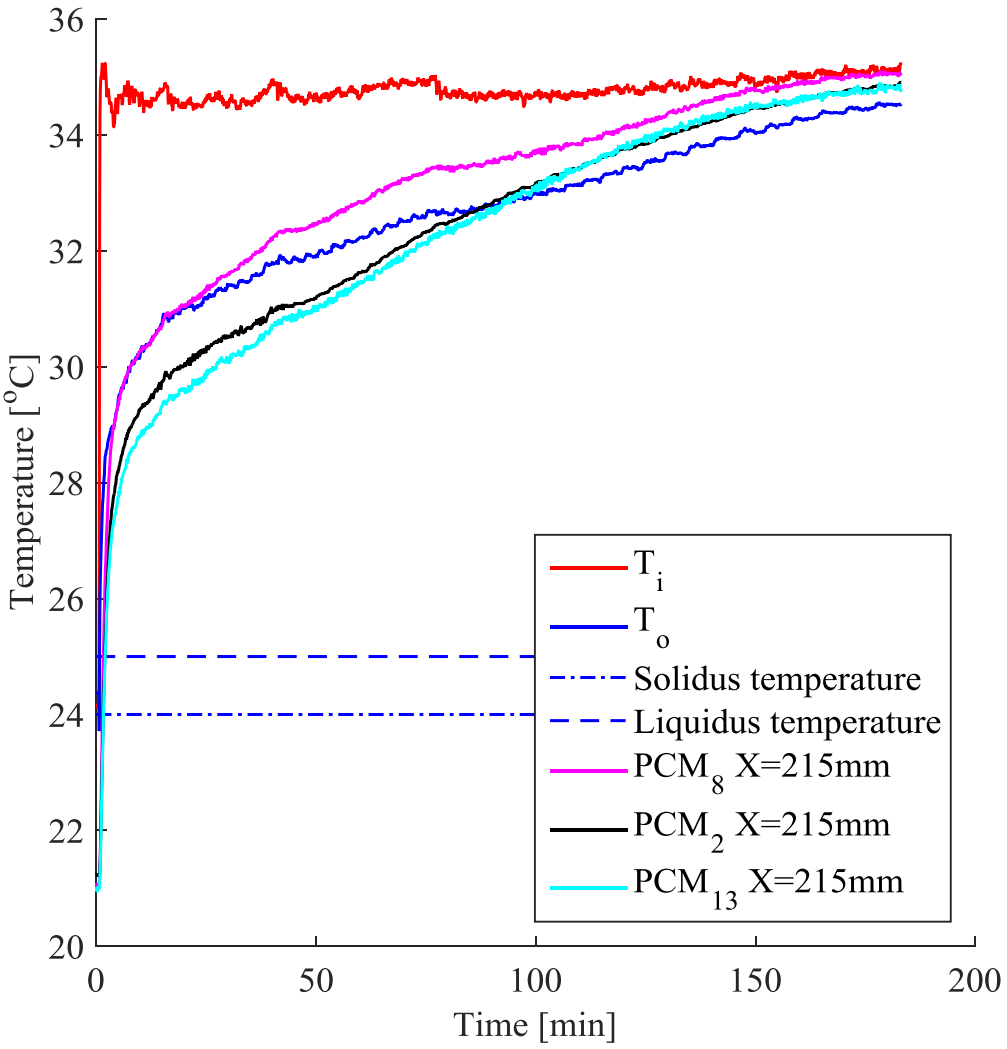

Figure D.27. PCM temperature distribution during melting for SP24E module for an inlet air temperature of 35 °C and air flow of 0.06 kg/s.

APPENDIX E. PCM MELT FRONT

This Appendix gives all the experimental results for the PCM temperature distribution in Plate 8 with thermocouples placed 145 mm, 215 mm and 315 mm from the plate leading edge.

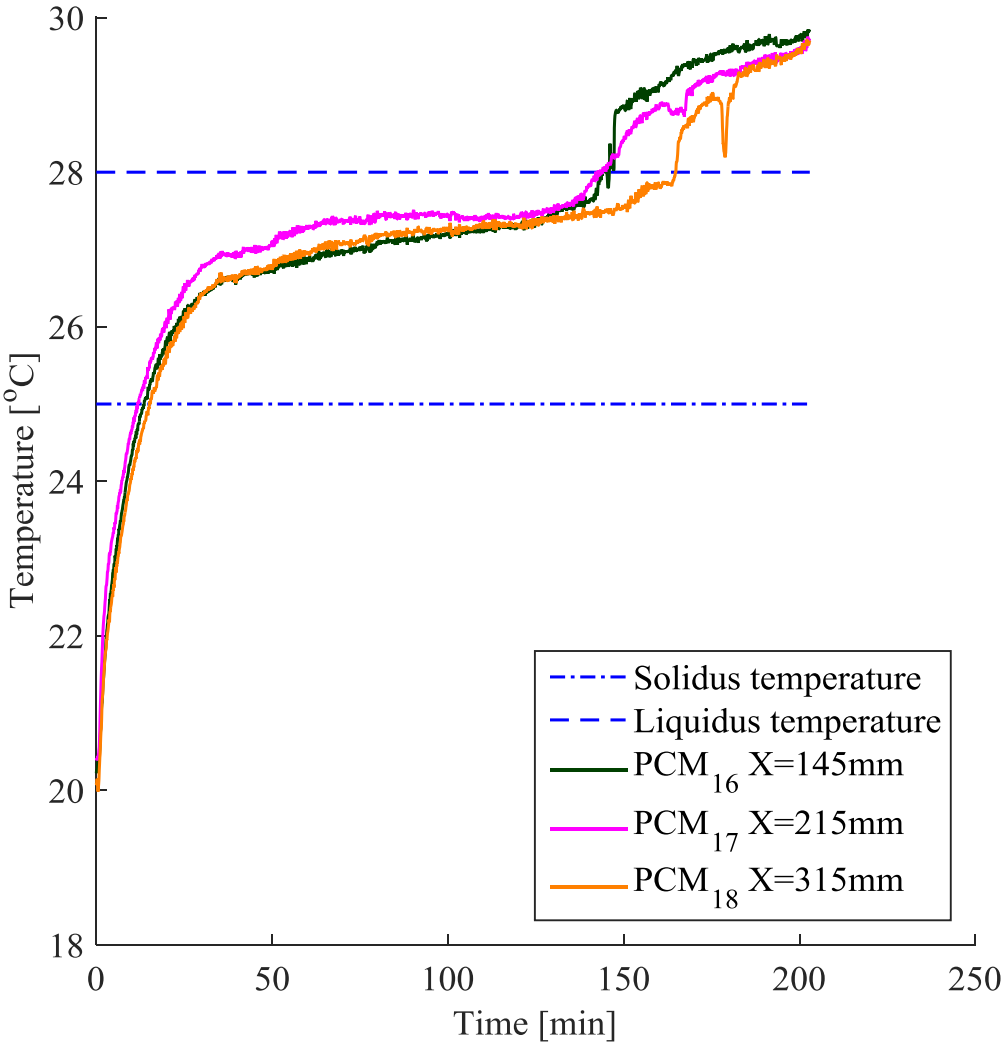

Figure E.1. PCM temperature distribution in plate 8; thermocouples placed 145 mm, 215 mm and 315 mm from the plate leading edge for RT27 for an air mass flow rate of 0.03 kg/s and an inlet temperature of 30 °C.

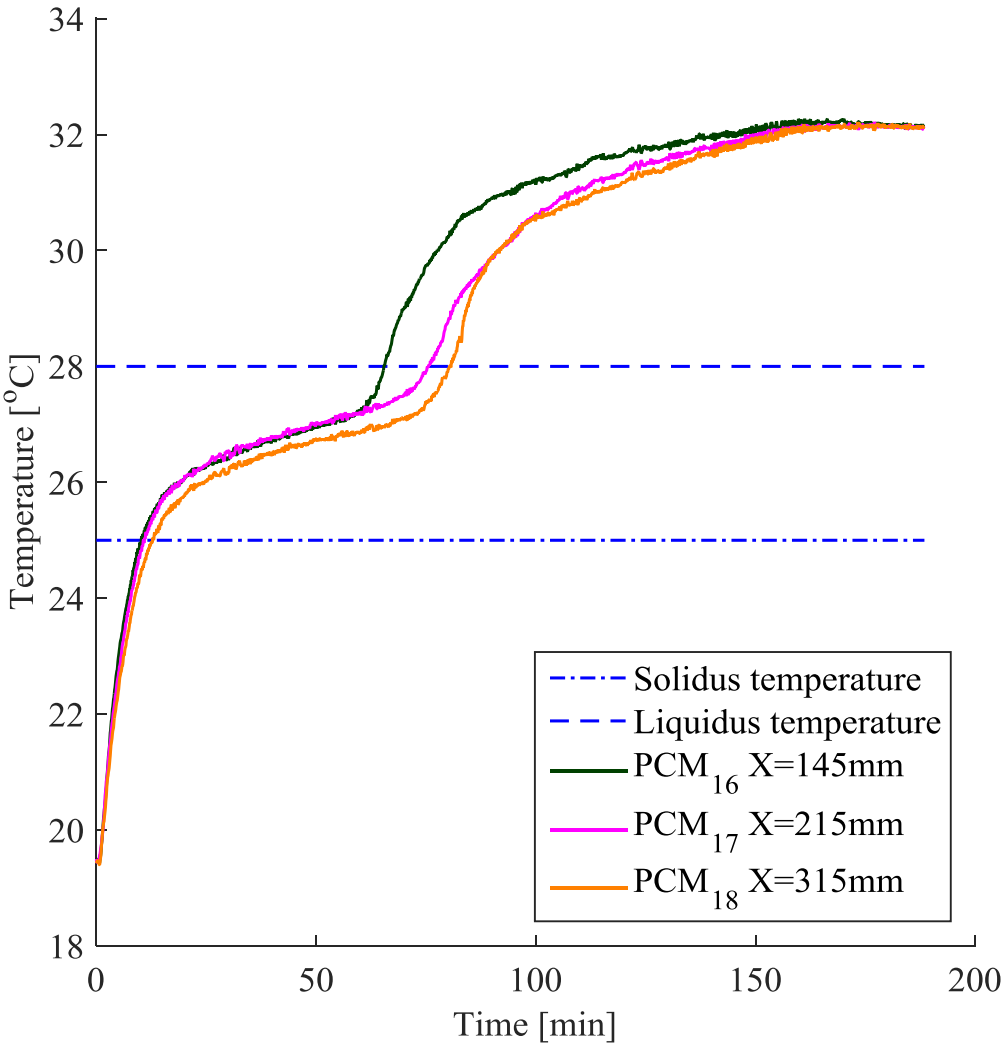

Figure E.2. PCM temperature distribution in plate 8; thermocouples placed 145 mm, 215 mm and 315 mm from the plate leading edge for RT27 for an air mass flow rate of 0.03 kg/s and an inlet temperature of 32 °C.

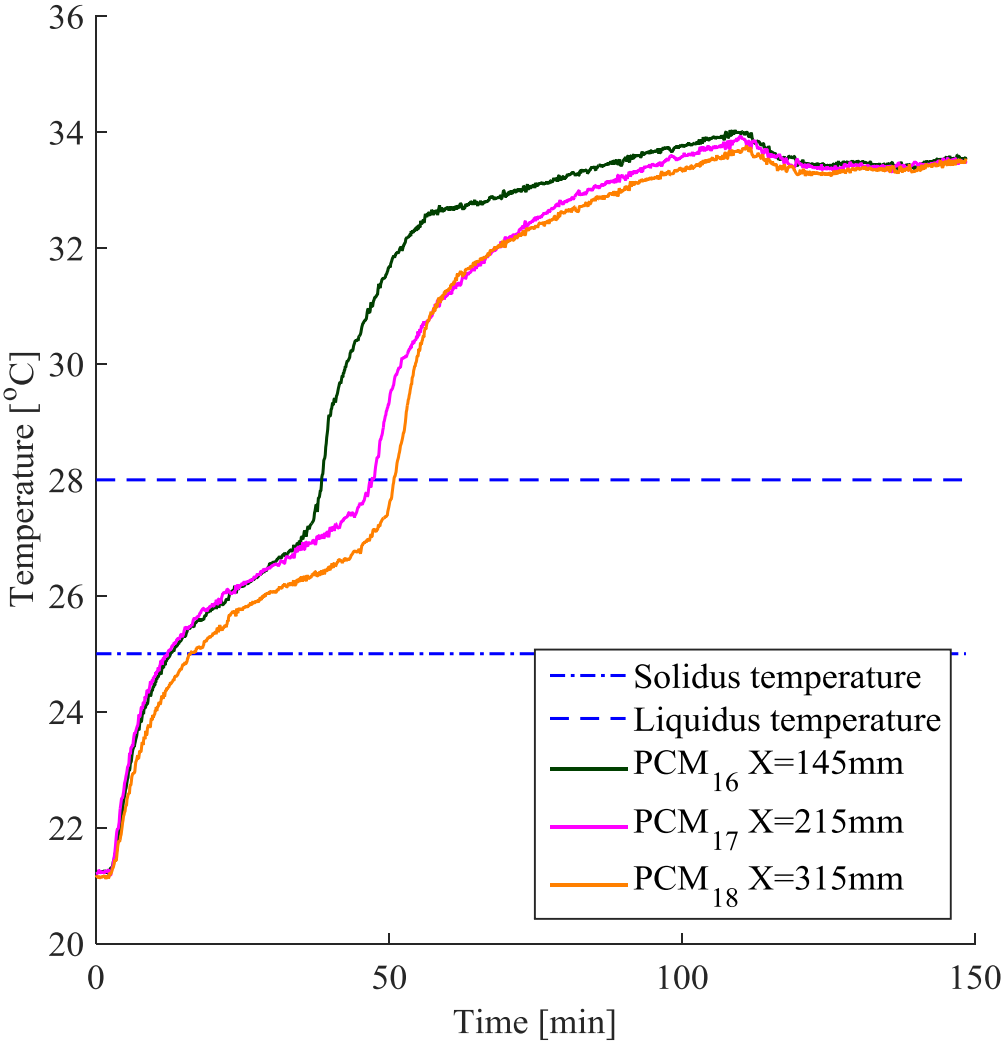

Figure E.3. PCM temperature distribution in plate 8; thermocouples placed 145 mm, 215 mm and 315 mm from the plate leading edge for RT27 for an air mass flow rate of 0.03 kg/s and an inlet temperature of 35 °C.

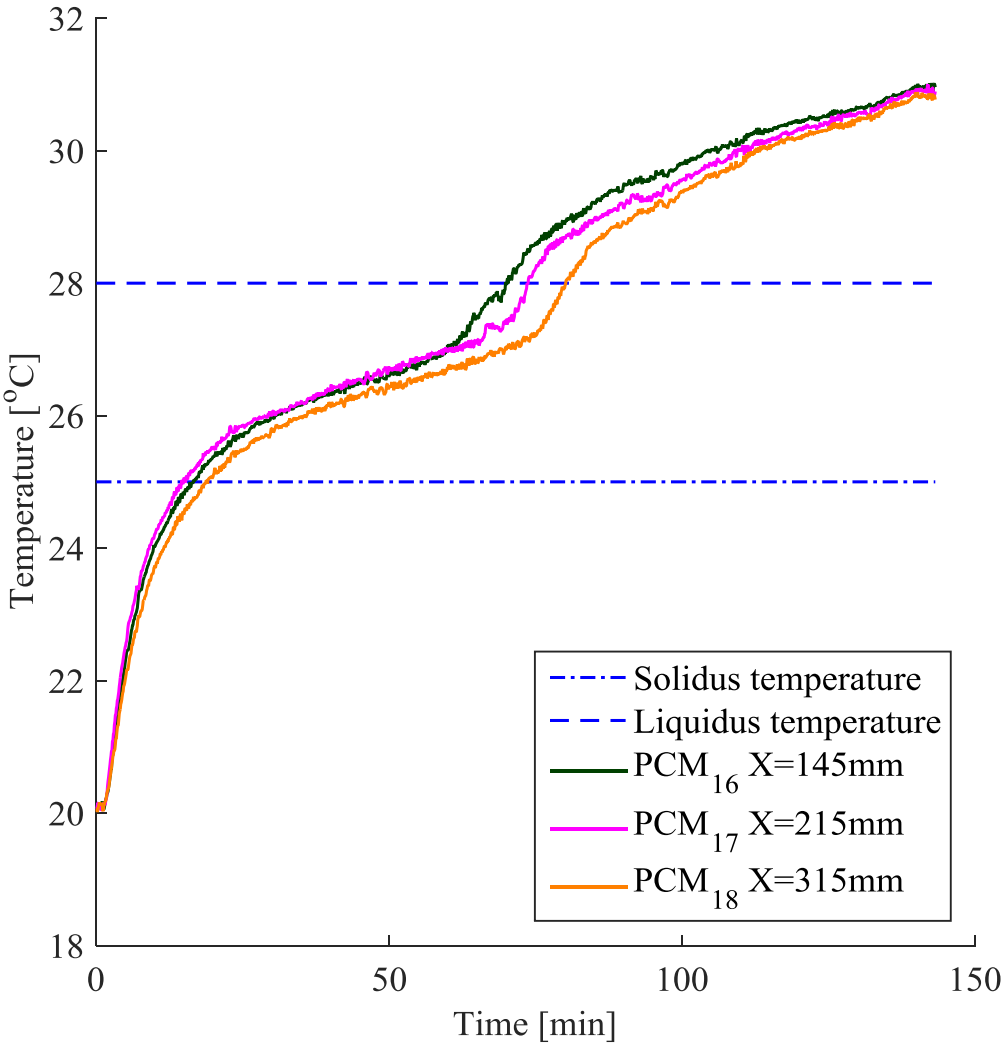

Figure E.4. PCM temperature distribution in plate 8; thermocouples placed 145 mm, 215 mm and 315 mm from the plate leading edge for RT27 for an air mass flow rate of 0.05 kg/s and an inlet temperature of 30 °C.

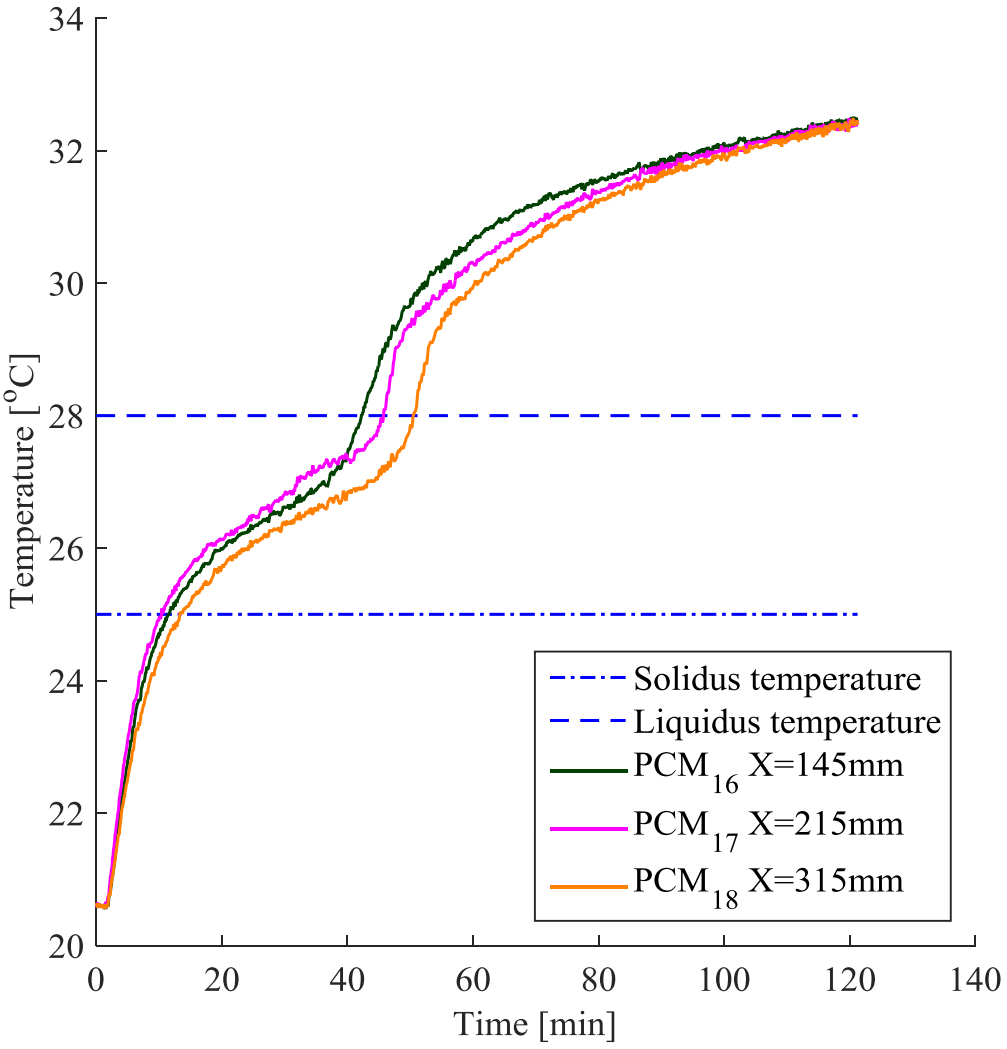

Figure E.5. PCM temperature distribution in plate 8; thermocouples placed 145 mm, 215 mm and 315 mm from the plate leading edge for RT27 for an air mass flow rate of 0.05 kg/s and an inlet temperature of 32 °C.

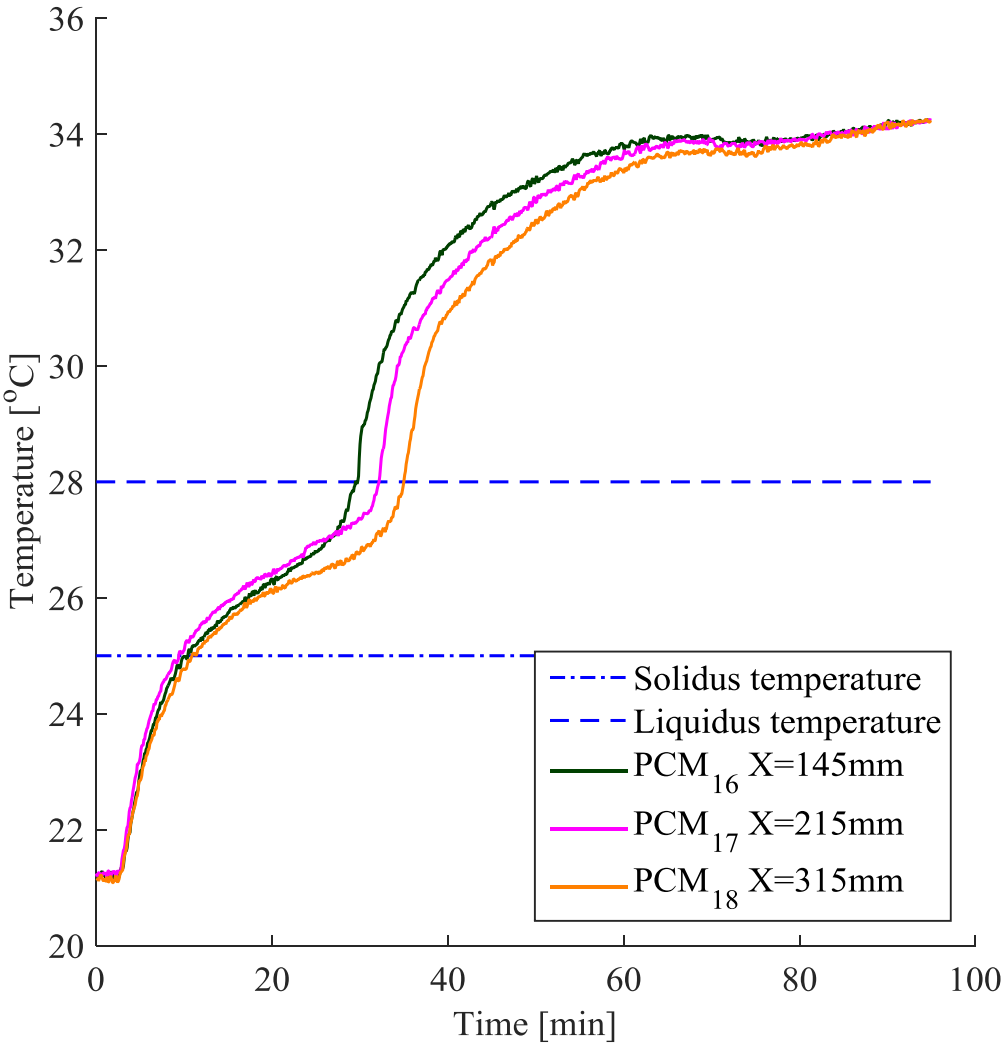

Figure E.6. PCM temperature distribution in plate 8; thermocouples placed 145 mm, 215 mm and 315 mm from the plate leading edge for RT27 for an air mass flow rate of 0.05 kg/s and an inlet temperature of 35 °C.

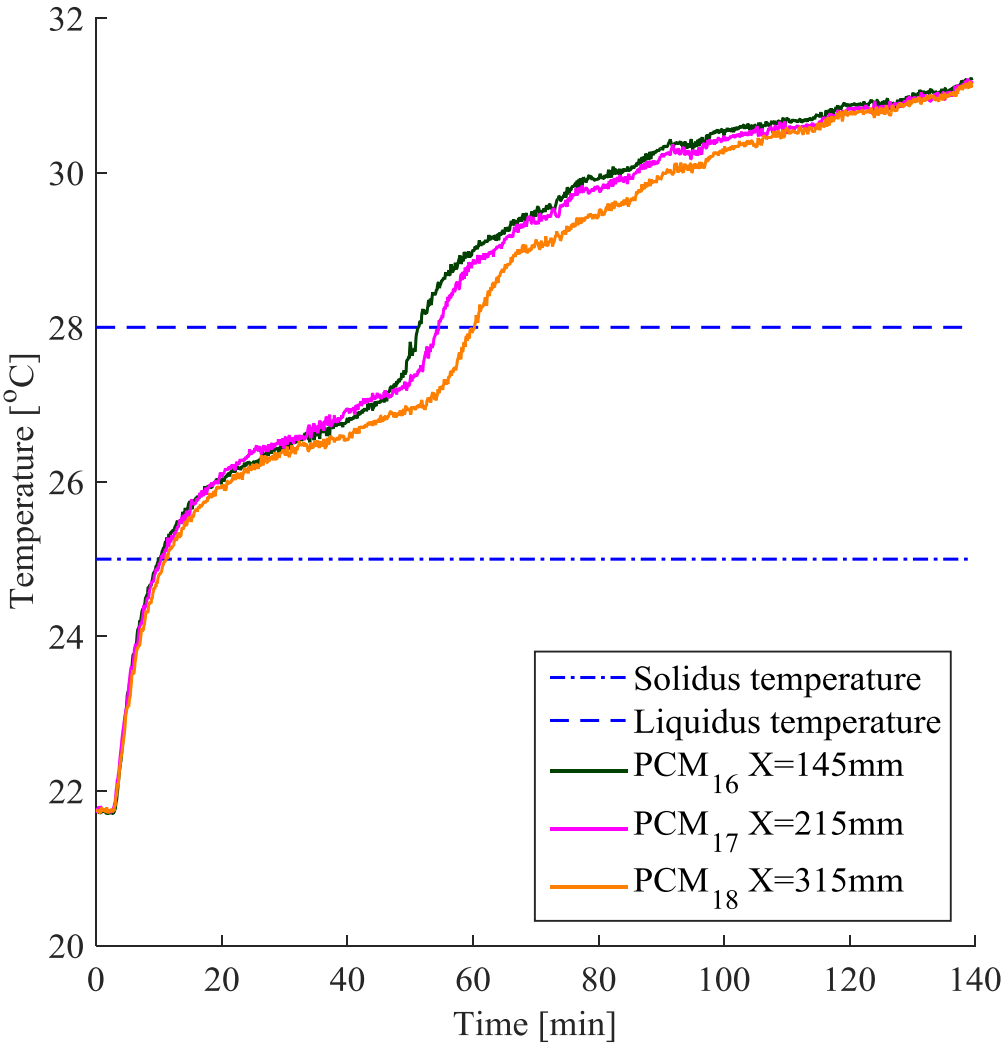

Figure E.7. PCM temperature distribution in plate 8; thermocouples placed 145 mm, 215 mm and 315 mm from the plate leading edge for RT27 for an air mass flow rate of 0.06 kg/s and an inlet temperature of 30 °C.

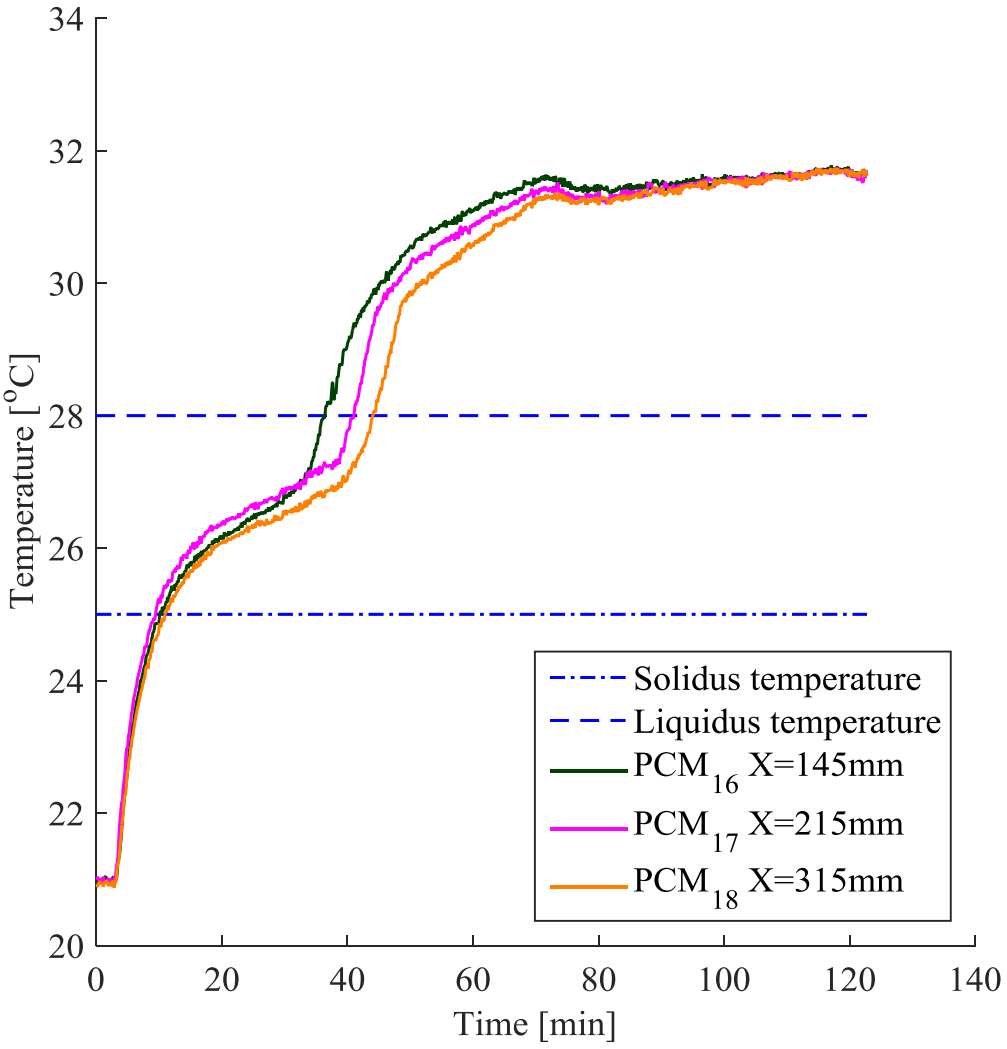

Figure E.8. PCM temperature distribution in plate 8; thermocouples placed 145 mm, 215 mm and 315 mm from the plate leading edge for RT27 for an air mass flow rate of 0.06 kg/s and an inlet temperature of 32 °C.

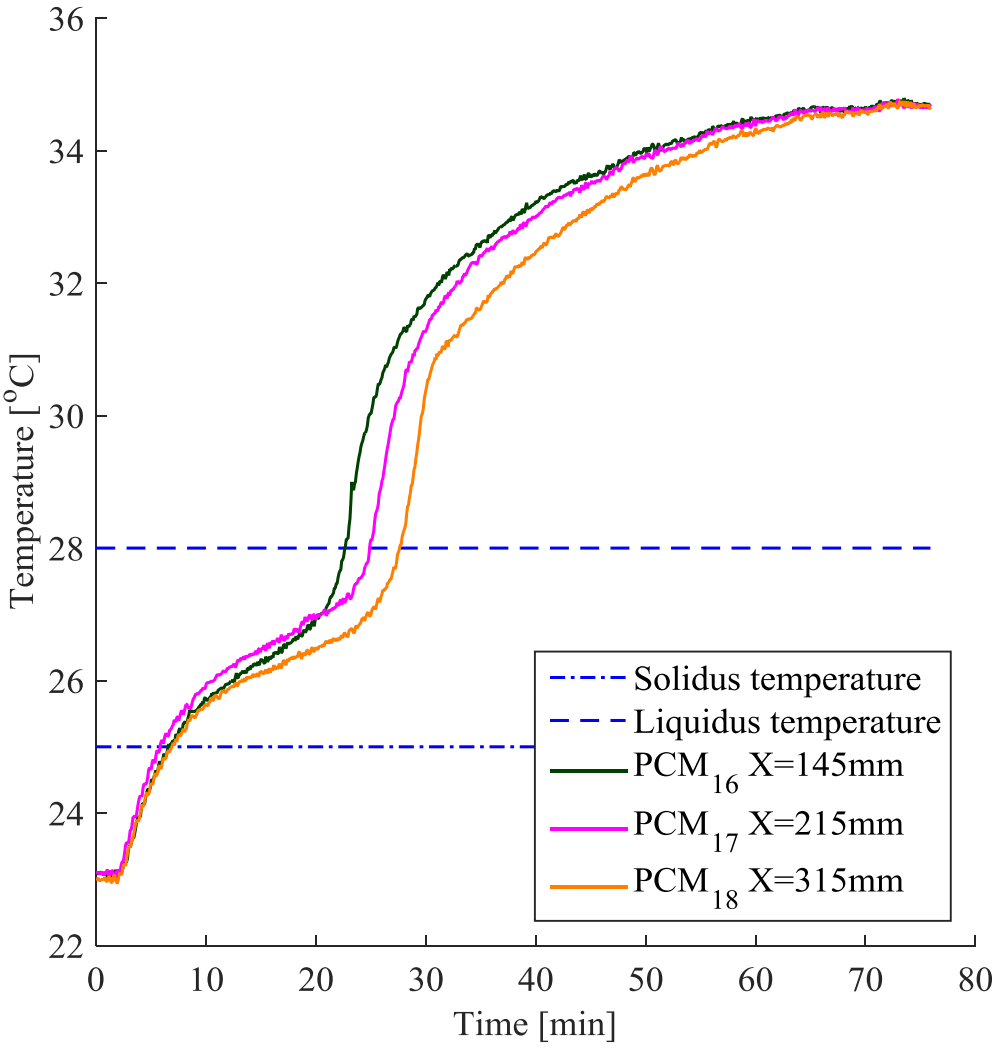

Figure E.9. PCM temperature distribution in plate 8; thermocouples placed 145 mm, 215 mm and 315 mm from the plate leading edge for RT27 for an air mass flow rate of 0.06 kg/s and an inlet temperature of 35 °C.

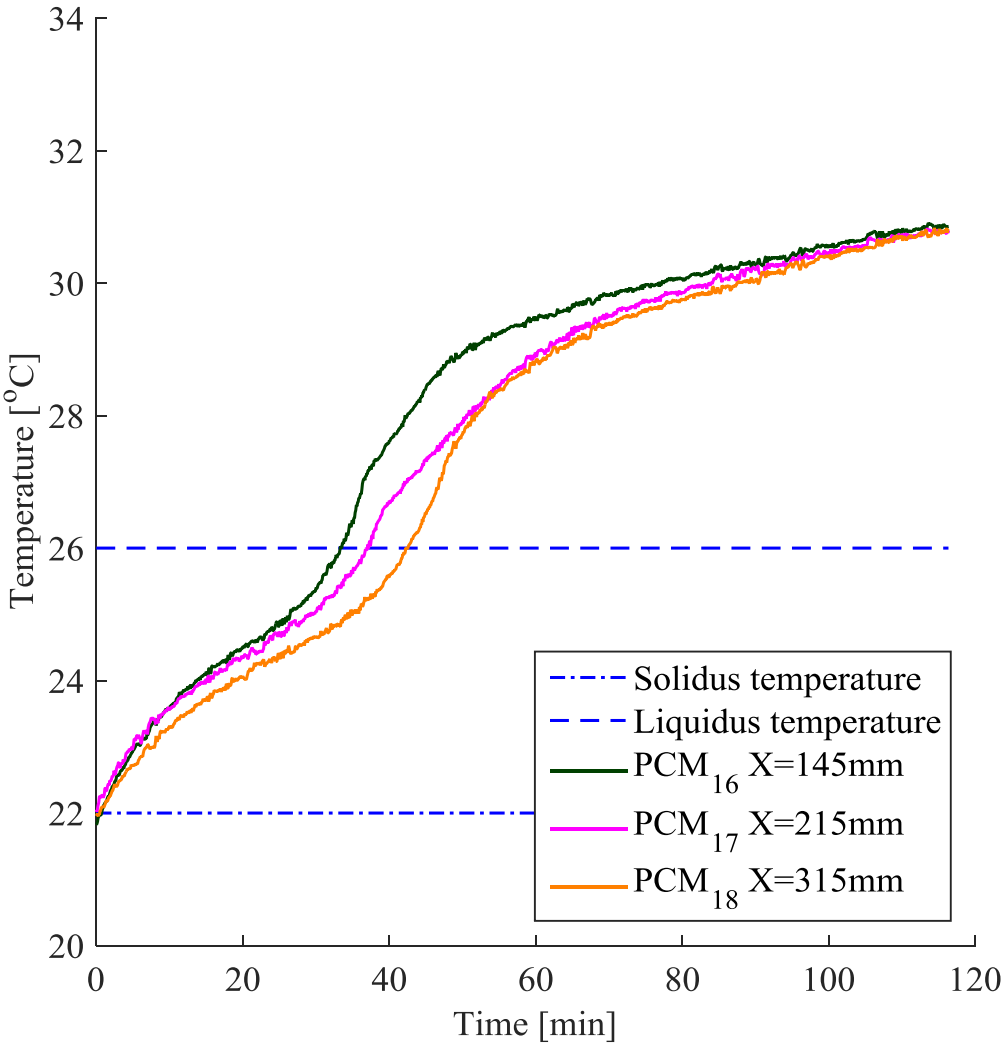

Figure E.10. PCM temperature distribution in plate 8; thermocouples placed 145 mm, 215 mm and 315 mm from the plate leading edge for RT25 for an air mass flow rate of 0.03 kg/s and an inlet temperature of 30 °C.

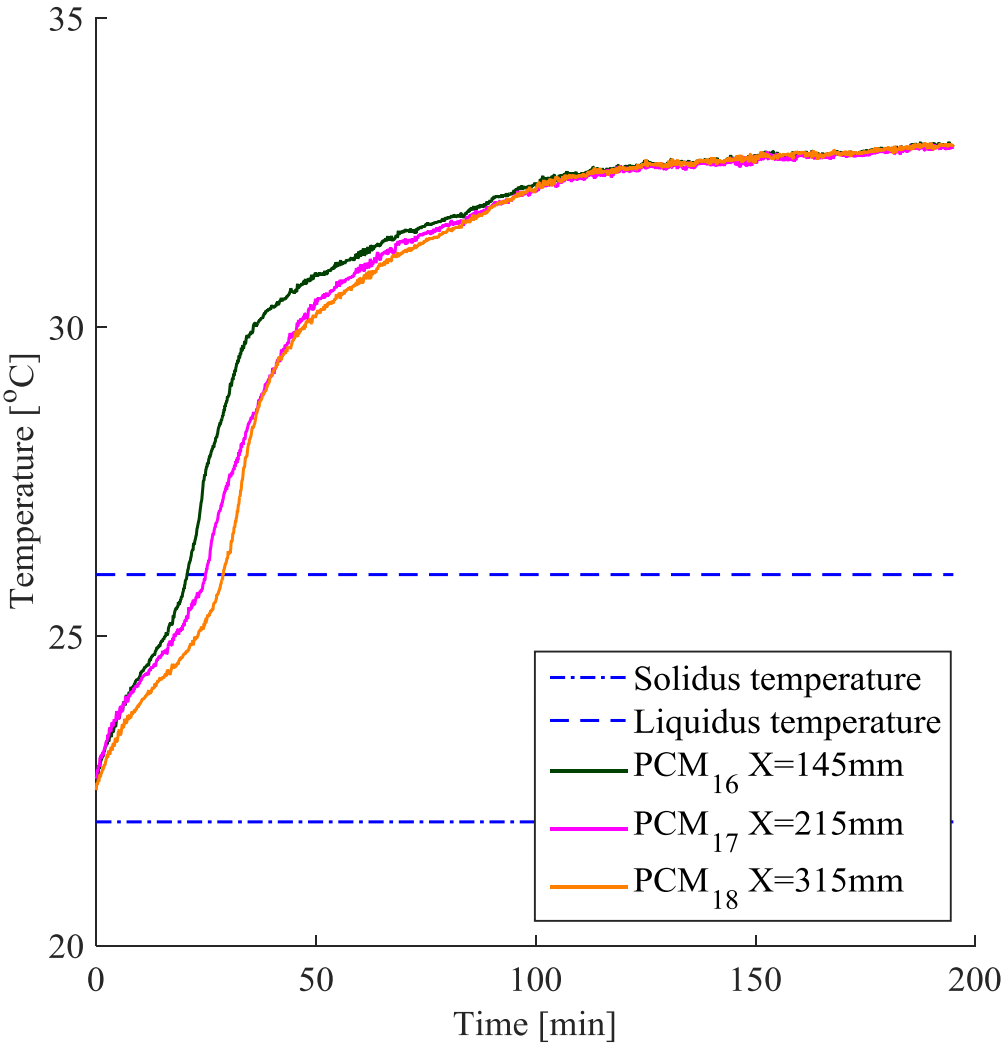

Figure E.11. PCM temperature distribution in plate 8; thermocouples placed 145 mm, 215 mm and 315 mm from the plate leading edge for RT25 for an air mass flow rate of 0.03 kg/s and an inlet temperature of 32 °C.

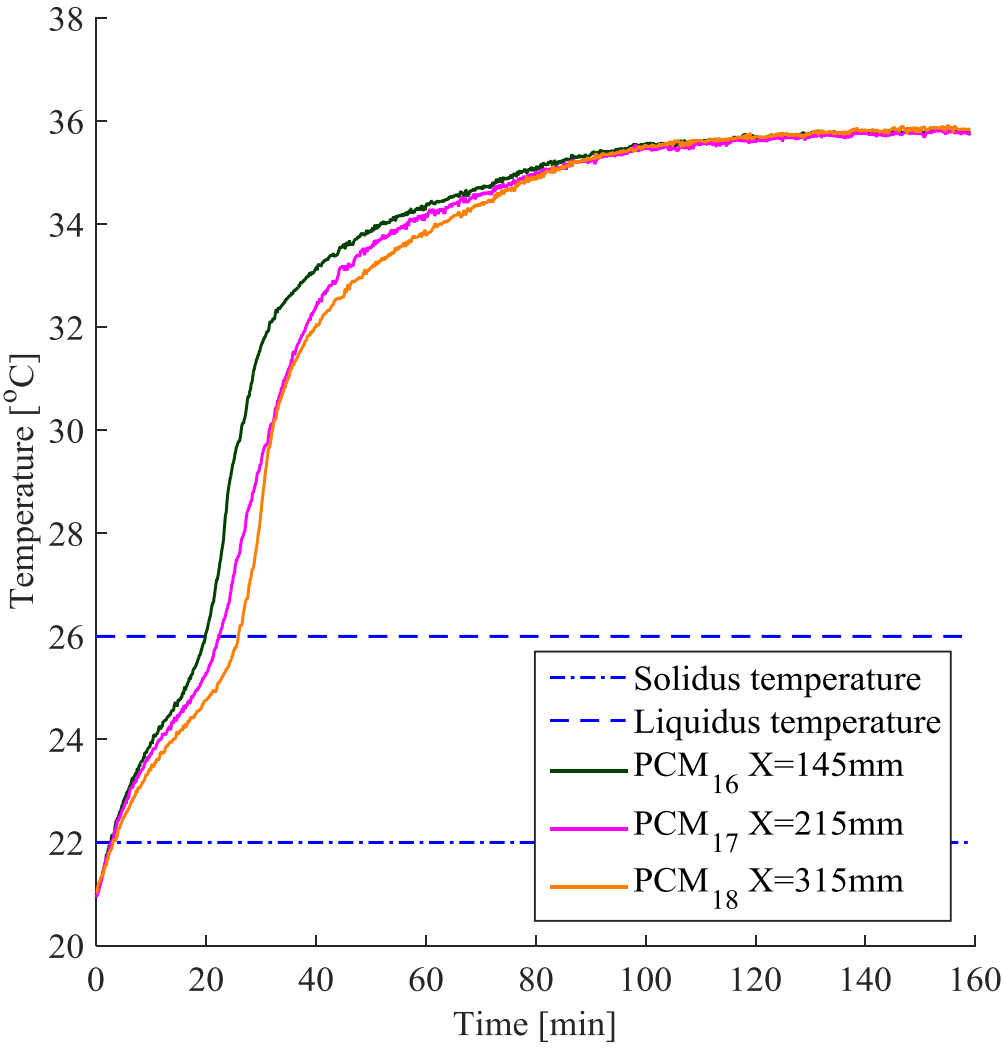

Figure E.12. PCM temperature distribution in plate 8; thermocouples placed 145 mm, 215 mm and 315 mm from the plate leading edge for RT25 for an air mass flow rate of 0.03 kg/s and an inlet temperature of 35 °C.

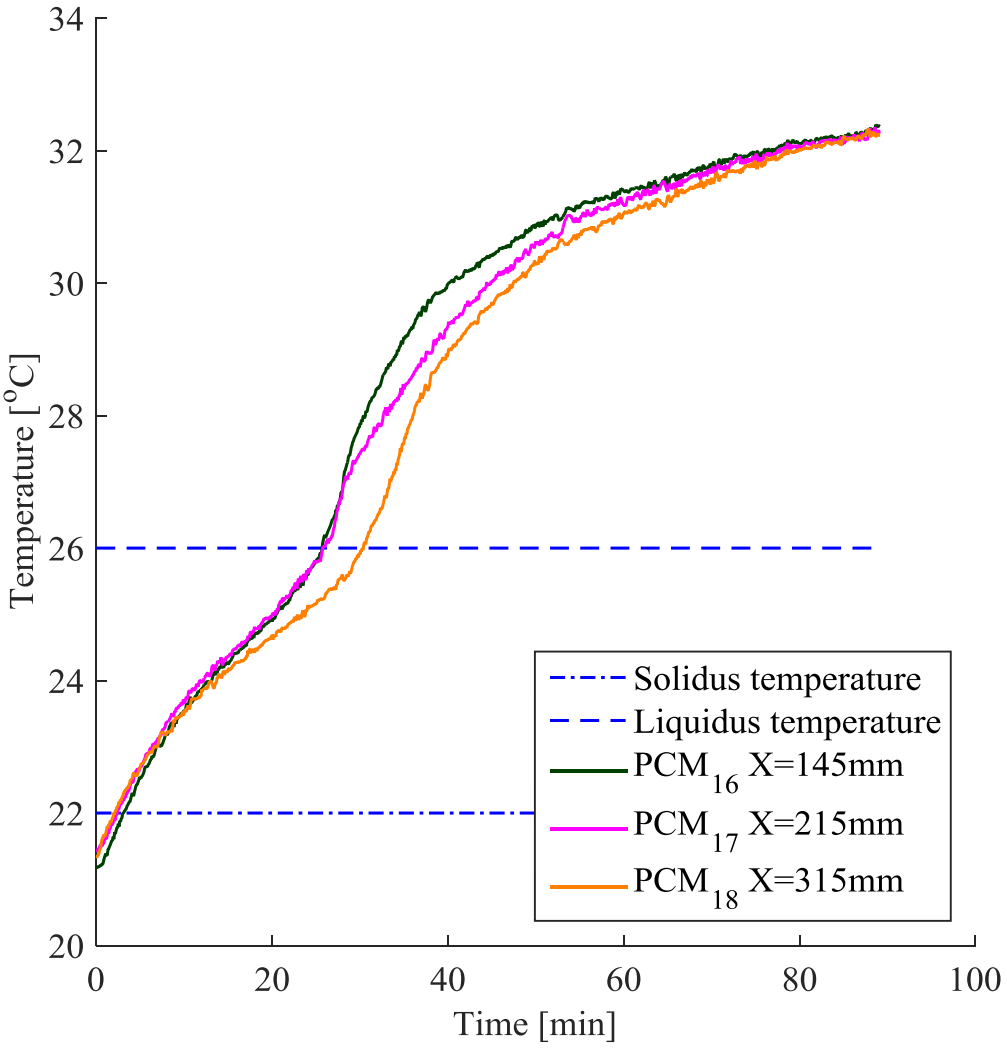

Figure E.13. PCM temperature distribution in plate 8; thermocouples placed 145 mm, 215 mm and 315 mm from the plate leading edge for RT27 for an air mass flow rate of 0.05 kg/s and an inlet temperature of 30 °C.

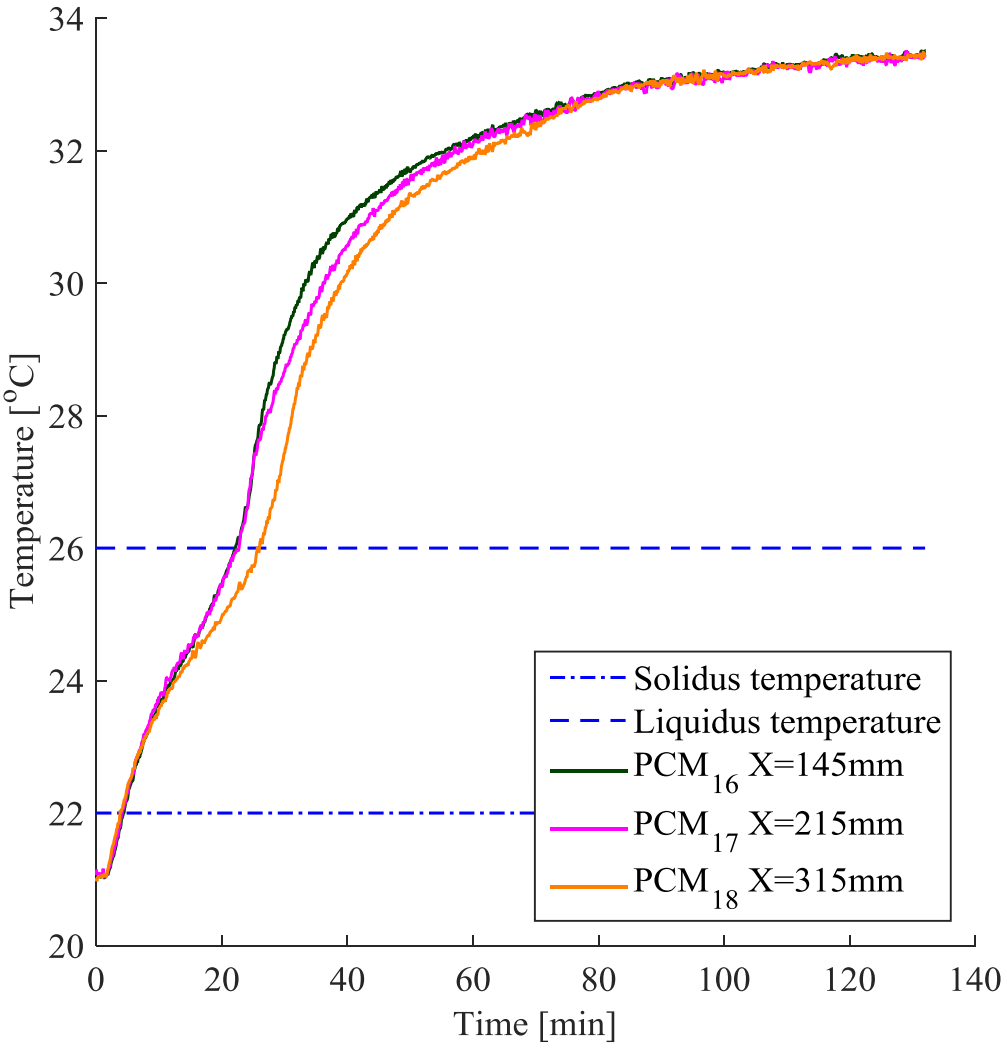

Figure E.14. PCM temperature distribution in plate 8; thermocouples placed 145 mm, 215 mm and 315 mm from the plate leading edge for RT25 for an air mass flow rate of 0.05 kg/s and an inlet temperature of 32 °C.

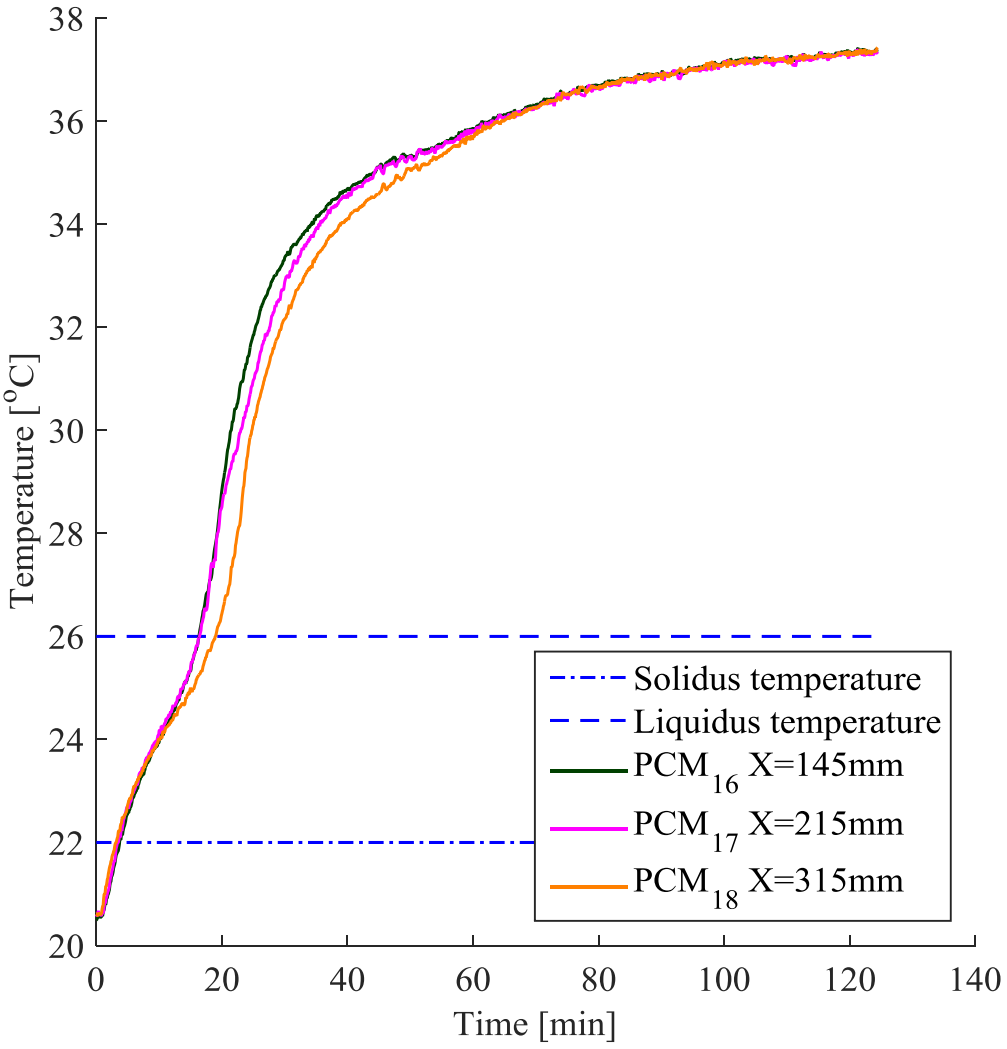

Figure E.15. PCM temperature distribution in plate 8; thermocouples placed 145 mm, 215 mm and 315 mm from the plate leading edge for RT25 for an air mass flow rate of 0.05 kg/s and an inlet temperature of 35 °C.

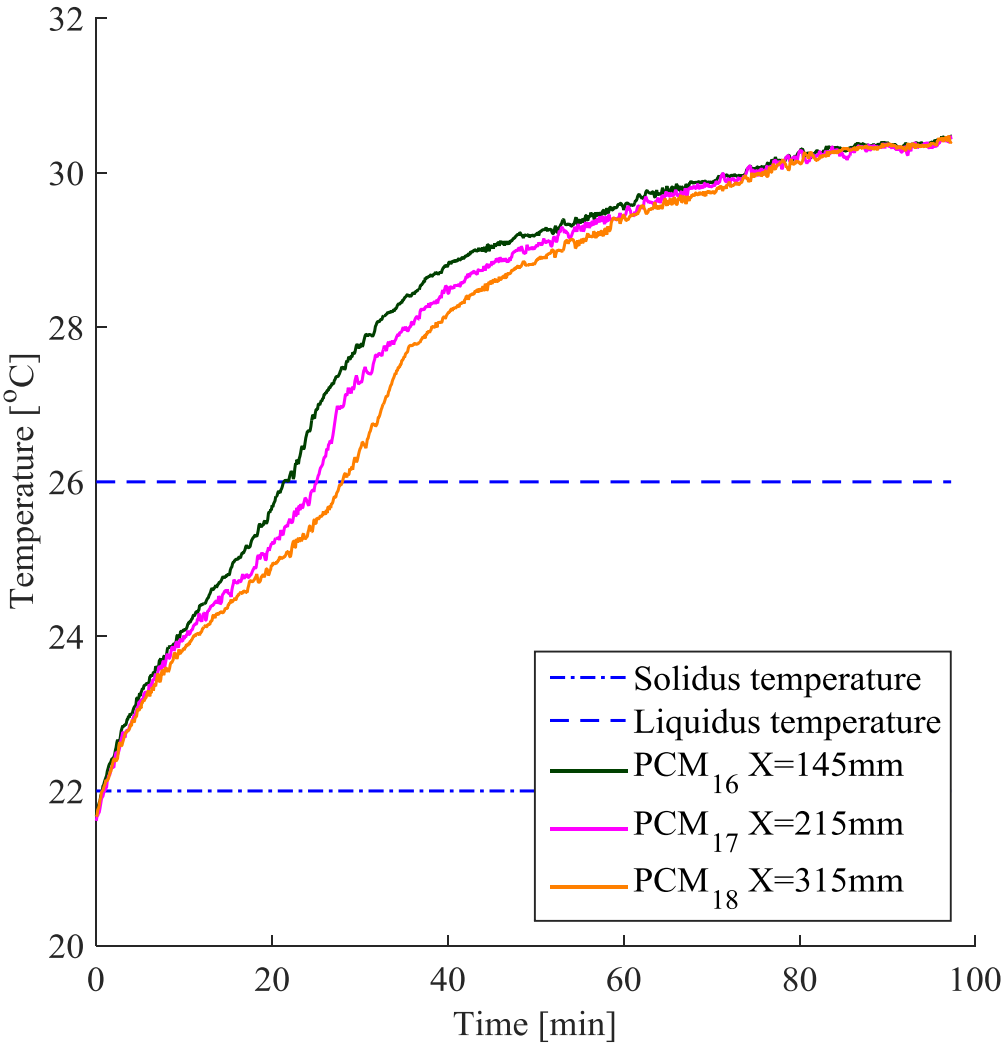

Figure E.16. PCM temperature distribution in plate 8; thermocouples placed 145 mm, 215 mm and 315 mm from the plate leading edge for RT25 for an air mass flow rate of 0.06 kg/s and an inlet temperature of 30 °C.

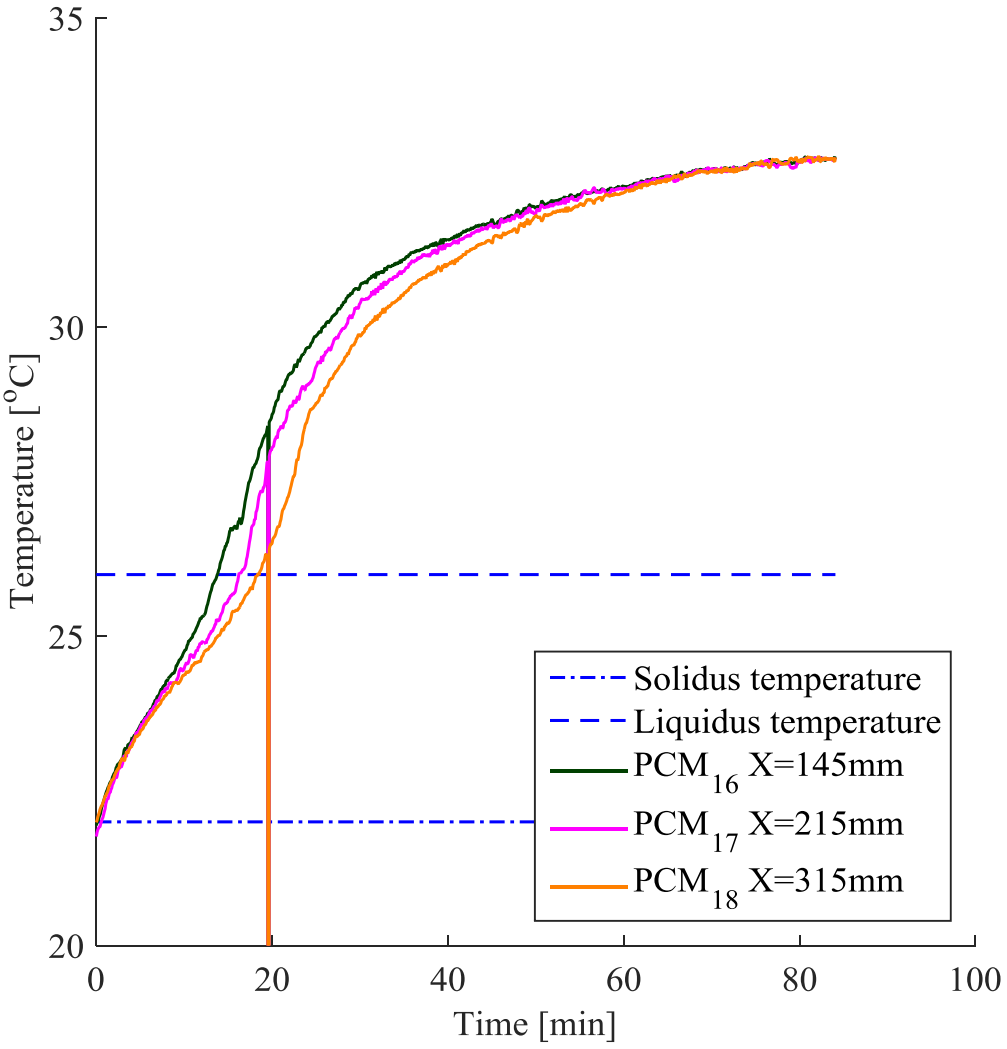

Figure E.17. PCM temperature distribution in plate 8; thermocouples placed 145 mm, 215 mm and 315 mm from the plate leading edge for RT25 for an air mass flow rate of 0.06 kg/s and an inlet temperature of 32 °C.

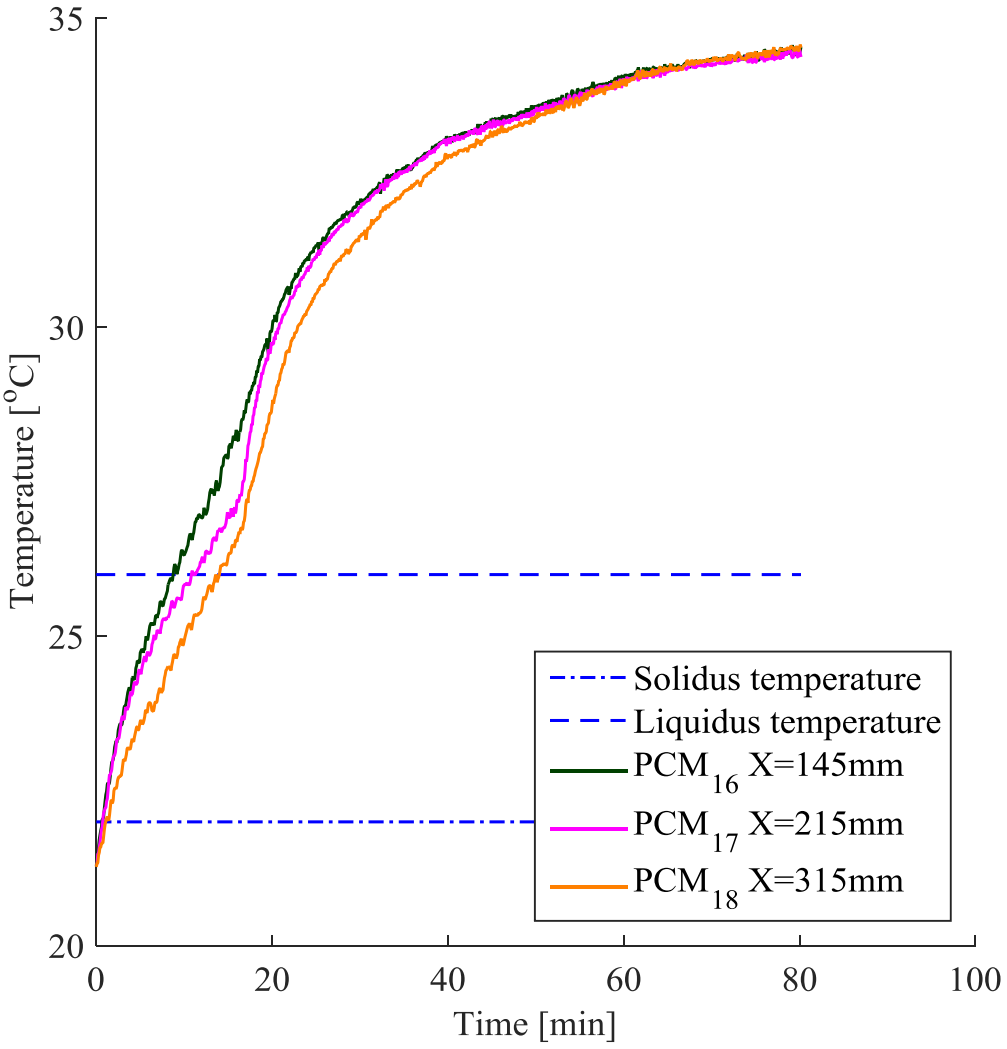

Figure E.18. PCM temperature distribution in plate 8; thermocouples placed 145 mm, 215 mm and 315 mm from the plate leading edge for RT25 for an air mass flow rate of 0.06 kg/s and an inlet temperature of 35 °C.

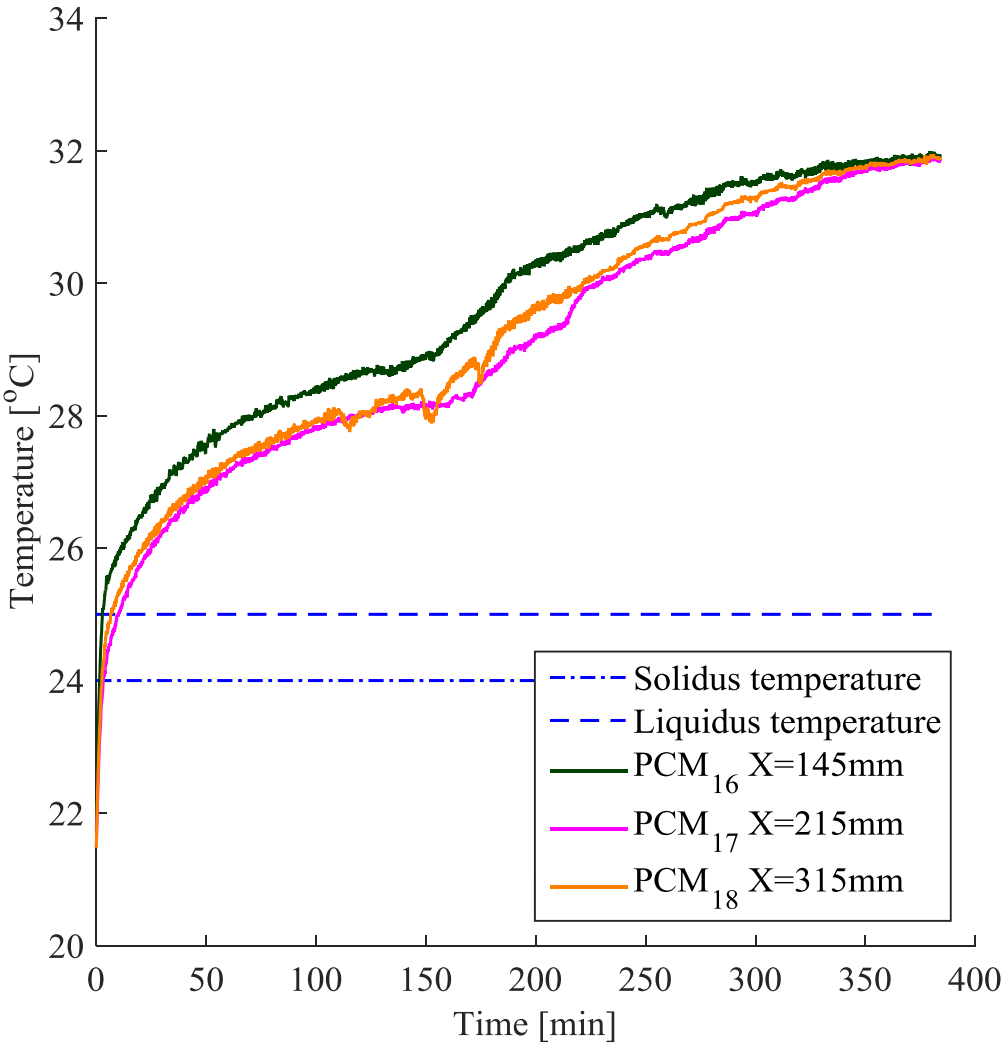

Figure E.19. PCM temperature distribution in plate 8; thermocouples placed 145 mm, 215 mm and 315 mm from the plate leading edge for SP24E for an air mass flow rate of 0.03 kg/s and an inlet temperature of 30 °C.

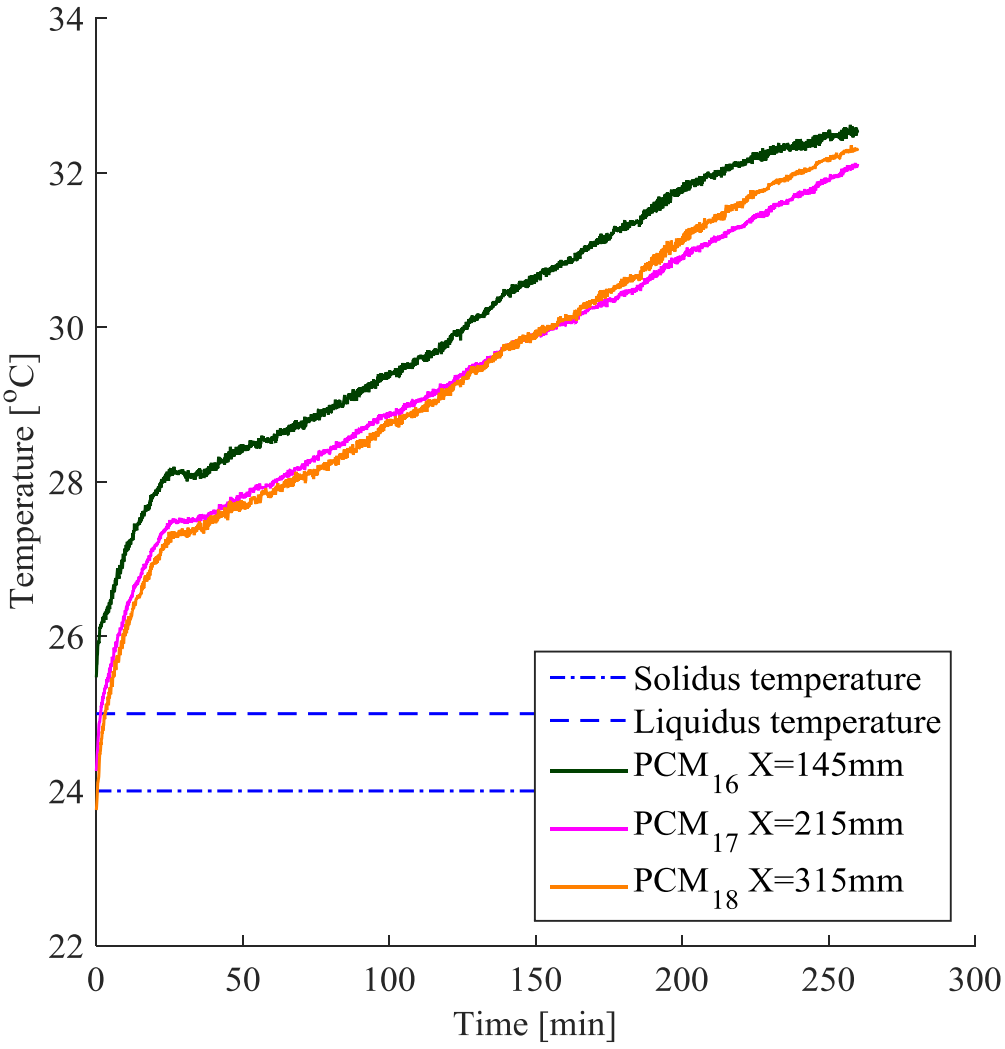

Figure E.20. PCM temperature distribution in plate 8; thermocouples placed 145 mm, 215 mm and 315 mm from the plate leading edge for SP24E for an air mass flow rate of 0.03 kg/s and an inlet temperature of 32 °C.

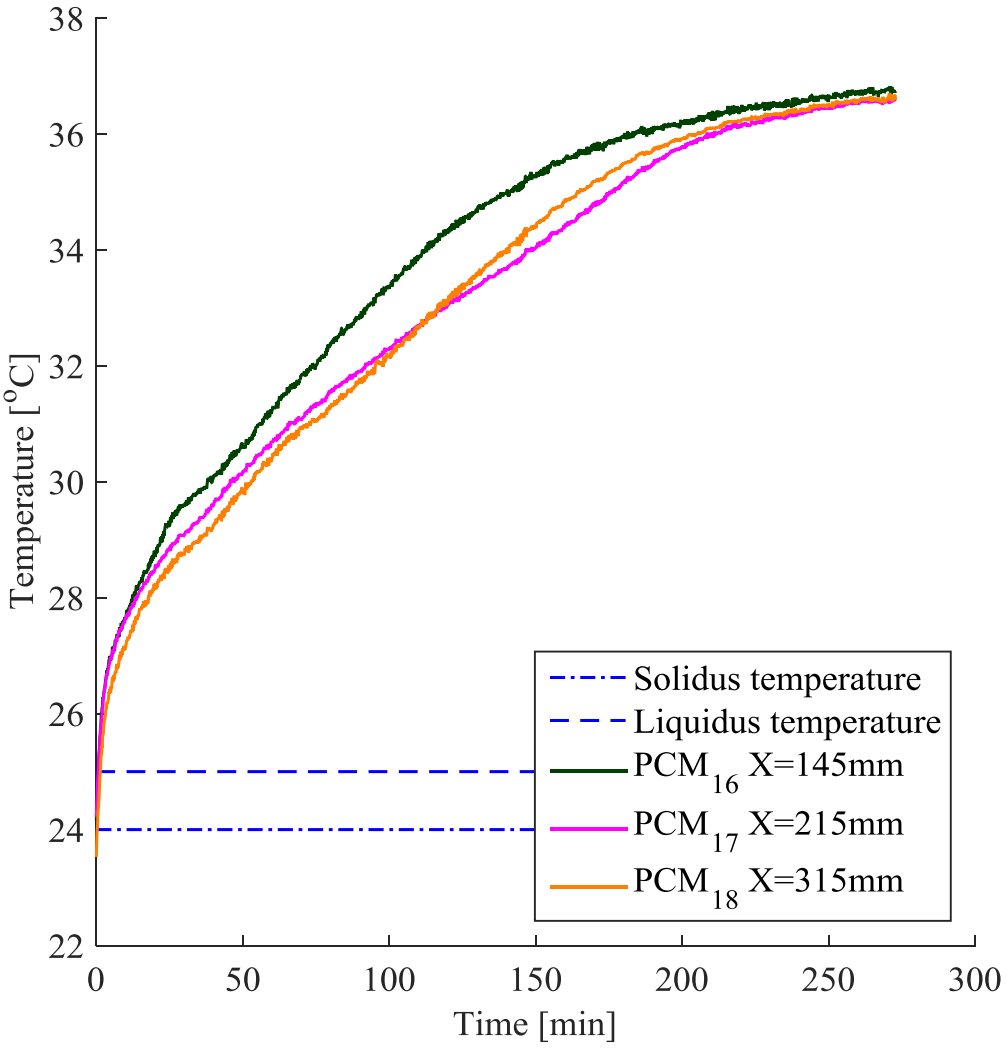

Figure E.21. PCM temperature distribution in plate 8; thermocouples placed 145 mm, 215 mm and 315 mm from the plate leading edge for SP24E for an air mass flow rate of 0.03 kg/s and an inlet temperature of 35 °C.

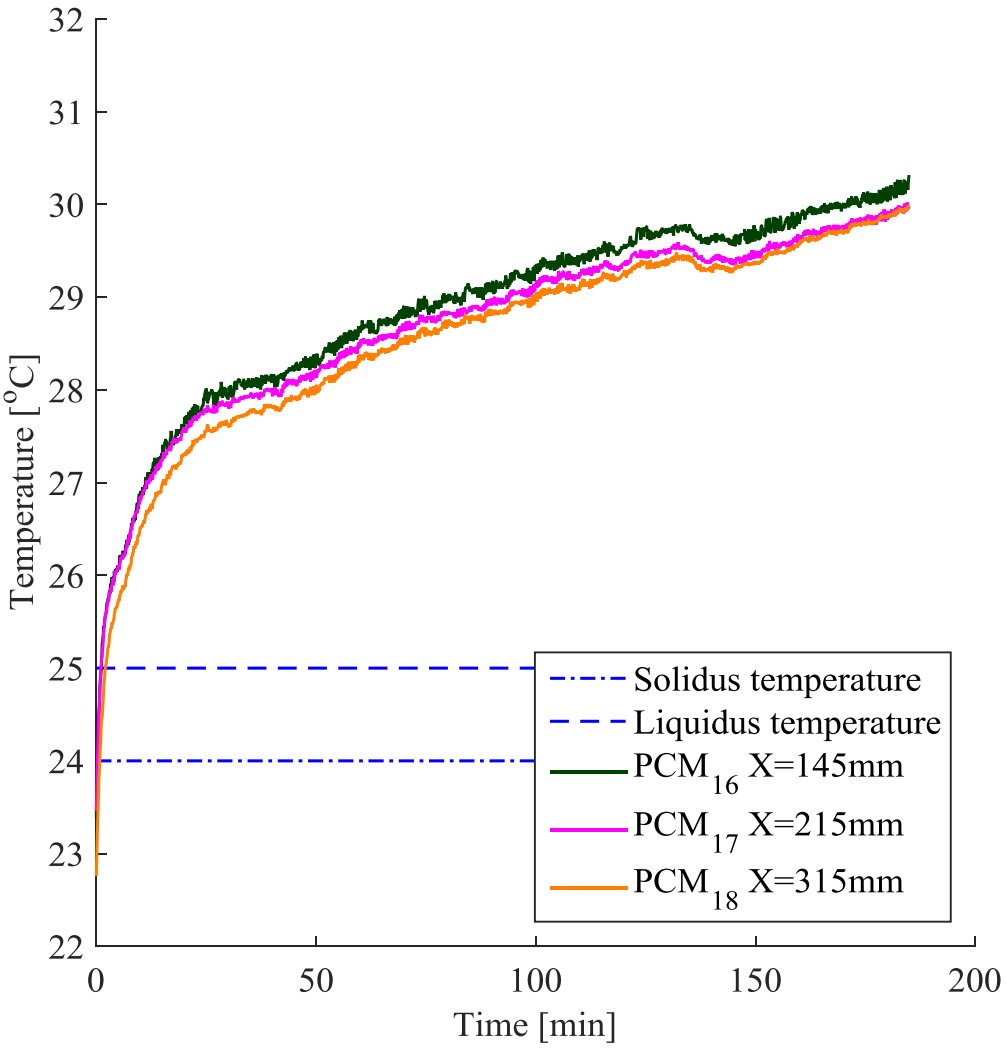

Figure E.22. PCM temperature distribution in plate 8; thermocouples placed 145 mm, 215 mm and 315 mm from the plate leading edge for SP24E for an air mass flow rate of 0.05 kg/s and an inlet temperature of 30 °C.

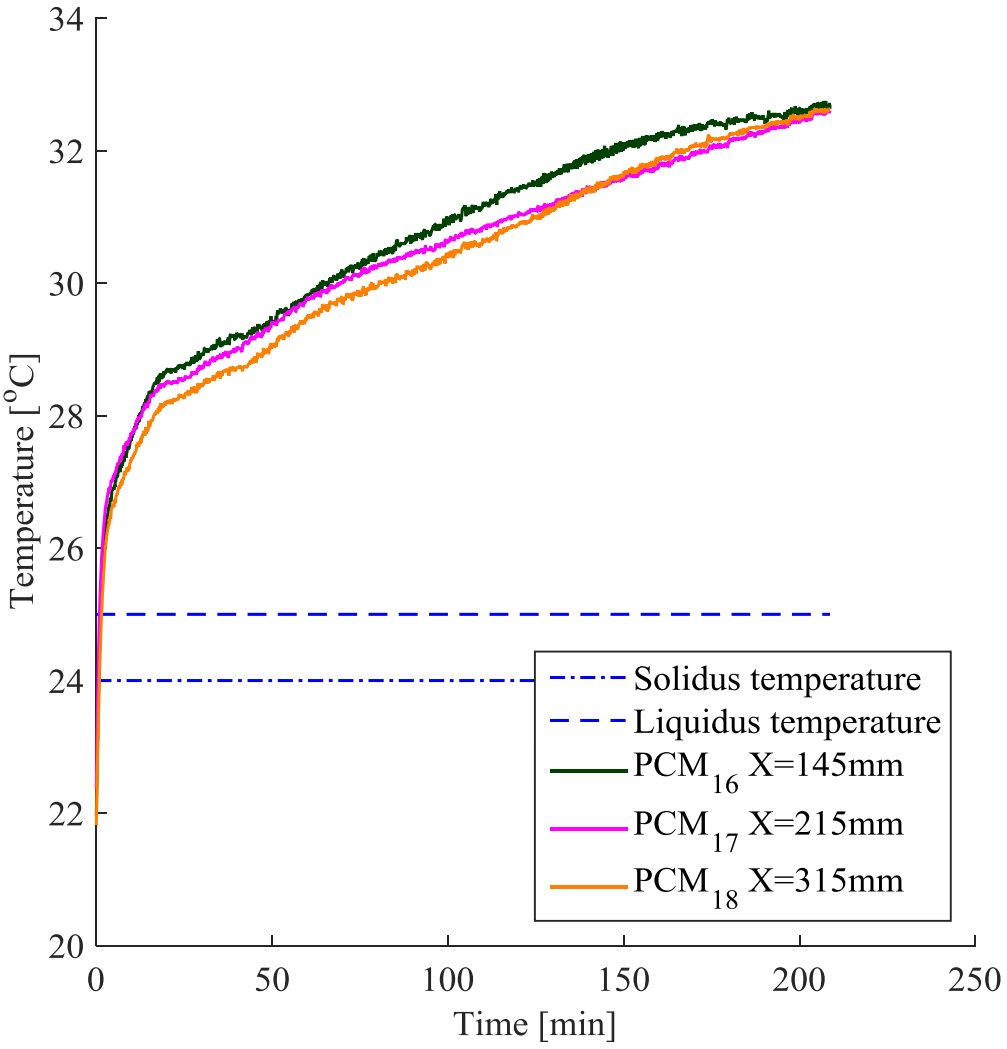

Figure E.23. PCM temperature distribution in plate 8; thermocouples placed 145 mm, 215 mm and 315 mm from the plate leading edge for SP24E for an air mass flow rate of 0.05 kg/s and an inlet temperature of 32 °C.

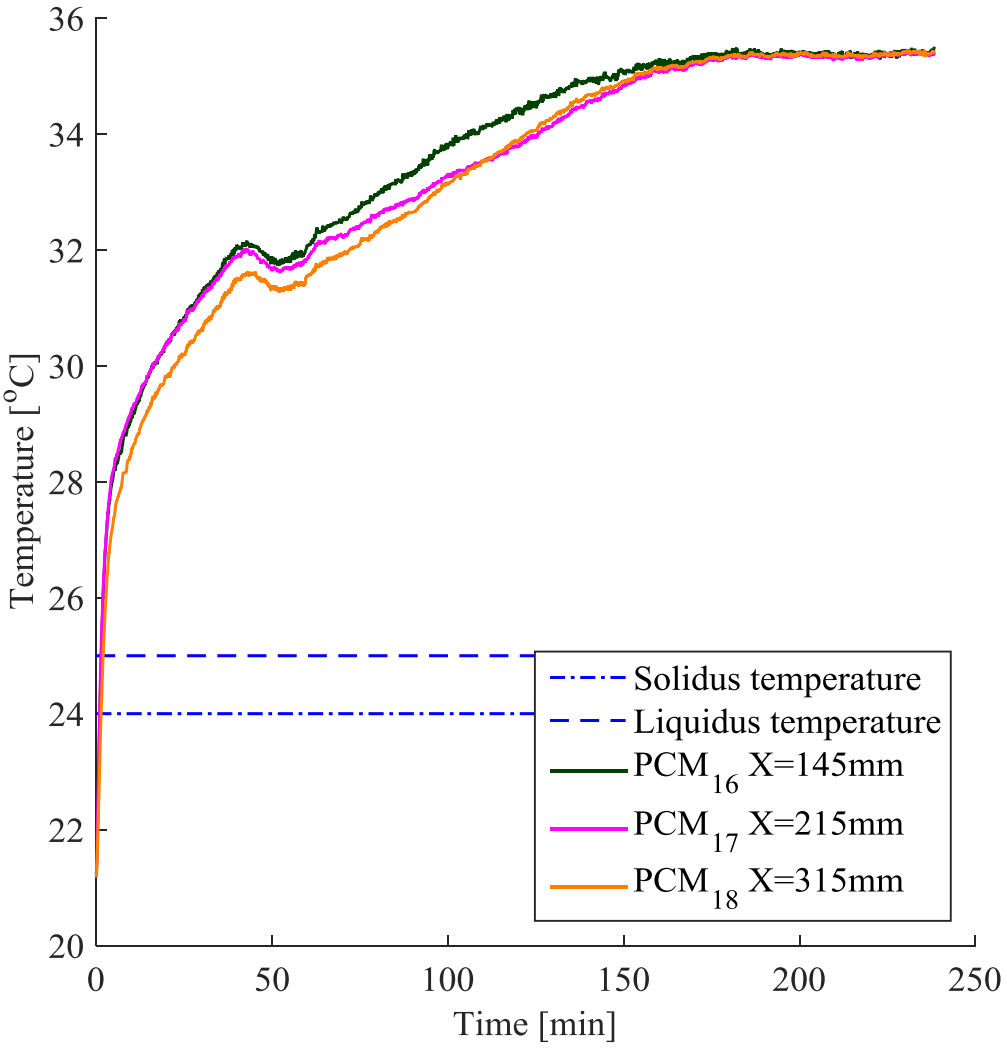

Figure E.24. PCM temperature distribution in plate 8; thermocouples placed 145 mm, 215 mm and 315 mm from the plate leading edge for SP24E for an air mass flow rate of 0.05 kg/s and an inlet temperature of 35 °C.

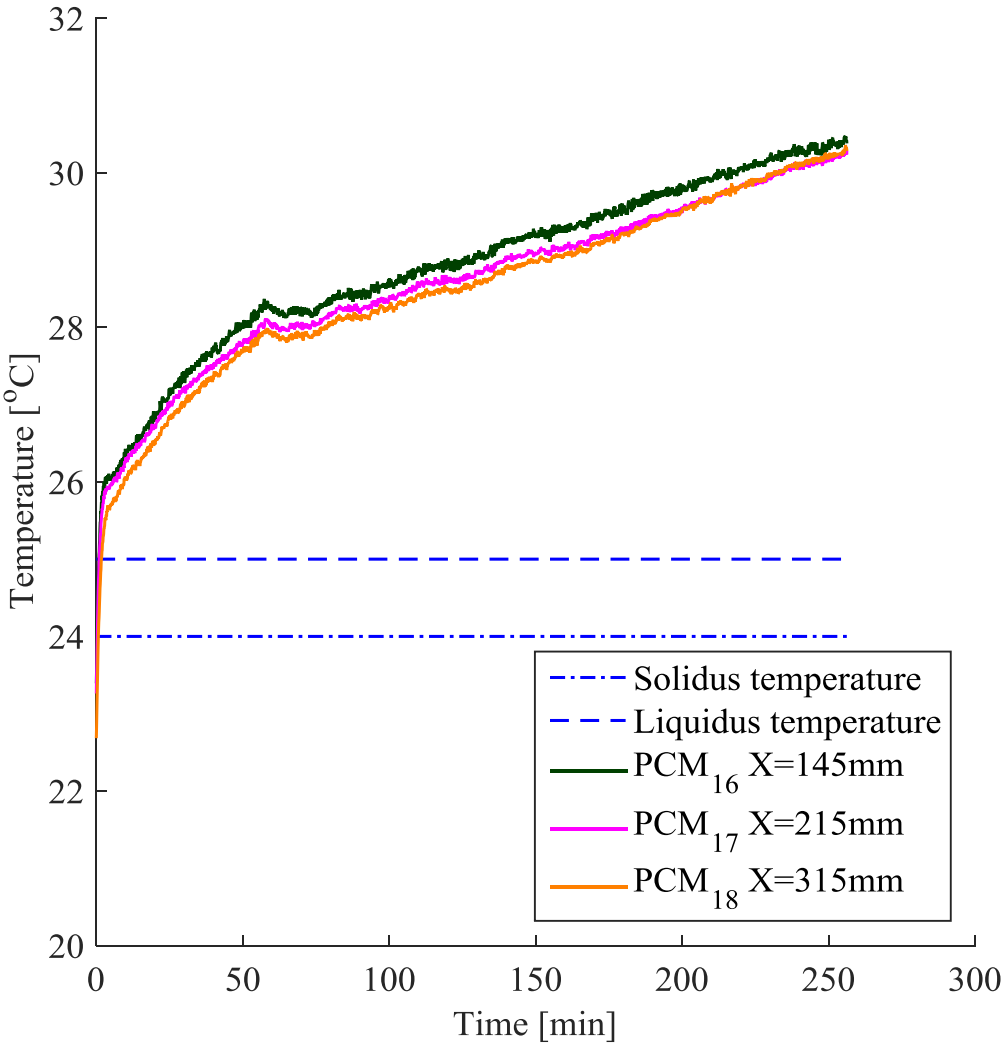

Figure E.25. PCM temperature distribution in plate 8; thermocouples placed 145 mm, 215 mm and 315 mm from the plate leading edge for SP24E for an air mass flow rate of 0.06 kg/s and an inlet temperature of 30 °C.

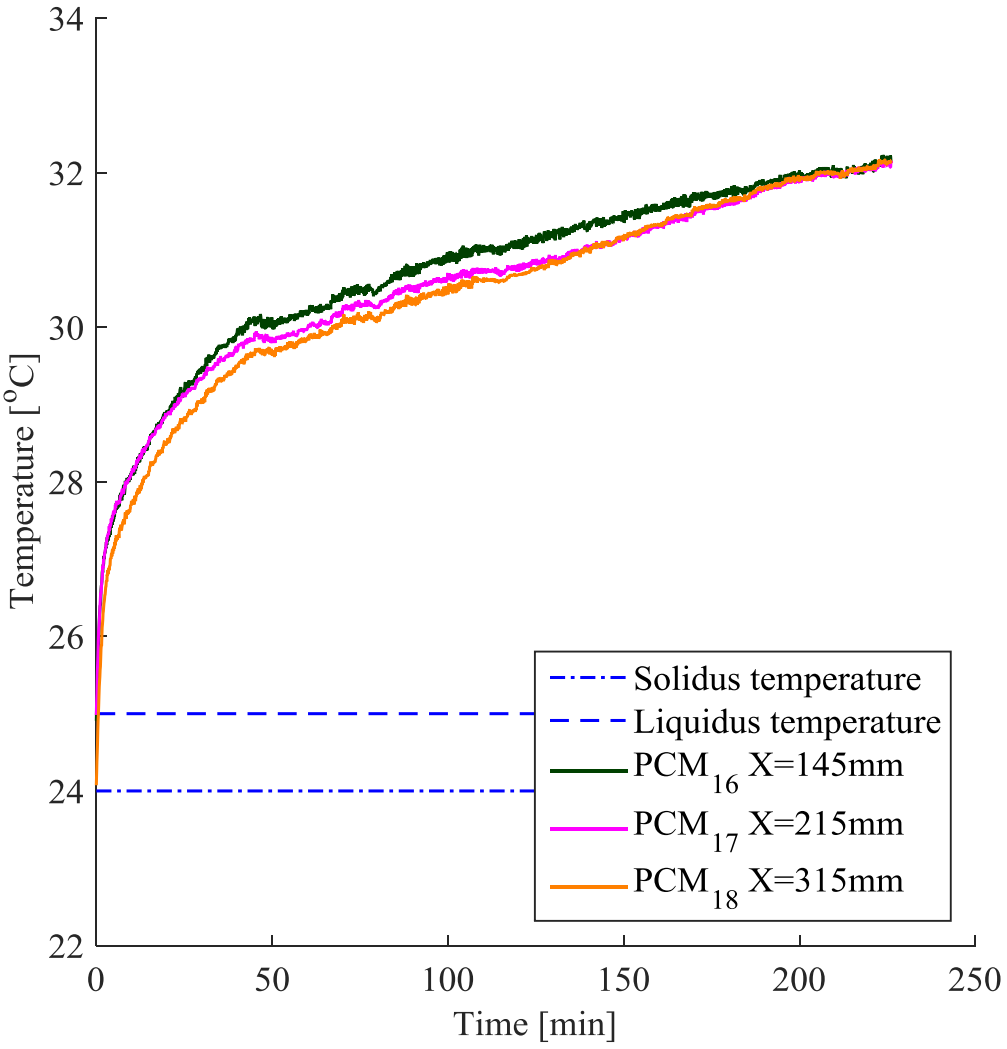

Figure E.26. PCM temperature distribution in plate 8; thermocouples placed 145 mm, 215 mm and 315 mm from the plate leading edge for SP24E for an air mass flow rate of 0.06 kg/s and an inlet temperature of 32 °C.

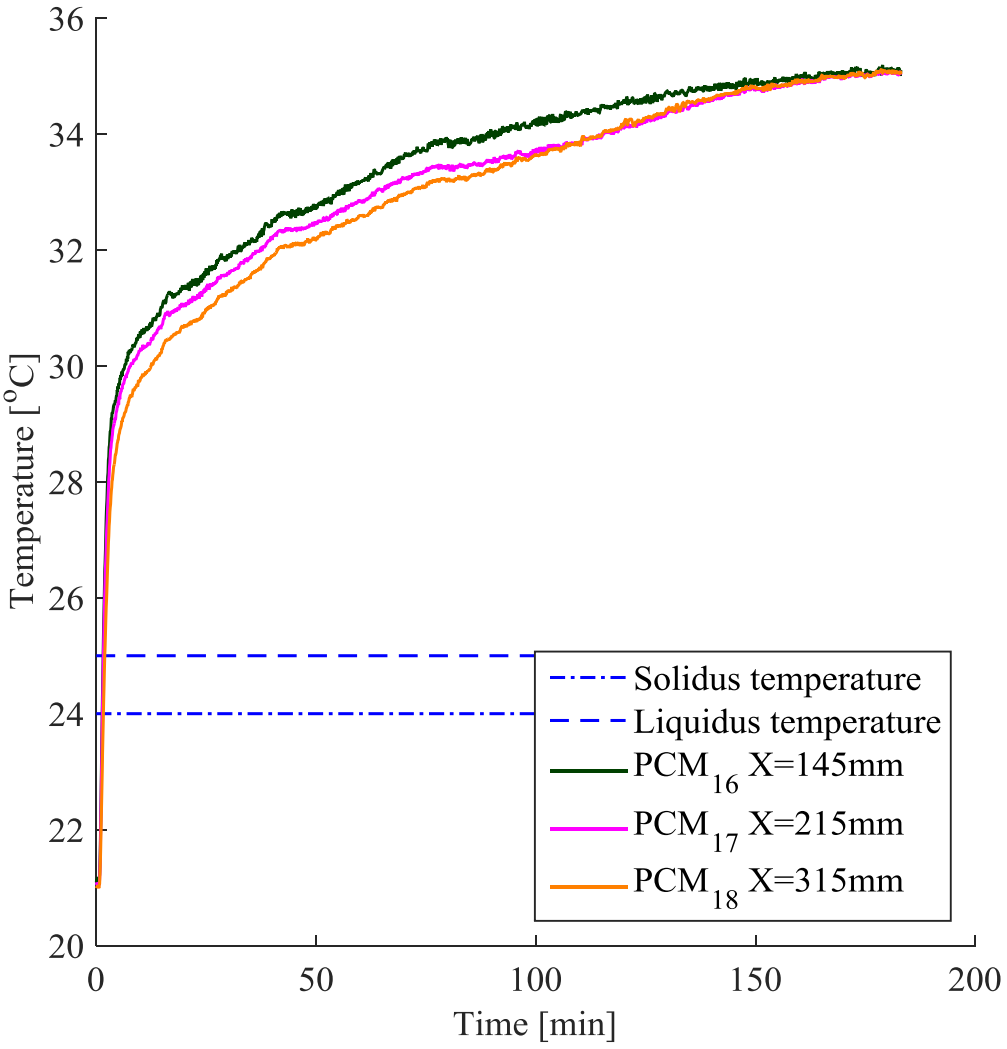

Figure E.27. PCM temperature distribution in plate 8; thermocouples placed 145 mm, 215 mm and 315 mm from the plate leading edge for SP24E for an air mass flow rate of 0.06 kg/s and an inlet temperature of 35 °C.

APPENDIX F. COMPARISON OF COOLING POWER FOR ALL MODULES

This Appendix gives all the experimental results for the comparison of the cooling power delivered by RT25, RT27 and SP24E PCMs.

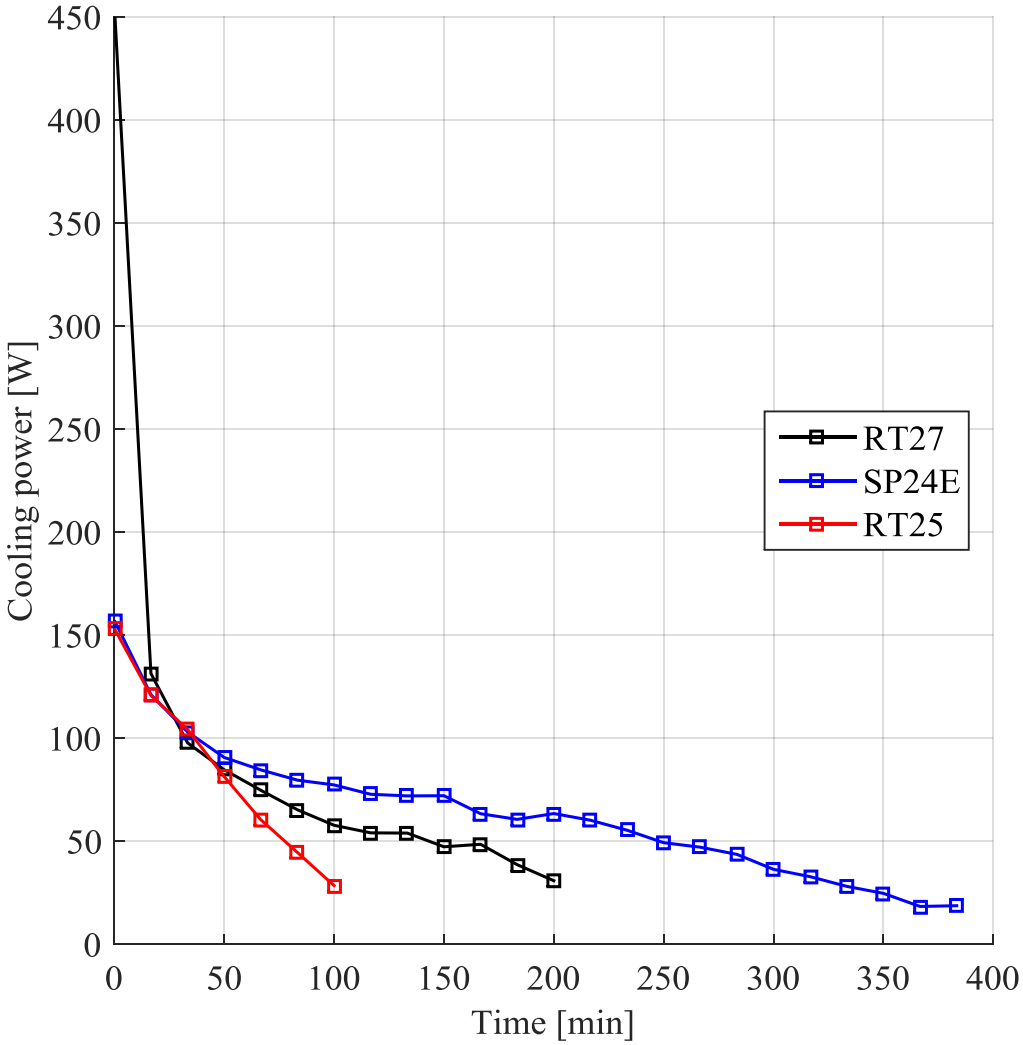

Figure F.1. Comparison of the cooling power delivered by RT25, RT27 and SP24E for an air flow rate of 0.03 kg/s and an air inlet temperature 30 °C.

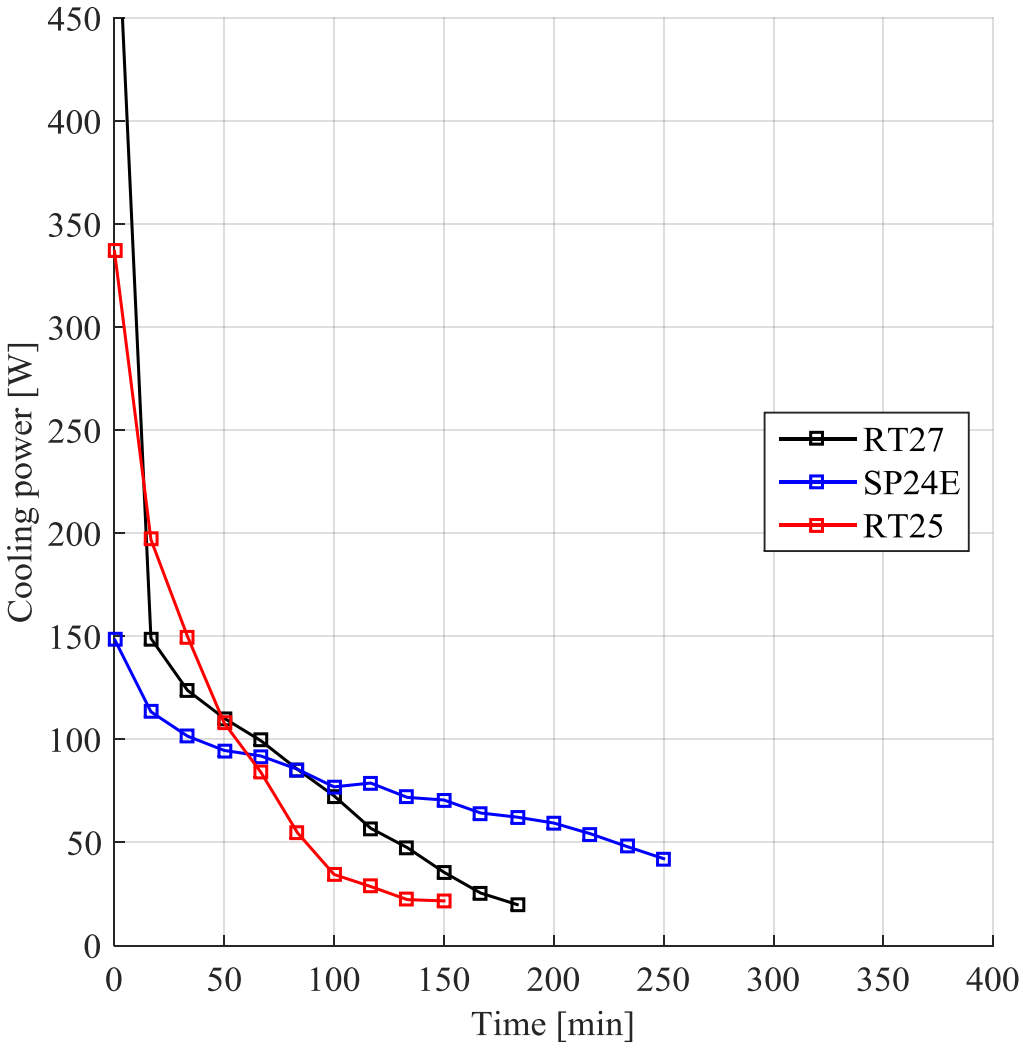

Figure F.2. Comparison of the cooling power delivered by RT25, RT27 and SP24E for an air flow rate of 0.03 kg/s and an air inlet temperature 32 °C.

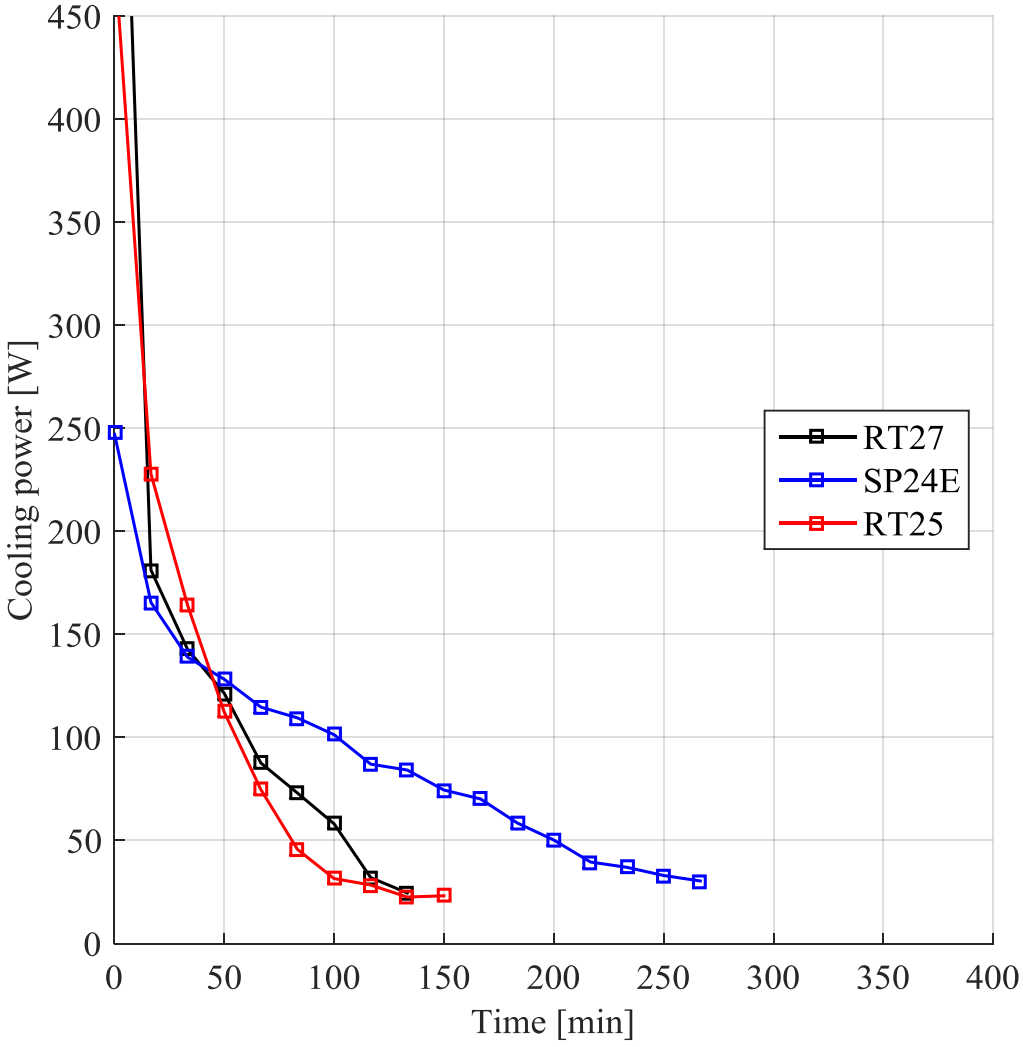

Figure F.3. Comparison of the cooling power delivered by RT25, RT27 and SP24E for an air flow rate of 0.03 kg/s and an air inlet temperature 35 °C.

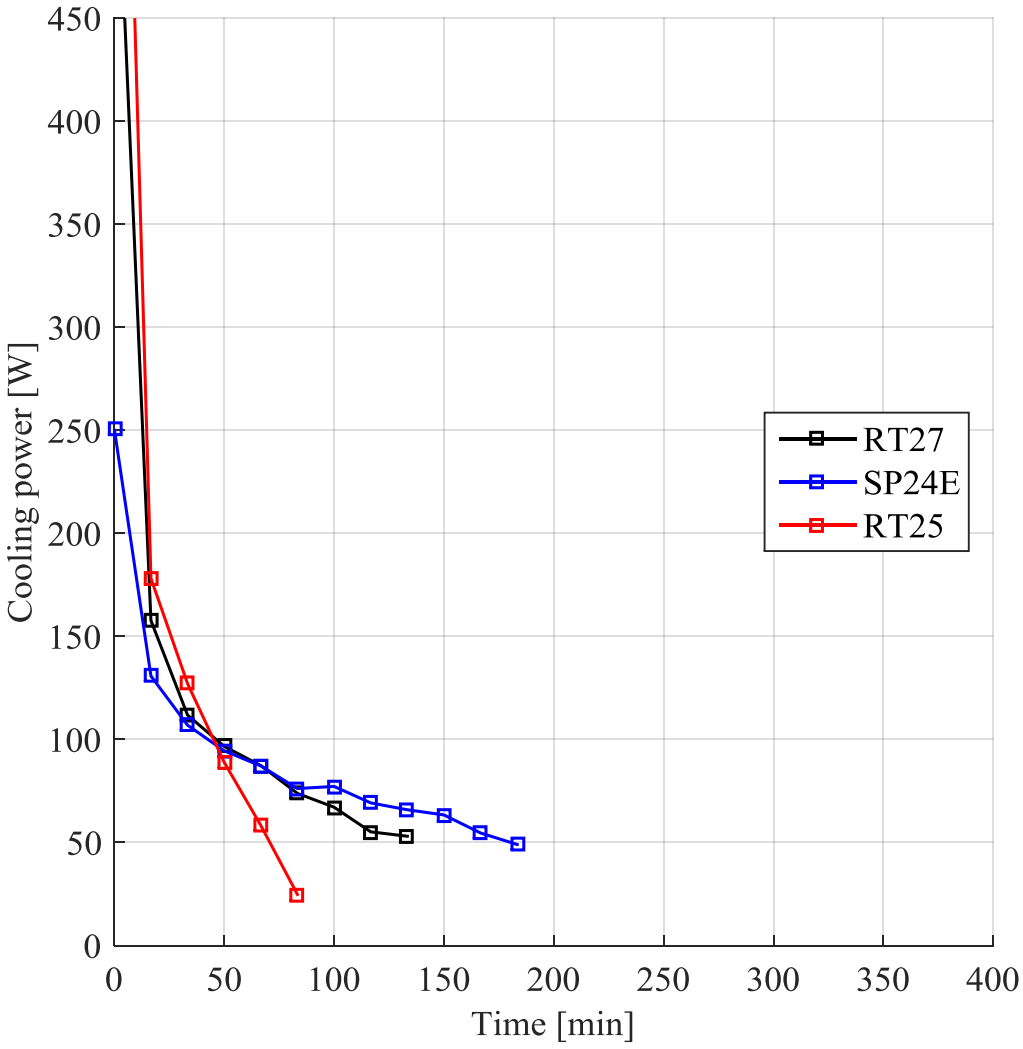

Figure F.4. Comparison of the cooling power delivered by RT25, RT27 and SP24E for an air flow 0.05 kg/s and an air inlet temperature 30 °C.

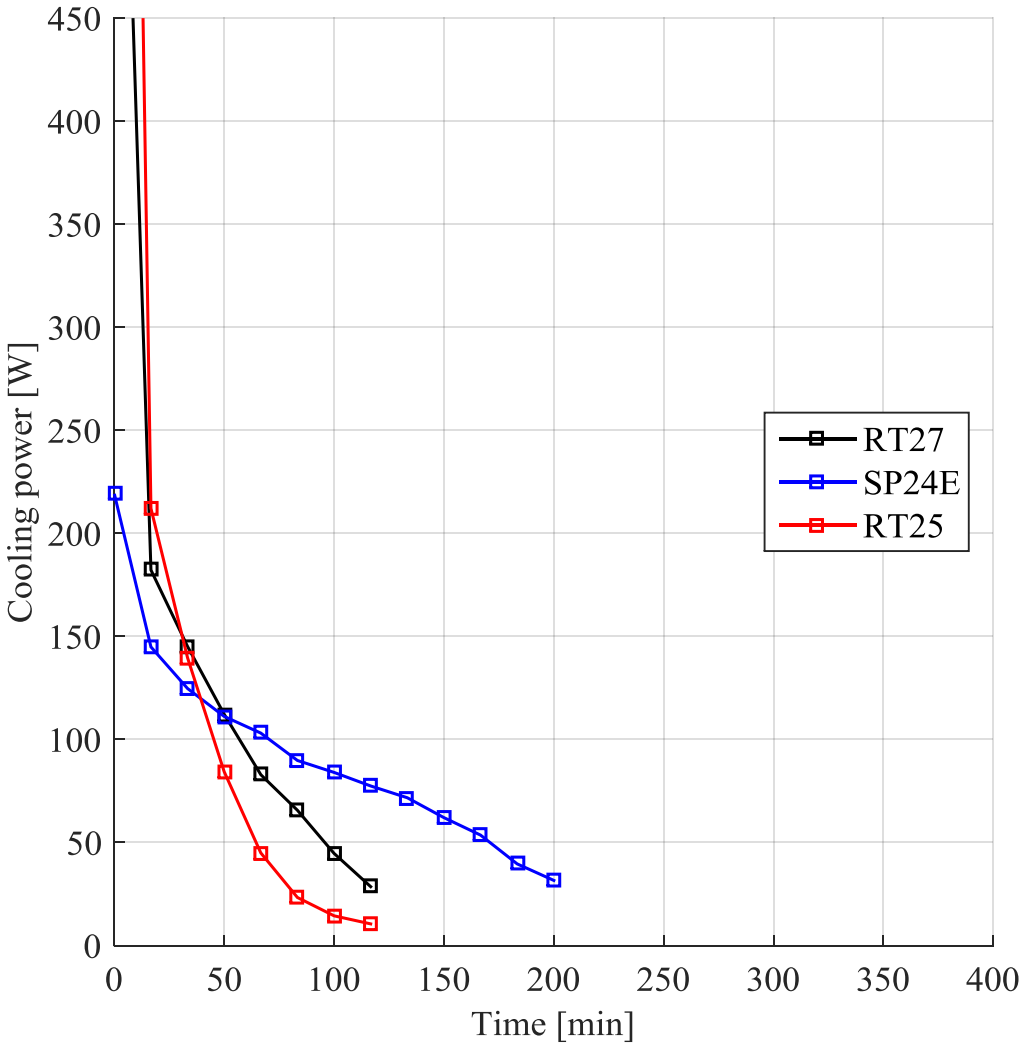

Figure F.5. Comparison of the cooling power delivered by RT25, RT27 and SP24E for air flow rate 0.05 kg/s and an air inlet temperature 32 °C.

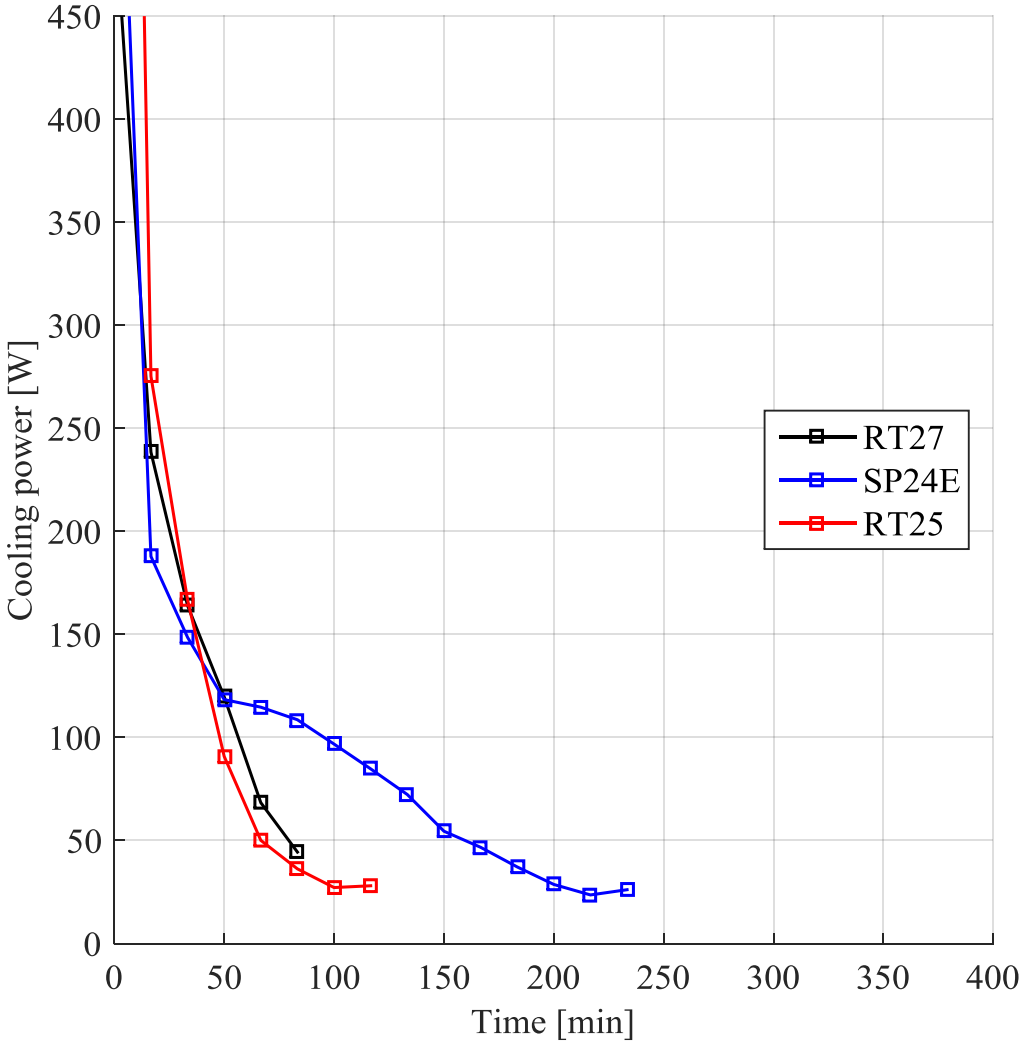

Figure F.6. Comparison of the cooling power delivered by RT25, RT27 and SP24E for an air flow rate of 0.05 kg/s and an air inlet temperature 35 °C.

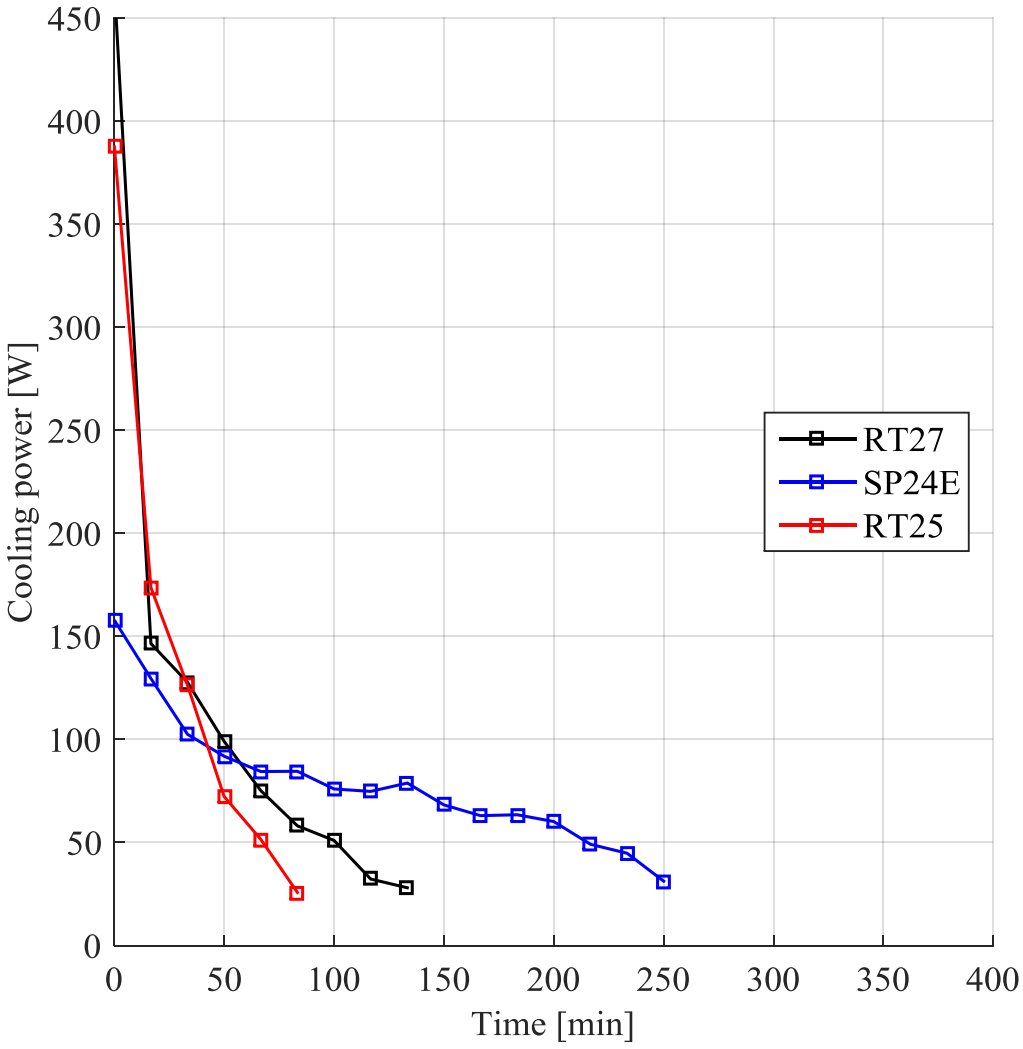

Figure F.7. Comparison of the cooling power delivered by RT25, RT27 and SP24E for an air flow rate of 0.06 kg/s and an air inlet temperature 30 °C.

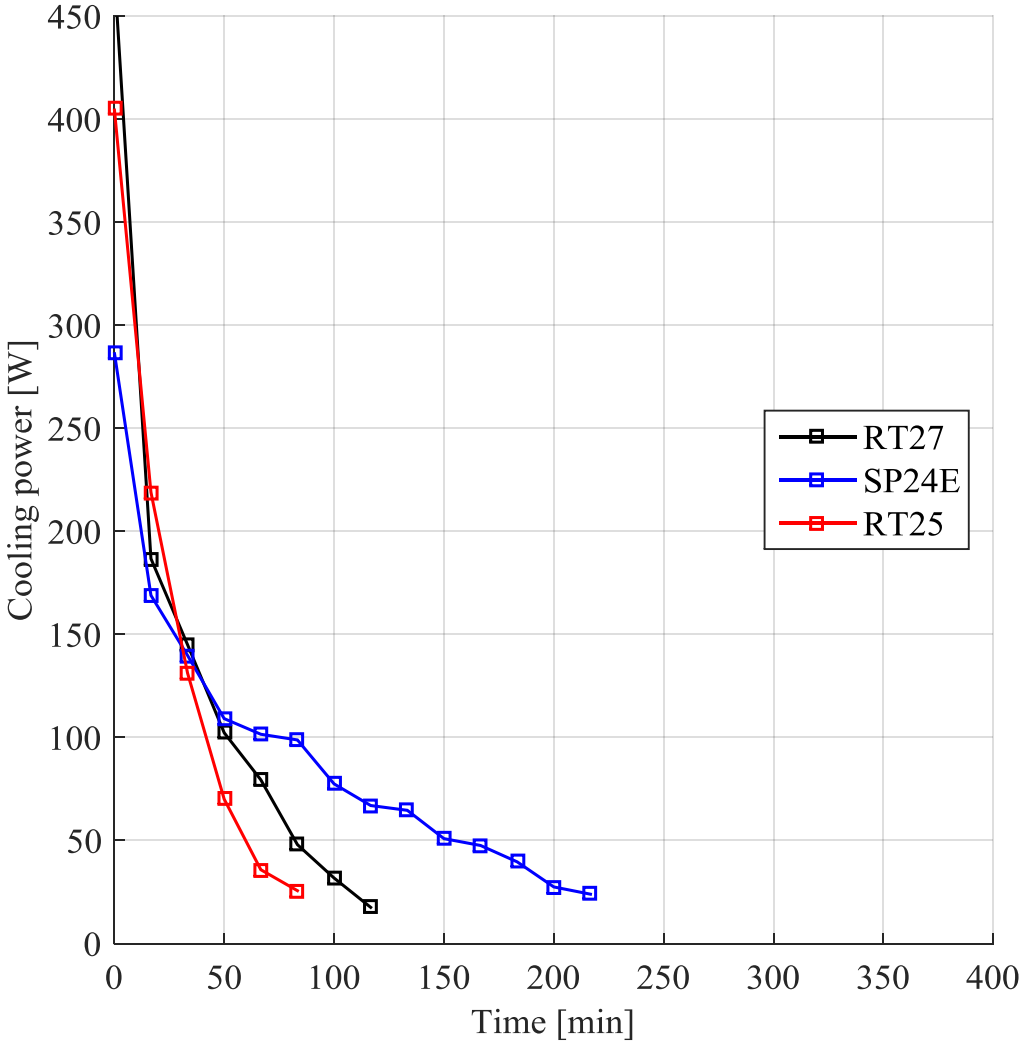

Figure F.8. Comparison of the cooling power delivered by RT25, RT27 and SP24E for an air flow rate of 0.06 kg/s and an air inlet temperature 32 °C.

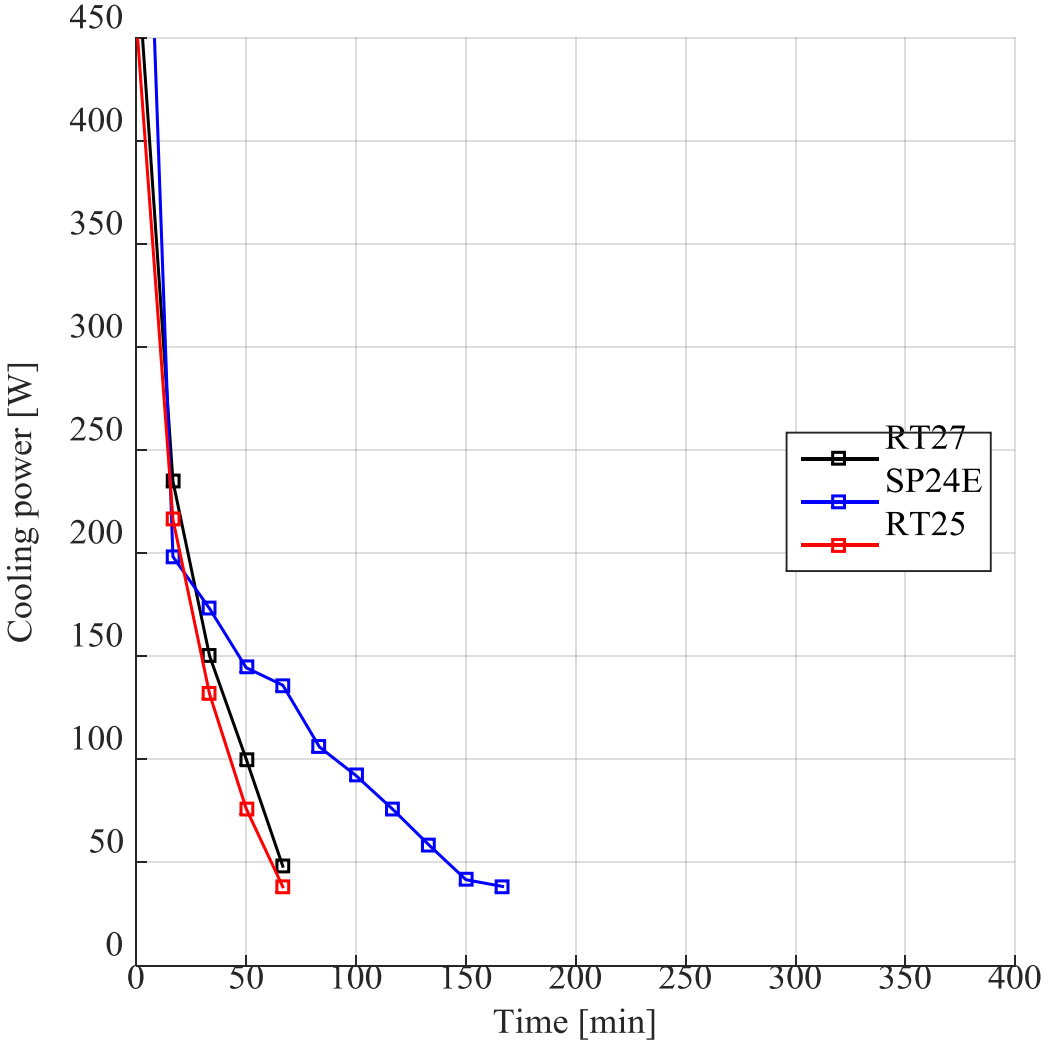

Figure F.9. Comparison of the cooling power delivered by RT25, RT27 and SP24E for an air flow rate of 0.06 kg/s and an air inlet temperature 35 °C.

APPENDIX G. EFFECT OF FLOW RATE ON COOLING POWER

This Appendix gives all the experimental results for the effect of the air mass flow rate on the cooling power delivered by the RT27, RT25 and SP24E modules.

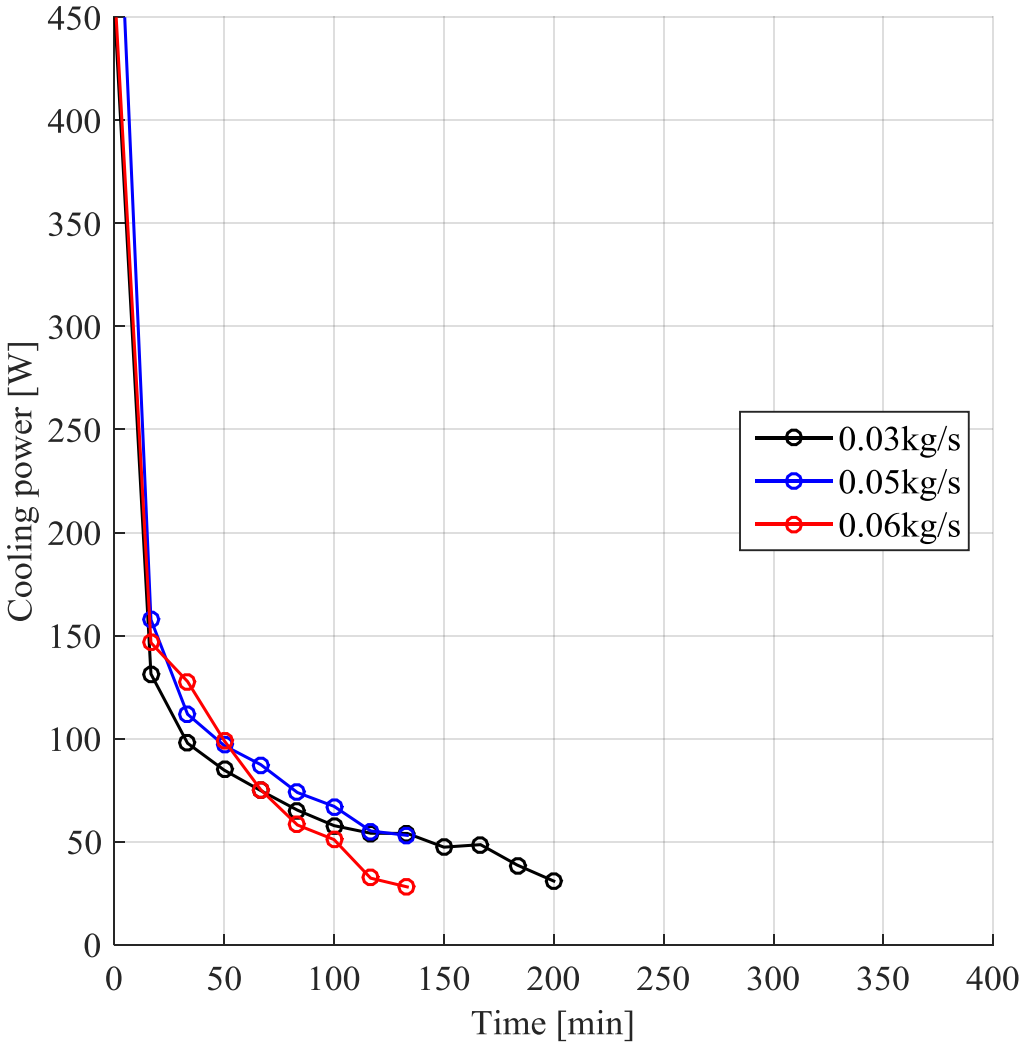

Figure G.1. Effect of the air mass flow rate on the cooling power delivered by an RT27 module at inlet air temperature of 30°C.

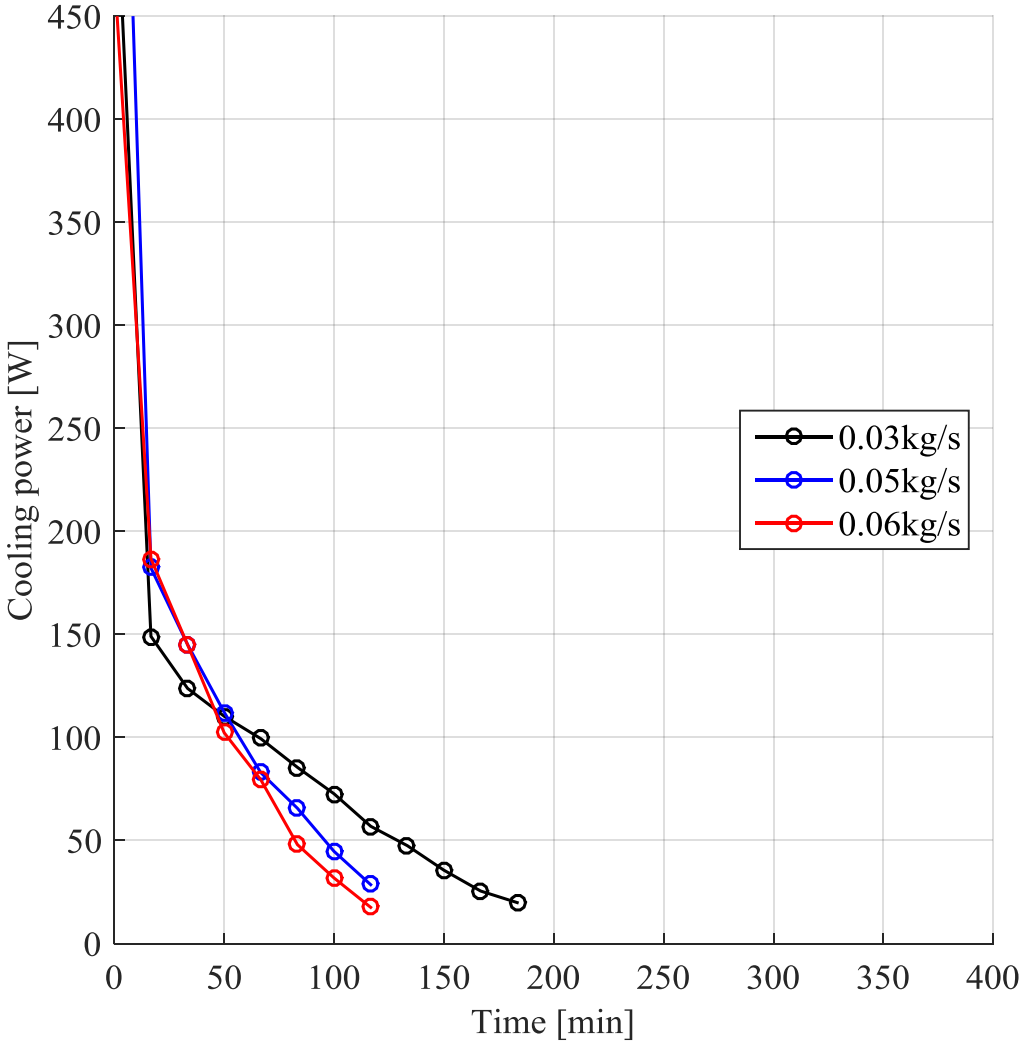

Figure G.2. Effect of the air mass flow rate on the cooling power delivered by an RT27 module at inlet air temperature of 32°C.

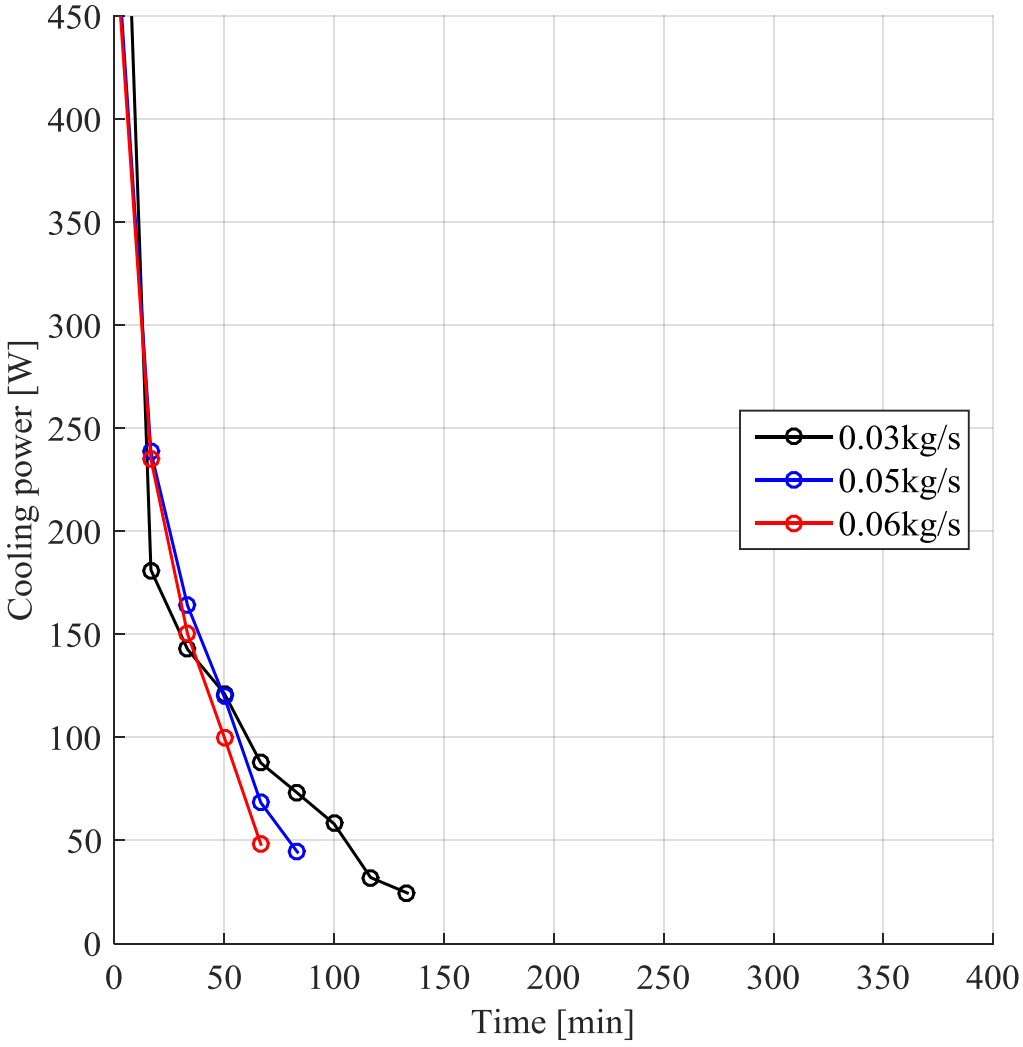

Figure G.3. Effect of the air mass flow rate on the cooling power delivered by an RT27 module at inlet air temperature of 35°C.

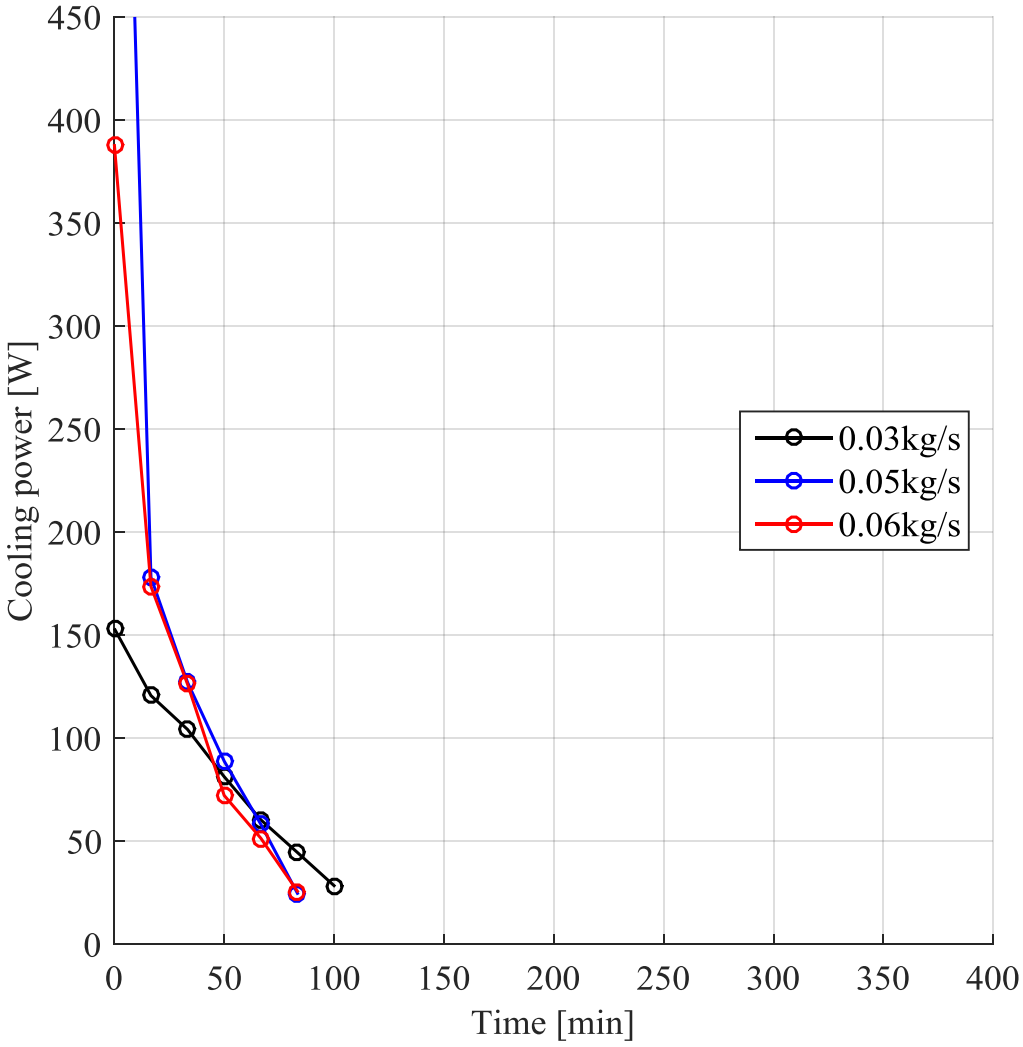

Figure G.4. Effect of the air mass flow rate on the cooling power delivered by an RT25 module at inlet air temperature of 30°C.

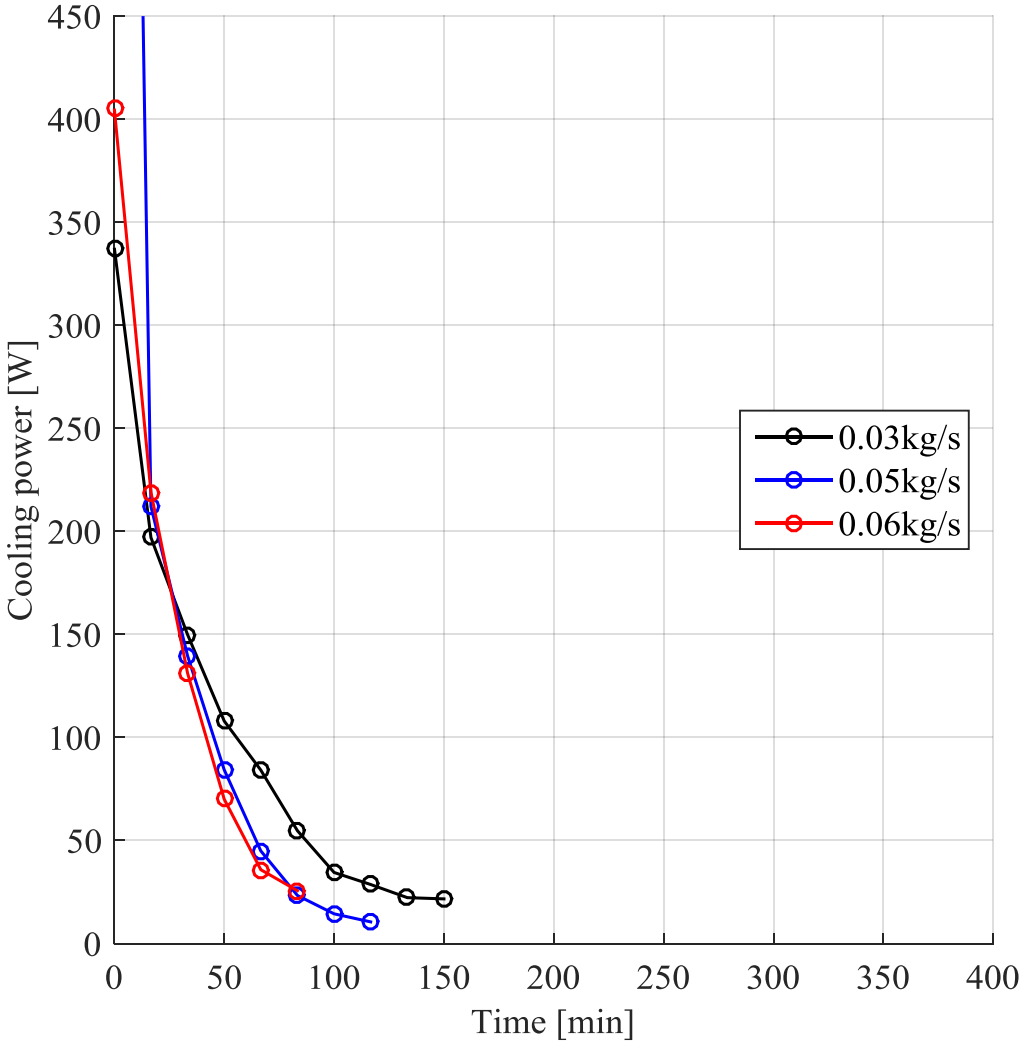

Figure G.5. Effect of the air mass flow rate on the cooling power delivered by an RT25 module at inlet air temperature of 32°C.

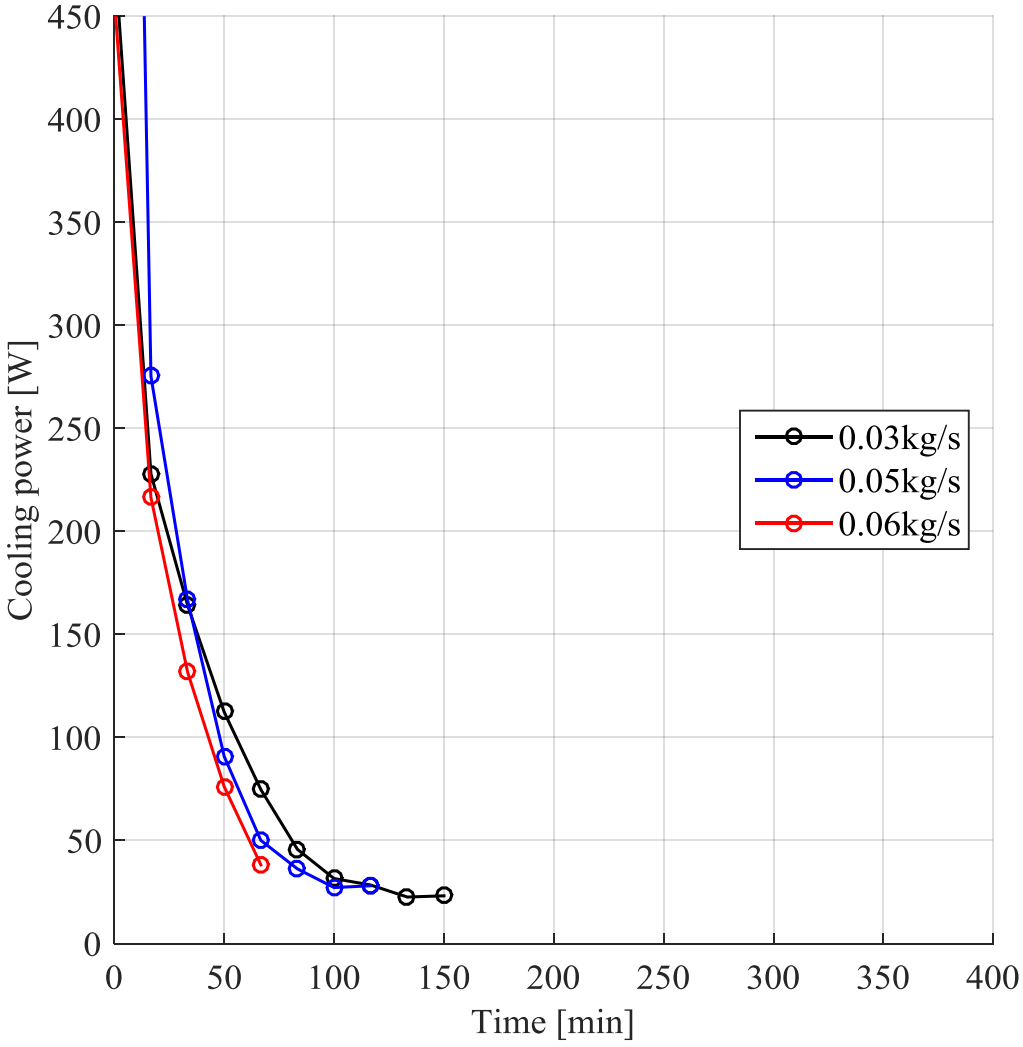

Figure G.6. Effect of the air mass flow rate on the cooling power delivered by an RT25 module at inlet air temperature of 35°C.

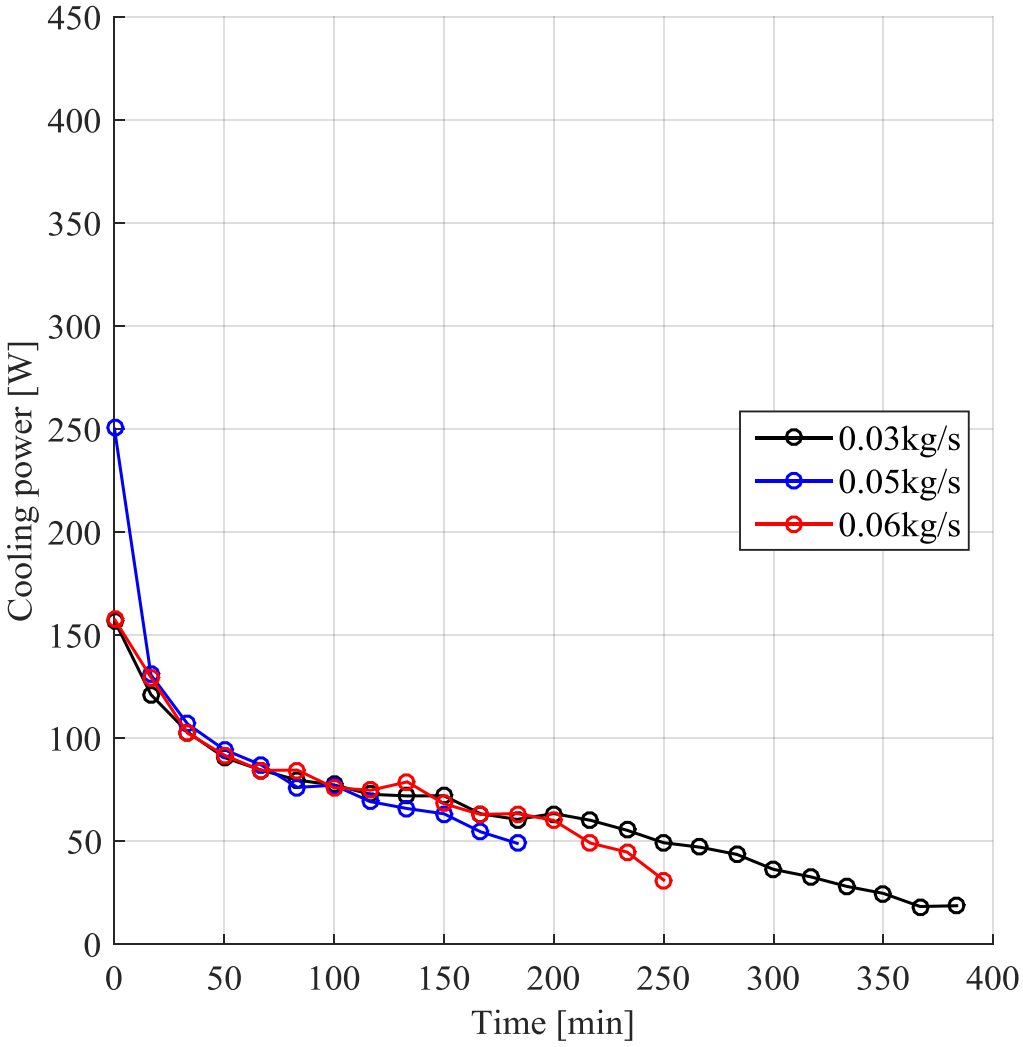

Figure G.7. Effect of the air mass flow rate on the cooling power delivered by an SP24E module at inlet air temperature of 30°C.

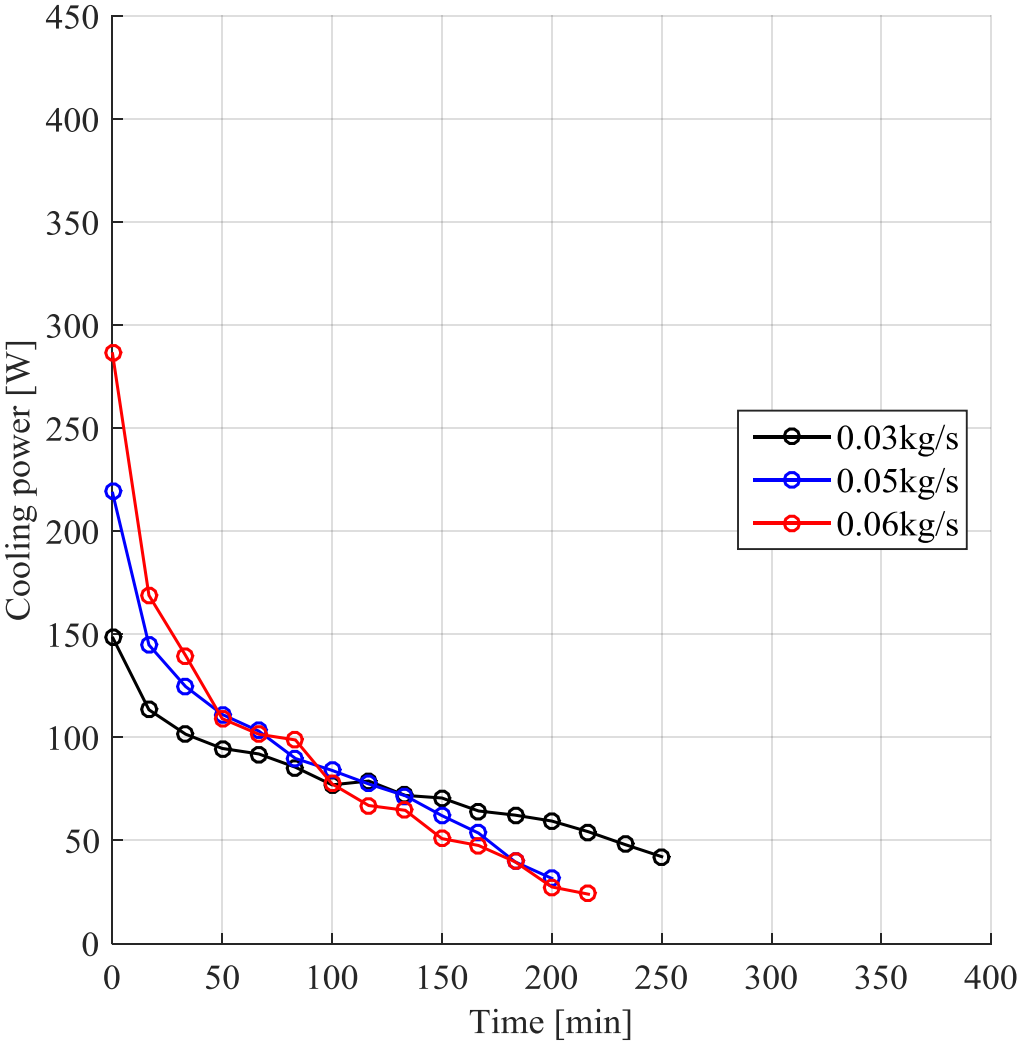

Figure G.8. Effect of the air mass flow rate on the cooling power delivered by an SP24E module at inlet air temperature of 32°C.

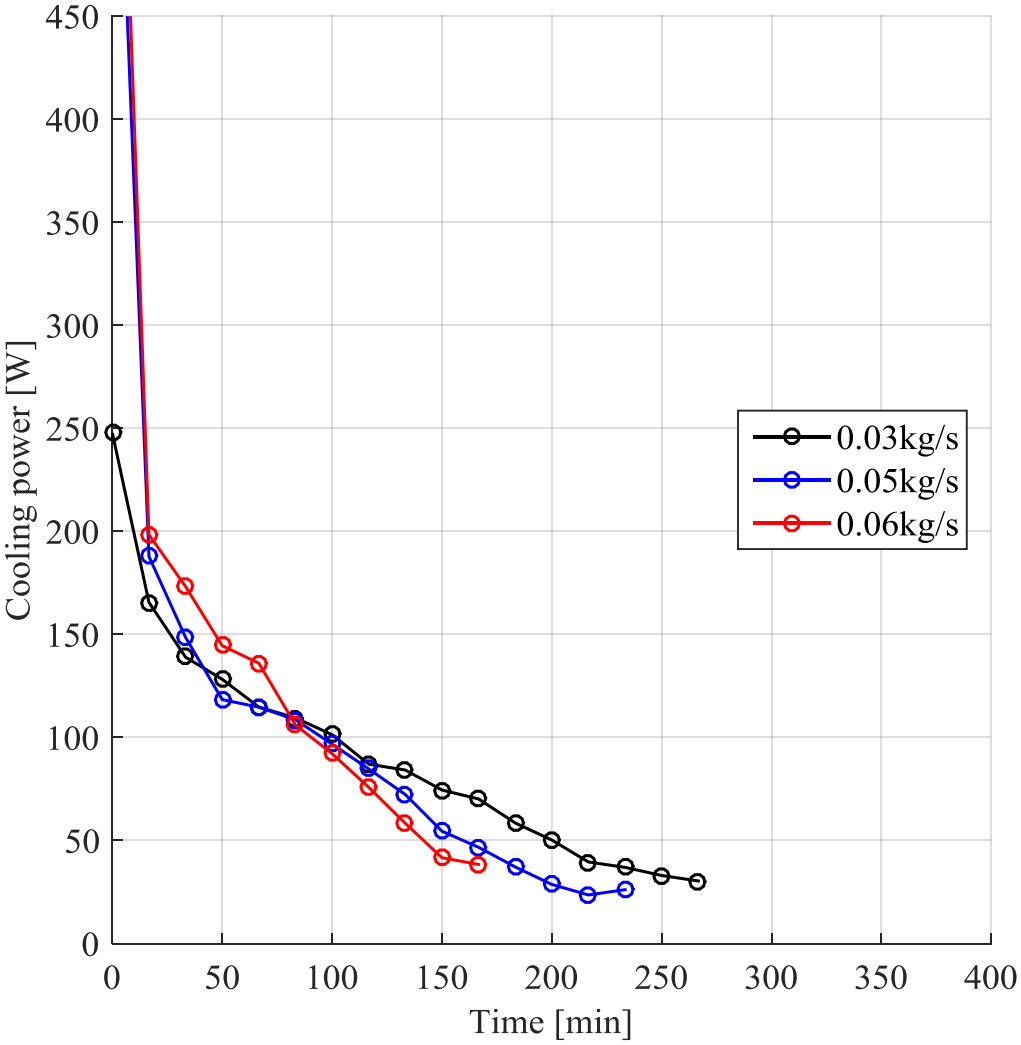

Figure G.9. Effect of the air mass flow rate on the cooling power delivered by an SP24E module at inlet air temperature of 35°C.

APPENDIX H. EFFECT OF INLET AIR TEMPERATURE ON COOLING POWER

This Appendix gives all the experimental results for the effect of the inlet air temperature on the cooling power delivered by the RT27, RT25 and SP24E modules.

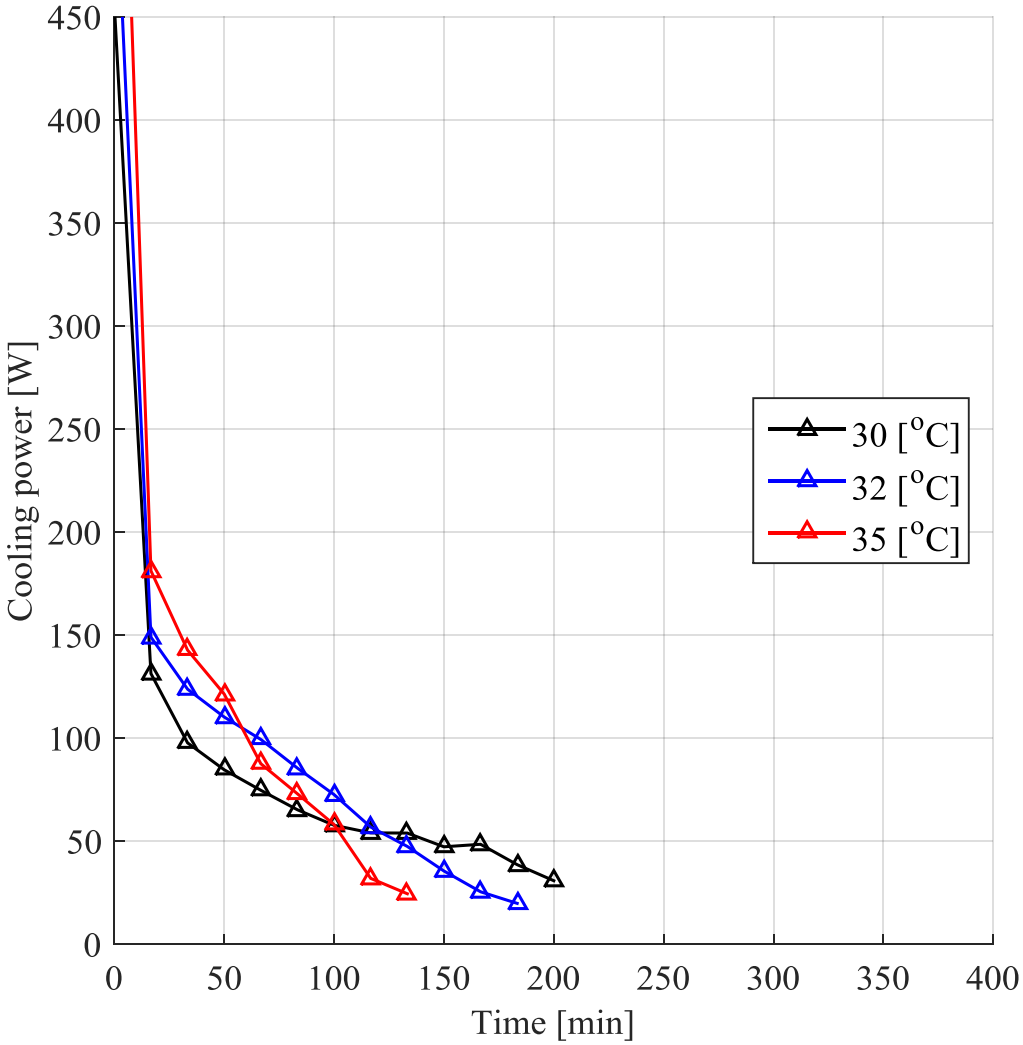

Figure H.1. Effect of the inlet air temperature on the cooling power delivered by an RT27 module at air mass flow rate of 0.03 kg/s.

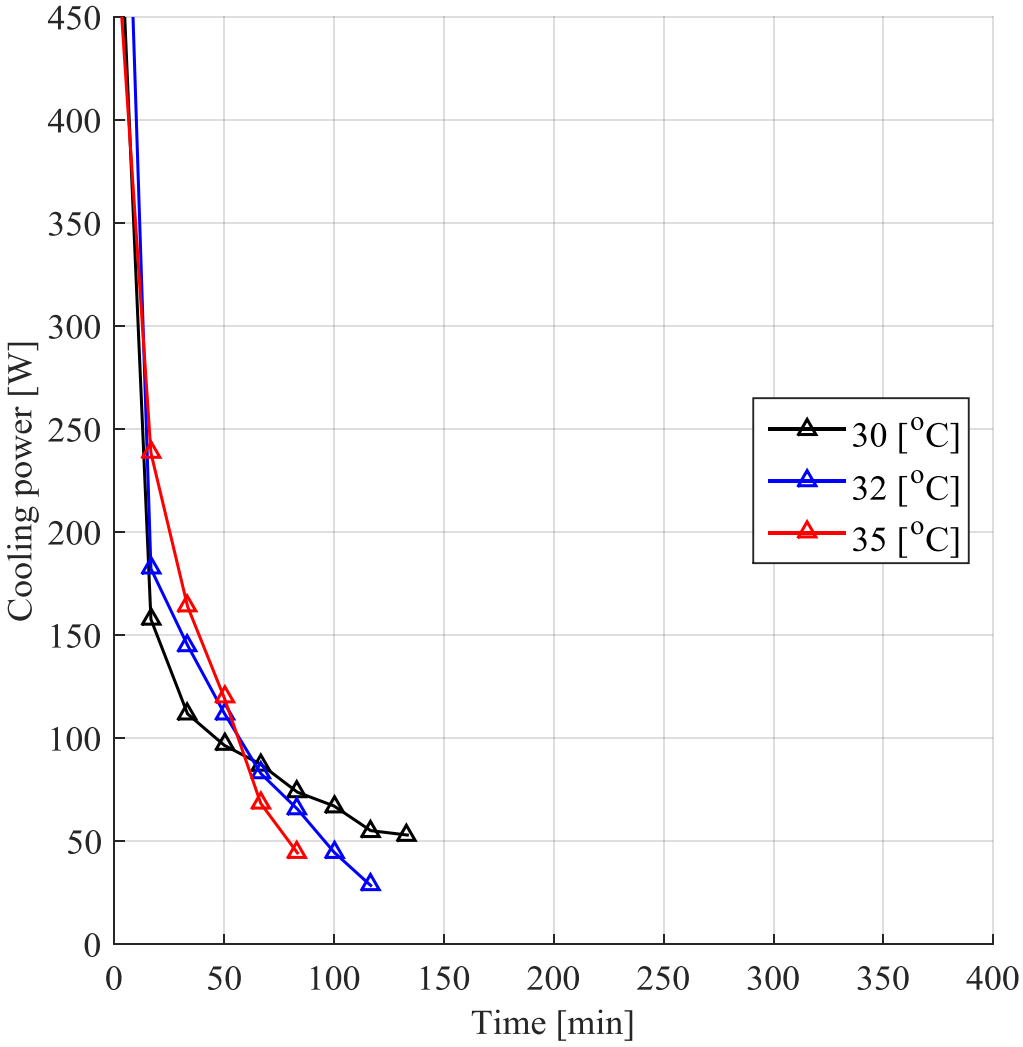

Figure H.2. Effect of the inlet air temperature on the cooling power delivered by an RT27 module at air mass flow rate of 0.05 kg/s.

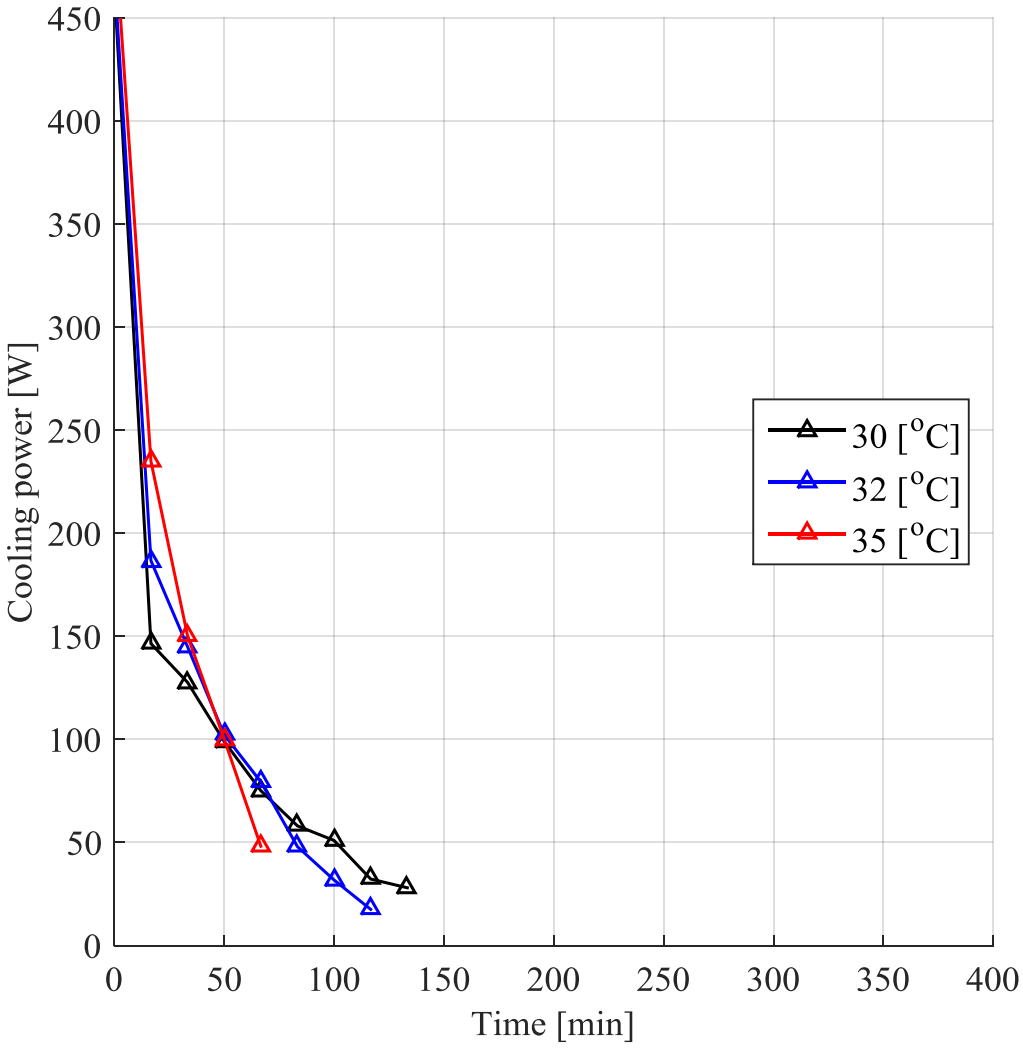

Figure H.3. Effect of the inlet air temperature on the cooling power delivered by an RT27 module at air mass flow rate of 0.06 kg/s.

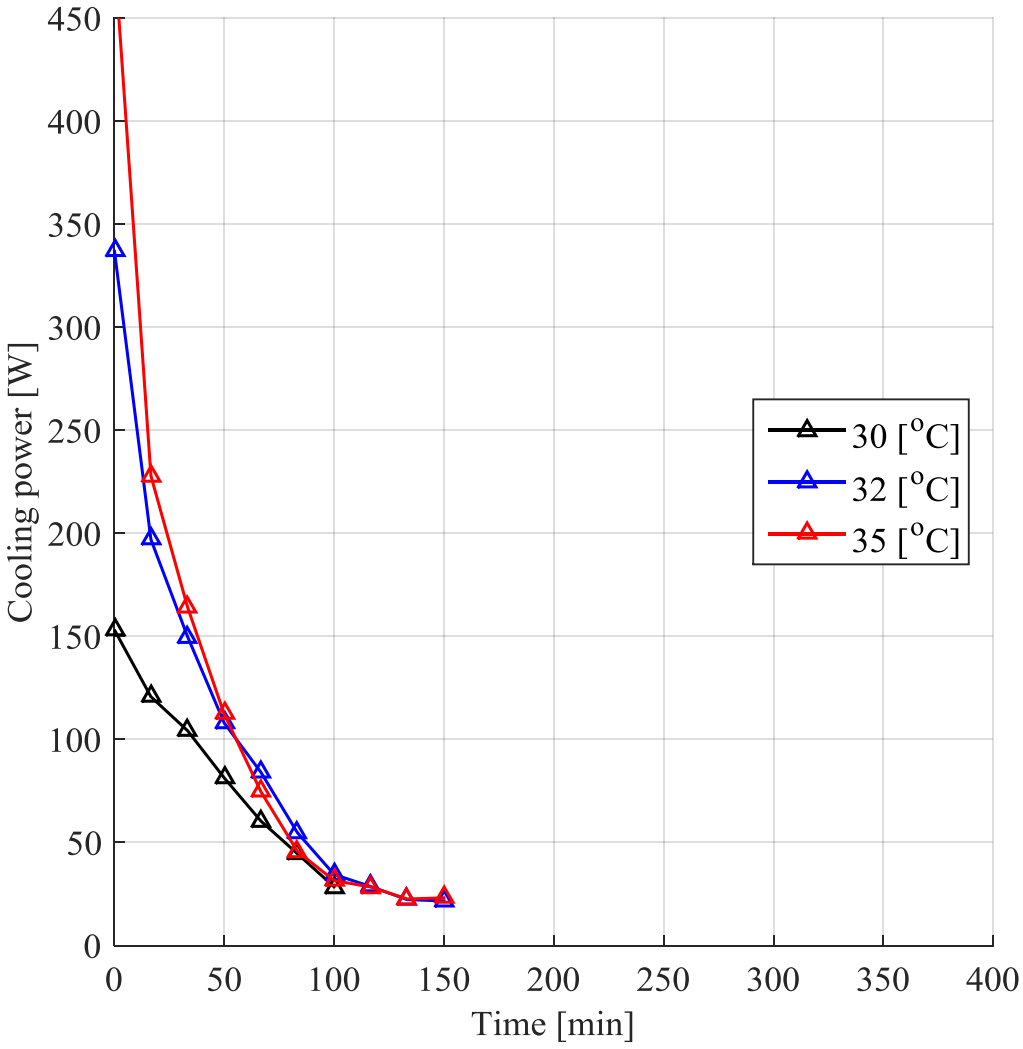

Figure H.4. Effect of the inlet air temperature on the cooling power delivered by an RT25 module at air mass flow rate of 0.03 kg/s.

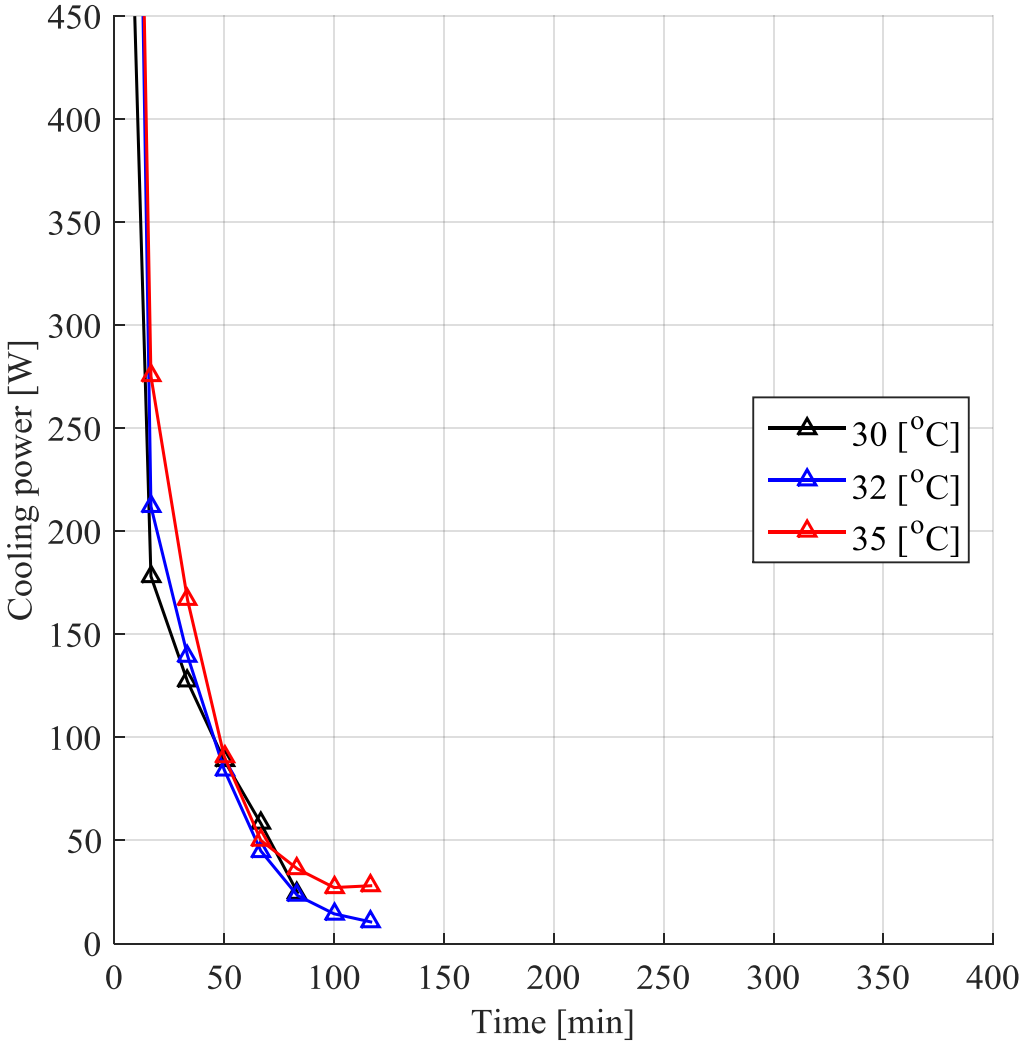

Figure H.5. Effect of the inlet air temperature on the cooling power delivered by an RT25 module at air mass flow rate of 0.05 kg/s.

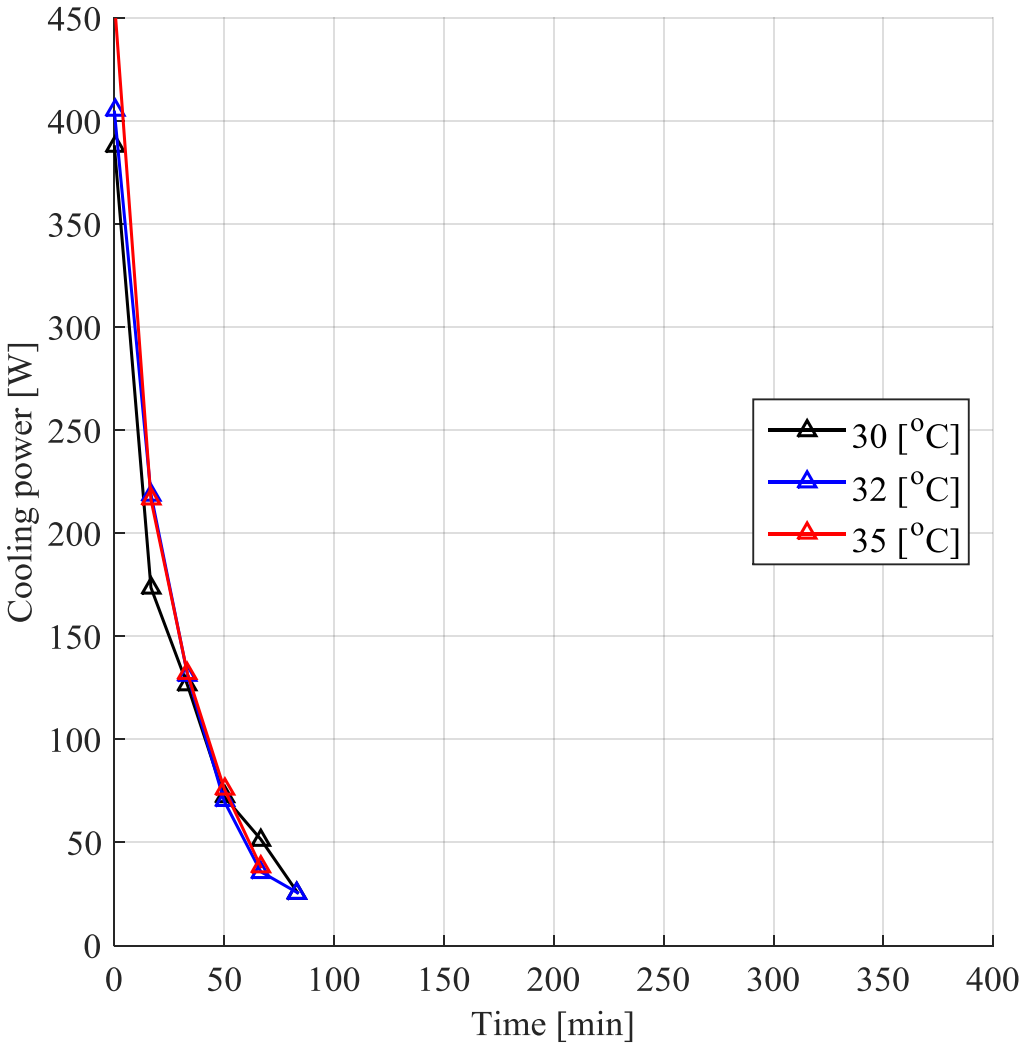

Figure H.6. Effect of the inlet air temperature on the cooling power delivered by an RT25 module at air mass flow rate of 0.06 kg/s.

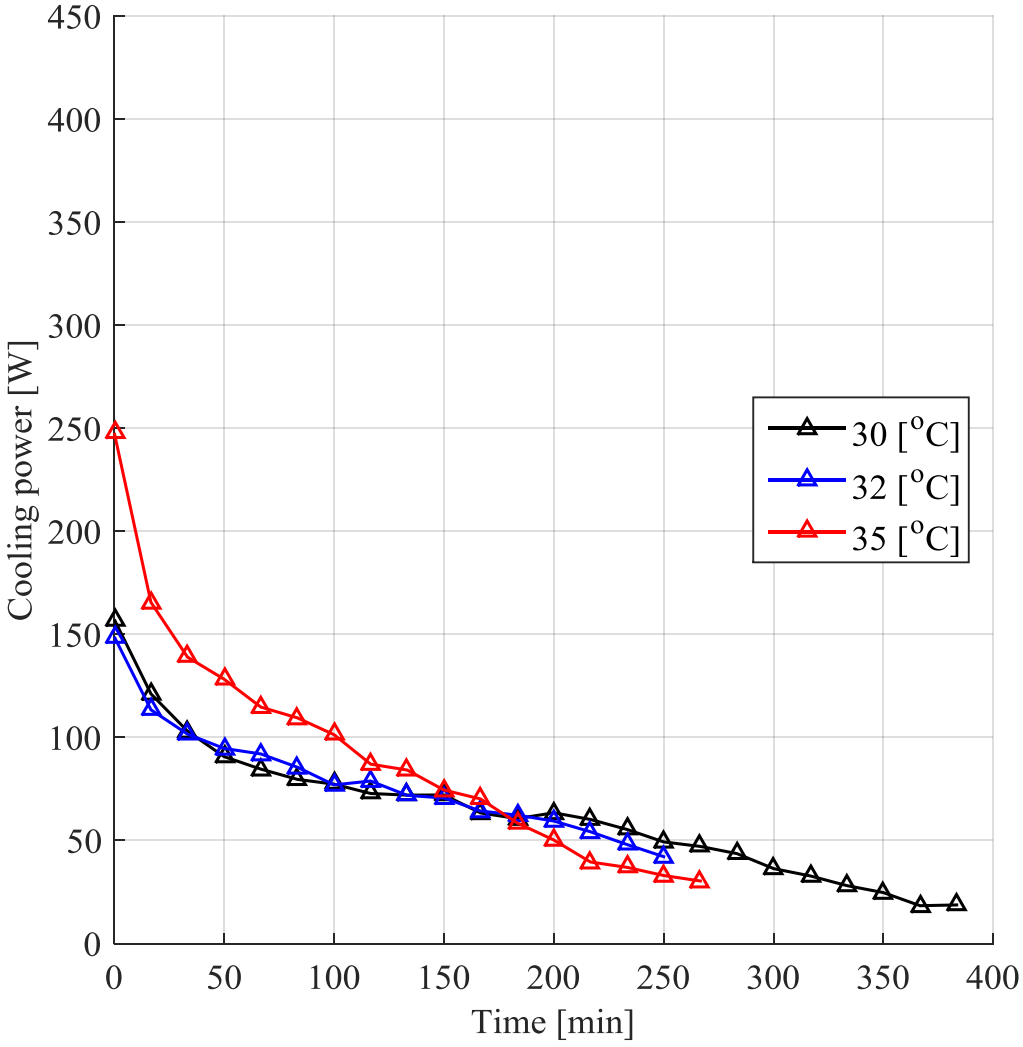

Figure H.7. Effect of the inlet air temperature on the cooling power delivered by an SP24E module at air mass flow rate of 0.03 kg/s.

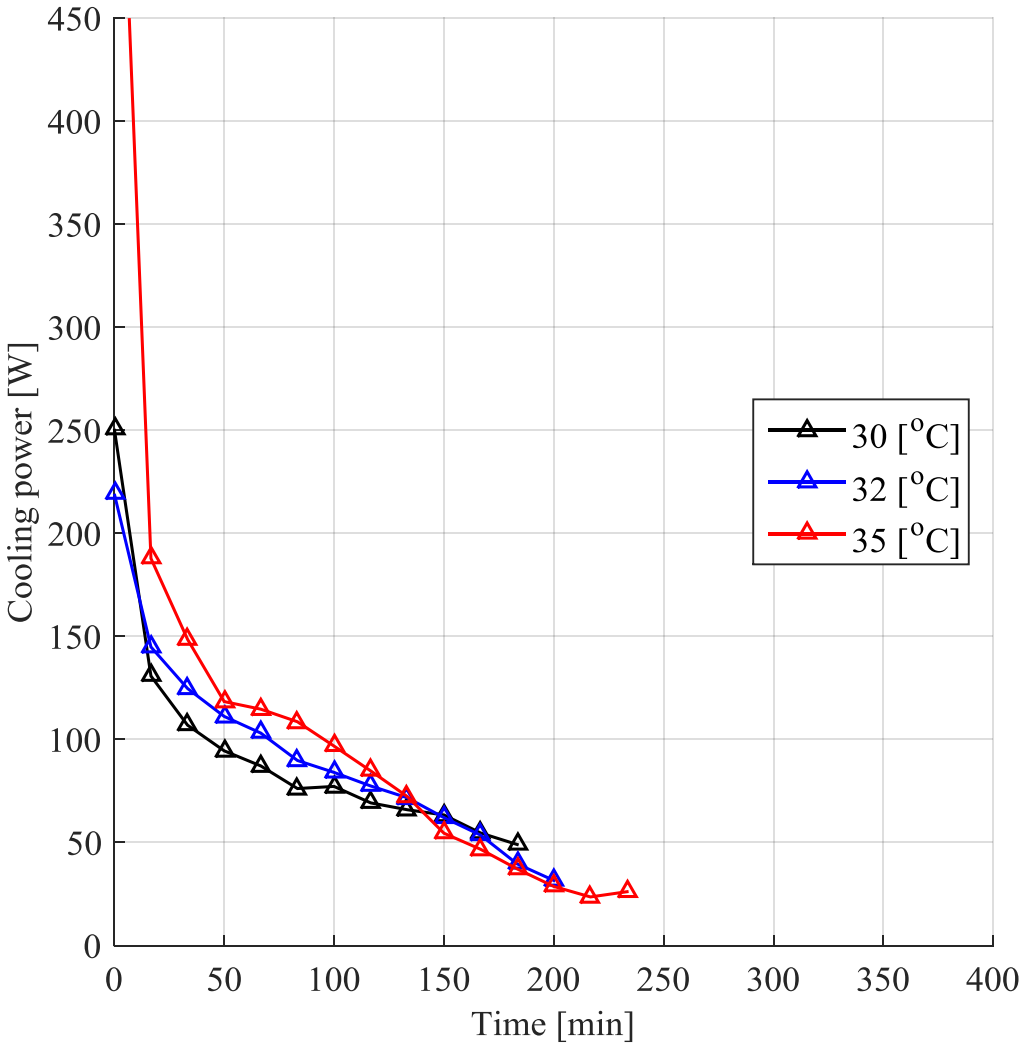

Figure H.8. Effect of the inlet air temperature on the cooling power delivered by an SP24E module at air mass flow rate of 0.05 kg/s.

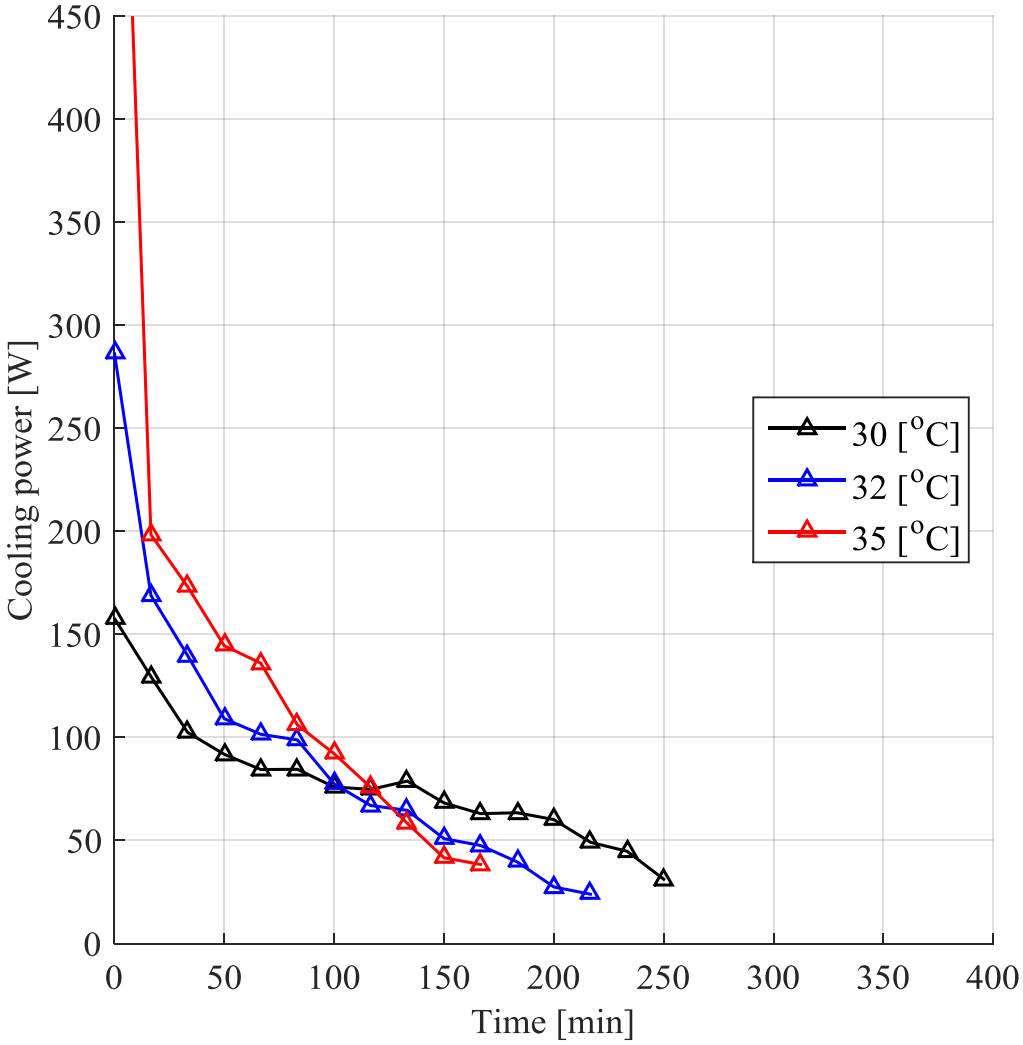

Figure H.9. Effect of the inlet air temperature on the cooling power delivered by an SP24E module at air mass flow rate of 0.06 kg/s.

APPENDIX I. COMPARISON CUMULATIVE ENERGY ABSORBED FOR ALL MODULES

This Appendix gives all the experimental results for the comparison of cumulative energy stored by the RT25, RT27 and SP24E modules.

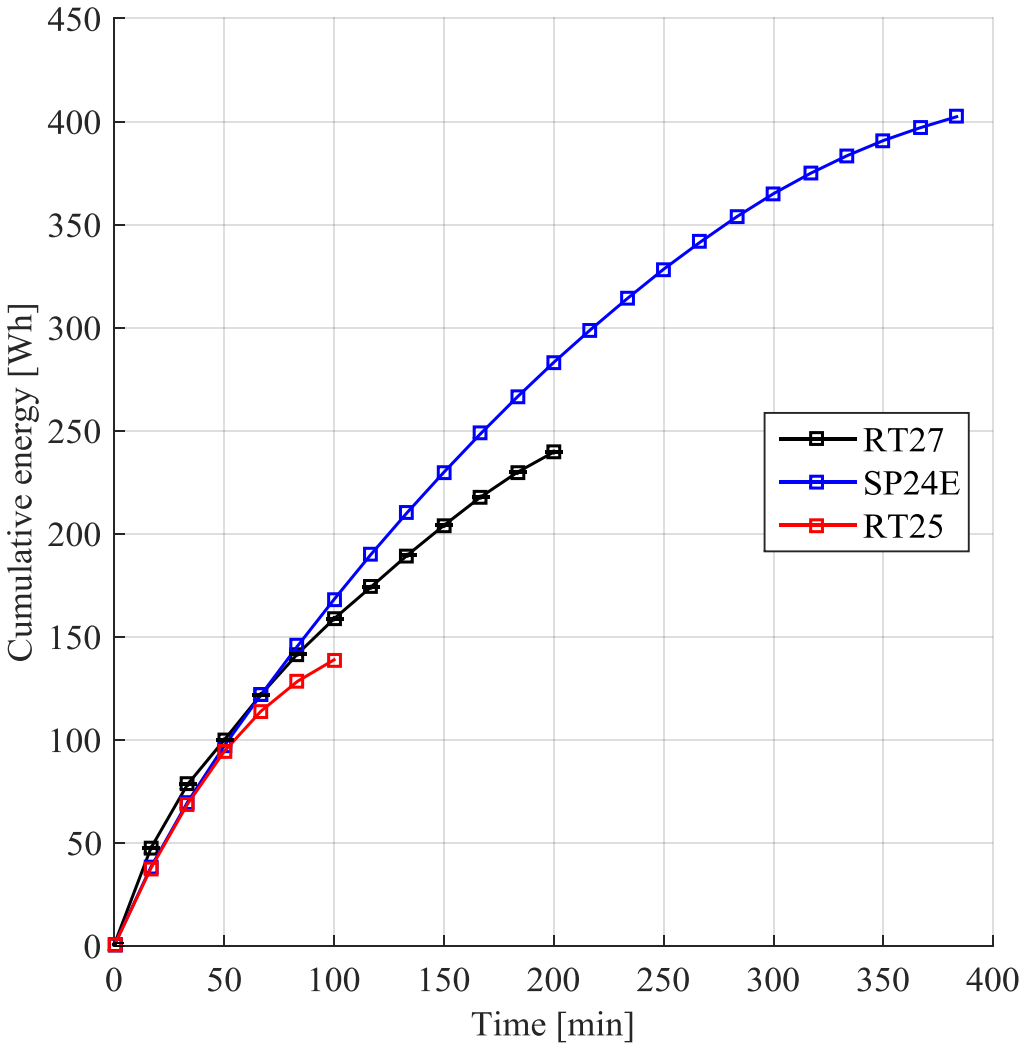

Figure I.1. Comparison of cumulative energy stored by the RT25, RT27 and SP24E modules for an air flow rate of 0.03 kg/s and an air inlet temperature 30 °C.

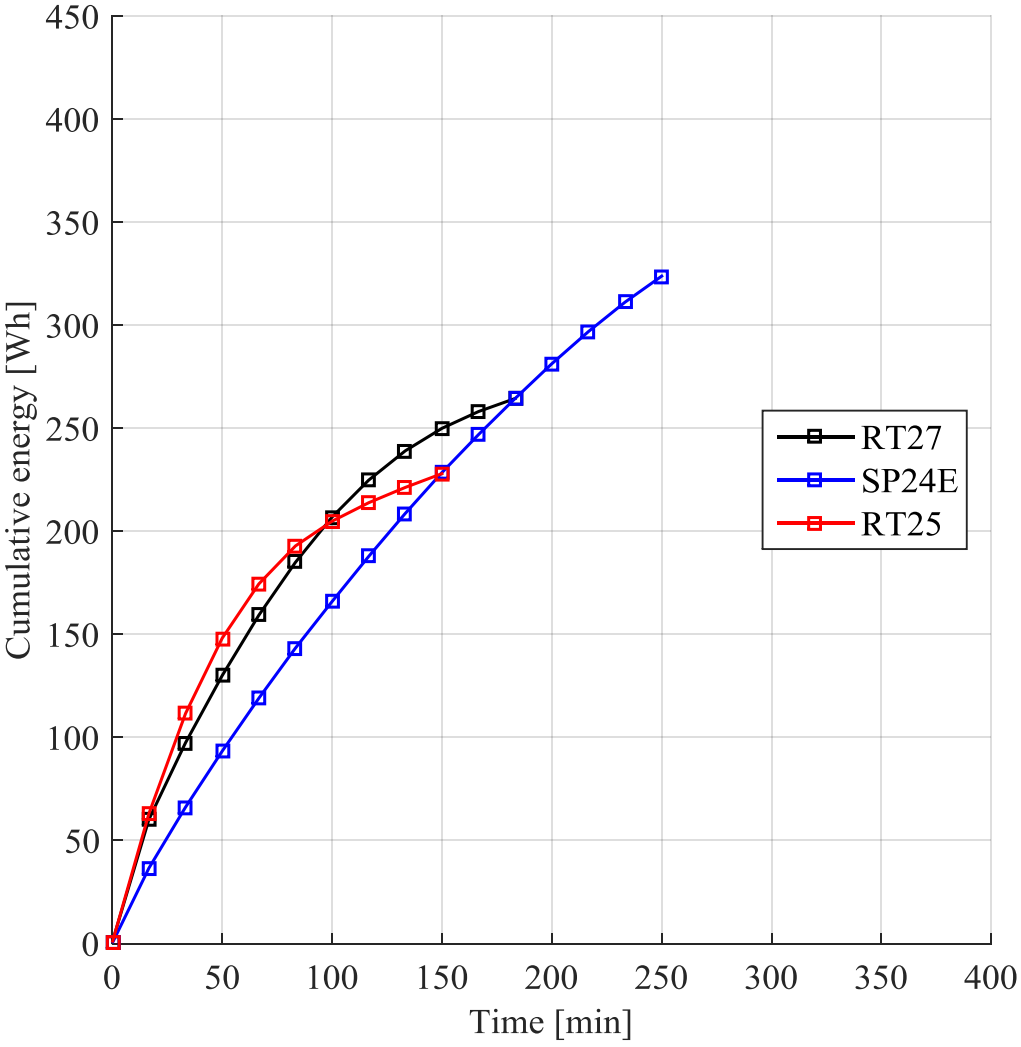

Figure I.2. Comparison of cumulative energy stored by the RT25, RT27 and SP24E modules for an air flow rate of 0.03 kg/s and an air inlet temperature 32 °C.

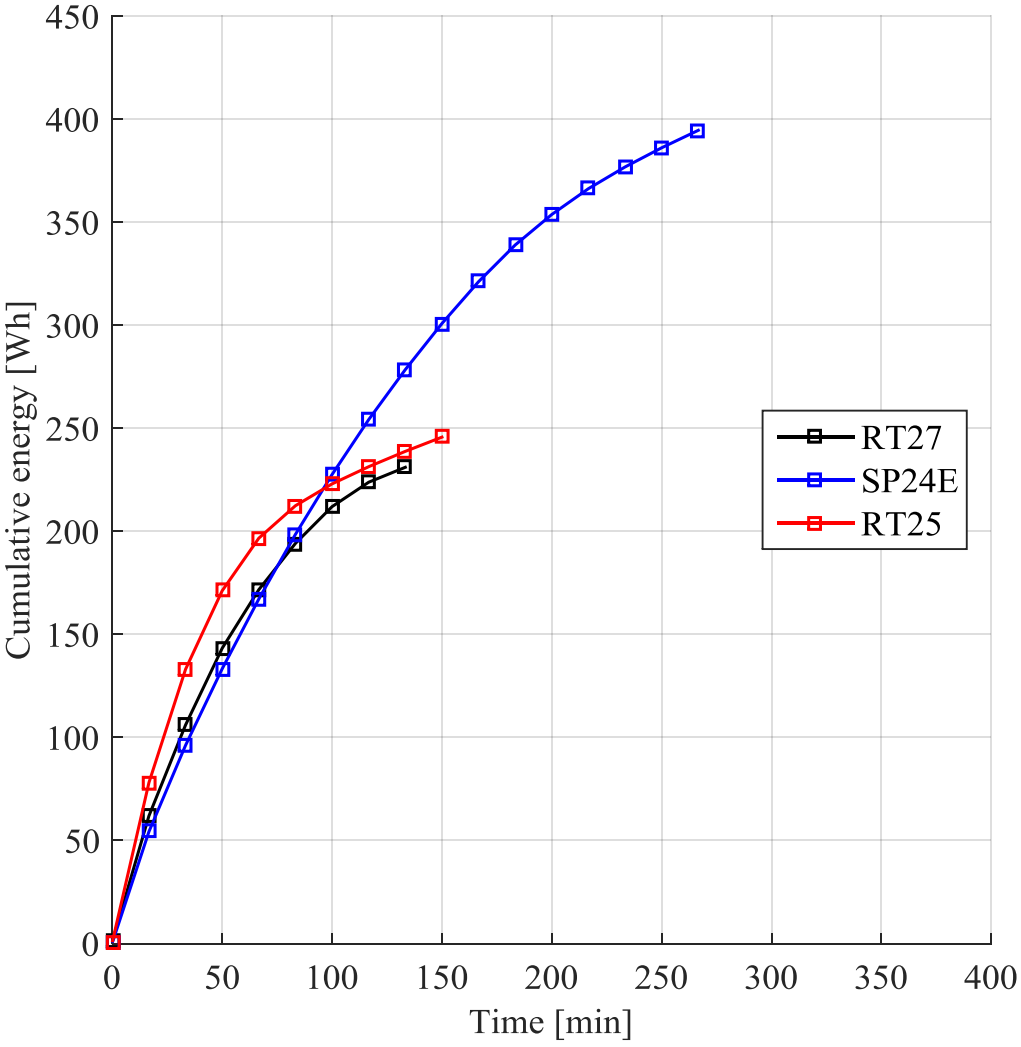

Figure I.3. Comparison of cumulative energy stored by the RT25, RT27 and SP24E modules for an air flow rate of 0.03 kg/s and an air inlet temperature 35 °C.

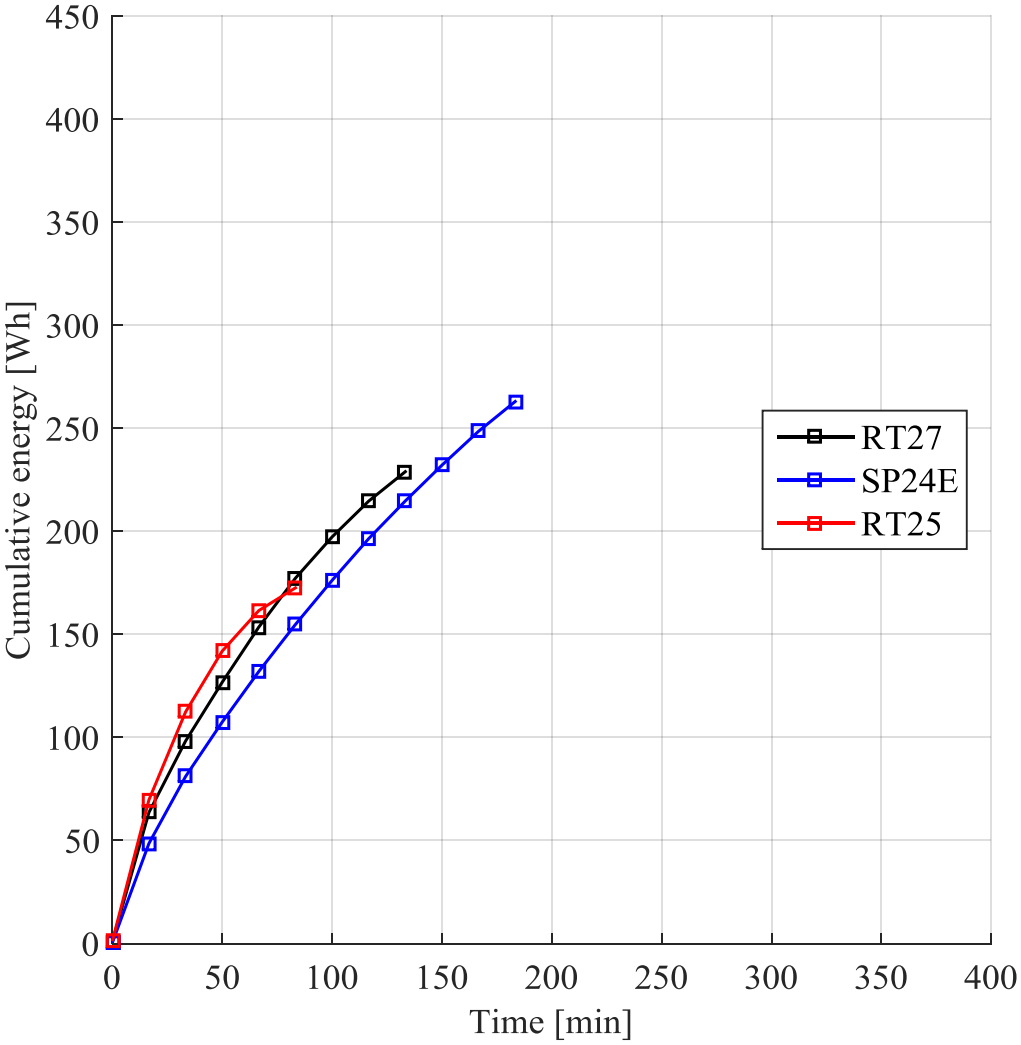

Figure I.4. Comparison of cumulative energy stored by the RT25, RT27 and SP24E modules for an air flow rate of 0.05 kg/s and an air inlet temperature 30 °C.

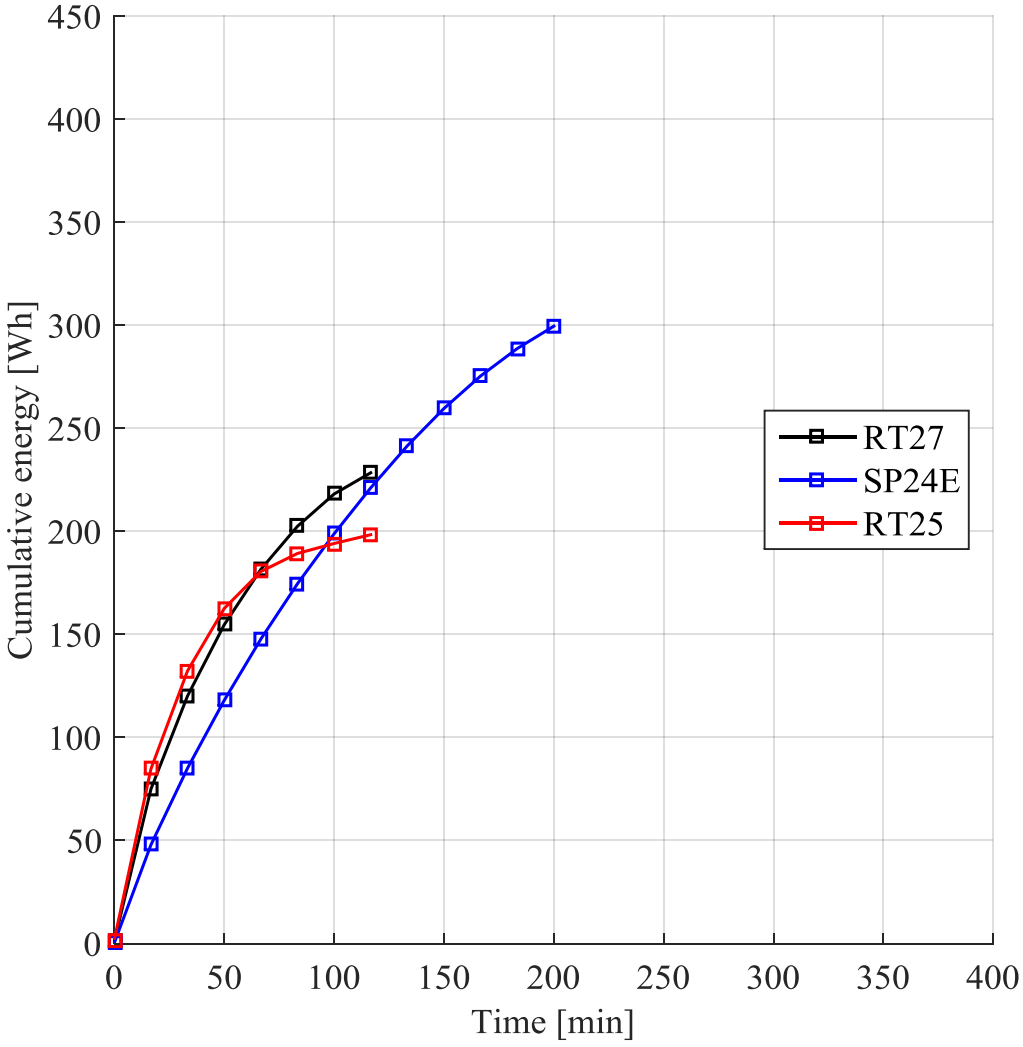

Figure I.5. Comparison of cumulative energy stored by the RT25, RT27 and SP24E modules for an air flow rate of 0.05 kg/s and an air inlet temperature 32 °C.

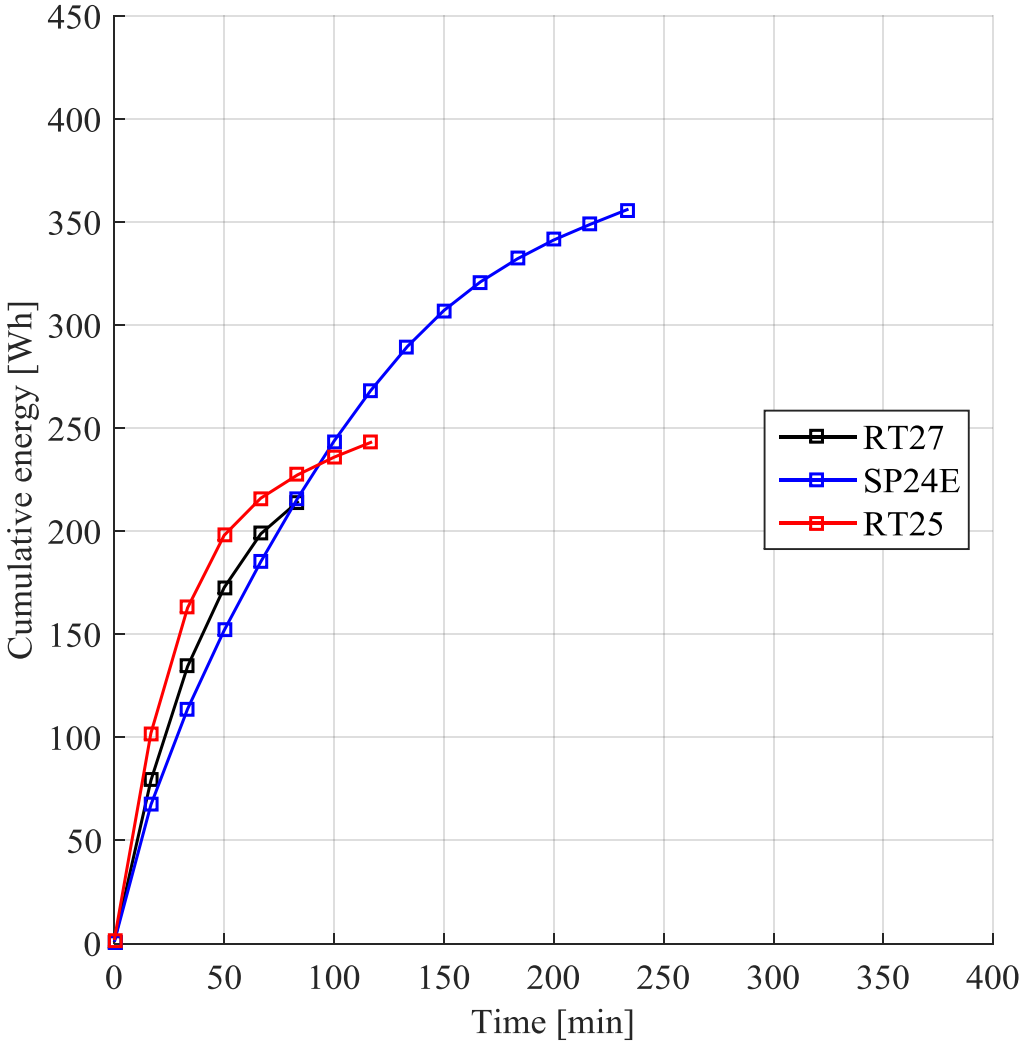

Figure I.6. Comparison of cumulative energy stored by the RT25, RT27 and SP24E modules for an air flow rate of 0.05 kg/s and an air inlet temperature 35 °C.

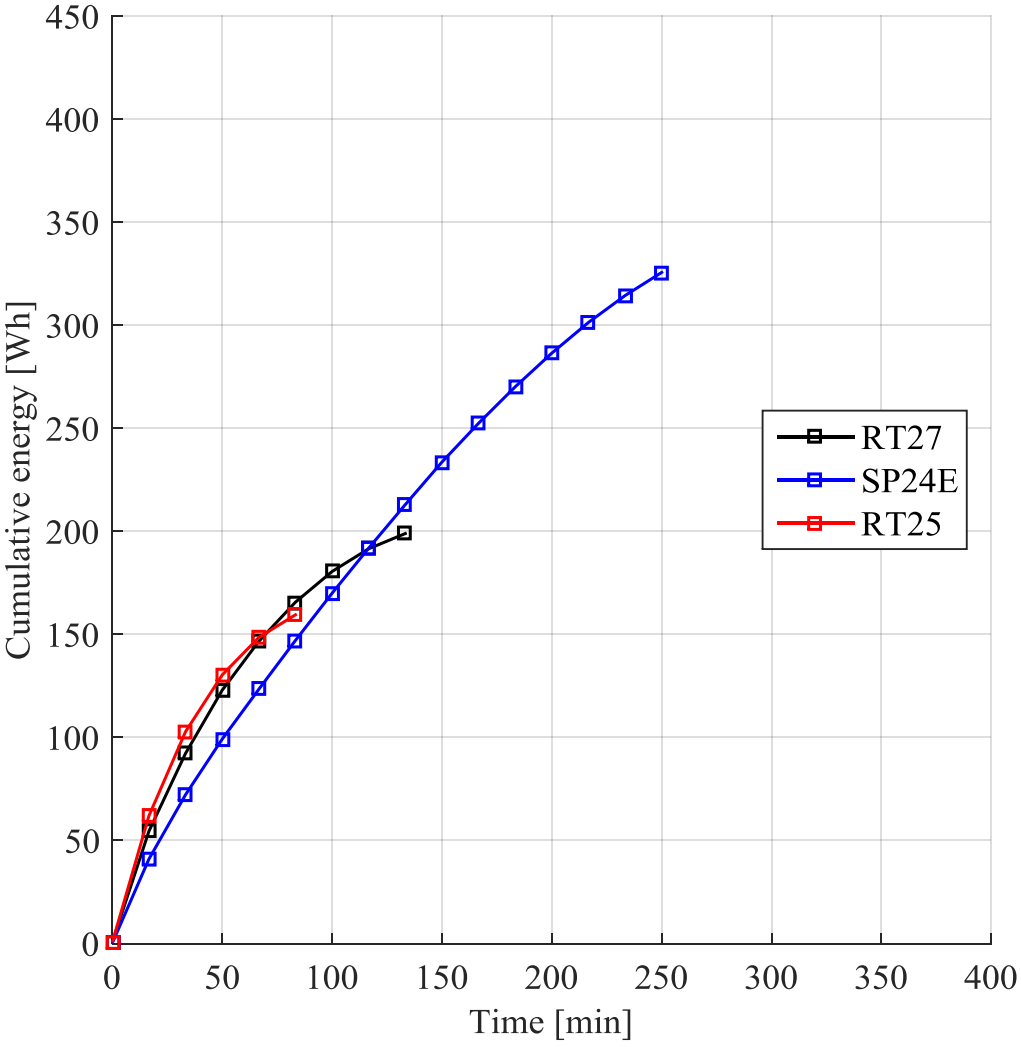

Figure I.7. Comparison of cumulative energy stored by the RT25, RT27 and SP24E modules for an air flow rate of 0.06 kg/s and an air inlet temperature 30 °C.

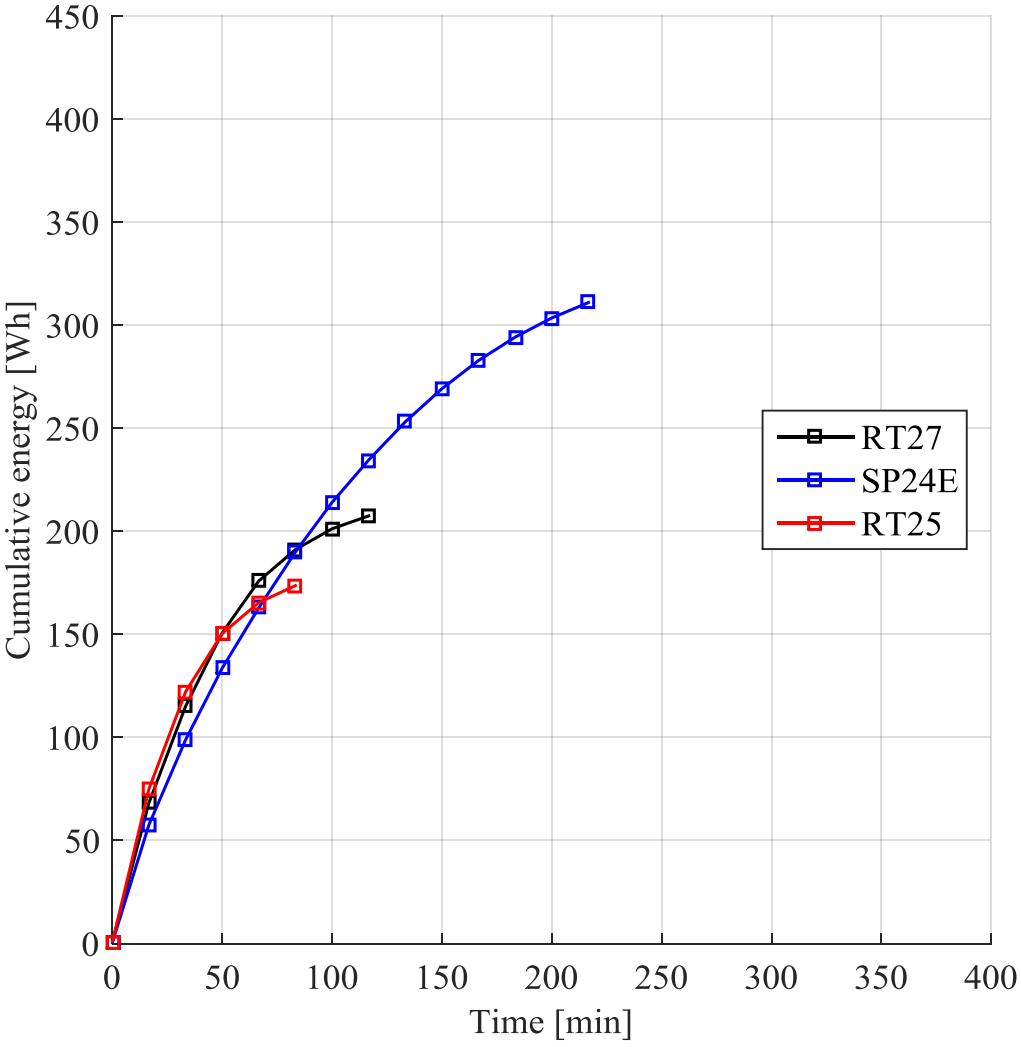

Figure I.8. Comparison of cumulative energy stored by the RT25, RT27 and SP24E modules for an air flow rate of 0.06 kg/s and an air inlet temperature 32 °C.

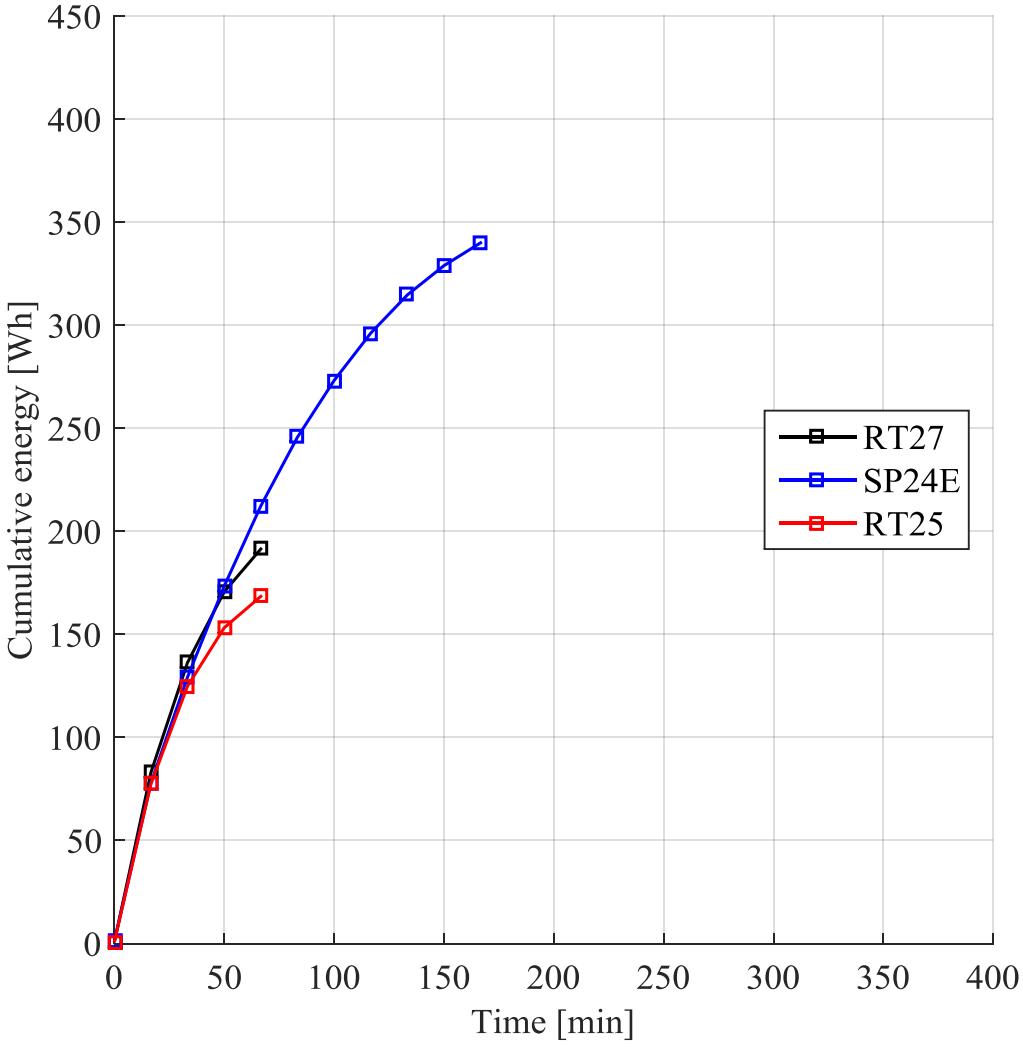

Figure I.9. Comparison of cumulative energy stored by the RT25, RT27 and SP24E modules for an air flow rate of 0.06 kg/s and an air inlet temperature 35 °C.

APPENDIX J. EFFECT OF AIR MASS FLOW RATE ON CUMULATIVE ENERGY ABSORBED

This Appendix gives all the experimental results for the effect of air mass flow rate on the cumulative energy absorbed by the RT25, RT27 and SP24E modules.

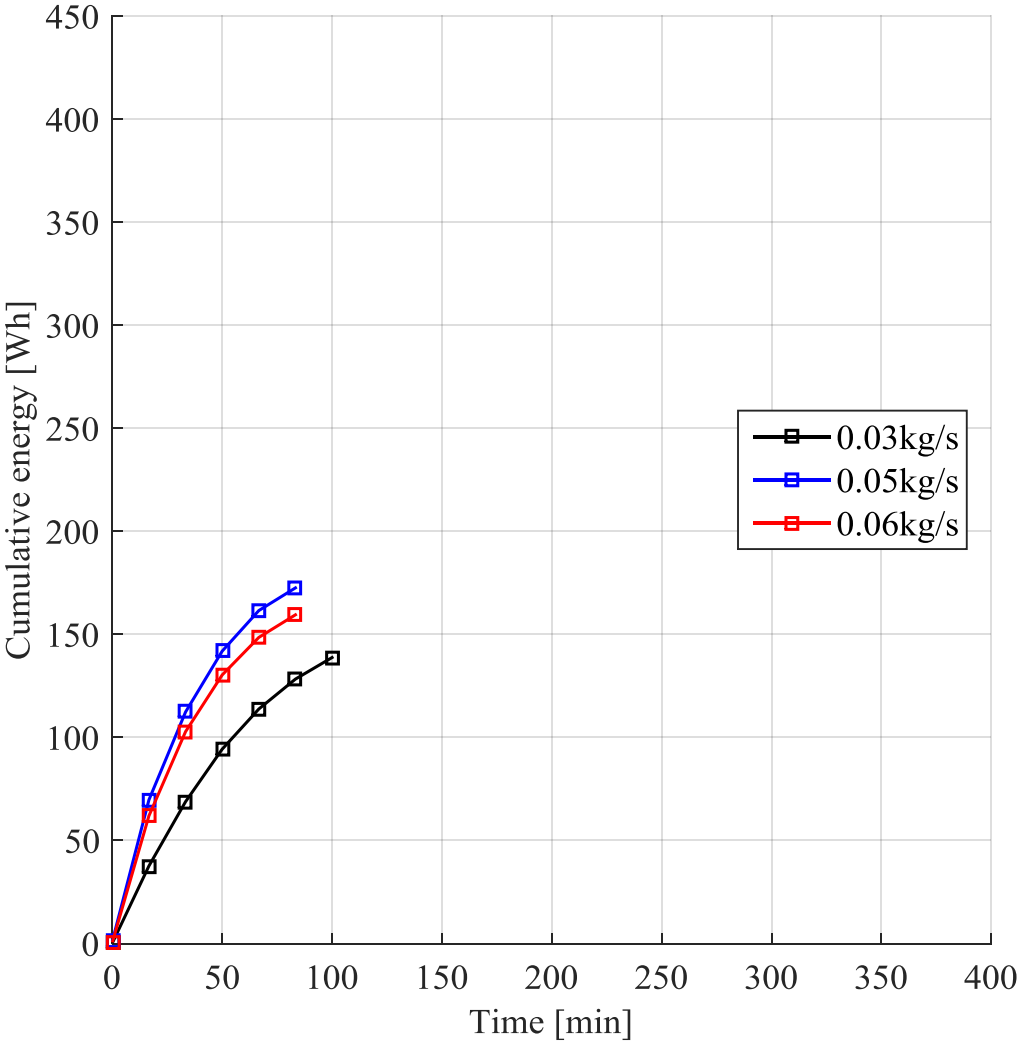

Figure J.1. Effect of air mass flow rate on the cumulative energy absorbed into an RT25 module with an air inlet temperature of 30°C.

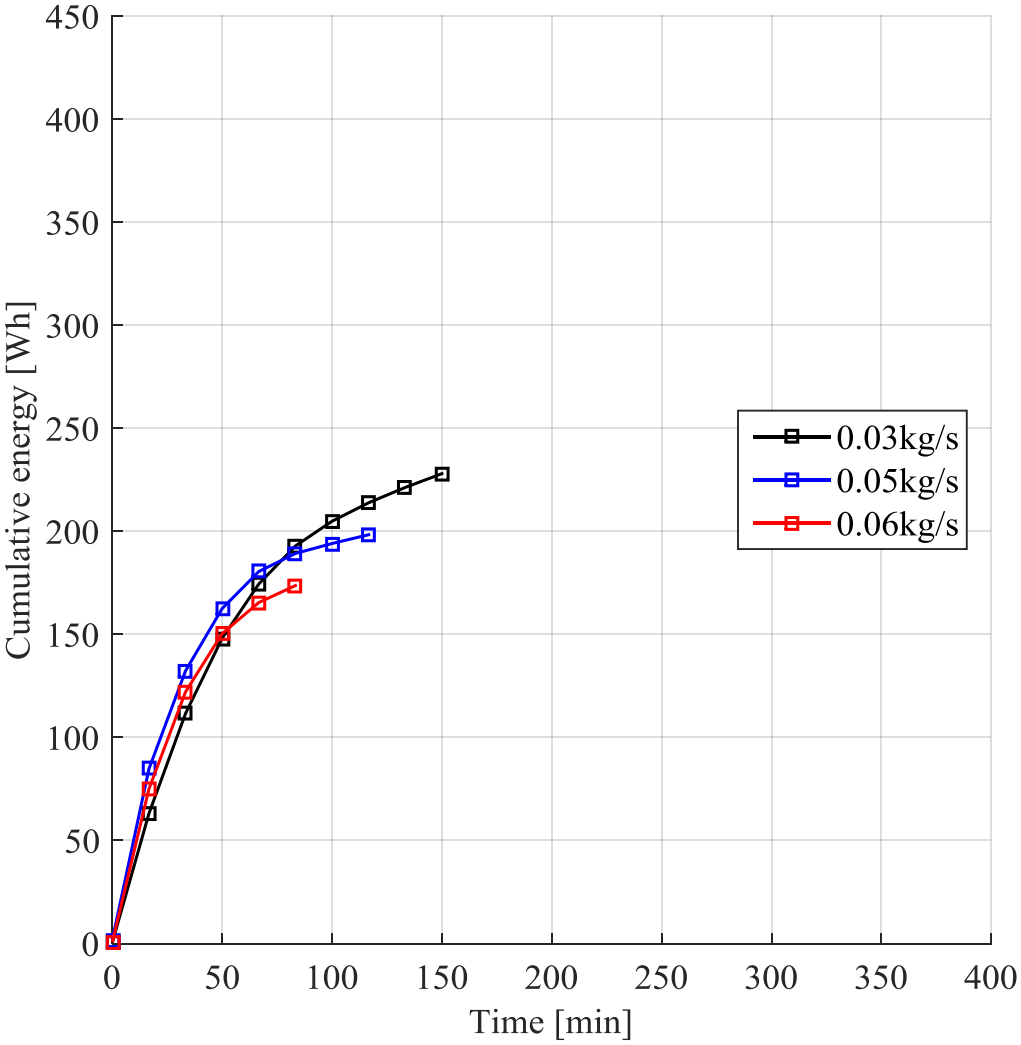

Figure J.2. Effect of air mass flow rate on the cumulative energy absorbed into an RT25 module with an air inlet temperature of 32°C.

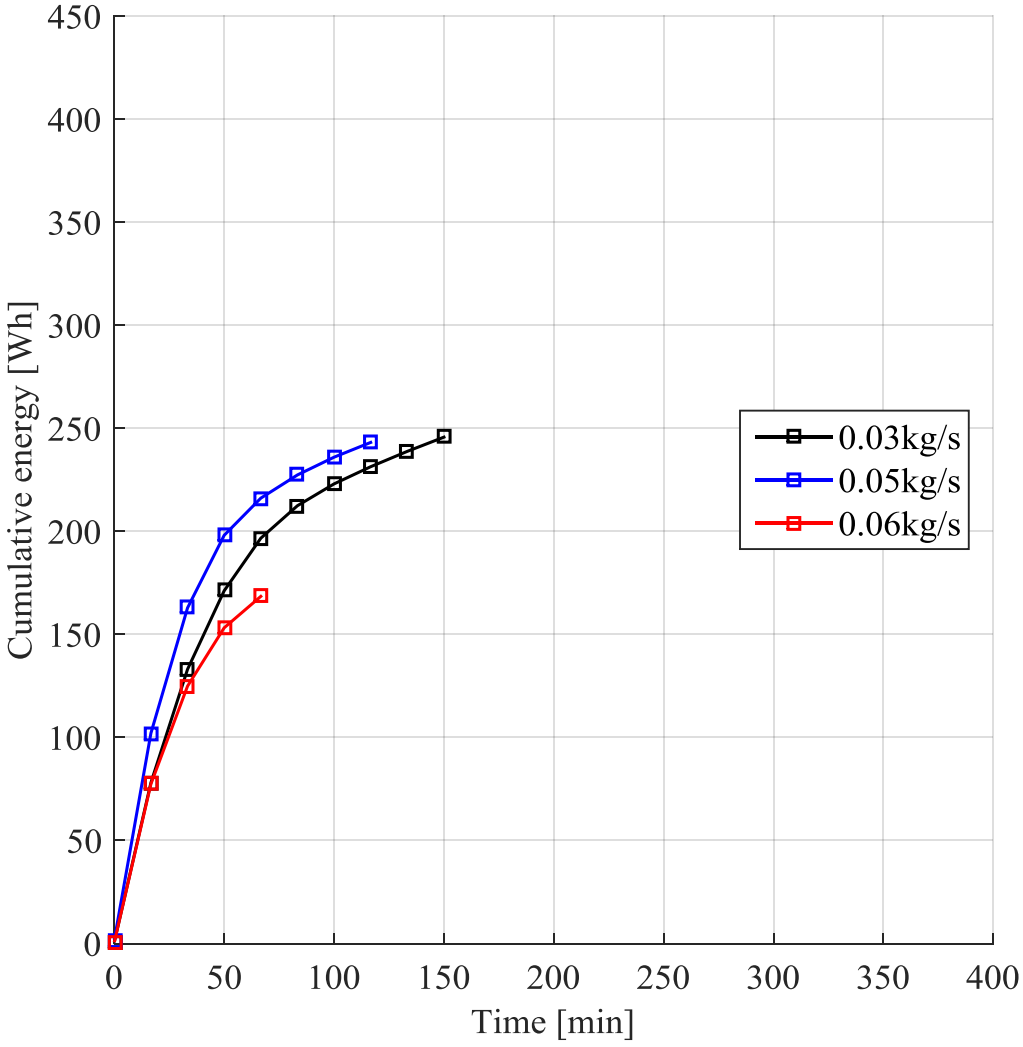

Figure J.3. Effect of air mass flow rate on the cumulative energy absorbed into an RT25 module with an air inlet temperature of 35°C.

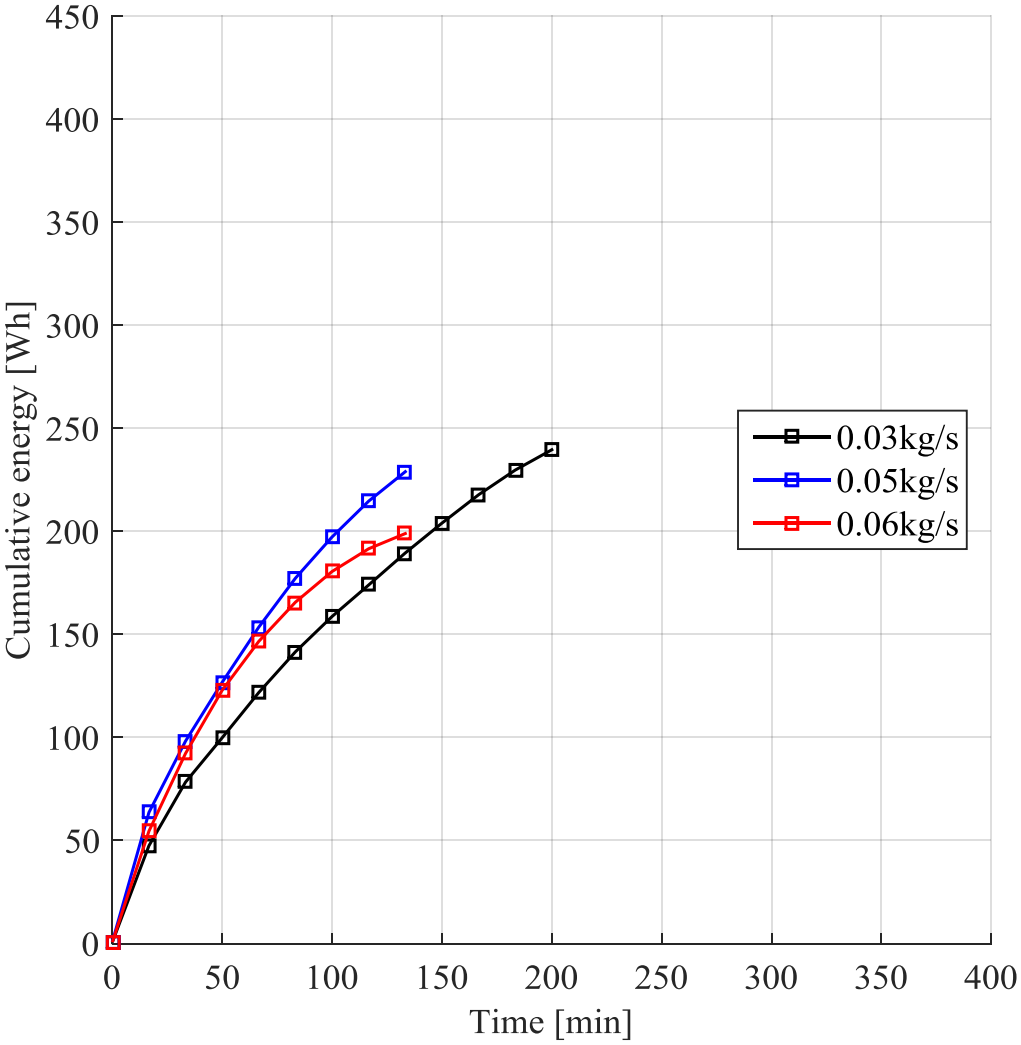

Figure J.4. Effect of air mass flow rate on the cumulative energy absorbed into an RT27 module with an air inlet temperature of 30°C.

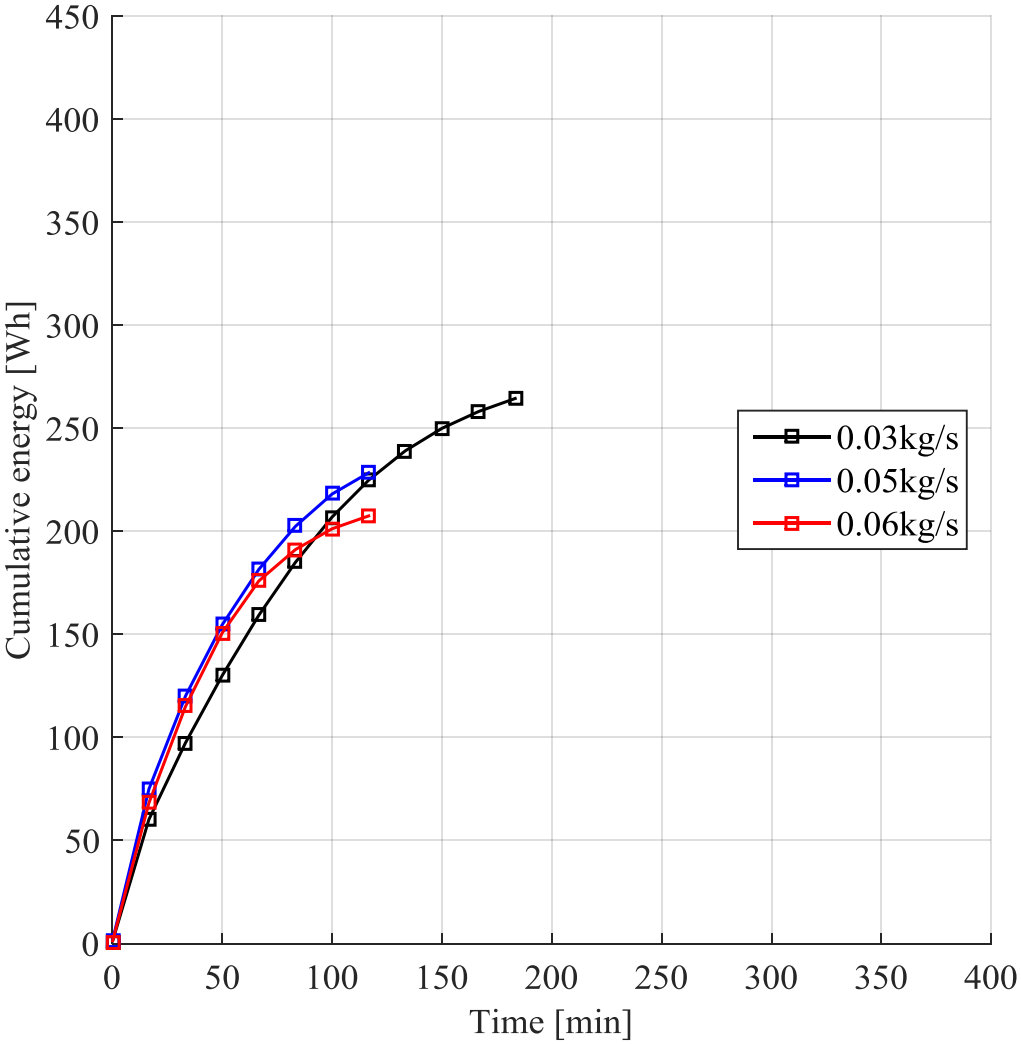

Figure J.5. Effect of air mass flow rate on the cumulative energy absorbed into anRT27 module with an air inlet temperature of 32°C.

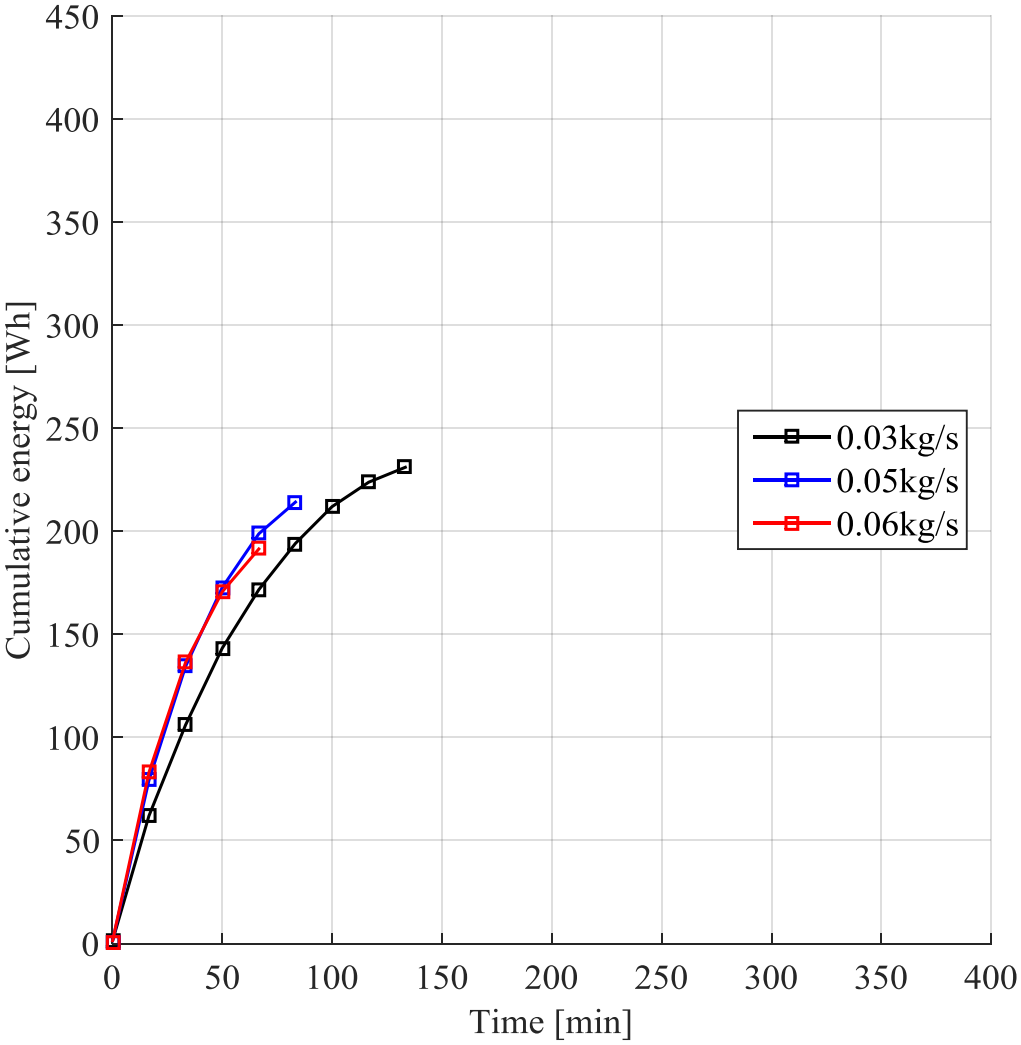

Figure J.6. Effect of air mass flow rate on the cumulative energy absorbed into an RT27 module with an air inlet temperature of 35°C.

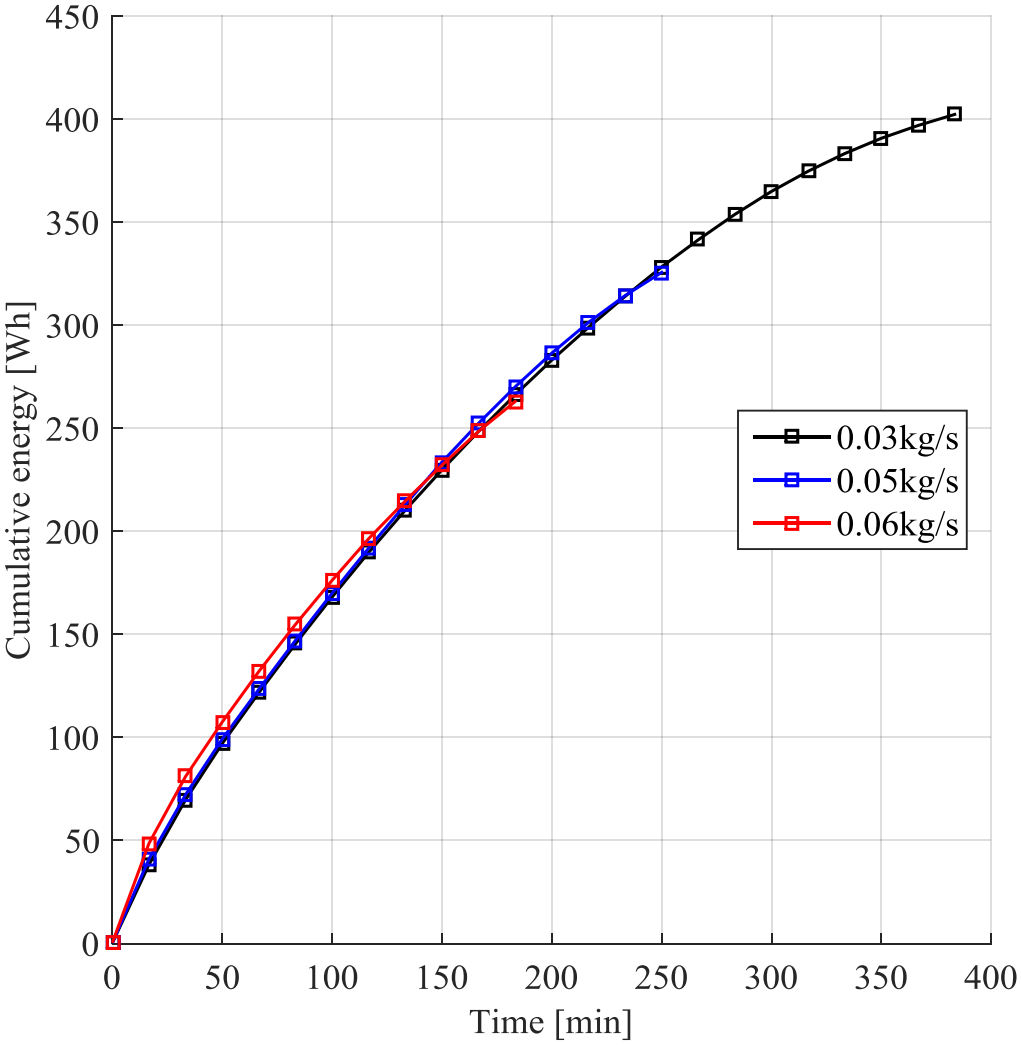

Figure J.7. Effect of air mass flow rate on the cumulative energy absorbed into an SP24E module with an air inlet temperature of 30°C.

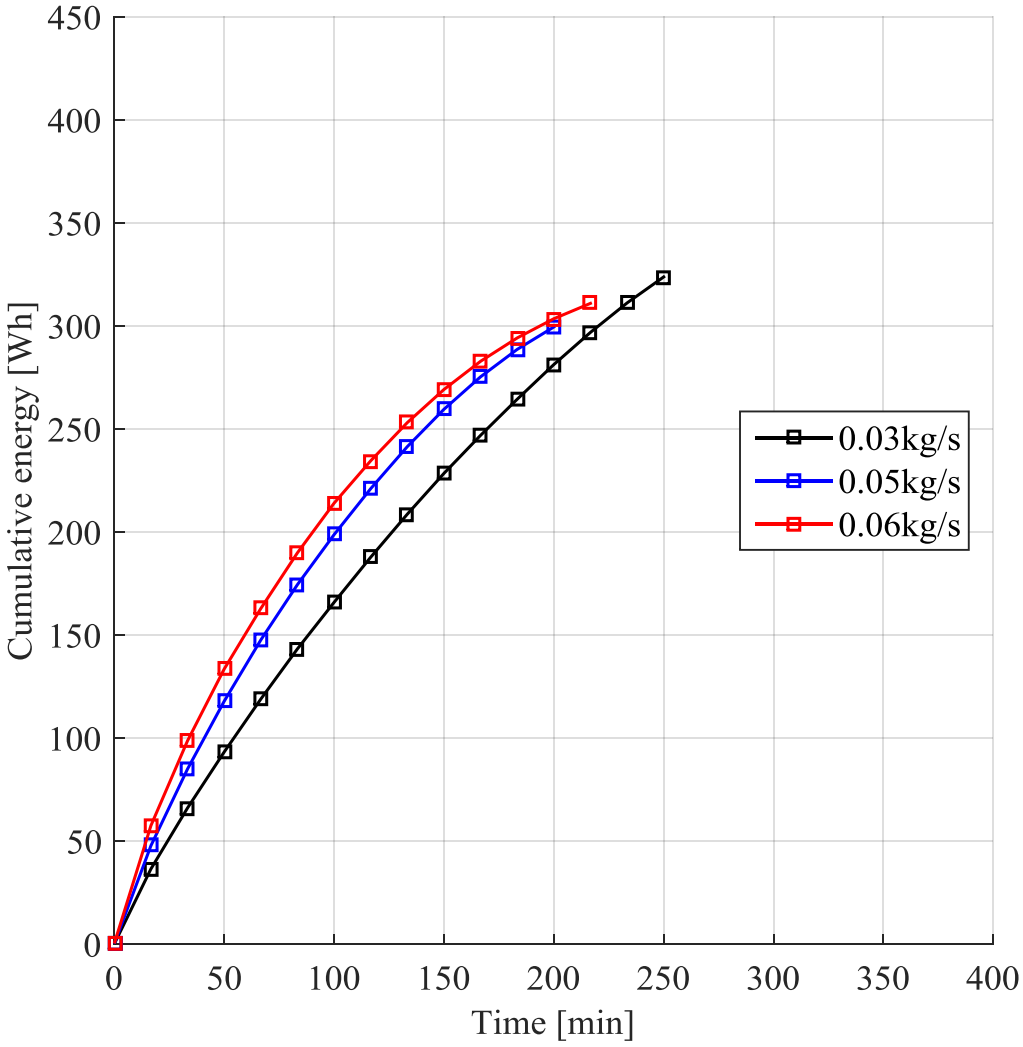

Figure J.8. Effect of air mass flow rate on the cumulative energy absorbed into an SP24E module with an air inlet temperature of 32°C.

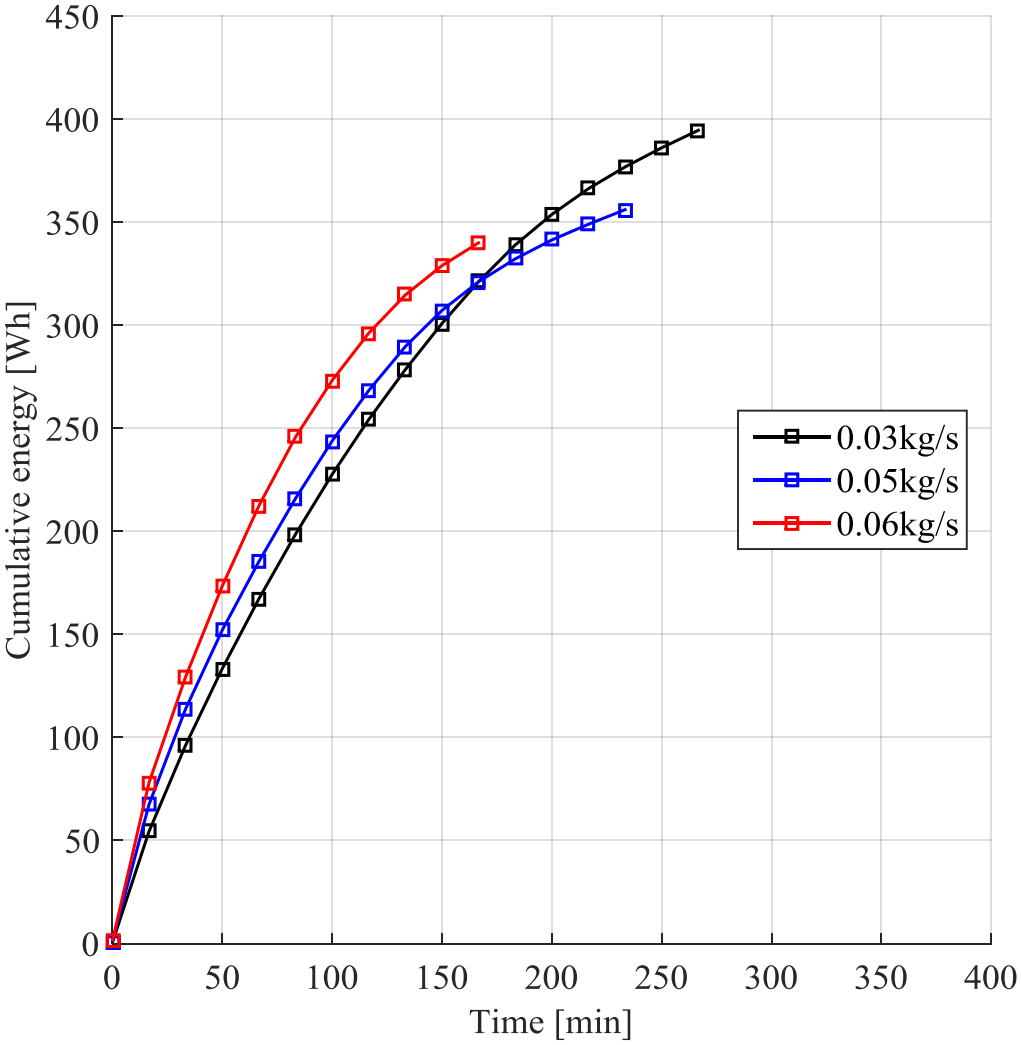

Figure J.9. Effect of air mass flow rate on the cumulative energy absorbed into an SP24E module with an air inlet temperature of 35°C.

APPENDIX K. EFFECT OF INLET AIR TEMPERATURE ON CUMULATIVE ENERGY ABSORBED

This Appendix gives all the experimental results for the effect of inlet air temperature on cumulative energy absorbed into the RT25, RT27 and SP24E modules.

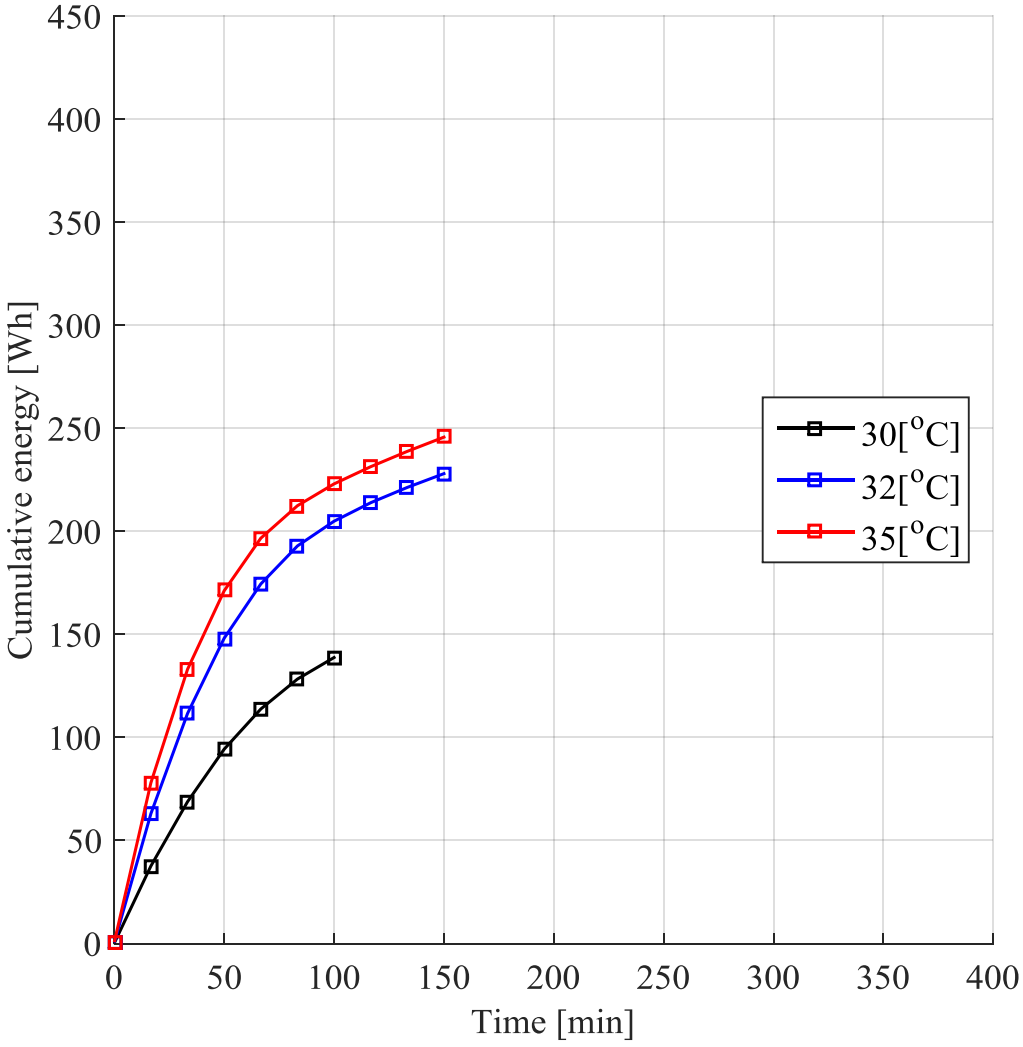

Figure K.1. Effect of the inlet air temperature on the cumulative energy absorbed into an RT25 module for an air mass flow rate of 0.03 kg/s.

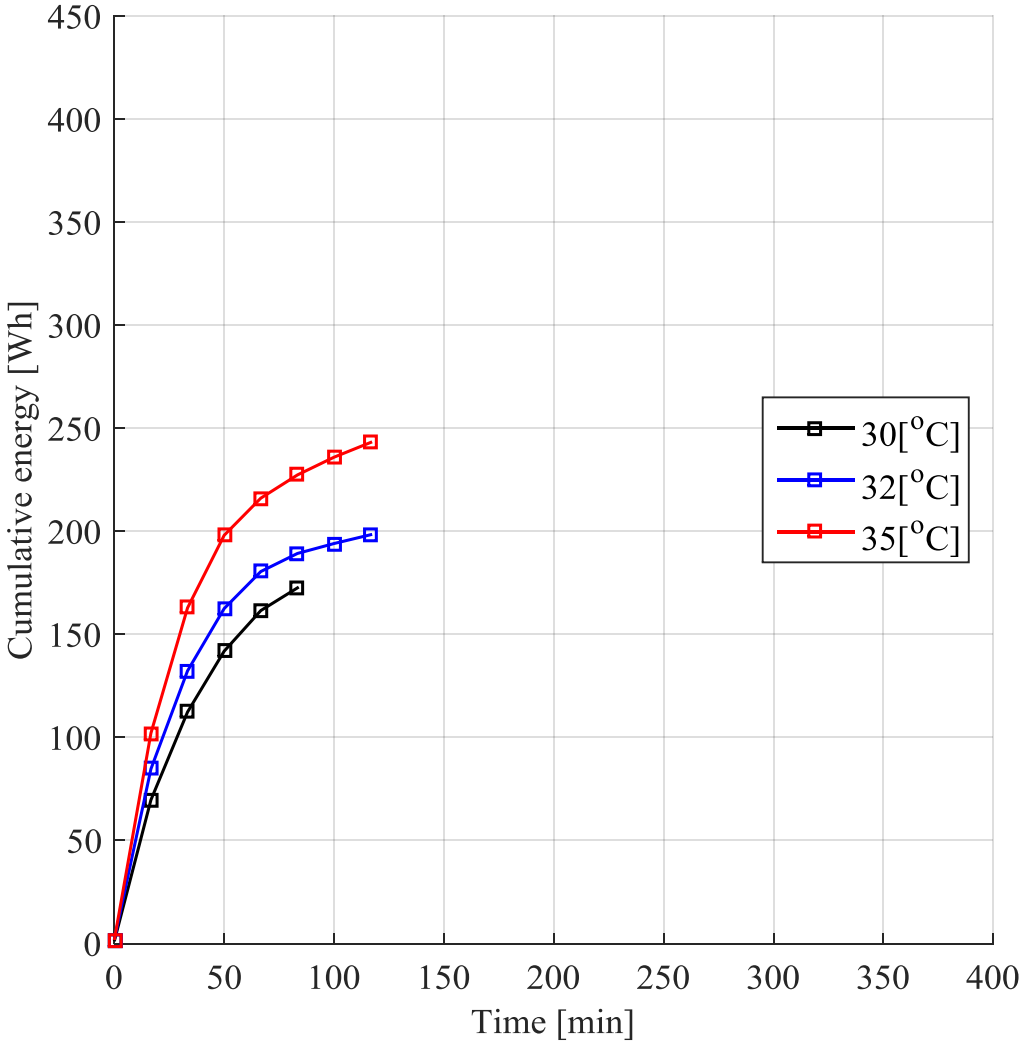

Figure K.2. Effect of the inlet air temperature on the cumulative energy absorbed into an RT25 module for an air mass flow rate of 0.05 kg/s.

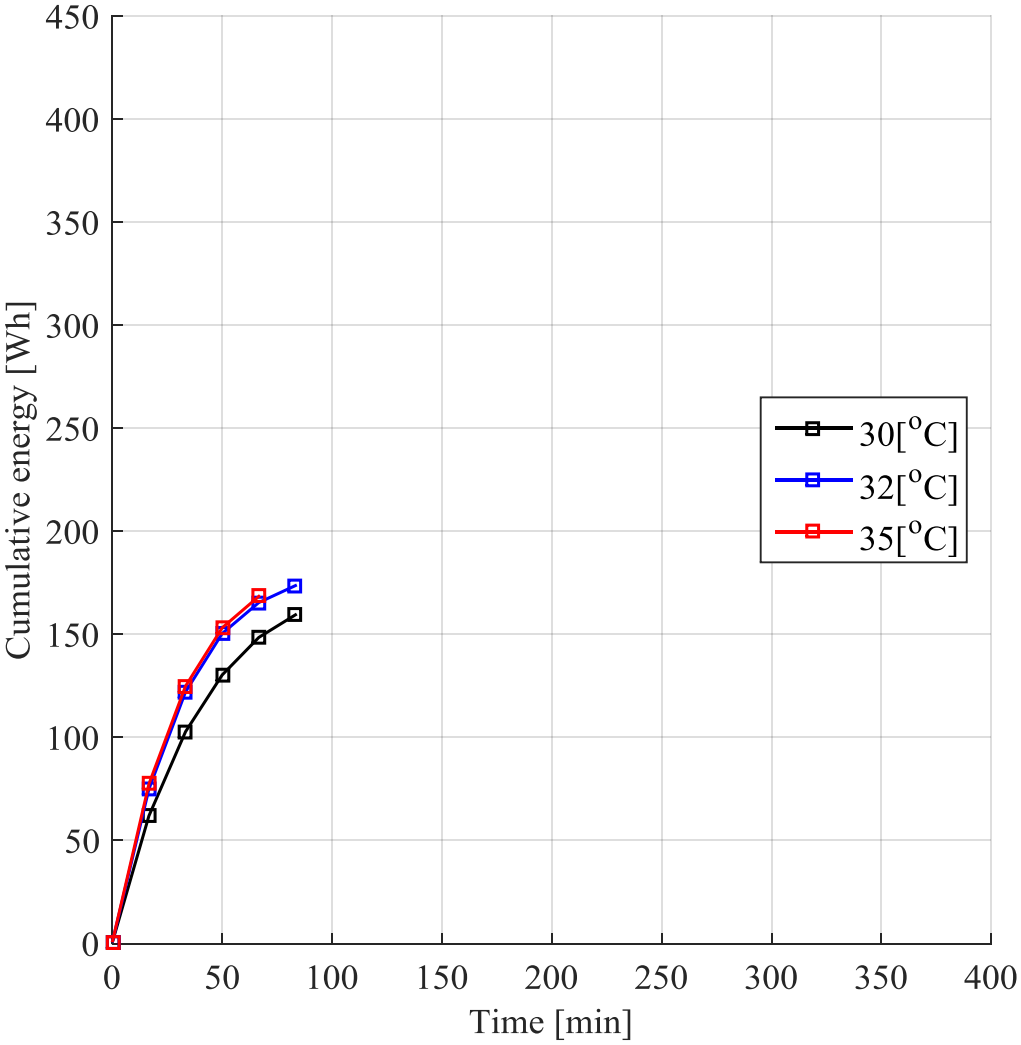

Figure K.3. Effect of the inlet air temperature on the cumulative energy absorbed into an RT25 module for an air mass flow rate of 0.06 kg/s.

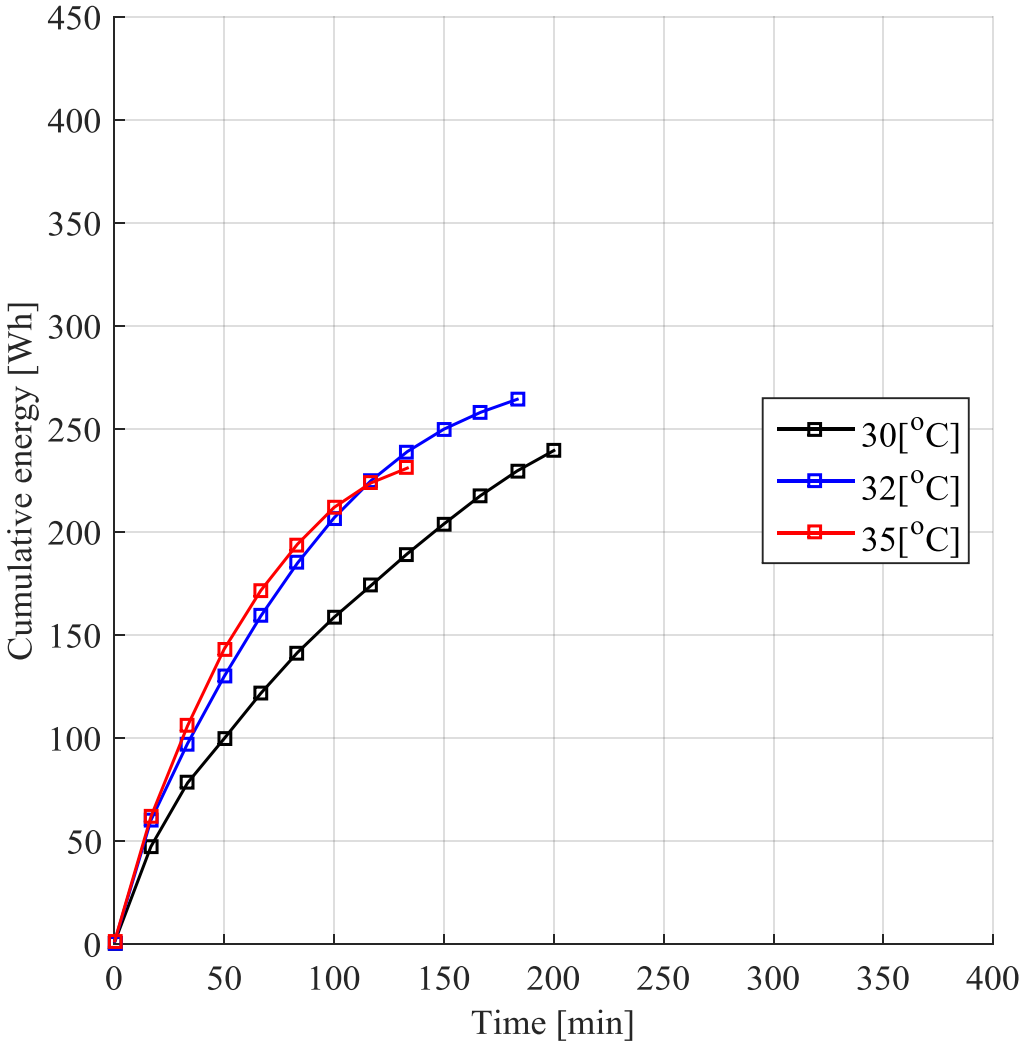

Figure K.4. Effect of the inlet air temperature on the cumulative energy absorbed into an RT27 module for an air mass flow rate of 0.03 kg/s.

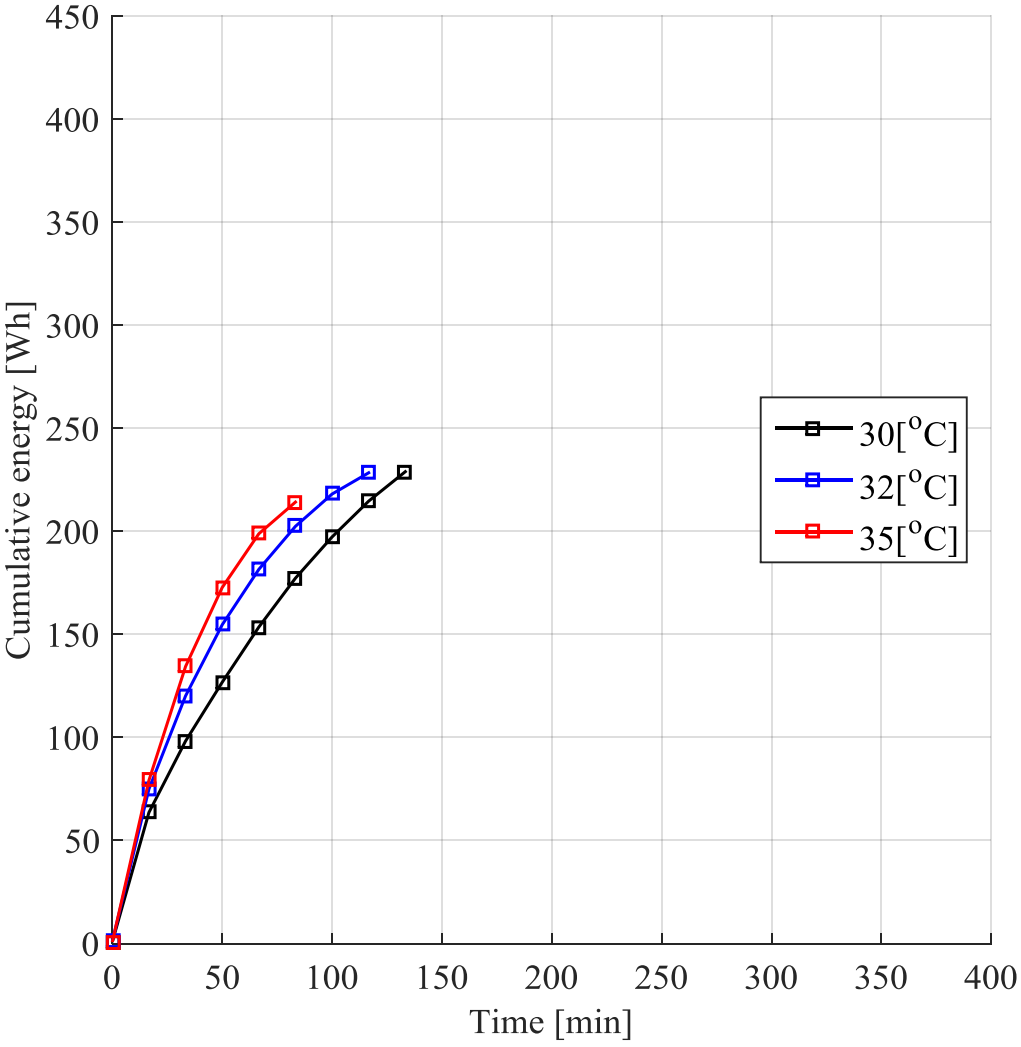

Figure K.5. Effect of the inlet air temperature on the cumulative energy absorbed into an RT27 module for an air mass flow rate of 0.05 kg/s.

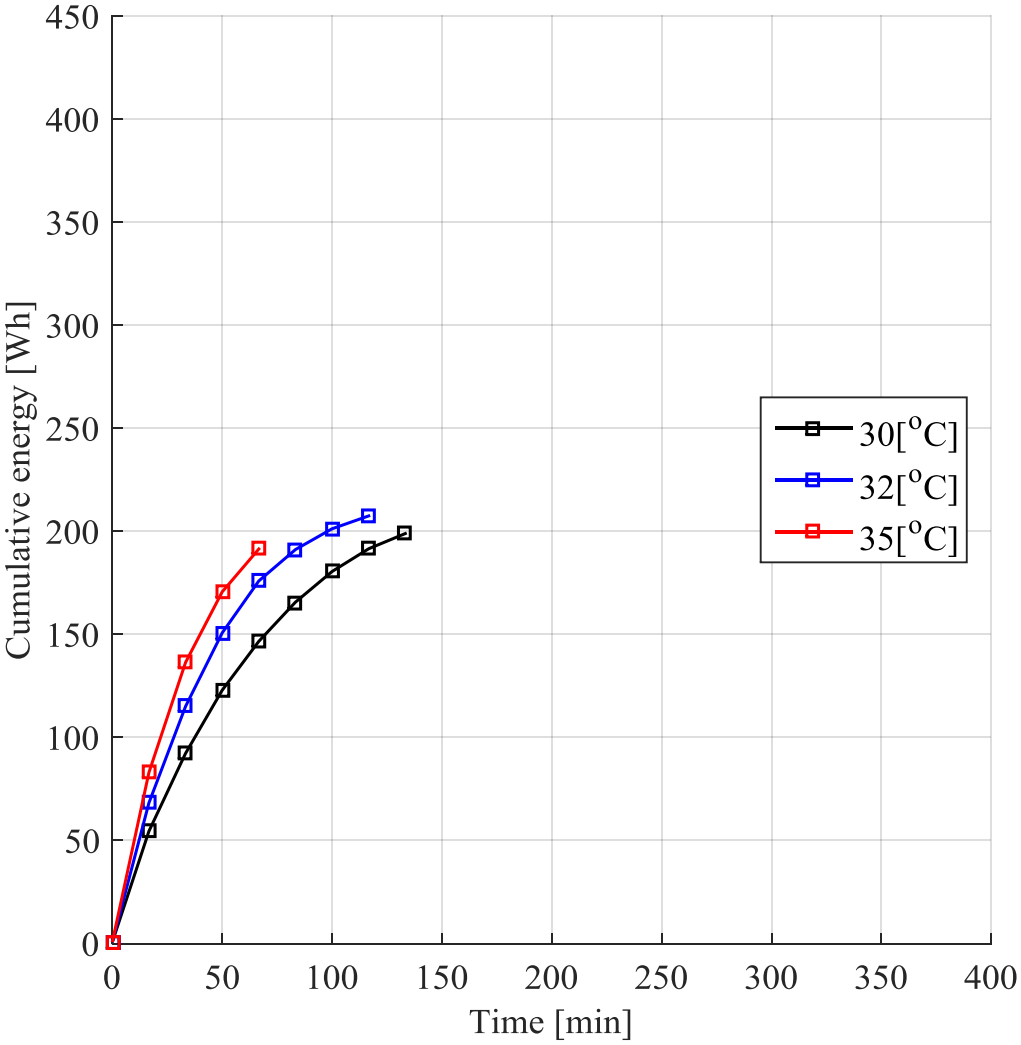

Figure K.6. Effect of the inlet air temperature on the cumulative energy absorbed into an RT27 module for an air mass flow rate of 0.06 kg/s.

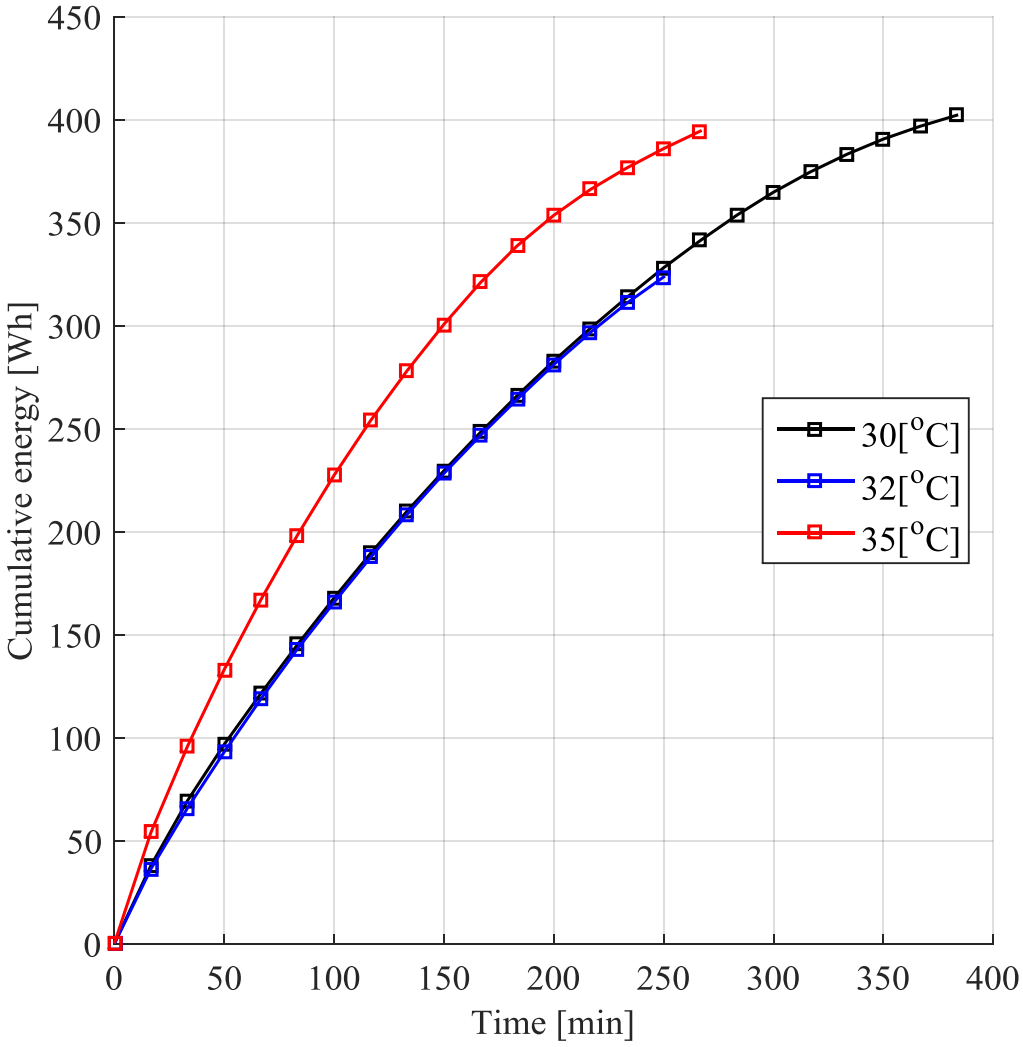

Figure K.7. Effect of the inlet air temperature on the cumulative energy absorbed into an SP24E module for an air mass flow rate of 0.03 kg/s.

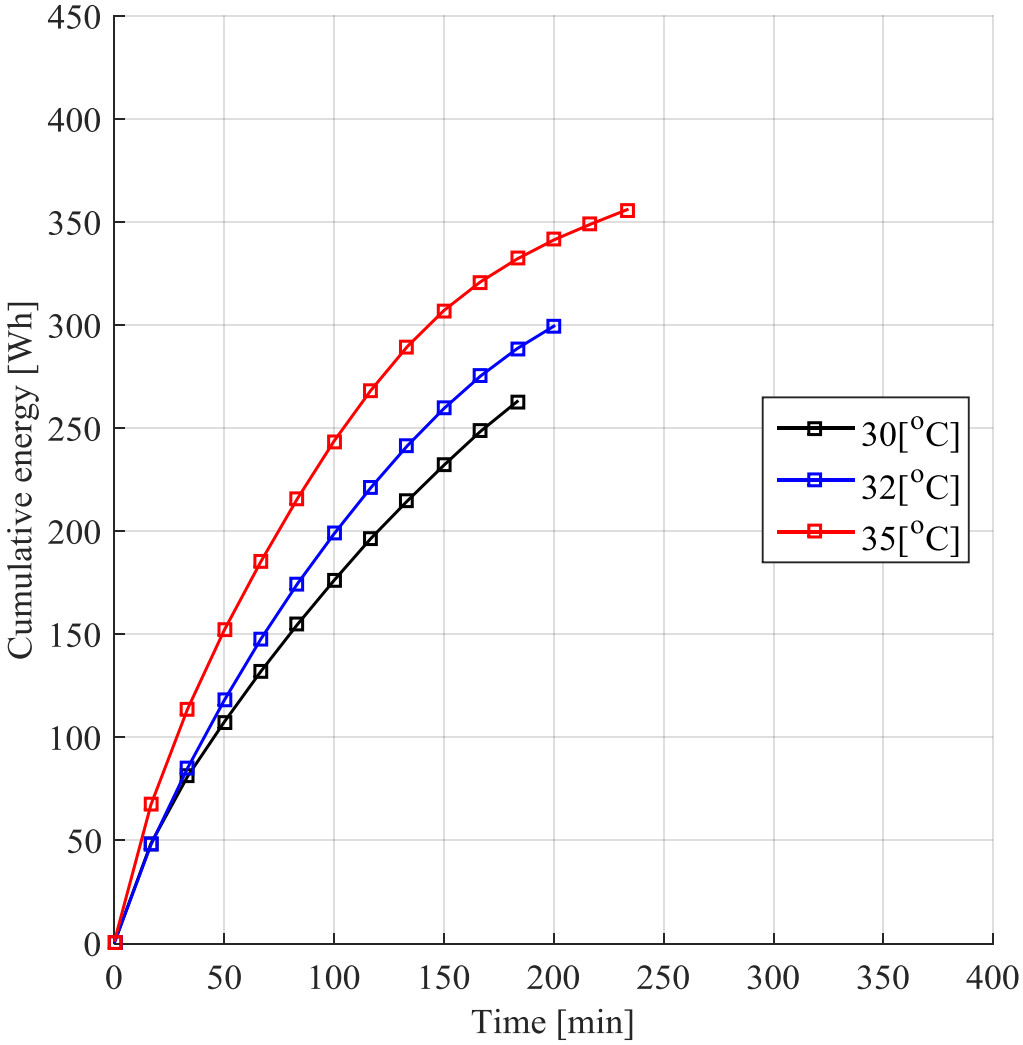

Figure K.8. Effect of the inlet air temperature on the cumulative energy absorbed into an SP24E module for an air mass flow rate of 0.05 kg/s.

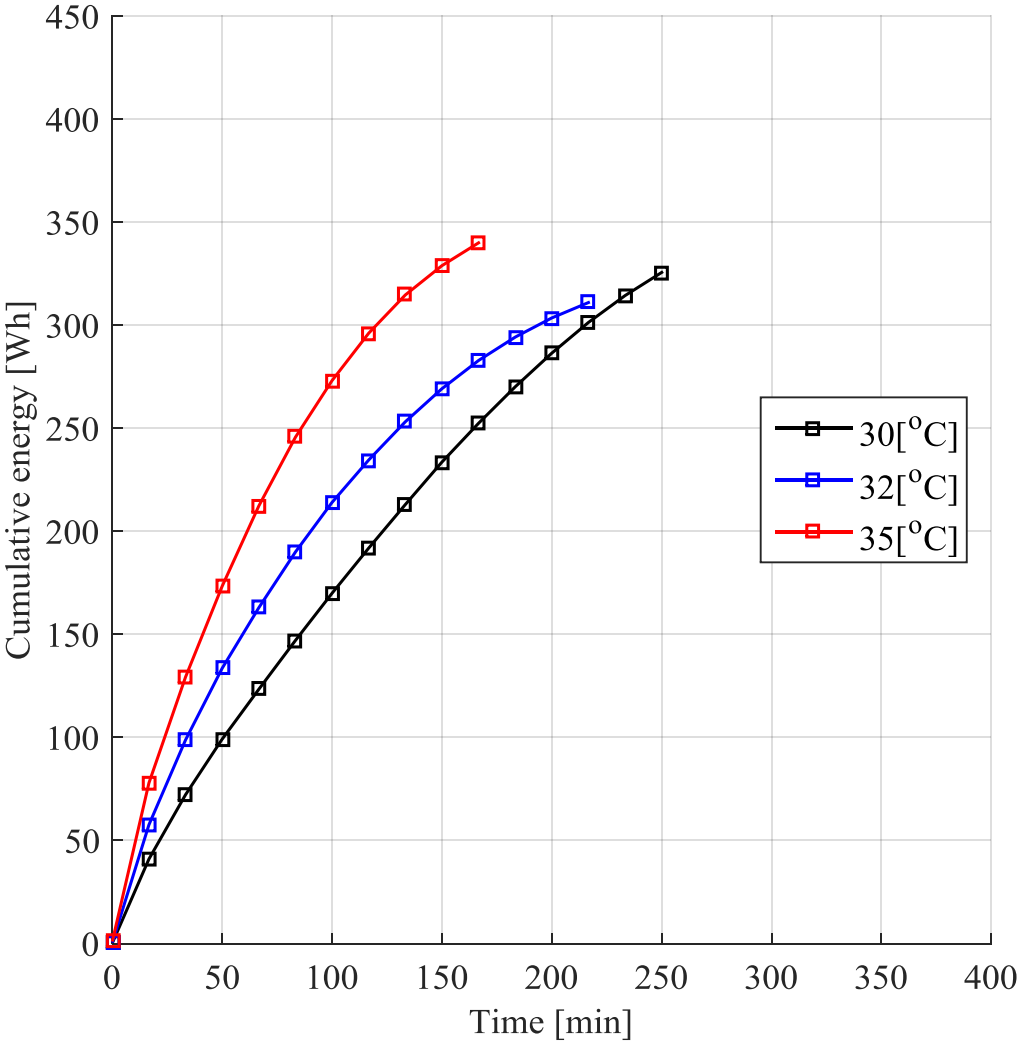

Figure K.9. Effect of the inlet air temperature on the cumulative energy absorbed into an SP24E module for an air mass flow rate of 0.06 kg/s.